# FABRICATION, STRENGTH AND OXIDATION OF MOLYDENUM–SILICON-BORON ALLOYS FROM REACTION SYNTHESIS

A Dissertation
Presented to
The Academic Faculty

By

Michael Robert Middlemas

In Partial Fulfillment
Of the Requirements for the Degree
Doctor of Philosophy in Materials Science and Engineering

Georgia Institute of Technology

May 2009

**FABRICATION, STRENGTH AND OXIDATION OF MOLYDENUM–SILICON-BORON ALLOYS FROM REACTION SYNTHESIS**

Approved by:

Dr. Joe. K. Cochran, Advisor
School of Materials Science and Engineering
*Georgia Institute of Technology*

Dr. Thomas H. Sanders, Jr.
School of Materials Science and Engineering
*Georgia Institute of Technology*

Dr. Kenneth H. Sandhage
School of Materials Science and Engineering
*Georgia Institute of Technology*

Dr. Naresh N. Thadhani
School of Materials Science and Engineering
*Georgia Institute of Technology*

Mr. Douglas M. Berczik
Materials and Process Engineering
*Pratt and Whitney*

Approved: March 27, 2009

# ACKNOWLEDGEMENTS

This work has been supported by the Office of Naval Research under Naval Air Systems Command contract N00421-05-1-0002. I would like to thank our project monitors Dave Shifler and Rob Kowalik, as well our past project monitors, Steve Fishman and Gil London, all of whom have given valuable guidance through the duration of this project. Many thanks go to Doug Berczik of Pratt & Whitney who has provided much support and advice on this project. His long running experience in the field of Mo-Si-B alloys has proven invaluable in helping steer the course of this project.

I would like to give my sincere appreciation to my committee members here at Georgia Tech, all of whom have had a significant influence on my experience here. My first exposure to research was through the SURF program administered by Dr. Thadhani and I am very thankful for that experience. Dr. Sanders and Dr. Sandhage both served on my master's thesis committee and I am honored to have them as a part of my Ph.D. committee. I am especially grateful to my advisor Dr. Cochran who has given much guidance in this project, but has also given me much freedom to help guide the project. It has been a pleasure to work an advisor who is so excited about the work.

The depth of this work would not have been possible without the help of my fellow group members Dr. Tammy McCoy, Chris Rockett and Will Daloz, as well as the other students in the department who have lent a hand. I would also like to acknowledge the professors who have collaborated on portions of this research. Dr. Arun Gokhale

from Georgia Tech provided the two-point correlation data sets and Dr. Sharvan Kumar of Brown University conducted the high-temperature tensile tests.

On a personal note, I would like to express deep gratitude to my family and friends for the support they have given me along the way. I am very thankful to my parents for instilling in me a love of learning and discovery. The friends I have made at Outdoor Recreation at Georgia Tech have helped keep my spirits up and I have enjoyed the kayaking adventures we have gone on together to California, Colorado, New Mexico, West Virginia, Mexico and across the southeast. I am especially grateful to my best friend Jessica Wood who has been by my side throughout this entire process.

TABLE OF CONTENTS

LIST OF TABLES

LIST OF FIGURES

# SUMMARY

Mo-Si-B alloys are a leading candidate for the next generation of jet turbine engine blades and have the potential to raise the operating temperatures by 300-400°C, which would dramatically increase power and efficiency. The alloys of interest are a three-phase mixture of the molybdenum solid solution ($Mo_{ss}$) and two intermetallic phases, $Mo_3Si$ (A15) and $Mo_5SiB_2$ (T2). A novel powder metallurgical method was developed which uses the reaction of molybdenum, silicon nitride ($Si_3N_4$) and boron nitride (BN) powders to synthesize a fine dispersion of the intermetallic phases in a $Mo_{ss}$ matrix. The covalent nitrides are stable in oxidizing environments up to 1000ºC, allowing for fine particle processing without the formation of silicon and boron oxides. The process developed uses standard powder processing techniques to create Mo-Si-B alloys in a less complex and expensive manner than previously demonstrated.

The formation of the intermetallic phases was examined by thermo-gravimetric analysis and x-ray diffraction. The start of the reactions to form the T2 and A15 phases were observed at 1140°C and 1193°C and the reactions have been demonstrated to be complete in as little as two hours at 1300°C. This powder metallurgy approach yields a fine dispersion of intermetallics in the $Mo_{ss}$ matrix, with average grain sizes of 2-4μm. Densities up to 95% of theoretical were attained from pressureless sintering at 1600°C and full theoretical density was achieved by hot-isostatic pressing (HIP). Low temperature sintering and HIPing was attempted to limit grain growth and to reduce the

equilibrium silicon concentration in the $Mo_{ss}$ matrix. Sintering and HIPing at 1300°C reduced the grain sizes of all three phases by over a factor of two.

Powder metallurgy provides an opportunity for microstructure control through changes in raw materials and processing parameters. Microstructure examination by electron back-scatter diffraction (EBSD) imaging was used to precisely define the location of all three phases and to measure the volume fractions and grain size distributions. Microstructural quantification techniques including two-point correlation functions were used to quantify microstructural features and correlate the BN powder size and morphology to the distribution of the intermetallic phases.

High-temperature tensile tests were conducted and yield strengths of 580MPa at 1100°C and 480MPa at 1200°C were measured for the Mo-2Si-1B wt.% alloy. The yield strength of the Mo-3Si-1B wt.% alloy was 680MPa at 1100°C and 420MPa at 1300°C. A review of the pertinent literature reveals that these are among the highest yield strengths measured for these compositions.

The oxidation resistance in air at 1000 and 1100°C was found to be comparable to the best values reported in the literature. The protective borosilicate surface layer was formed quickly due to the close spacing of intermetallic particles and pre-oxidation treatment was developed to further limit the transient oxidation behavior. An oxidation model was developed which factors in the different stages of oxidation to predict compositions which minimize the total metal recession due to oxidation.

# CHAPTER 1

# INTRODUCTION

The performance and efficiency of jet turbine engines are dependent on the temperatures achievable in the hottest region of the engine. Current technologies rely on nickel-based superalloys, and material advances including the development of directionally solidified and single crystal materials have led to increased service temperatures and extended lifetimes. The turbine blades in modern jet engines now operate at temperatures up to 1150ºC, approaching 85% of their melting point. By utilizing technologies such as thermal barrier coatings, internal cooling and film cooling, the temperature inside the engines can be pushed as high as 1500ºC [1]. Dramatic increases in power and efficiency can be gained through higher operating temperatures, but the gains are offset by the systems necessary to cool the airfoils. The development trend for the maximum service temperature of nickel superalloys has approached a limit over the past six decades and there is a need for a new class of high-temperature structural materials for the continued advancement of jet turbine engine technology.

Refractory metals such as molybdenum have high melting points and excellent high temperature mechanical properties; however, the oxidation resistance of these metals is poor. An alloy system that has gained much attention is the Mo-Si-B ternary. Molybdenum silicides are well known for their oxidation resistance due to the formation of a protective silicate scale. Boron addition decreases the viscosity of the glass and

improves the oxidation resistance by promoting better surface coverage [2]. The Mo-Si-B phase diagram was developed by Nowotny in 1957 and later refined by Perepezko [3]. Berczik initiated investigations on the use of Mo-Si-B compositions in the molybdenum rich corner of the phase diagram for turbine blades [4,5]. The alloys of interest are in the three phase region consisting of the molybdenum solid solution ($Mo_{ss}$) and two intermetallic phases $Mo_3Si$ (A15) and $Mo_5SiB_2$ (T2). All three phases have melting points above 2000ºC and the phase field is stable to room temperature, making these alloys excellent candidates for high temperature structural use. Crack bridging and entrapment by the more ductile $Mo_{ss}$ phase improves the fracture toughness, and the intermetallic phases impart high-temperature creep resistance and form the protective borosilicate surface layer which provides oxidation resistance.

Mo-Si-B alloys have potential for the next generation of jet turbine engines but efforts to develop a viable alloy have failed to obtain a suitable combination of mechanical properties and oxidation resistance. To achieve high strength and fracture toughness the alloys must be processed in a manner that creates a continuous $Mo_{ss}$ matrix. In addition, a fine dispersion of the intermetallics phases is necessary to form a continuous glass layer. Previous research has focused on melt-based processes or the sintering of pre-alloyed powders. These methods typically yield coarse grained microstructures with isolated regions of molybdenum in an intermetallic matrix [6,7]. Unlike many alloys, the Mo-Si-B system does not lend itself to microstructural improvement by heat treating. The compositional homogeneity of the three-phase region extends over a wide temperature range and eliminates the opportunity to reform the microstructure via phase transformations.

One of the objectives of this work is to demonstrate the ability to synthesize the intermetallic phases and control their distribution as a fine, uniform dispersion in a continuous molybdenum matrix. Powder metallurgy creates an opportunity to optimize microstructural parameters through changes in starting materials and processing conditions, but previous efforts to create Mo-Si-B alloys by powder processing routes have presented difficulties. In many cases hot-pressing was required to densify the alloys due to the large particle sizes of the powders used, and impurity levels are difficult to control because fine silicon and boron powders are prone to oxidation during processing [8]. In a process developed at Georgia Tech, Mo-Si-B alloys are formed by the reaction of molybdenum, silicon nitride ($Si_3N_4$) and boron nitride (BN) powders [9,10,11]. The covalent nitrides are stable in oxidizing environment up to 1000ºC, which allows for fine particle processing without the formation of silicon and boron oxides. Both nitrides have high equilibrium nitrogen partial pressures and small free energies at high temperatures that promote formation of A15 and T2. The intermetallic phases form by the reactions:

$$3Mo + \tfrac{1}{3} Si_3N_4 \rightarrow Mo_3Si + \tfrac{2}{3} N_2 \quad (1.1)$$

$$5Mo + \tfrac{1}{3} Si_3N_4 + 2BN \rightarrow Mo_5SiB_2 + \tfrac{5}{3} N_2 \quad (1.2)$$

The resulting alloys have low impurity levels and microstructures with a fine dispersion of intermetallics in a continuous molybdenum matrix. This processing route allows for microstructural control through adjustments in processing, raw materials and firing parameters. The methods used are common powder processing techniques that are standard in industry practice, making the process relatively inexpensive and viable for industrial scale up.

The development of Mo-Si-B alloys is presented in the Literature Review chapter and a comprehensive survey of past and current fabrication methods is given. The properties of the alloys are closely linked to the microstructure and an emphasis is placed on the relationship between processing and microstructure. The strength and fracture toughness of Mo-Si-B alloys are reviewed and related to the morphology of the $Mo_{ss}$ phase. The oxidation mechanisms that occur for different compositions and in different temperature regimes are discussed. Examples of the mechanical properties and oxidation resistance are given for alloys of similar composition to those studied in this research. The formation of Mo-Si-B alloys by the reaction synthesis method is introduced and potential issues with the powder processing method developed are discussed.

The Experimental Procedures chapter describes the raw materials and the procedures used to prepare, sinter and characterize the Mo-Si-B alloys. The raw materials were selected on the basis of high-purity and commercial availability in large quantities. Different boron nitride reactants were selected to investigate the effects of the particle size and morphology on the distribution of the T2 phase. The processing route developed was based on common industry practices in order to make the approach relatively inexpensive and viable for scale up. The characterization methods used include thermal analysis, x-ray diffraction (XRD), scanning electron microscopy (SEM) and electron backscatter diffraction (EBSD) imaging. The stereological techniques used to quantify the distribution of the intermetallic phases are described.

Chapter 4 begins with an examination of the reactions between molybdenum and the nitrides to form the intermetallic phases. The reactions were investigated for both the pure phases and the formation of the three-phase $Mo_{ss}$-A15-T2 alloys. The densification

of Mo-Si-B alloys produced by the reaction synthesis method was studied as a function of composition, firing temperature and hold time. The microstructures of the resulting alloys have been related to the powder processing and sintering conditions.

Molybdenum and the intermetallic phases can be distinguished in SEM images, but not the individual A15 and T2 phases. EBSD imaging was used to map the location of all three phases in the microstructures and to quantify the volume fractions and grain size distributions. Chapter 5 reviews the analytical methods such as stereology line counts and two-point correlation functions that were used to quantify and interpret the distribution of the intermetallic phases in order to direct changes in processing methodology to better engineer microstructures. The effect of the size and morphology of boron nitride reactant powder on the dispersion of the T2 phase was examined, as well as changes in the dispersion of the intermetallics for alloys with varying $Mo_{ss}$ contents.

Initial examinations of the materials properties of the alloys produced by the reaction synthesis method are given. Chapter 6 reports the high-temperature strengths measured for the alloys and the oxidation resistance of the Mo-3Si-1B wt.% alloy is investigated in Chapter 7. The oxidation of Mo-Si-B alloys is the result of two mechanisms; a transient period of rapid weight loss that occurs during the formation of the surface oxide, followed by diffusion controlled oxidation after the surface has sealed. A pre-oxidation treatment was developed to study the formation of the surface oxide and to minimize the transient weight loss during the initial formation of the surface layer. A model for oxidation is presented in Chapter 8 which relates the composition and microstructure of the alloys to the total oxidation that occurs across the two kinetic regimes. Finally, conclusions and recommendations for further research are made.

# CHAPTER 2

# LITERATURE REVIEW

The development of Mo-Si-B alloys is reviewed in the following chapter. The properties of Mo-Si-B alloys are microstructure dependent, thus an emphasis is placed on the relationship between the processing methods used and the resulting microstructure. Examples of the mechanical properties and oxidation resistance of select alloys are given and the formation of Mo-Si-B alloy by the reaction synthesis method is introduced.

## 2.1 Materials for Jet Turbine Engines

The components used in jet turbine engines are subject to a combination of high thermal and mechanical stresses due to rapid thermal cycling, large temperature gradients, vibration and rotational forces. The superalloys currently used in the high-pressure region are required to operate for thousands of hours at 85% of their melting point and under stresses on the order of 140 MPa, all while maintaining tight dimensional tolerances [12]. In addition to the high stresses, the materials used in the combustion chamber are subjected to a high-temperature oxidizing atmosphere. These factors make the modern jet turbine engine one of the most demanding environments for materials.

The nickel superalloy airfoils used in modern jet turbine engines are limited to a maximum operating temperature of 1150ºC; however, by implementing technologies such as thermal barrier coatings and elaborate cooling schemes the combustion chamber of the engines can run as high as 1500ºC [7]. There is a call for higher operating

temperatures as the power output of turbine engines are a function of the maximum combustion temperature. Figure 2.1 plots the increase in jet engine power starting from the first jet engine developed by Whittle in 1937, and the inset image shows a modern turbine blade with the complex network of holes which are used to cool the blade [1]. The equation in the figure relates the specific core power to the rotor inlet temperature of the engine ($T_4$) and the fan inlet temperature ($T_2$). The fan inlet temperature is fixed by the temperature of the air entering the engine; therefore the power of the engine is mainly a function of the rotor inlet temperature. $R$ is the gas constant and $\gamma$ is the ratio of heat capacities, $C_P/C_V$. The stoichiometric limits at the compressor mark the maximum power possible for a given compressor exit temperature ($T_3$). Early power increases were afforded by materials improvements, allowing for increases in the maximum service temperature of the base metals used in the engines. Further temperature increases are achieved by forced air cooling of the turbine blades. The power of the engine is increased but the systems needed to cool the airfoils decrease the overall efficiency of the engine. It can be seen that the future development of turbine engines is trending farther away from ideal performance and toward increased efficiency losses. This trend marks a clear need for the development of higher temperature materials suitable for the harsh conditions present in jet engines.

The progression of the maximum operating temperature for the base metals used in engines is charted in Figure 2.2 [13]. The reduced creep rates of directionally solidified (DS) and later single crystal (SX) superalloy blades have allowed for increases in the maximum service temperatures. Despite these advances it is evident that the development of nickel-based superalloys has stalled.

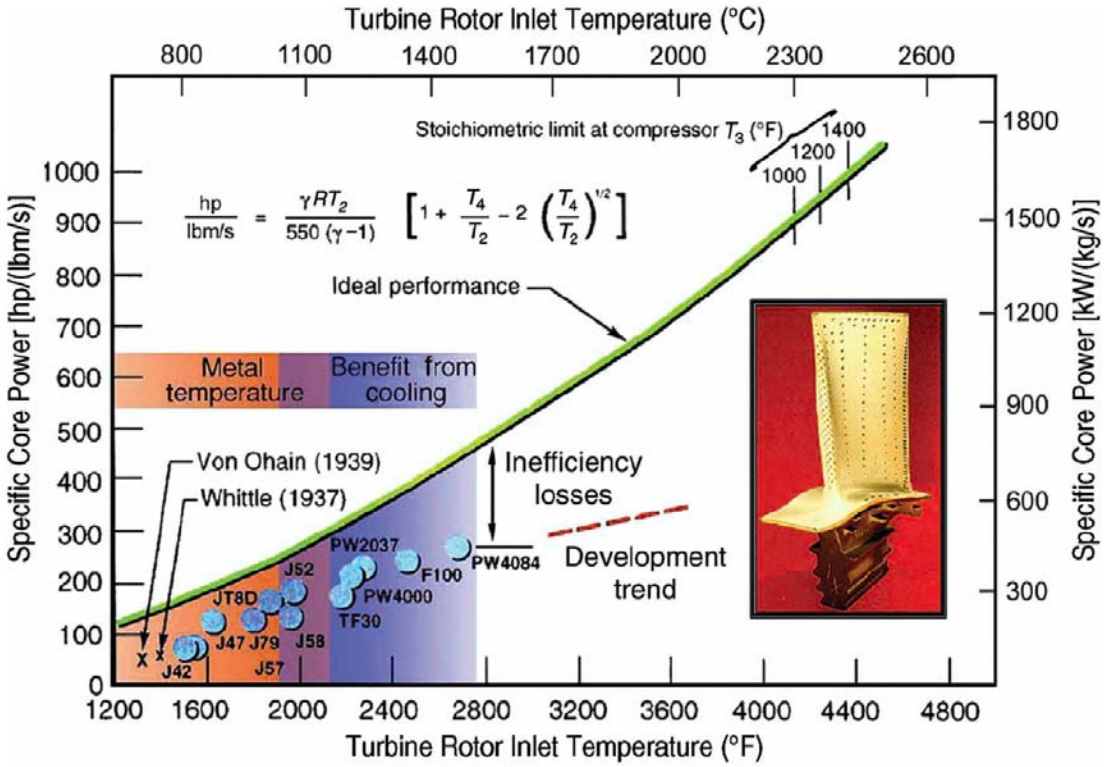


Figure 2.1: The specific core power output of a jet engine plotted as a function of the turbine rotor inlet temperature. The equation given relates the specific core power to the fan inlet temperature ($T_2$) and the rotor inlet temperature of the engine ($T_4$). The inset image shows a turbine blade with its complex network of cooling holes [1].

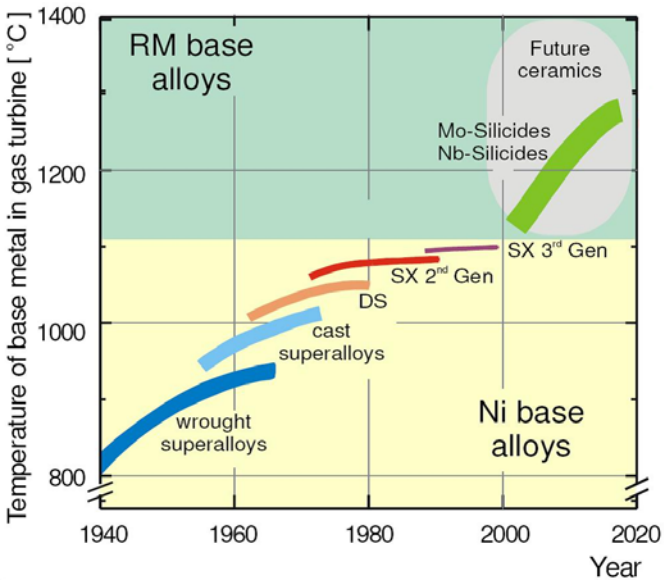


Figure 2.2: The progression of the maximum service temperature of the base metals as a result of improvements in nickel-based superalloys. The potential increases that could be gained from the use of refractory metal based alloys are illustrated [13].

As the traditional jet turbine engine blade technologies are approaching their engineering limits, the continued improvement of jet engine performance will require major advancements in high-temperature structural materials. Figure 2.2 also illustrates the potential increases that could be gained from the use of refractory metal (Nb and Mo) based alloys. If such alloys are brought into service, the payoff in the maximum operating temperatures of the engines could eclipse the increases gained over the past 50 years of superalloy research.

### 2.1.1 Refractory Metals

Refractory metal alloys are an attractive option for the highest temperature applications. They exhibit excellent high-temperature mechanical properties and good thermal stability due to their high melting points. Table 2.1 compares properties of some of the refractory metals to those of pure nickel.

Table 2.1: Select physical properties of molybdenum compared to other refractory metals and nickel [14].

| | $T_m$ °C | Density g/cc | CTE $10^{-6}$/K | Specific Heat J/g·K | Thermal Conductivity W/m·K |
|---|---|---|---|---|---|
| Molybdenum | 2623 | 10.2 | 4.8 | 0.25 | 138.0 |
| Niobium | 2477 | 8.6 | 7.3 | 0.27 | 53.7 |
| Tantalum | 3017 | 16.4 | 6.3 | 0.14 | 57.5 |
| Tungsten | 3422 | 19.3 | 4.5 | 0.13 | 174.0 |
| Nickel | 1455 | 8.9 | 13.4 | 0.45 | 90.7 |

Molybdenum is of particular interest for use in ultra-high temperature applications. It has the sixth highest melting point of all the elements. Molybdenum also has a low coefficient of thermal expansion and high thermal conductivity, imparting good thermal shock and fatigue resistance [15]. It has a much lower density than tantalum and

tungsten which is critical for aerospace applications. Niobium-based alloys are also under investigation as a next generation turbine blade material [16,17]. There have been promising results, but as seen from Table 2.1, the thermal properties of niobium are not as favorable as molybdenum.

Molybdenum-based alloys are used in a wide range of commercial applications, including glass melting, furnace construction, electrical interconnects and x-ray anodes. Dispersion hardened molybdenum alloys such as the titanium, zirconium and carbon (TZM) and hafnium and carbon (MHC) alloys are used in the highest temperature and stress conditions, such as forging dies for superalloys and titanium [18]. The mechanical and physical properties of molybdenum are well suited for high temperature applications, but only in reducing or inert atmospheres. In high-temperature oxidizing environments, molybdenum undergoes catastrophic failure due to rapid oxidation. Unlike other oxides such as silica and alumina, molybdenum oxide forms no barrier against oxidation. $MoO_3$ becomes volatile at temperatures as low as 700ºC. Attempts to improve the oxidation resistance by the application of environmental protective coatings have shown limited success due to spalling or damage to the coatings. There is much interest in using alloying additions to increase the inherent oxidation resistance of the molybdenum.

### 2.1.2 Molybdenum Silicides

Intermetallic compounds of molybdenum and silicon have long been known for their excellent oxidation resistance. Molybdenum and silicon forms three silicide phases, $Mo_3Si$, $Mo_5Si_3$ and $MoSi_2$. One of the most commonly used molybdenum compounds is $MoSi_2$, which is used for heating elements able to withstand continuous use in air up to 1700ºC. The oxidation resistance of this material stems from the formation of a

protective $SiO_2$ surface scale. Upon heating the molybdenum and silicon are oxidized, the $MoO_3$ evaporates and $SiO_2$ forms a continuous passivating layer [19]. After this initial stage further oxidation of the material is limited by atomic and molecular diffusion of oxygen through the glass layer. The layer is also self healing, unlike applied environmental barrier coatings. When the surface oxide is damaged the silicon in the underlying material oxidizes and repairs the coating.

One of the main drawbacks of $MoSi_2$ is a phenomenon called 'pesting' in which rapid oxidation at low temperatures (375-500°C) leads to catastrophic failure of the material. At low temperatures $SiO_2$ is too viscous to coalesce and seal off the surface of the material. The grain boundary diffusion rate of oxygen is higher than the surface diffusion rate and results in the formation of oxides on internal boundaries. The volume change (250%) associated with the formation of $MoO_3$ and $SiO_2$ causes microcracks that lead to further oxidation and results in complete disintegration of the material [20].

Poor creep resistance at high temperatures is another drawback of $MoSi_2$. This has been improved by creating composites with $Si_3N_4$ or SiC, but room temperature brittleness and low strength at high temperature are still problems [21]. The other intermetallics in the Mo-Si binary system have been studied extensively as alternatives for $MoSi_2$ due to its poor mechanical properties. The $Mo_3Si$ phase has been investigated as a structural material but it has poor inherent oxidation resistance [22,23]. $Mo_5Si_3$ has creep rates an order of magnitude lower than $MoSi_2$ due to its more complex crystal structure, but poor oxidation resistance by comparison. Akinc and Meyer found that small additions of boron (1-3wt%) increase the oxidation resistance up to five orders of magnitude and bring it close to that of $MoSi_2$ [2]. In their experiments doping with

1.24wt% boron reduced the oxide scale thickness from several hundred microns to less than 10μm. The addition of boron lowered the viscosity of the silica scale which increased oxidation resistance by improving surface coverage. The borosilicate glass surface layer was also less porous and prone to flaking than pure silica layers.

## 2.2 Mo-Si-B Ternary Alloys

The Mo-Si-B phase diagram was first developed by Nowotny in 1957 and later refined by Perepezko, Figure 2.3 [3]. In addition to the binary intermetallics there is the ternary intermetallic phase $Mo_5SiB_2$. Early investigations for high-temperature structural applications were focused on the $Mo_3Si$ (A15)-$Mo_5Si_3$ (T1)-$Mo_5SiB_2$ (T2) phase field. The intermetallics in this system have better mechanical properties and creep resistance than $MoSi_2$, but are still poor candidates for high stress environments due to low fracture toughness. More recent efforts have focused on the $Mo_{ss}$-A15-T2 phase triangle. The mechanical properties of these alloys benefit from the presence of the more ductile molybdenum solid solution phase. Berczik pioneered investigations of Mo-Si-B alloys for use in jet engines and filed patents in 1997 on alloys ranging in composition from 1.0-4.5 wt.% silicon with 0.5-4.0 wt.% boron (3.2-10.8 at.% Si, 4.2-24.9 at.% B) [4,5]. The alloys of interest in this work are located in the highlighted region of the phase diagram, Figure 2.3. The isothermal phase diagram is plotted at 1600°C but this three-phase region is stable down to room temperature with only slight changes in the solid solution limits of the phases.

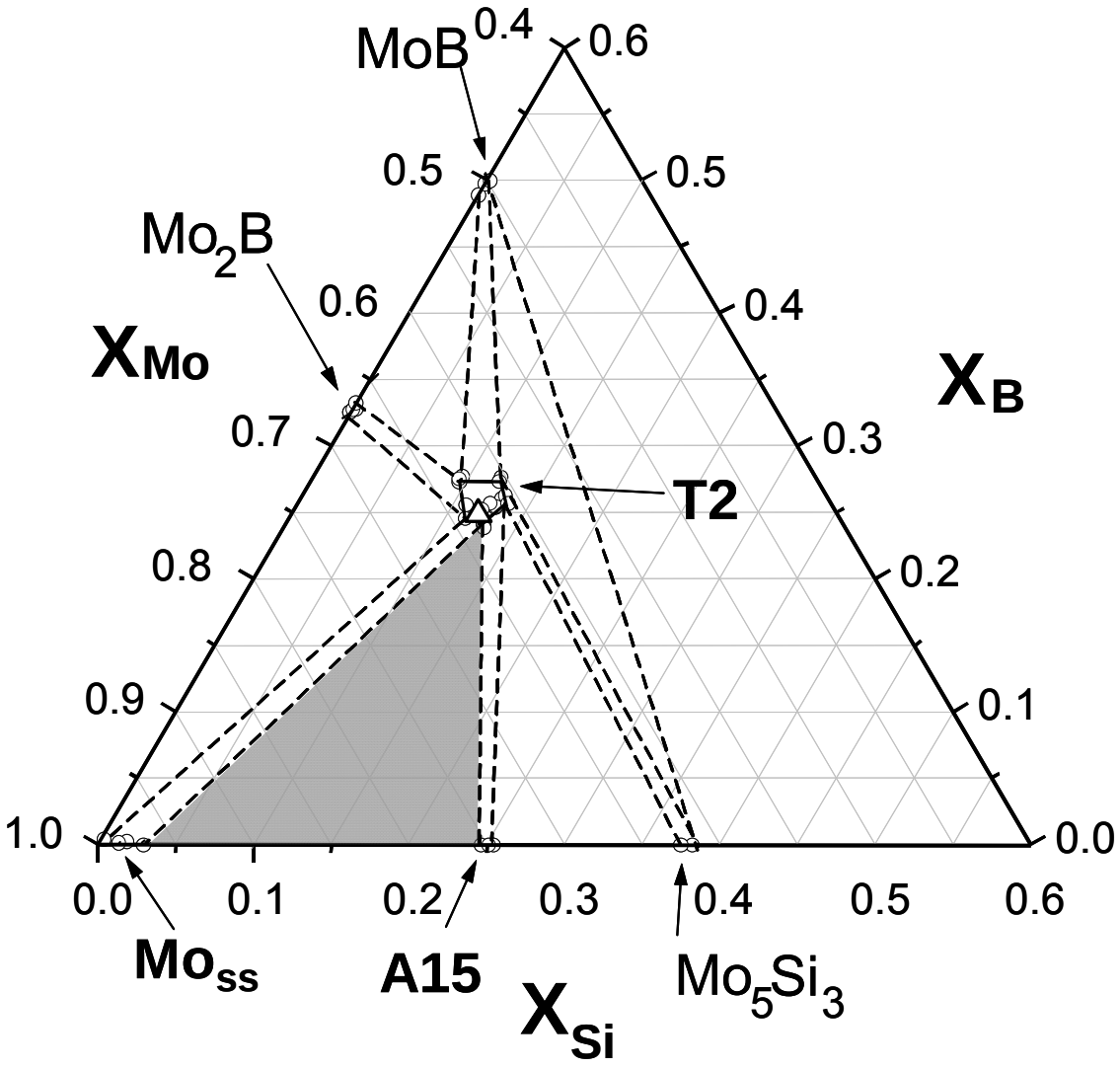


Figure 2.3: The 1600°C isothermal section of the Mo-rich portion of the Mo-Si-B phase diagram, with the $Mo_{ss}$-A15-T2 phase field highlighted. The stoichiometric composition of the T2 phase is labeled by a triangle [3].

Molybdenum has a body-centered cubic (BCC) crystal structure. The molybdenum-silicon binary phase diagram shows that silicon has limited solubility in molybdenum, with a maximum value of approximately 4 at.% at the peritectic temperature of 2025°C, Figure 2.4 [24]. The molybdenum-boron binary phase diagram indicates that boron has negligible solubility in molybdenum, which is a valid assertion for the process temperatures being investigated, i.e. < 1600°C, Figure 2.5. At the eutectic temperature of 2175°C the maximum solubility boron in molybdenum is only approximately 1 at.% [25].

The $Mo_3Si$ phase is commonly referred to as A15 in reference to its crystal structure designation. It has a BCC unit cell that consists of 6 molybdenum atoms and 2 silicon atoms. Early phase diagrams show $Mo_3Si$ as a stoichiometric line compound but Rosales and Schneibel have shown that it has a slightly variable composition, and in equilibrium with molybdenum contains 24 at.% silicon [26].

The $Mo_5SiB_2$ unit cell is body-centered tetragonal (BCT) and consists of 20 molybdenum atoms, 4 silicon atoms and 8 boron atoms. The T2 phase exhibits a wide range of composition, as seen in the phase diagram. The composition and lattice parameters of T2 in equilibrium with molybdenum solid solution and A15 was determined by Perepezko et al. using electron probe microanalysis and XRD [27]. The composition was reported to be 63.65 at.% Mo with a B/Si ratio of 1.992, giving the chemical formula $Mo_5Si_{0.95}B_{1.90}$. The crystal structures of molybdenum, A15 and T2 are illustrated in Figure 2.6 and select physical properties are listed in Table 2.2.

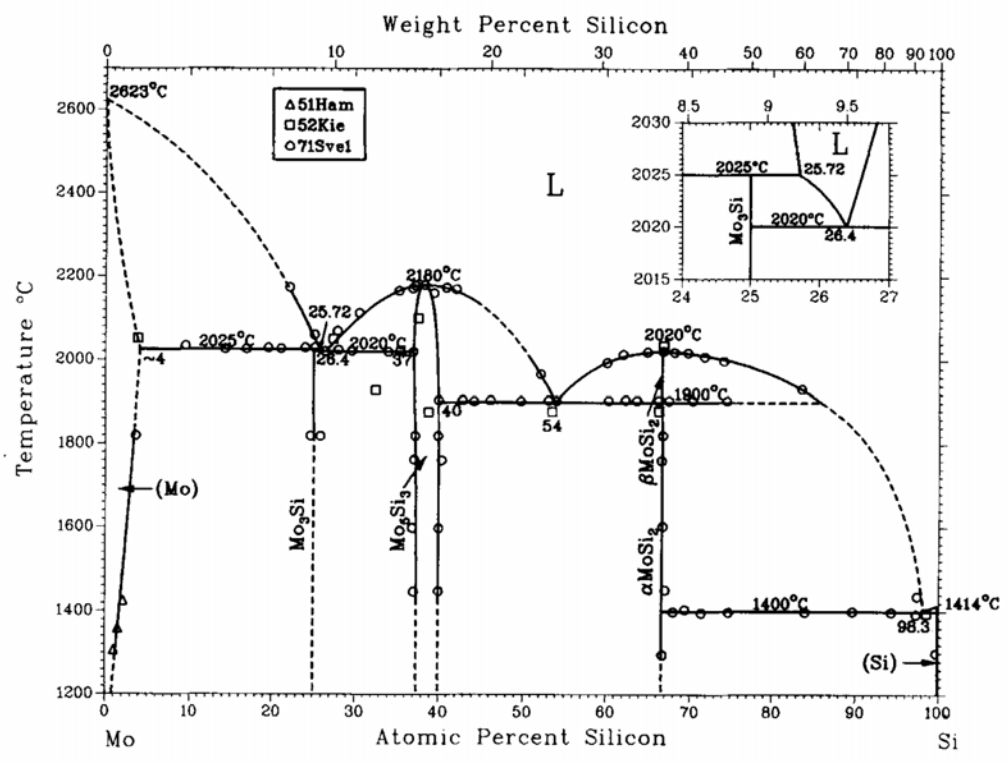


Figure 2.4: The molybdenum-silicon binary phase diagram [24].

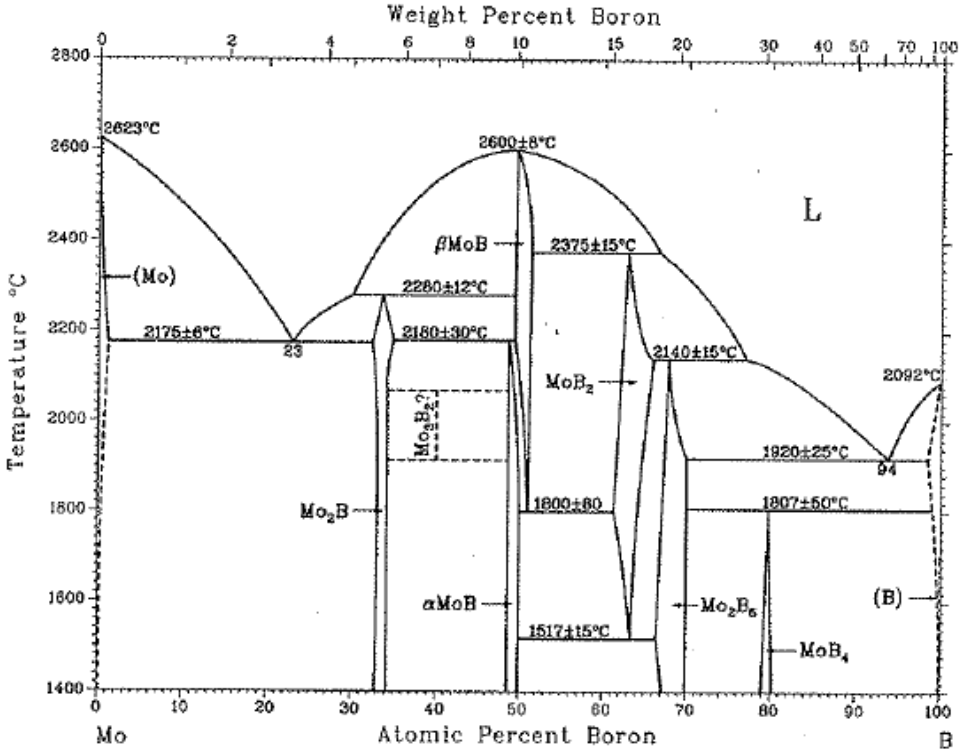


Figure 2.5: The molybdenum-boron binary phase diagram [25].

The physical properties of the three phases are well suited to high temperature applications, with all having melting points over 2000°C. In addition to exposure to high temperatures the materials used in jet-engines must also endure many rapid heating and cooling cycles. The coefficients of thermal expansion (CTE) of the three materials are similar which minimizes thermal shock. The stability of the phase field also prevents the stresses due to volumetric changes induced by phase transformations.

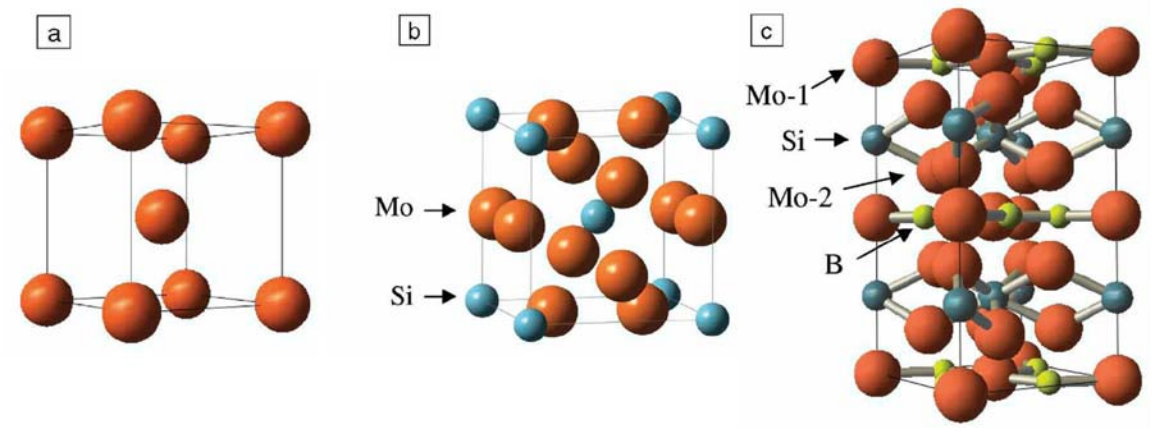


Figure 2.6: The crystal structures of: (a) molybdenum (b) A15 and (c) T2 [1].

Table 2.2: Select physical properties of the Mo, A15 and T2 phases [14,26,27,28,29].

| | **Mo** | **A15** | **T2** |
|---|---|---|---|
| Crystal Structure | BCC | BCC | BCT |
| Lattice Parameter (Å) - a | 0.3165 | 0.4890 | 0.6029 |
| - c | - | - | 1.1095 |
| Theoretical Density (g/cc) | 10.22 | 9.05 | 8.68 |
| CTE ($10^{-6}$/K) - a | 4.8 | 7.1±0.5 | 7.9±0.1 |
| - c | - | - | 7.5±0.2 |
| Melting Point (°C) | 2623 | 2025 | >2100 |

## 2.3 Microstructural Engineering of Mo-Si-B Alloys

The oxidation resistance and mechanical properties of Mo-Si-B alloys are highly microstructure dependent and the requirements for the two properties often conflict. High silicon and boron contents increase the intermetallic fraction and improve oxidation resistance, whereas fracture and fatigue resistance are met with a high volume fraction of the $Mo_{ss}$ phase. The ability to optimize the microstructure both in terms of mechanical properties and oxidation resistance will be a key element in the development and implementation of Mo-Si-B alloys.

Melt processing is one of the most commonly cited methods for the preparation of Mo-Si-B alloys. Arc-melting of elemental powders provides a simple means of preparing alloy compositions with low impurity levels but the resulting microstructures are coarse-grained and often contain non-equilibrium phases. The solidification pathways of Mo-Si-B alloys are complex and involve crossing a number of eutectic and peritectic phase regions. This problem is illustrated by the solidification pathway of the stoichiometric T2 phase, which follows as [3]:

$$\begin{aligned} &L \rightarrow MoB + L_1 \rightarrow MoB + T2 + L_2 \rightarrow MoB + T2 + Mo_5Si_3 + L_3 \rightarrow \\ &MoB + T2 + Mo_5Si_3 + Mo_3Si + L_4 \rightarrow MoB + T2 + Mo_5Si_3 + Mo_{ss} + Mo_3Si \end{aligned} \tag{2.1}$$

The non-equilibrium phases are difficult to remove once formed. The slow diffusion rates which impart Mo-Si-B alloys with excellent phase stability and creep resistance lead to long annealing times. Furthermore, melt-based processing typically creates microstructures with discrete molybdenum particles in an intermetallic matrix. This is due to primary solidification of the $Mo_{ss}$ phase which has a higher melting point

than both the A15 and T2 intermetallics. One of the great difficulties with Mo-Si-B alloys is that unlike many structural alloys, they do not lend themselves to microstructural improvement through heat treatment. Their compositional homogeneity over a wide temperature range eliminates the possibility for microstructural reformation via phase transformations. Dimiduk and Perepezko liken this system a ceramic in that "the initial synthesis methods largely dictate the final microstructure" [1]. Berczik concluded that for suitable mechanical properties, these alloys need to be processed in such a way that molybdenum is present as a continuous network. In his patents on Mo-Si-B alloys, two possible paths for achieve this microstructure are suggested: "1) blending molybdenum powder with either a pre-alloyed intermetallic powder (such as molybdenum borosilicide) or boron and silicon powder, followed by consolidating the powder at a temperature below the melting temperature of the alloy; or 2) rapidly solidifying a melt containing molybdenum, silicon and boron, followed by consolidating the rapidly solidified material at a temperature below the melting temperature." [4,5].

In following section a review of past and present techniques used to create Mo-Si-B alloys is given, including investigations of two and three phase alloys. The methods suggested by Berczik as well as efforts using melt processing, hot working and mechanical alloying are discussed.

### 2.3.2 Processing of Alloys in the $Mo_{ss}$ –$Mo_5SiB_2$ Two-Phase Field

Many early investigations of Mo-Si-B alloys focused on compositions in the two-phase field consisting of $Mo_{ss}$ and T2. Sakidja et al. developed a quasi-binary phase diagram for $Mo_{ss}$-T2, illustrated in Figure 2.7 [30].

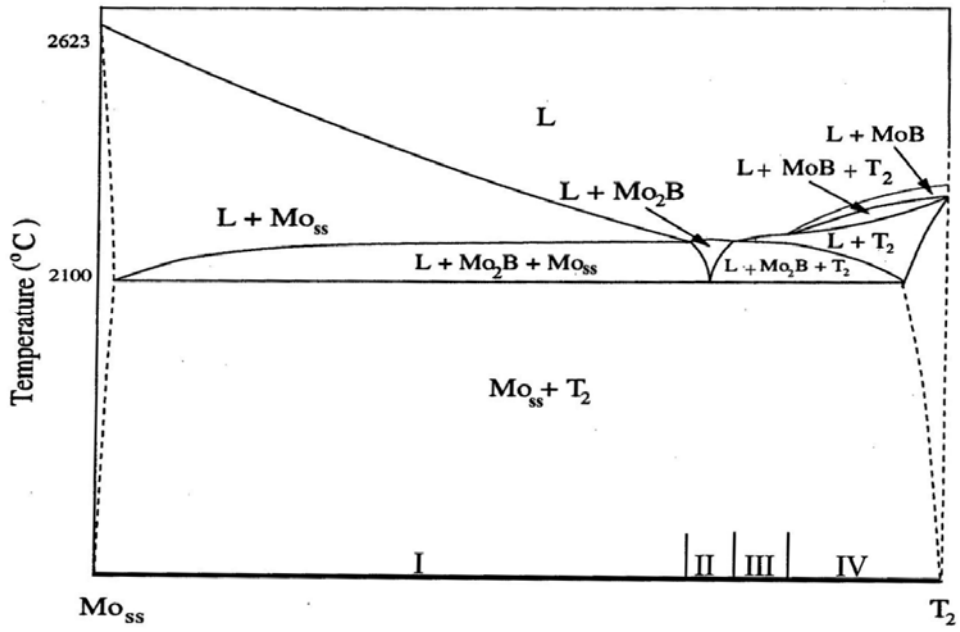


Figure 2.7: The estimated quasi-binary $Mo_{ss}$–T2 phase diagram with the four regions of primary solidification indicated [30].

The phase diagram is divided into four regions of primary solidification, as indicated. Alloys with the high volume fractions of $Mo_{ss}$ necessary for continuity are found in the first region of the phase diagram. Solidification begins with the precipitation of the $Mo_{ss}$ phase, often in the form of dendrites, followed by the formation of the intermetallic phases. This leads to a microstructure in which the $Mo_{ss}$ phase is dispersed in an interconnected intermetallic matrix. Furthermore, in all four regions of the phase diagram molybdenum boride phases form when cooled from the melt. The solidification of $Mo_2B$ causes a shift in the melt toward a silicon rich composition, leading to the formation of $Mo_3Si$. These non-equilibrium phases persist in the alloy through cooling due to slow diffusion.

Figure 2.8a shows a back-scatter electron (BSE) image of a Mo-7Si-14B at.% alloy prepared by Sakidja et al. using arc-melting. Note that the contrast in BSE images is a function of the average atomic number of the phase and that the $Mo_{ss}$ phase appears brighter than the intermetallic phases. The alloy composition is near the $Mo_{ss}$-T2 eutectic and should have an equilibrium phase composition of approximately 50 vol.% $Mo_{ss}$ and 50 vol.% T2, but significant fractions of $Mo_2B$ and $Mo_3Si$ are present in the as-cast condition [31]. Complete dissolution of the non-equilibrium phases was accomplished only after annealing at 1600°C for 150 hours [30]. The high temperature required to equilibrate the alloy lead to significant coarsening and the molybdenum phase appears to be present in an intermetallic matrix, Figure 2.8b.

Several methods have been developed to avoid the formation of non-equilibrium boride and silicide phases during melt-based processing. Yamaguchi et al. used the optical floating zone method to create two-phase alloys free of additional phases directly from the melt, Figure 2.9a [32]. This was accomplished for the $Mo_{ss}$–T2 eutectic composition Mo-9Si-18B at.%, although this yields an alloy with only 28 vol.% $Mo_{ss}$. The molybdenum occured in two different morphologies, large particles and eutectic lamellae present in a T2 matrix. Producing material using this method required a prohibitively long time as the two-phase microstructure was only achieved at growth rates of less than 5mm/h.

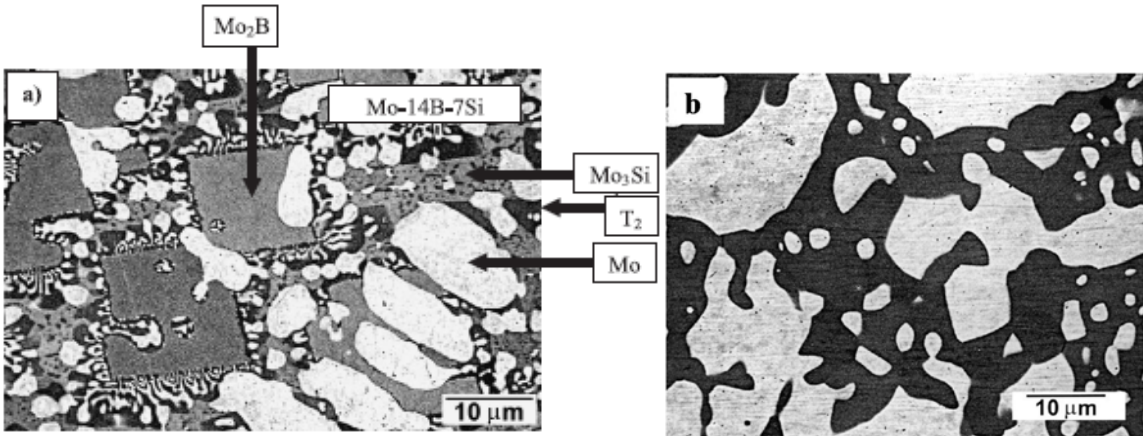


Figure 2.8: BSE images of a Mo-7Si-14B at.% alloy prepared by Sakidja et al.: (a) as-cast condition [31] and (b) after annealing for 150 hours at 1600°C [30]. The as-cast microstructure has a significant fraction of non-equilibrium phases. The annealed microstructure has molybdenum particles (brighter phase) in an intermetallic (darker phase) matrix.

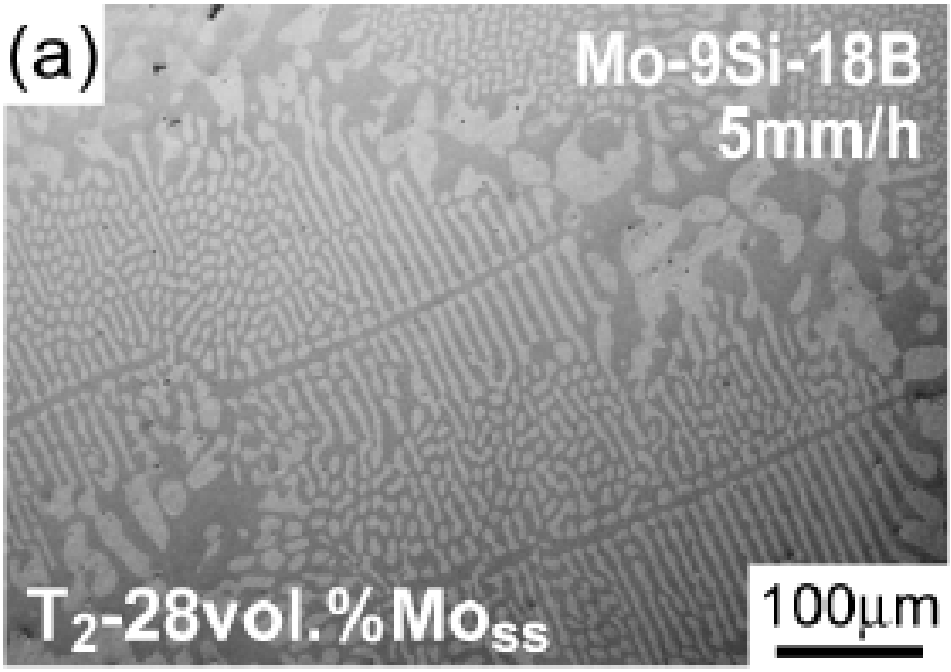


Figure 2.9: BSE image of a Mo-9Si-18B at.% alloy prepared by Yamaguchi et al. using the optical floating zone method at a growth rate of 5mm/h. The image is taken in the plane perpendicular to the growth direction [32].

Rapid solidification has also been successfully used to prevent the formation of non-equilibrium phases during cooling. Sakidja et al. experimented with splat quenching and drop tube processing of $Mo_{ss}$–T2 alloys [30]. With sufficiently high cooling rates it was possible to undercool the mixture into the two-phase field before the precipitation of $Mo_2B$ occurred. The splat quenched alloys with high molybdenum content (>80 at.%) formed cellular molybdenum grains surrounded by a $Mo_{ss}$–T2 eutectic. Lower molybdenum contents (75-80 at.%) yielded crystalline dendrites in an amorphous matrix of 5-95 vol.%. Annealing of the amorphous matrix lead to a dispersion of fine $Mo_{ss}$ particles in a T2 matrix, Figure 2.10.

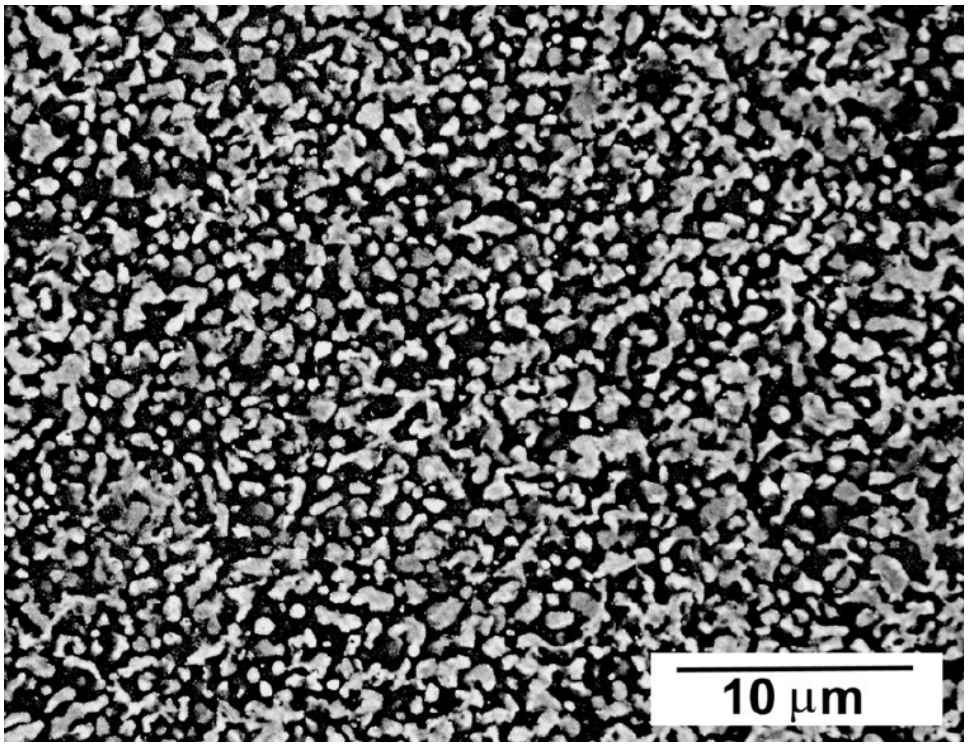


Figure 2.10: BSE image of a splat quenched Mo-7Si-14B at.% alloy after annealing at 1200°C for 150 hours. The $Mo_{ss}$ phase is present as uniformly spaced particles in a T2 matrix [30].

Rapid solidification experiments using drop tube processing were reported to produce fully crystalline alloys, indicating very high cooling rates are necessary to suppress crystallization [30]. DTA measurements of the partially amorphous alloys determined a crystallization temperature of only $0.5T_m$ and it was concluded that the Mo-Si-B system only has a marginal glass forming ability in the two-phase field. This precludes the formation of large parts by rapid solidification and limits the technique to the formation of powders.

### 2.3.3 Preparation of Alloys in the $Mo_{ss}$-$Mo_3Si$–$Mo_5SiB_2$ Three-Phase Field

Alloys in the three-phase field of $Mo_{ss}$-$Mo_3Si$–$Mo_5SiB_2$ have a higher Si/B ratio than the two-phase alloys which improves oxidation resistance. A number of methodologies have been attempted to create these alloys with the desired combination of a continuous $Mo_{ss}$ matrix and a fine dispersion of intermetallics.

#### 2.3.2.1 Melt Processing

Many investigations of three-phase Mo-Si-B alloys have relied on arc-melting to fabricate samples. Nunes et al. plotted the projection of the liquidus surfaces for the molybdenum rich portion of the Mo-Si-B phase diagram, Figure 2.11 [6]. The molybdenum liquidus surface extends over the entire molybdenum rich portion of the $Mo_{ss}$-A15-T2 phase field. As with the $Mo_{ss}$-T2 alloys, primary solidification of molybdenum forms dendrites in an intermetallic matrix rather than the continuous phase necessary for mechanical properties. The $Mo_{ss}$-T2 eutectic trough lies in a region with a small fraction of the $Mo_{ss}$ phase. Similarly, an invariant eutectic reaction $L \rightarrow Mo_{ss}$ + A15 + T2 exists at point $I_1$ but the composition yields an alloy comprised mostly of the A15 phase.

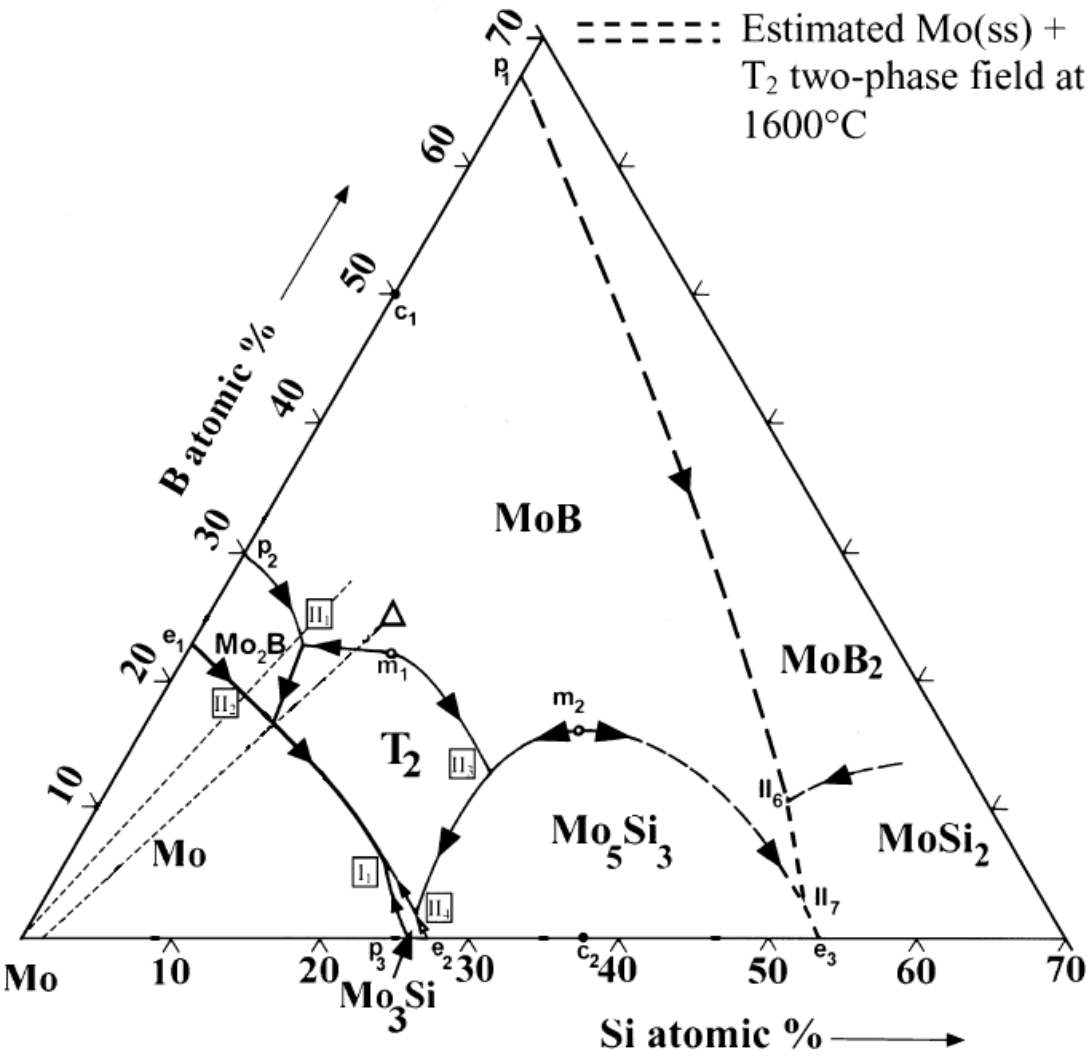


Figure 2.11: The liquidus projection plotted by Nunes et al. for the Mo-rich portion of the Mo-Si-B phase diagram, with the different regions of primary solidification indicated. The invariant eutectic for $Mo_{ss}$-A15-T2 is marked at point $I_1$ [6].

Liquid phase fabrication in this system results in a segregated microstructures in which the molybdenum is present as a dispersed phase. Representative micrographs of three-phase alloys prepared by Nunes et al. using arc-melting are shown in Figure 2.12 for the as-cast condition. The alloys both have compositions near the $Mo_{ss}$-T2 eutectic trough, but are on opposite sides. Composition (a) is on the side of the T2 liquidus surface and solidification begins with the formation of large T2 dendrites, and as it proceeds the liquid composition shifts to the invariant eutectic $I_1$. Composition (b) is on the side of the $Mo_{ss}$ liquidus surface and the cast microstructure consists of $Mo_{ss}$-T2 eutectic regions surrounded by the A15 eutectic [6]. Annealing of cast alloys reduces phase segregation but fails to create a molybdenum matrix, which is evident from the microstructures of arc-cast alloys annealed for 24 hours at 1600ºC, Figure 2.13 [33]. Note that a small amount of niobium has been added as a solid solution strengthener to alloy (b). Sakidja et al. have demonstrated that niobium is completely miscible with molybdenum, soluble in the A15 and T2 phases, and does not affect the phase stability or relative phase fractions at low levels [34].

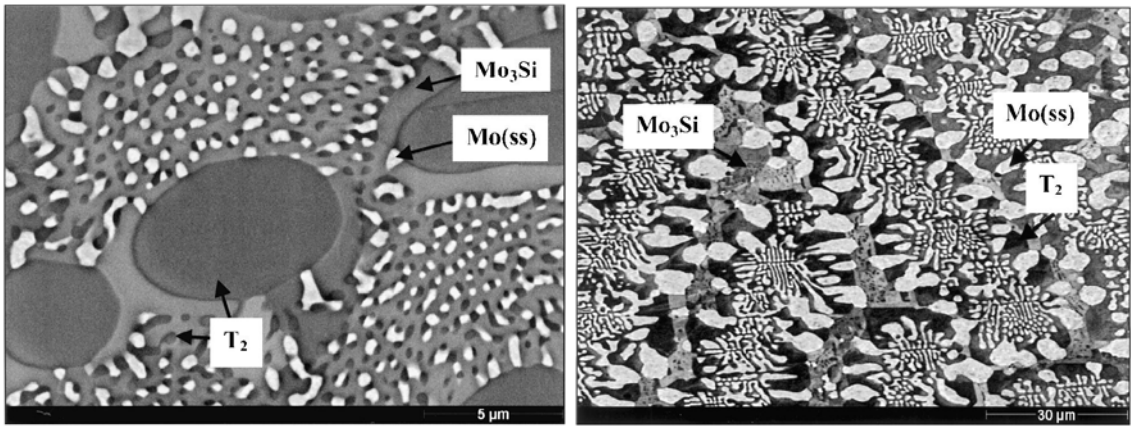


Figure 2.12: BSE images of arc-melted alloys in the as-cast condition: (a) Mo-13Si-15B and (b) Mo-9.6Si-14.2B at.% [6]. Note the images are shown at different magnifications.

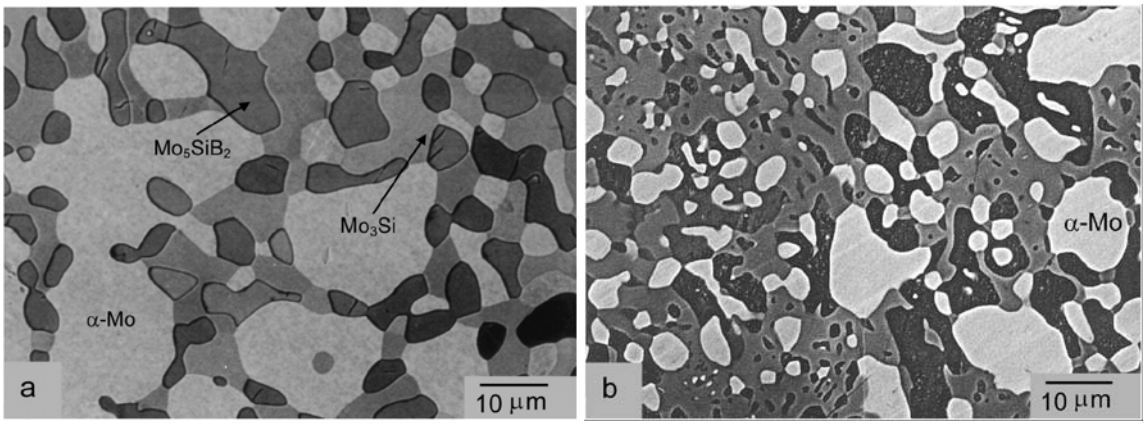


Figure 2.13: BSE images of arc-melted alloys after annealing at 1600ºC for 24 hours: (a) Mo-12Si-8.5B and (b) Mo-12Si-10Nb-8.5B at.% [33].

2.3.2.2 Hot-Working

Melt-based processing has not proven successful for producing Mo-Si-B alloys with the necessary molybdenum matrix. A number of attempts have been made to break up the intermetallic matrix by hot working. Schneibel et al. reported on various attempts to extrude arc-cast alloys of varying compositions, all without success [35]. Extrusion of a Mo-12Si-8.5B at.% billet at 1450°C was aborted because the load capacity of the press was reached. The same composition was successfully extruded at 1550°C, but the material was severely cracked. Similar results were obtained for a Mo-14Si-10B at.% alloy extruded at 1600°C and a Mo-12Si-12B at.% alloy extruded at 1800°C. The difficulties encountered are due to the high silicon and boron contents which reduce the volume fraction of the $Mo_{ss}$ phase to only 41%, 28% and 33% for the respective compositions.

Other researchers have successfully hot worked alloys with higher molybdenum contents. Following one of the methods discussed in his patents, Berczik used rapid solidification and hot working to produce two-phase $Mo_{ss}$-T2 alloys with a dispersion of T2 particles in a continuous molybdenum matrix, Figure 2.14 [4,5]. The alloy was rapidly solidified by splat quenching at a sufficient cooling rate to create a super-saturated molybdenum solid solution. The powder was sealed in an evacuated molybdenum can, extruded and swaged to consolidate, and then heat treatments were used to control the precipitation of the T2 phase from the super-saturated solution.

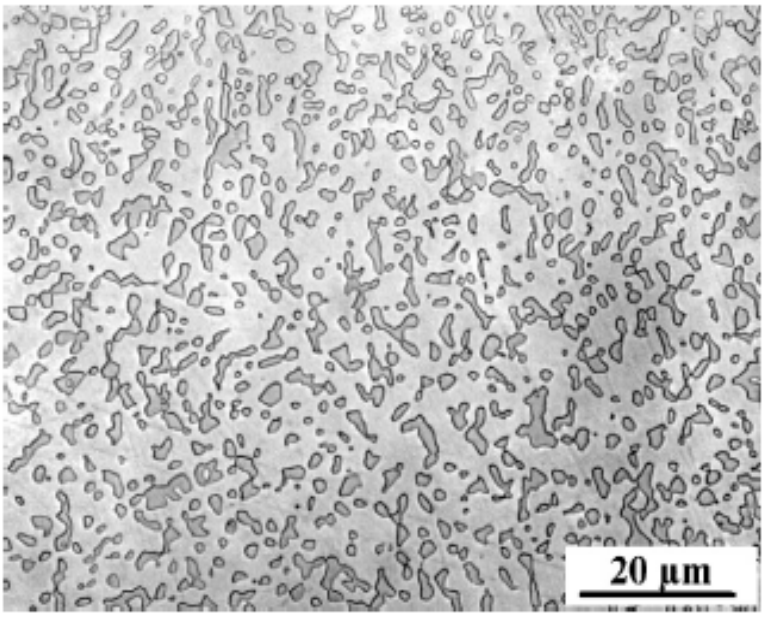


Figure 2.14: A $Mo_{ss}$–T2 alloy with a continuous molybdenum matrix produced Pratt & Whitney (East Harford, CT). A super-saturated $Mo_{ss}$ powder was produced by rapid solidification and consolidated by extrusion. A controlled heat treatment was used to precipitate T2 as a discrete dispersoids in a $Mo_{ss}$ matrix [36].

Jéhanno et al. attempted to replicate the work of Berczik for alloys in the $Mo_{ss}$-A15-T2 phase field, with the ultimate goal to achieve a microstructure similar to the two-phase alloy shown in Figure 2.14. Elemental powders were sintered into a rod and atomized using the electrode induction gas atomization (EIGA) method [7]. In this case the powders solidified into the three-phase mixture of $Mo_{ss}$-A15-T2 rather than the desired super-saturated molybdenum solid solution. It was concluded that using argon as the cooling agent did not create a high enough cooling rate to prevent the formation of the intermetallic phases; however the alloy was cooled into the three-phase field quickly enough to prevent the formation of non-equilibrium intermetallic phases. The resulting microstructure has a combination of large $Mo_{ss}$ particles and dendrites in an intermetallic matrix, Figure 2.15. The smaller droplets formed the dendritic microstructure without the

large molybdenum particles due to their higher cooling rate. The atomized powder was sealed in an evacuated canister and consolidated by hot-isostatic pressing at 1500°C. The resulting microstructure closely matches the atomized powders, Figure 2.16. In an attempt break up the intermetallic matrix, the HIPed billet was extruded at 1760°C with a 6:1 area reduction. Figure 2.17 shows a microstructure cross-section taken parallel to the extrusion direction. Although the extruded alloy has some large molybdenum regions and a high level of contiguity between the intermetallic particles, it is a significant improvement over the initial microstructure.

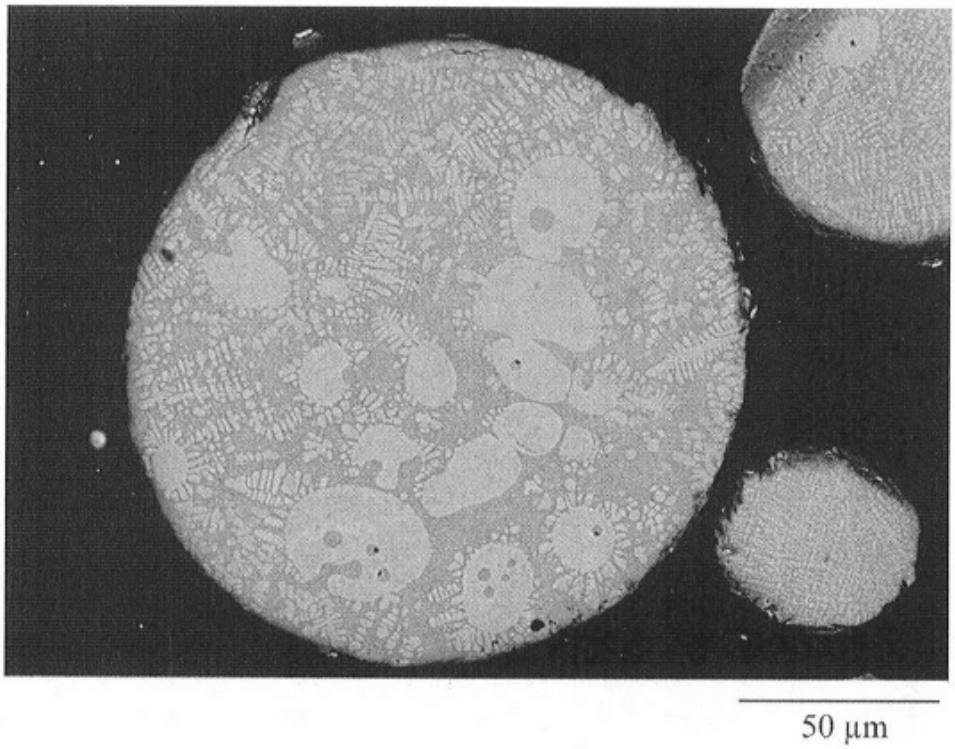


Figure 2.15: Microstructure cross-section of a Mo-3Si-1B wt.% alloy powder produced by Jéhanno et al. using EIGA. Large molybdenum particles and dendrites are present in an intermetallic matrix [7].

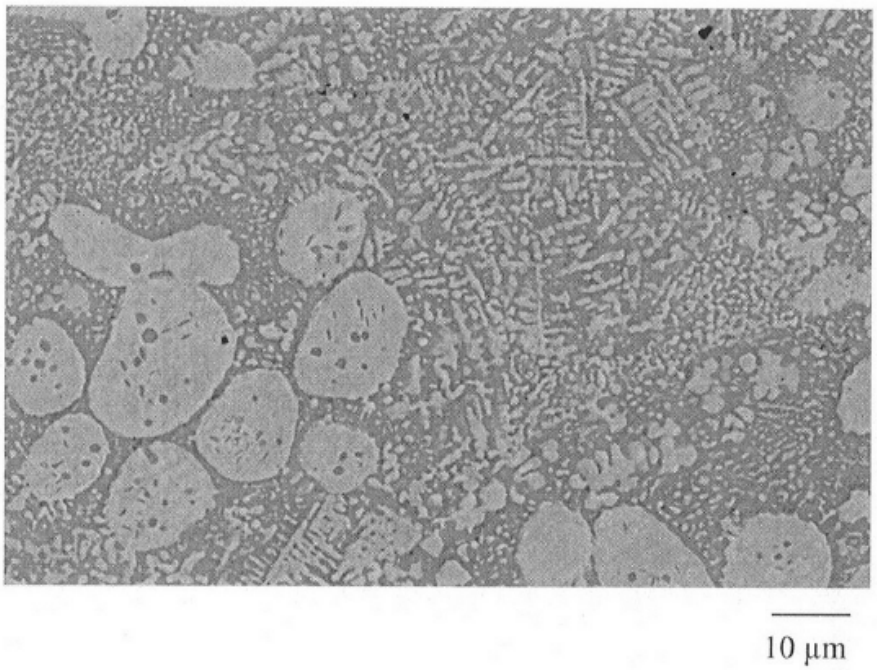


Figure 2.16: The microstructure cross-section of the Mo-3Si-1B wt.% EIGA powder shown in Figure 2.15 after consolidation by hot-isostatic pressing [7].

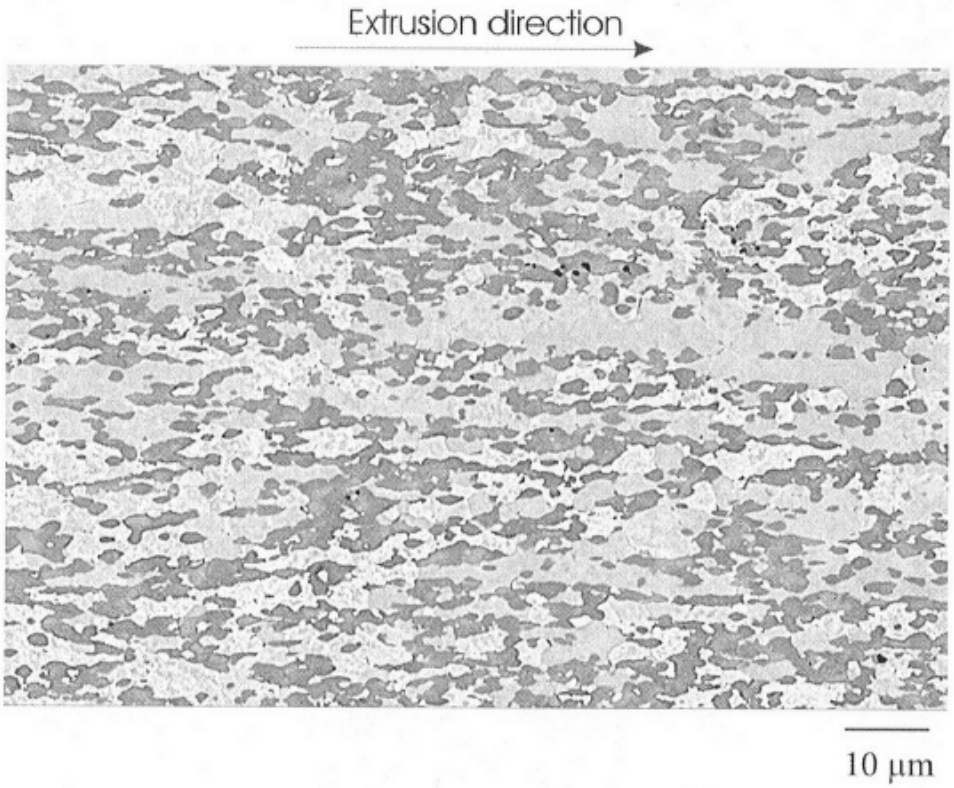


Figure 2.17: Microstructure of the HIPed Mo-3Si-1B wt.% billet produced from the EIGA powder after a 6:1 reduction extrusion at 1760°C [7].

Alur et al. used isothermal forging to create two-phase Mo-2Si-1B wt.% alloys with a fine dispersion of T2 particles [37]. The alloy powders were made using the plasma rotating electrode (PREP) process and consolidated by hot isostatic pressing at 1760°C and 200 MPa. The resulting microstructure had large primary molybdenum dendrites surrounded by a fine mixture of $Mo_{ss}$ and T2, Figure 2.18. The HIPed billet was reduced at a 6:1 ratio by isothermal forging at 1760°C. The forging process broke up the intermetallic regions and yielded a molybdenum matrix, although occasional large clusters of the T2 phase were still present as shown in the inset image, Figure 2.19.

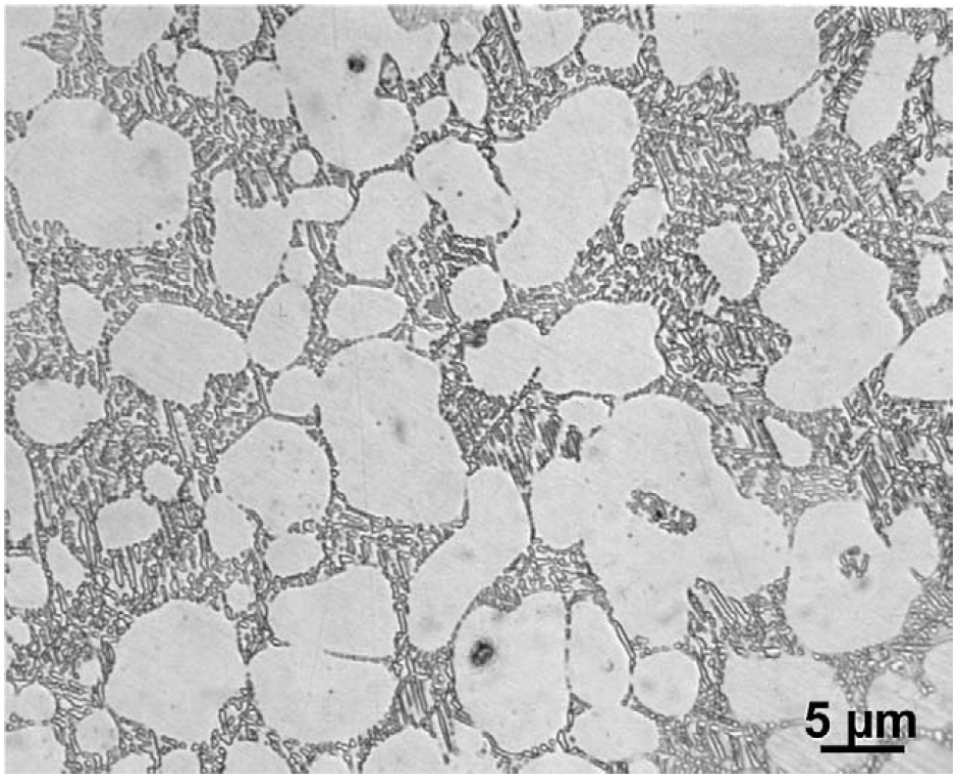


Figure 2.18: Microstructure of a Mo-2Si-1B wt.% alloy prepared by Alur et al. from powder created by the PREP and consolidated by hot-isostatic pressing [37].

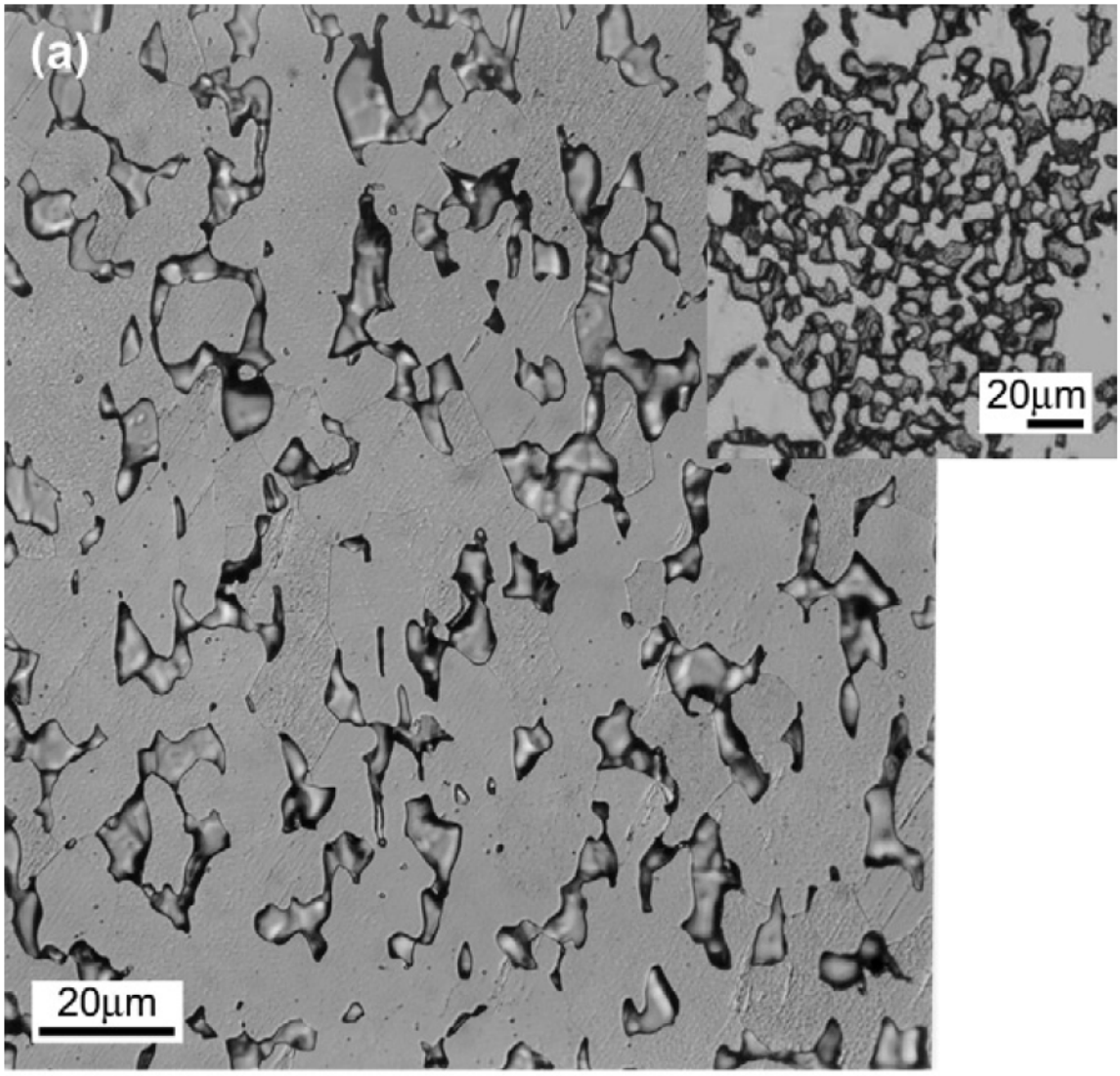


Figure 2.19: An optical micrograph the Mo-2Si-1B wt.% alloy shown in Figure 2.18, following a 6:1 isothermal forging at 1760°C. Occasional clusters of the T2 phase are encountered in the microstructure (inset image) [38].

The microstructures achieved by hot-working are close to the desired combination of finely dispersed intermetallics in a continuous molybdenum matrix. Breaking up the intermetallic matrix leads to dramatic improvements in the mechanical properties of the alloys, which will be discussed further in Section 2.4.

2.3.2.3 Powder Processing

Hot working of Mo-Si-B alloys has been successfully used to create microstructures with dispersed intermetallics in a molybdenum matrix, but the processes used are difficult and expensive. Powder metallurgy provides a means to control microstructure through changes in raw materials and processing techniques and is already used extensively in the production of refractory metal products. Nieh et al. produced Mo-9.4Si-13.8B at.% alloys from elemental molybdenum, silicon and boron powders [39]. The powders were mixed in argon and hot-pressed at 1650°C, followed by annealing at 1400°C to homogenize the microstructures, Figure 2.20. The alloy has a fine grain size but the molybdenum phase does not appear continuous. There was a high level of carbon (600 wppm) from the graphite dies used for hot pressing and a significant fraction of silicate inclusions were created due to high levels of oxygen impurities (1100 wppm).

Schneibel et al. developed two powder metallurgy methods to create a continuous $Mo_{ss}$ matrix in $Mo_{ss}$-A15-T2 alloys. In the first method arc-cast ingots of A15 and T2 were crushed into powders, mixed with molybdenum powder and consolidated by hot isostatic pressing [35]. The resulting microstructure is shown in Figure 2.21. In the second method an intermetallic alloy (Mo-20Si-10B at.%) consisting of a mixture A15 and T2 was produced by arc melting and then crushed into a powder [40,41]. The powder was vacuum annealed at 1600°C for two days to evaporate silicon from the surface, leaving a molybdenum surface layer. The powder was then consolidated by hot-isostatic pressing. The microstructure has a continuous molybdenum matrix of 49 vol.%, Figure 2.22. Both methods produced the desired molybdenum matrix, but not on a fine scale due to the coarse size (50-230μm) of the pre-alloyed powders.

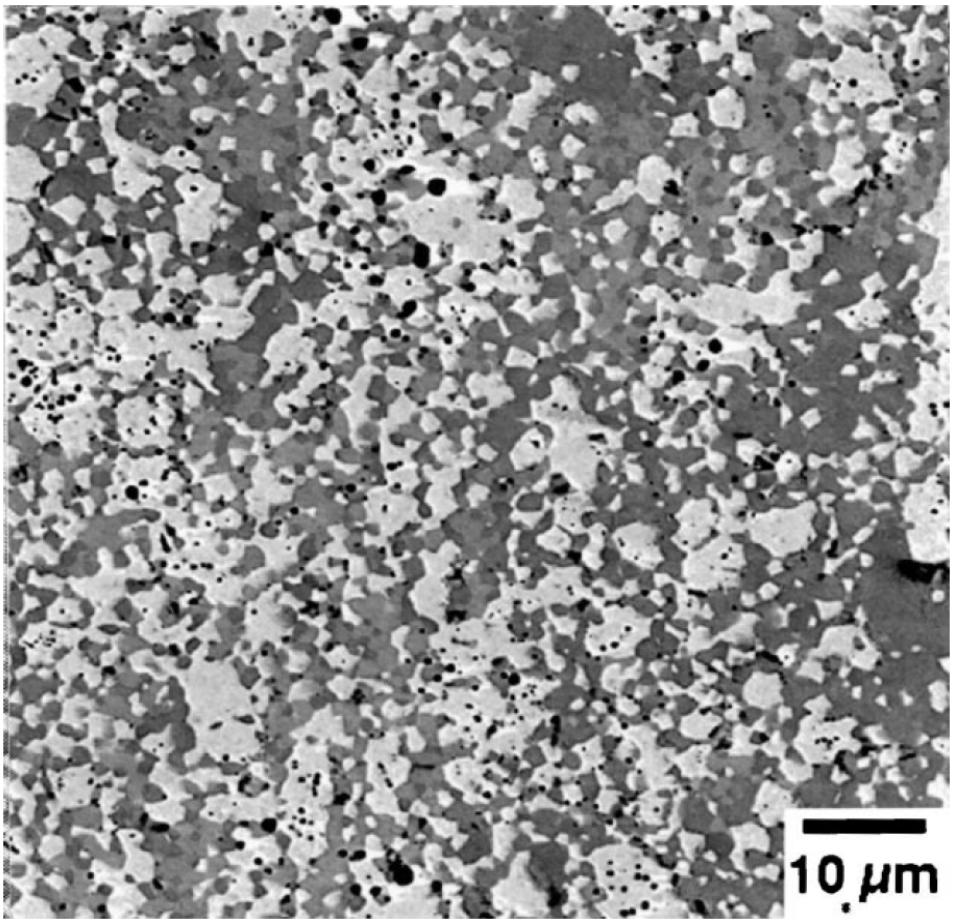


Figure 2.20: BSE micrograph of a Mo-9.4Si-13.8B at.% alloy prepared by Nieh et al. by hot pressing of elemental molybdenum, silicon and boron powders. The black regions are in the image are silica inclusions [39].

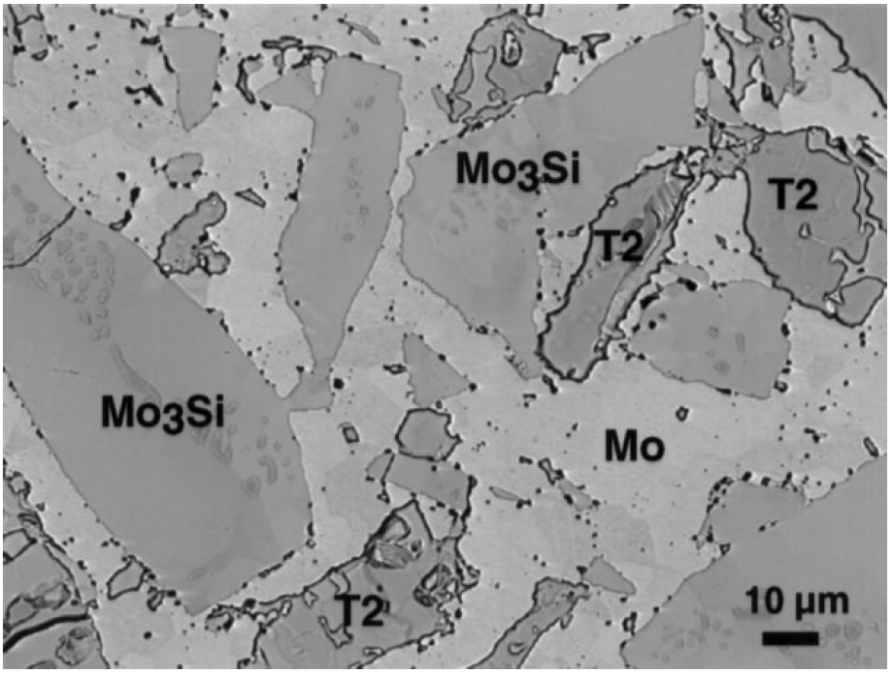

Figure 2.21: BSE micrograph of a Mo-12Si-8.5B at.% (~40 vol.% $Mo_{ss}$) alloy prepared by Schneibel et al. formed by HIPing of molybdenum powder mixed with crushed A15 and T2 powders [35].

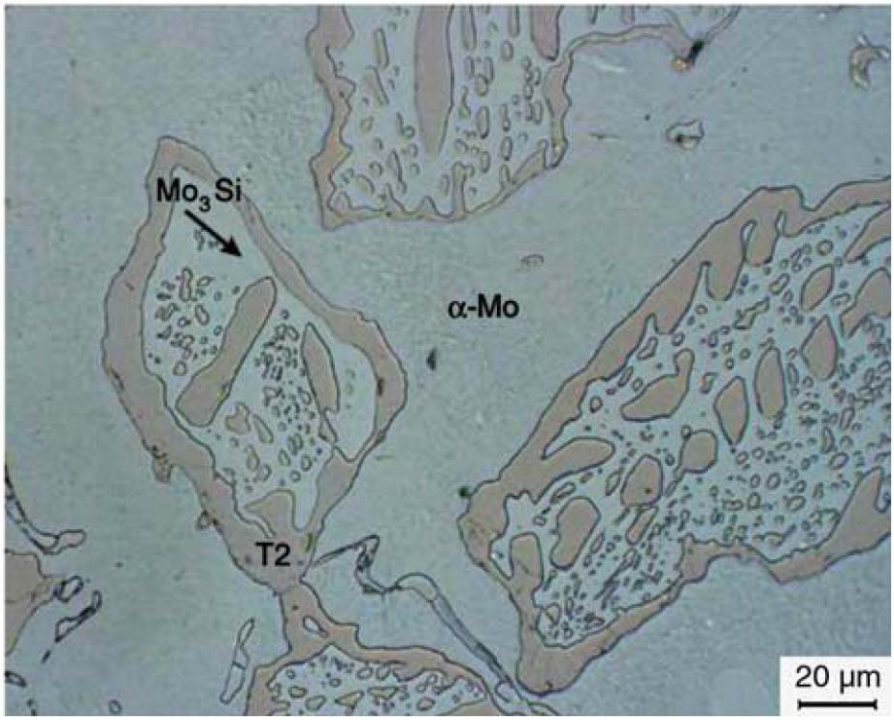

Figure 2.22: Optical micrograph of an alloy produced by Kruzic et al. using a technique in which intermetallic powders were vacuum annealed to create a molybdenum surface layer and HIPed to consolidate [41].

One of the major problems associated with the powder metallurgy approaches presented is high residual oxygen levels. The starting materials are prone to oxidation and do not lend themselves to fine powder processing. Surface oxidation of silicon and boron, as well as the molybdenum silicides, is not easily reduced and is carried into the sintered alloys. The alloys produced by Schneibel et al. have much lower oxygen contents than the hot-pressed alloys produced by Liu et al., mainly due to the much coarser powders used.

2.3.2.4 Mechanical Alloying of Molybdenum, Silicon and Boron

Berczik demonstrated that microstructures with well dispersed intermetallic particles in a molybdenum matrix can be achieve from precipitation of the intermetallics from a supersaturated molybdenum solid solution, Figure 2.14. Jéhanno et al. proposed using mechanical alloying (MA) as a route to achieve supersaturation of silicon and boron in molybdenum, rather than the rapid solidification technique employed by Berczik [36]. Elemental powders were mechanically alloyed for 10 hours and then consolidated by sintering and hot-isostatic pressing at 1500°C. The resulting microstructure had a finely interspersed mixture of intermetallics and molybdenum, Figure 2.23. The average grain sizes were reported to be 0.7μm for the molybdenum and 0.8μm for the intermetallic regions. The large molybdenum regions were attributed to inhomogeneities in the MA molybdenum due to the short milling time. Annealing at 1700°C was used to coarsen the microstructure which resulted in improved continuity of the molybdenum matrix phase, Figure 2.24.

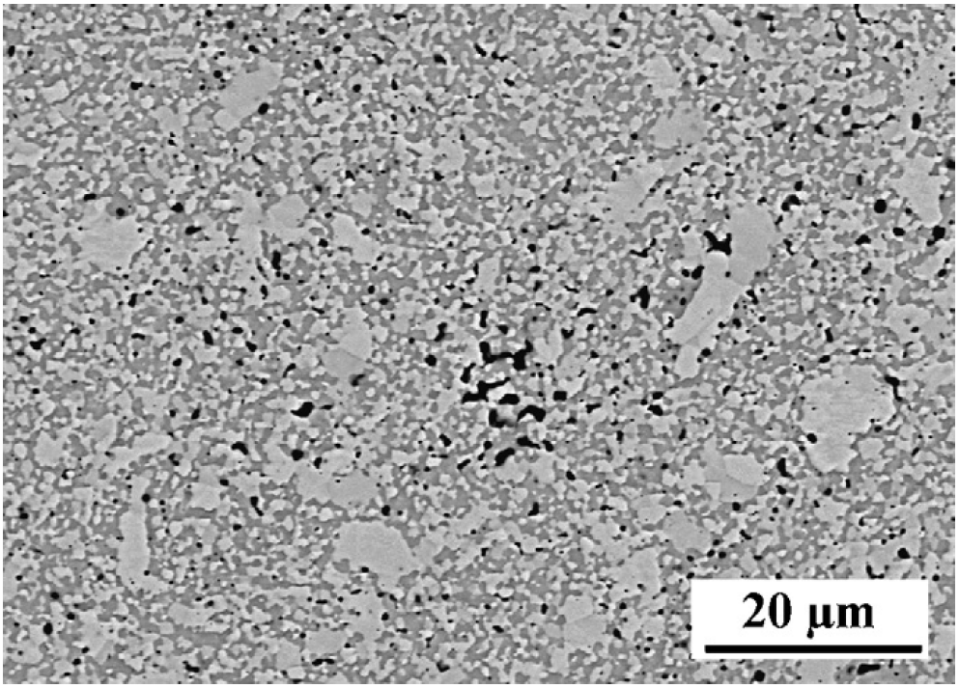


Figure 2.23: A Mo-2.7Nb-8.9Si-7.7B at.% alloy prepared by the consolidation of mechanical alloyed Mo, Nb, Si and B powders, Jéhanno et al. [36].

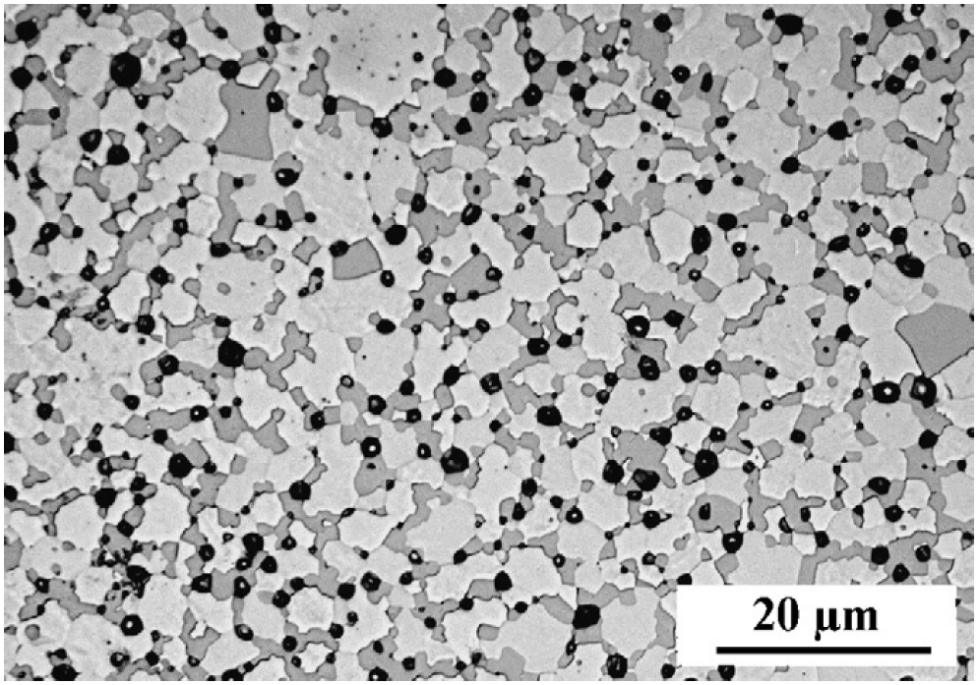


Figure 2.24: The mechanically alloyed Mo-2.7Nb-8.9Si-7.7B at.% alloy prepared by Jéhanno et al., shown in Figure 2.23, following a high-temperature anneal at 1700°C for 10 hours [36].

As with the other powder processing techniques cited, a problem with the MA approach is high residual oxygen levels in the alloys. This is evident from the high fraction of silica inclusions visible in the micrographs of the alloys. Mechanical alloying incorporates the thin oxide layers present on the surface of the powders into the molybdenum along with the silicon and boron. The initial MA work by Jéhanno et al. reported oxygen levels of 3000 wppm for the sintered alloys [36,42]. In more recent work, firing in a hydrogen atmosphere has been reported to decrease the oxygen level in the sintered alloys to 100-500 ppm by weight, despite initial levels of 1500-5000 ppm in the as-milled powders [43].

## 2.4 Mechanical Properties of Mo-Si-B Alloys

The mechanical properties of Mo-Si-B alloys vary widely with intermetallic content, thus the research reviewed is narrowed to compositions with high fractions of the $Mo_{ss}$ phase and focused mainly on the Mo-2Si-1B and Mo-3Si-1B wt.% alloys. Comparing the alloys produced by different methods highlights the role of the microstructural morphology on mechanical properties.

### 2.4.1 Strength and Deformation Behavior of Mo-Si-B Alloys

Jéhanno et al. conducted high-temperature tensile testing of the alloy pictured in Figure 2.16, which was produced by inert gas atomization and had a coarse dispersion of molybdenum in an intermetallic matrix [44]. The strength of the alloy and elongation-to-fracture are plotted in Figure 2.25 for tests conducted at a strain rate of $10^{-4}$ $s^{-1}$.

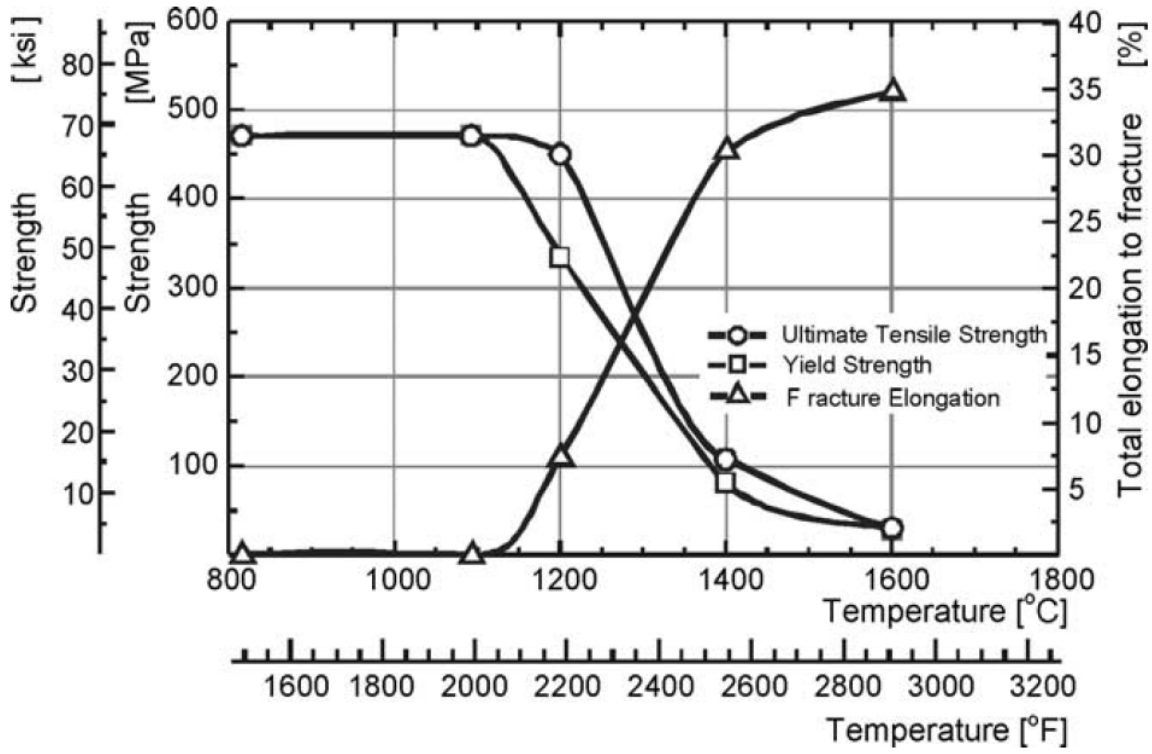


Figure 2.25: The temperature dependence of the ultimate tensile strength (○), 0.2% yield strength (□) and elongation-to-fracture (Δ) of the Mo-3Si-1B wt.% alloy shown in Figure 2.16. Jéhanno et al. produced the material by hot-isostatic pressing of powder made by inert gas atomization [44].

It can be seen that the alloy has a high DBTT, which is likely due the intermetallic matrix. Jéhanno et al. succeeded in breaking up the intermetallic matrix by high-temperature extrusion, Figure 2.17. The ultimate tensile strength of the extruded alloy and the elongation-to-fracture are plotted as a function of temperature in Figure 2.26 and Figure 2.27. The results are compared to those of the unextruded alloy, a commercial molybdenum alloy and a state-of-the-art, single crystal superalloy commonly used in jet turbine engines [7].

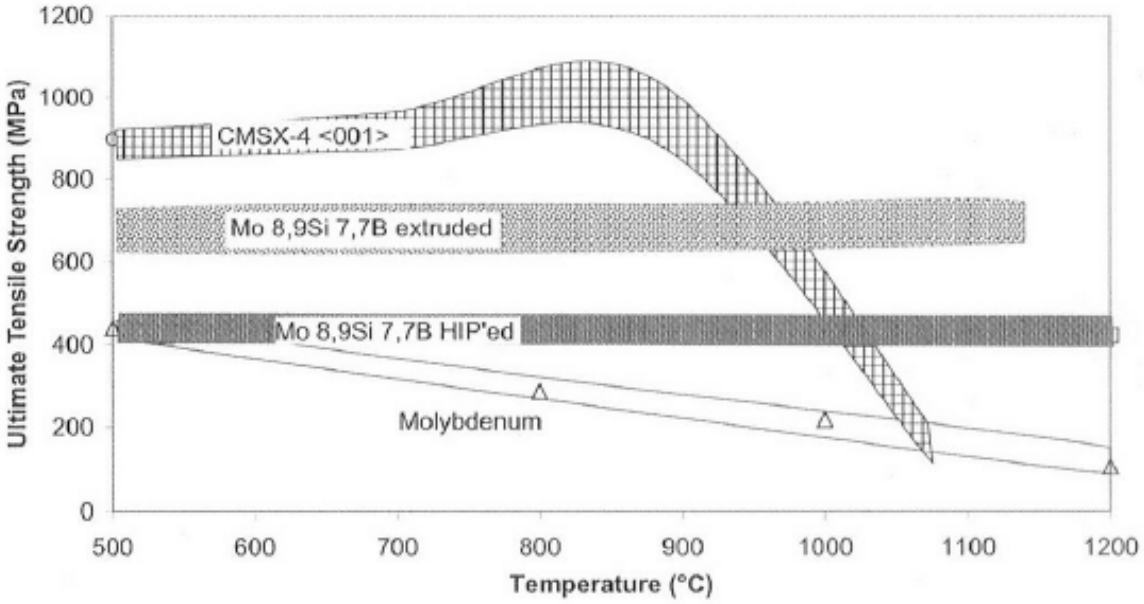


Figure 2.26: The ultimate tensile strength of Mo-3Si-1B wt.% alloys in the as-HIPed and the extruded states, compared to data for a commercial molybdenum alloy and a single crystal Ni-based superalloy, Jéhanno et al. [7].

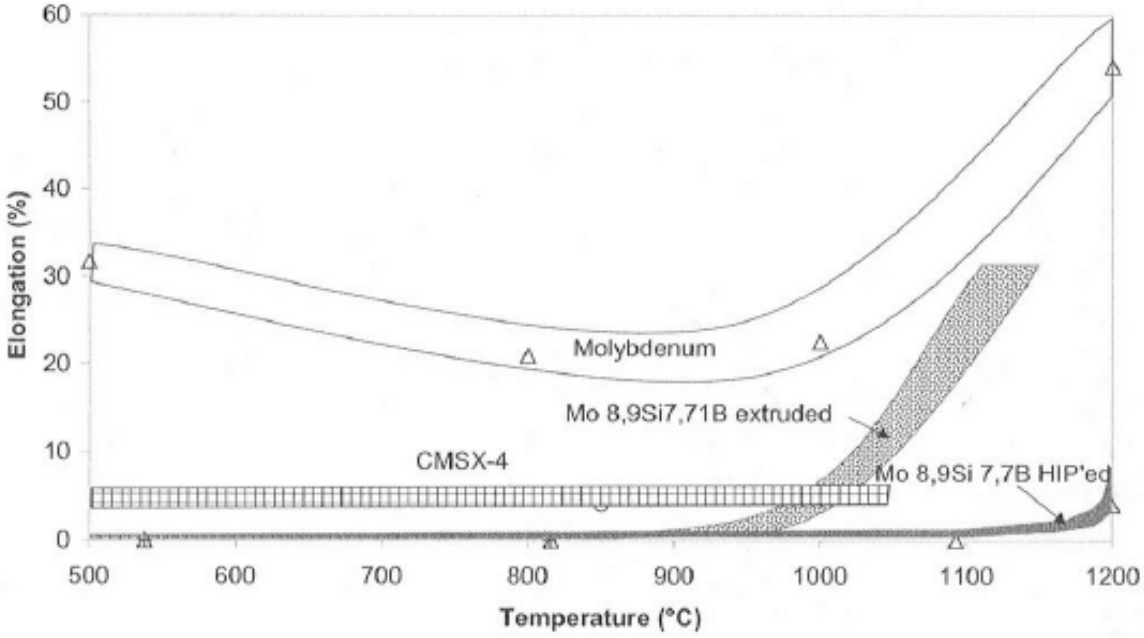


Figure 2.27: The elongation-to-fracture of Mo-3Si-1B wt.% alloys in the as-HIPed and the extruded states, compared to data for a commercial molybdenum alloy and a single crystal Ni-based superalloy, Jéhanno et al. [7].

The high-temperature strength of the Mo-Si-B alloys is greatly improved by the presence of the intermetallic phases, as compared to the commercial molybdenum alloy. Modification of the Mo-Si-B microstructure via extrusion from an intermetallic matrix to a partially continuous $Mo_{ss}$ matrix resulted in over a 50% increase in the tensile strength. Although the low temperature strength trailed that of the superalloy material, the extruded alloy surpassed the superalloy above 1000ºC. The extrusion process also decreased the DBTT of the Mo-Si-B alloy by approximately 200ºC. While this is an improvement, below 900ºC the extruded alloy had near zero ductility. This may be due to the high level of contiguity between the intermetallic particles and additional decreases in the DBTT temperature may be achievable through an improved dispersion of intermetallics.

Alur et al. compared the compressive response of both Mo-2Si-1B wt.% (two-phase) and Mo-3Si-1B wt.% (three-phase) alloys. Powders formed by the PREP process were consolidated and isothermally forged. The microstructure of the two-phase alloy is illustrated in Figure 2.19. The flow stresses of both alloy compositions were nearly identical between 1200ºC and 1400ºC, over the range of strain rates investigated ($10^{-4}$ to $10^{-7}$ $s^{-1}$), and it was concluded that the deformation behavior of the alloys were controlled by the $Mo_{ss}$ matrix [37].

Jéhanno et al. also investigated the mechanical properties of the Mo-3Si-1B wt.% alloys produced by mechanical alloying, Figure 2.23. Super-plastic deformation was observed at 1300°C for a strain rate of $10^{-4}$ $s^{-1}$ and at 1400°C for a rate of $10^{-3}$ $s^{-1}$, Figure 2.28 [36,42]. Elongation-to-fracture values of 300% and 400% were achieved at 1300°C and 1400°C respectively. The advent of super-plasticity was attributed to the sub-micron

grain size of the alloy which allows for grain boundary sliding. This work is of interest because the super-plastic behavior may permit hot-working of the alloys at much lower temperatures than has been previously demonstrated. A 1700°C anneal was used to achieve grain growth in order to recover the creep resistance, Figure 2.24, but the resulting mechanical properties were not reported.

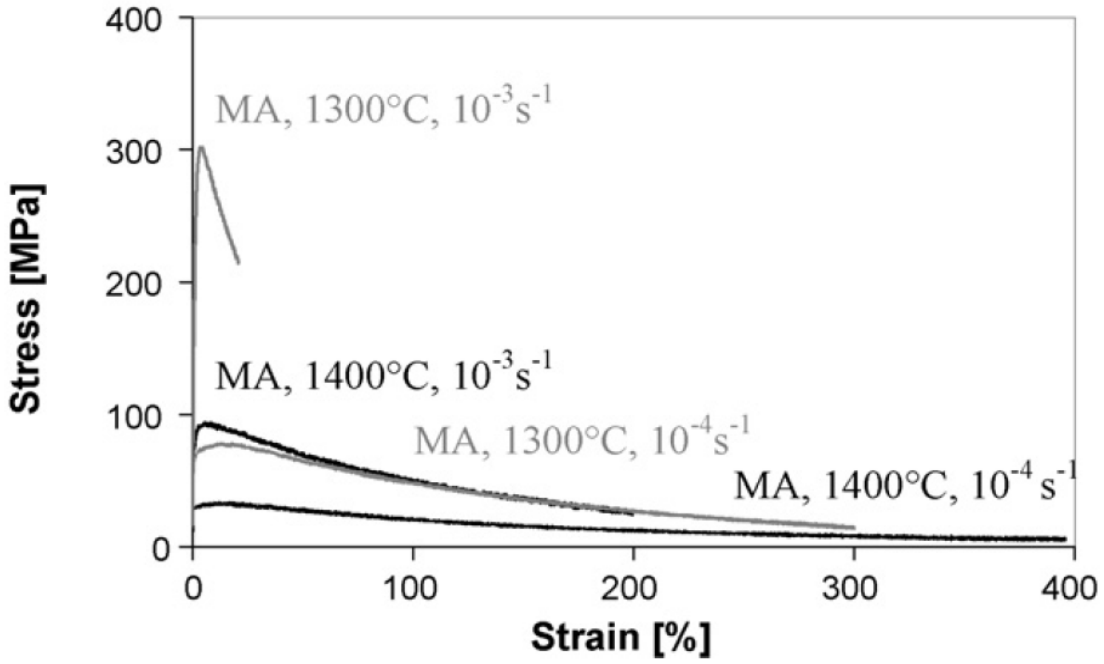


Figure 2.28: Evidence of super-plasticity for a Mo-2.7Nb-8.9Si-7.7B wt.% alloy prepared by hot-isostatic pressing of mechanical alloyed powders, Jéhanno et al. [36].

### 2.4.2 Fracture Toughness of Mo-Si-B Alloys

One of the major concerns with molybdenum-based alloys is low temperature brittleness. Molybdenum inherently has a limited degree of ductility due to its BCC crystal structure which has few slip planes to accommodate deformation. The fracture toughness of molybdenum is also highly affected by solid solution additives. Sturm et al. investigated the effect of the silicon solid solution content on the fracture toughness of molybdenum, Figure 2.29 [45]. It can be seen that there is a sharp decrease in toughness with only small additions of silicon. This is attributed in part to the significant solid solution strengthening effect of silicon which has been shown to extend as high as 1200°C [46]. Moreover, the presence of silicon was reported to shift the fracture mode from transgranular to intergranular at even the lowest addition tested (0.1 wt.%), Figure 2.30. The additional embrittlement of molybdenum due to impurities gained during processing will be discussed in Section 2.7.

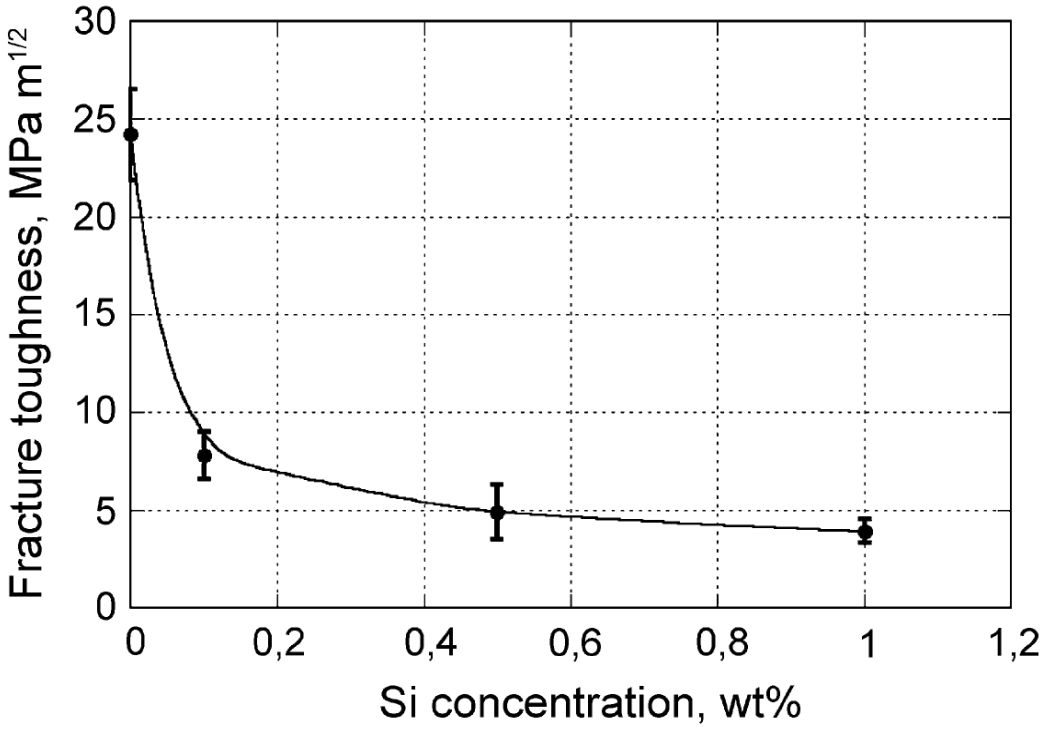


Figure 2.29: The room temperature fracture toughness of molybdenum as a function of silicon concentration, measured by Sturm et al. Note that the equilibrium concentration of silicon at 1600°C is 0.87 wt.% [45].

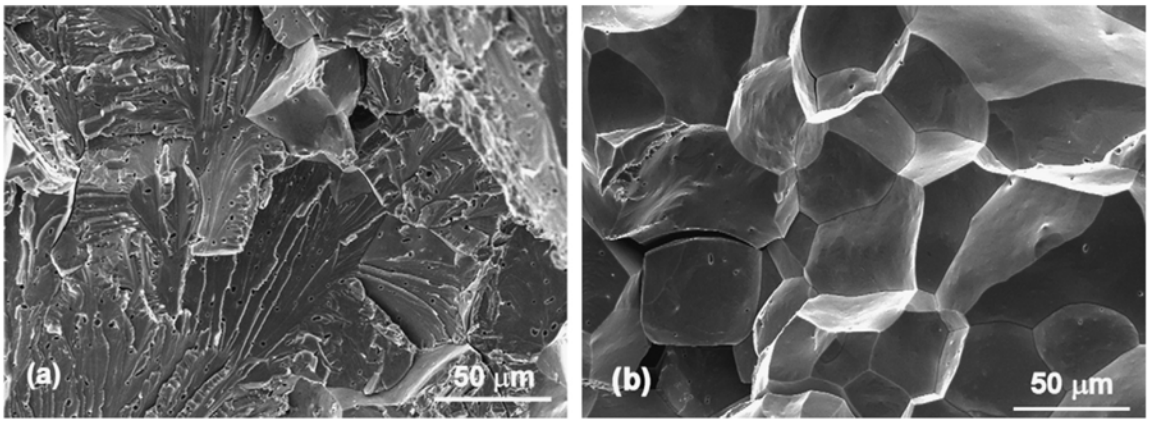


Figure 2.30: SEM images of the room temperature fracture surfaces demonstrating the change in the fracture mechanism between (a) pure molybdenum and (b) Mo-0.1 wt.% Si, Sturm et al. [45].

Intermetallic materials are generally known to be brittle. Chu et al. used crack length measurements from Vickers hardness indents to calculate the room temperature fracture toughness of $Mo_5SiB_2$ [47]. The value determined was 3.2 MPa√m, but the samples examined were a three-phase mixture of $Mo_5SiB_2$, $Mo_3Si$ and a molybdenum boride phase which may have affected the measurement. Ihara et al. calculated values of 1.5-2.0 MPa√m from single crystal samples, also from Vickers hardness indentations [48]. The fracture toughness of polycrystalline $Mo_3Si$ was measured as 3.0 MPa√m by Rosales and Schneibel using notched 3-point bend specimens [26]. Rosales later determined the fracture toughness of single crystal $Mo_3Si$ from Vickers indentation cracks, with values ranging between 2.1 and 2.45 MPa√m for the (100) and (110) directions respectively [49]. The brittle nature of the intermetallic phases is observed up to very high temperatures. Based on values of other intermetallic compounds with the A15 crystal structure, $Mo_3Si$ is expected to have a DBTT above 1200°C [50]. Ito et al. conducted high temperature compression tests on T2 single crystals of varying orientation and at 1500°C the samples failed by brittle fracture in three of the five crystallographic orientations tested [51].

The poor fracture toughness of the intermetallic phases highlights the importance of processing Mo-Si-B alloys in a manner that disperses A15 and T2 in a continuous molybdenum matrix. For alloys with an intermetallic matrix, the presence of the $Mo_{ss}$ particles improves fracture resistance by crack trapping or crack bridging, but Choe et al. reported a room temperature fracture toughness of only 7 MPa√m for the alloy pictured in Figure 2.13a [52]. The fracture toughness of the alloys increases as the molybdenum particles become more connected. Liu et al. measured the room temperature fracture

toughness values of their Mo-9.4Si-13.8B at.% alloy (~42 vol.% $Mo_{ss}$) prepared by hot pressing of elemental powders, Figure 2.20. The contiguity of the molybdenum particles resulted in a toughness of 7.9 MPa√m in the as-hot-pressed condition, which was increased to 10 MPa√m after a 150 hour anneal at 1400°C [53].

The crack tip is forced to interact with the more ductile $Mo_{ss}$ phase when it is present as a fully continuous matrix. Kruzic et al. reported a room temperature fracture toughness of 21 MPa√m for an alloy with a fully continuous $Mo_{ss}$ matrix, Figure 2.22 [41]. Although this result bodes well for the possibility of engineering a Mo-Si-B alloy with good room temperature mechanical properties, it seems likely that the large molybdenum regions (~50μm) would hinder the formation of a continuous borosilicate layer.

Alur and Kumar studied the fracture toughness of the isothermally forged Mo-2Si-1B wt.% alloy shown in Figure 2.19. The toughness was measured as a function of temperature, with values ranging from 8 MPa√m at 25°C to 25 MPa√m at 1400°C, Figure 2.31 [54]. As was also observed by Liu et al., the room temperature toughness was improved by annealing and increased to 9 MPa√m following a 48 hour anneal at 1600°C. The room temperature toughness of this alloy is lower than that measured by Kruzic et al., but the finer distribution of intermetallics is likely to give a better compromise between mechanical properties and oxidation resistance.

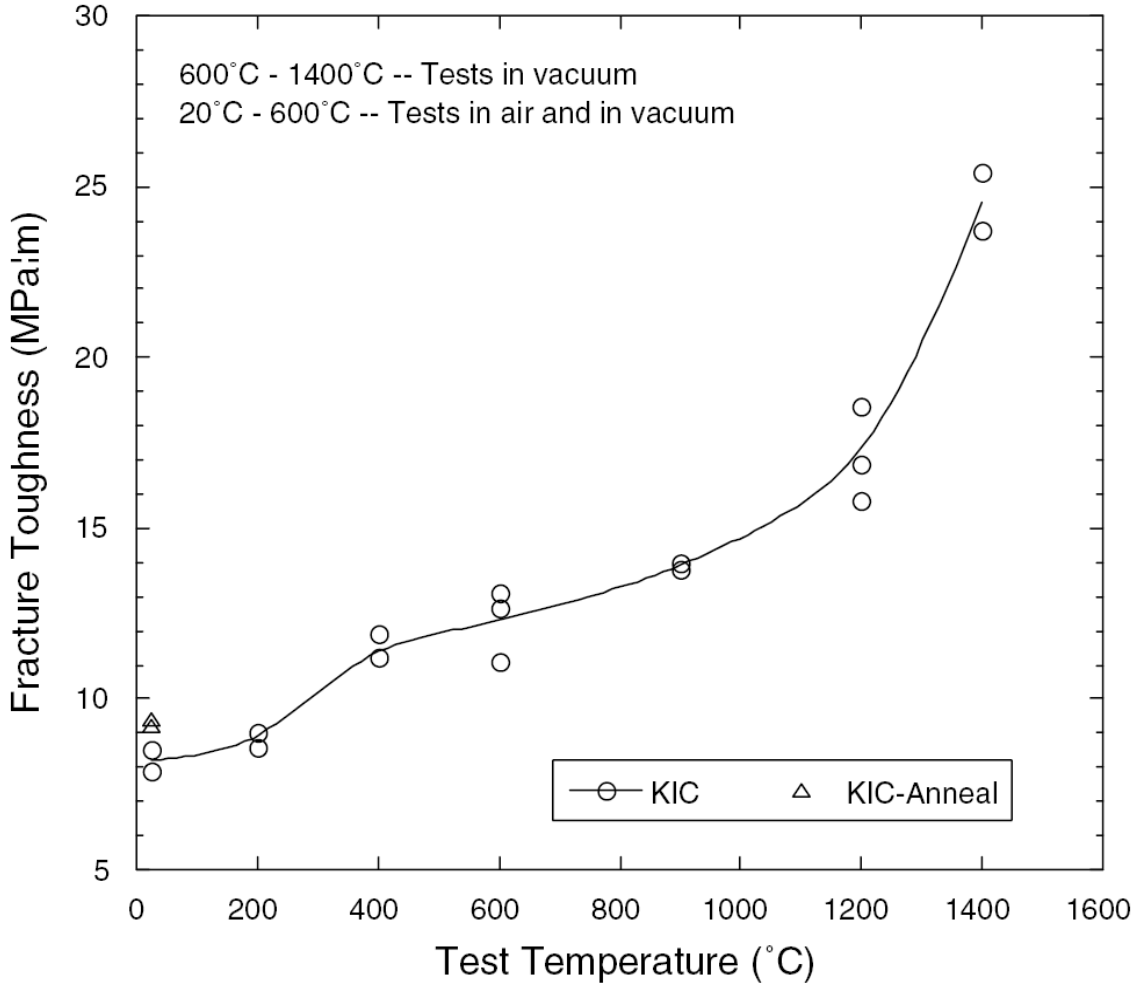


Figure 2.31: The fracture toughness as a function of temperature for a two-phase Mo-2Si-1B wt.% alloy formed by isothermal forging at 1760°C, Alur and Kumar [54].

## 2.5 Oxidation Resistance of Mo-Si-B Alloys

### 2.5.1 Oxidation Mechanisms of Mo-Si-B Alloys

The oxidation of Mo-Si-B alloys occurs in two rate regimes controlled by different mechanisms. Upon the initial exposure to oxidizing conditions, the alloys undergo a transient period of rapid weight loss due to the evaporation of $MoO_3$ and the oxidation rate is controlled by gaseous diffusion of oxygen to the alloy surface. After the borosilicate glass flows together and a continuous layer is formed, oxidation is limited by atomic and molecular diffusion of oxygen. Weight loss continues due to the evaporation of dissolved molybdenum oxide from the surface of the glass.

Akinc and Meyer conducted early work on the mechanisms of Mo-Si-B oxidation resistance for intermetallic alloys in the A15-T1-T2 phase triangle [2,19]. They investigated the relationship between the oxidation rate and the composition of the borosilicate surface scale. The diffusivity of oxygen in glasses is known to be a function of the viscosity, which decreases with increasing boron content. The oxidation rates were compared for alloys with different borosilicate compositions, with the assumption that the B/Si ratio of the glass was equal to that of the base alloy. Following the transient weight loss period, the steady state mass loss rate was modeled as linear. The mass loss rate at 1000°C is plotted as a function of the scale viscosity, which was estimated from known values for borosilicate glass compositions, Figure 2.32.

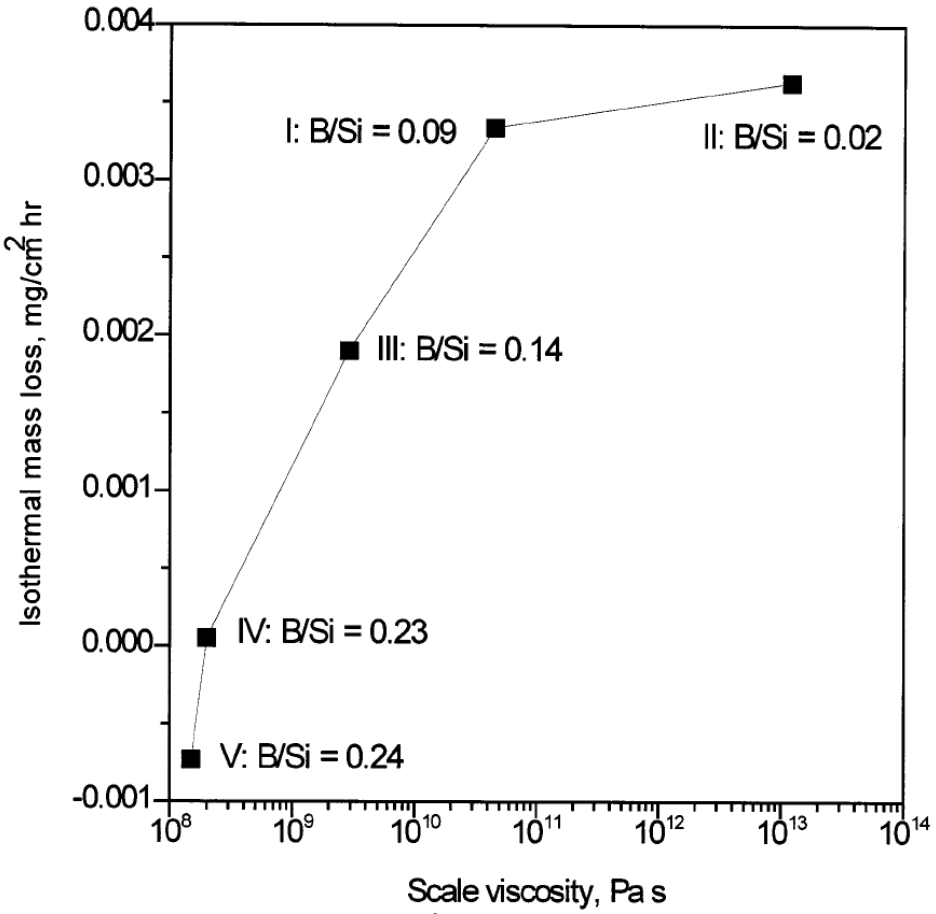


Figure 2.32: Isothermal mass loss (mg/cm$^2$·hr) at 1000°C as a function of scale viscosity (Pa·s), measured by Akinc and Meyer. The scale viscosities have been estimated using values known for borosilicate compositions glasses with the same B/Si ratios as the base alloy [2].

The rate of oxidation decreased with the glass viscosity for the compositions examined. It was concluded that the initial porosity of the borosilicate layer will dictate the oxidation rate if viscous flow does not seal the pores. In this case the oxidation rate is controlled by the permeation of oxygen gas through the porous surface layer. Two scenarios were proposed for the formation of the oxide scale and are illustrated in Figure 2.33. In the first, the alloy forms a porous, low viscosity scale; and in the second, the alloy forms a low porosity, high viscosity scale. As the alloys are heated above 600°C,

the $MoO_3$ evaporates and leaves pores through the surface scale. In the first case, the low viscosity scale will flow together to create a continuous, passivating layer. The oxidation rate will then be controlled by atomic and molecular diffusion of oxygen through the glass. For the fine scale pores, oxidation protection stems from the reduced diffusion of gaseous oxygen to the interface. The approximate oxygen partial pressures at the glass/alloy interface as well as the diameter of the pores are labeled for the different stages of glass formation. When a continuous glass layer is formed, the partial pressure at the interface is low enough that silicon and boron are preferentially oxidized and a molybdenum layer forms. Suppressing the formation of $MoO_3$ dramatically slows mass loss due to vaporization.

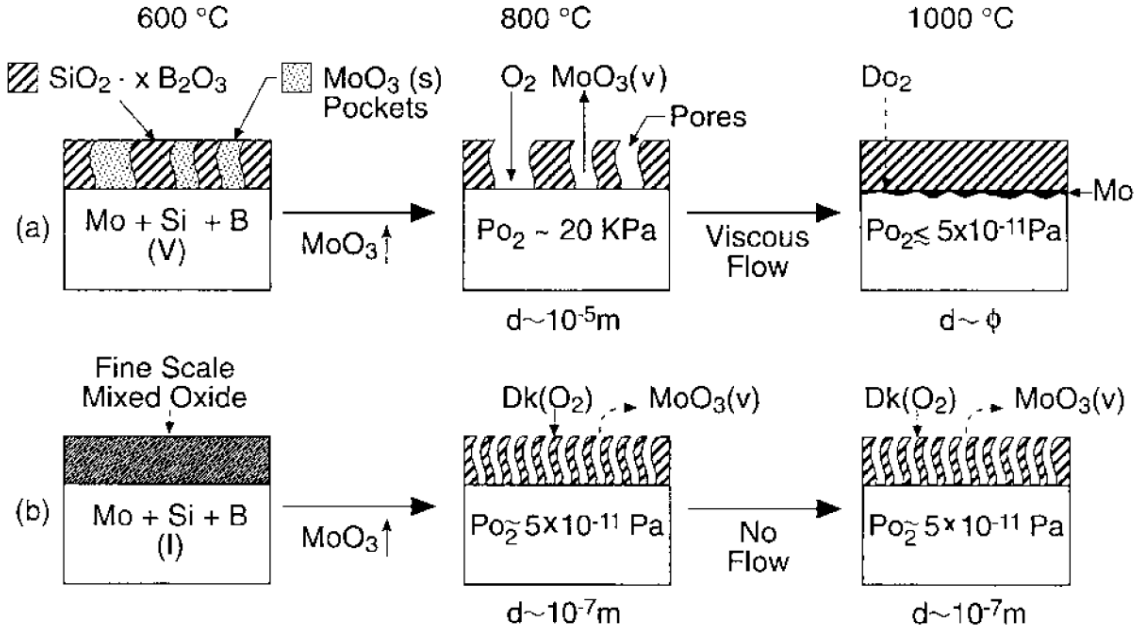


Figure 2.33: Schematic the of oxidation processes proposed by Akinc and Meyer, for (a) a porous, low viscosity scale and (b) a low porosity, high viscosity scale [19].

The A15-T1-T2 intermetallic alloys exhibit good oxidation resistance, but the presence of the more ductile $Mo_{ss}$ phase is necessary for fracture toughness and ductility. Molybdenum has no inherent oxidation resistance and the ability of the glass scale to flow together into a continuous layer is especially important for alloys in the $Mo_{ss}$-A15-T2 phase triangle. Perepezko and Dimiduk stated that the performance of these materials varies widely because "the oxidation resistance for these alloys derives from a delicate balance established during transient oxidation behavior" [1]. Helmick et al. investigated the formation of borosilicate layers on Mo-3Si-1B wt.% alloys and found that the transient period of rapid weight loss continues after the formation of the borosilicate layer due to channels in the glass that extend to the alloy interface [55]. If it is assumed that these channels occur over the $Mo_{ss}$ phase regions, the oxidation resistance can then be considered a function of the microstructural morphology as well as the intermetallic content and the B/Si ratio. Under this scenario, is important to create a microstructure with a fine dispersion of the intermetallic phases so that a continuous glass layer forms quickly, especially for the T2 phase which forms a low viscosity glass.

The oxidation kinetic behavior of Mo-Si-B alloys is known to vary across different temperature regimes. Parthasarathy et al. investigated the oxidation behavior of a Mo-12Si-12B at.% alloy (corresponding to 33 vol.% $Mo_{ss}$) over a range of temperatures in order to determine the underlying mechanisms [56,57]. The oxidation of pure molybdenum was compared to evaluate the role of silicon and boron on oxidation resistance at low temperatures. They reported that the alloys undergo either linear or parabolic oxidation kinetic over different temperature ranges. Linear oxidation was observed when no protective oxide layer was formed and the rate of mass loss was linear

with respect to time. The proposed oxidation kinetic behaviors are illustrated schematically in Figure 2.34 for the four temperature regimes examined. In the 500°C-600°C range, pure molybdenum showed weight gain due to the formation of a $MoO_3$ surface layer. At these low temperatures, $MoO_3$ is not volatile and it formed an adherent layer that resulted in parabolic weight gain. The presence of silicon and boron oxide in the mixed oxide scale lowered the rate of mass gain in this regime for the Mo-Si-B alloy. Evaporation of $MoO_3$ around 700°C lead to linear mass loss for pure molybdenum, with a rate which increased with temperature. Linear weight loss was also observed for the Mo-Si-B alloy around 700°C, which was also slowed by the presence of silica and boron oxide. It was at moderate temperatures (650-750°C) that Mo-Si-B alloys were found to have the worst oxidation resistance. The oxides formed a porous scale that allows oxygen to permeate to the interface and $MoO_3$ to bubble out. The kinetic behavior began to show parabolic mass loss as the temperature was increased to approximately 800°C and the parabolic rate constant was actually found to decrease with further increases in temperature. The improved oxidation resistance at increasing temperatures was attributed to evaporation of $B_2O_3$ from the borosilicate scale, which increased the viscosity of the glass and decreased oxygen diffusion to the interface.

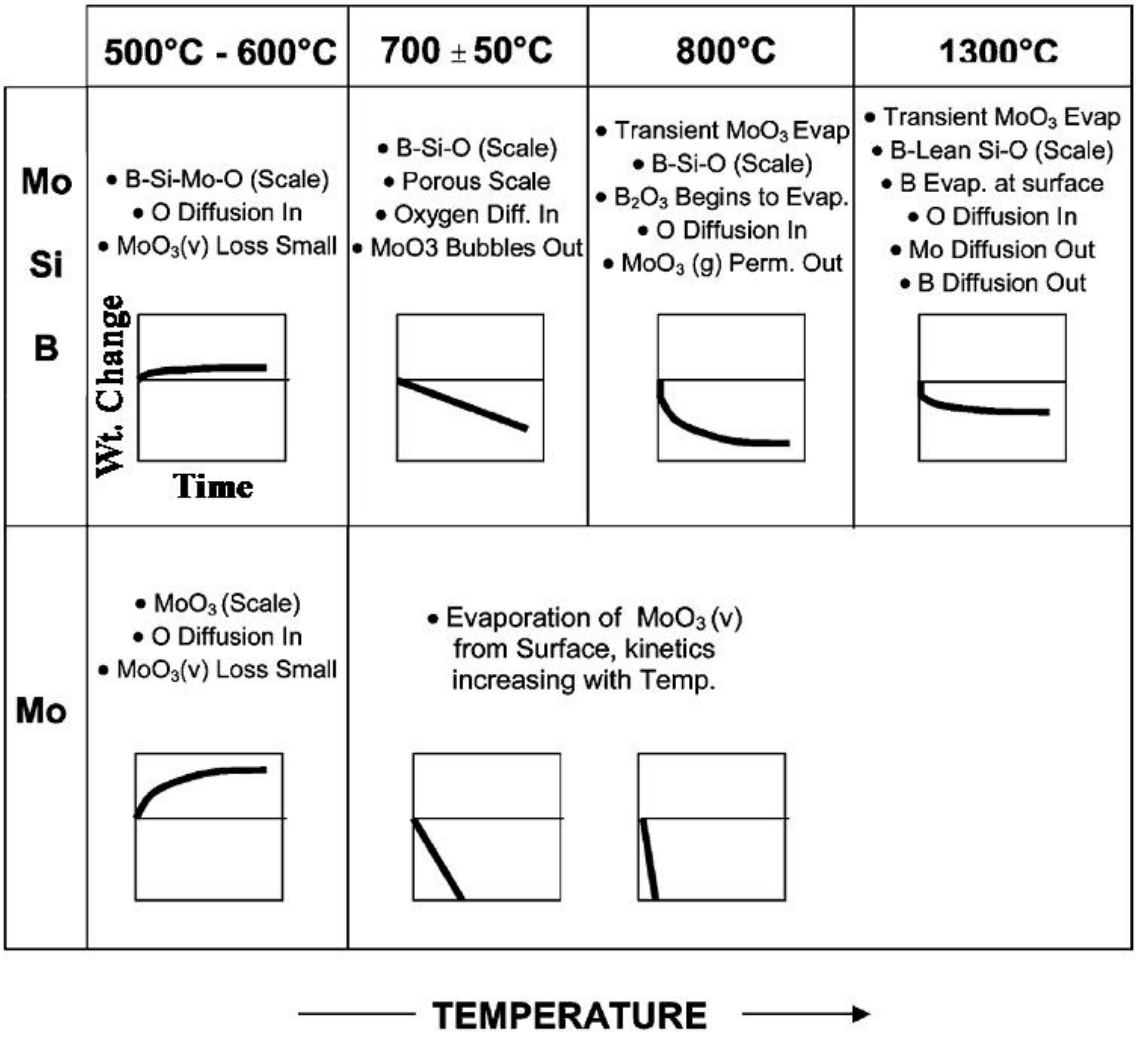


Figure 2.34: The different kinetic oxidation regimes for molybdenum and Mo-Si-B alloys, proposed by Parthasarathy et al. [56].

Parthasarathy et al. conducted an experiment to confirm that $B_2O_3$ in the glass did in fact increase the oxidation rate of Mo-Si-B alloys [56]. A molybdenum sample was coated with an approximately 1μm thick pure silica layer and tested in cyclic oxidation at 700°C with 1 hour intervals. Almost zero mass change was observed after 8 cycles, confirming that boron increased the oxidation rate. However, further testing was ceased due to spalling of the silica layer which indicated that boron was necessary to create a more adherent glass. A second experiment was conducted to examine the effect of boron oxide evaporation on the parabolic mass loss rate [56]. A Mo-11Si-11B at.% (40 vol.% $Mo_{ss}$) alloy specimen was pre-oxidized at 1300°C for one hour before testing at 800°C. The mass loss of the pretreated alloy is compared to that of untreated specimens tested at 800°C and 1300°C in Figure 2.35. Cross-sections of the untreated samples tested at 800°C and 1300°C for 200 hours are compared in Figure 2.36. The sample tested at 800°C had a much thicker borosilicate layer (note that the images have different sized scale bars) and there were a large numbers of pores in the glass, presumably formed by $MoO_3$ bubbles.

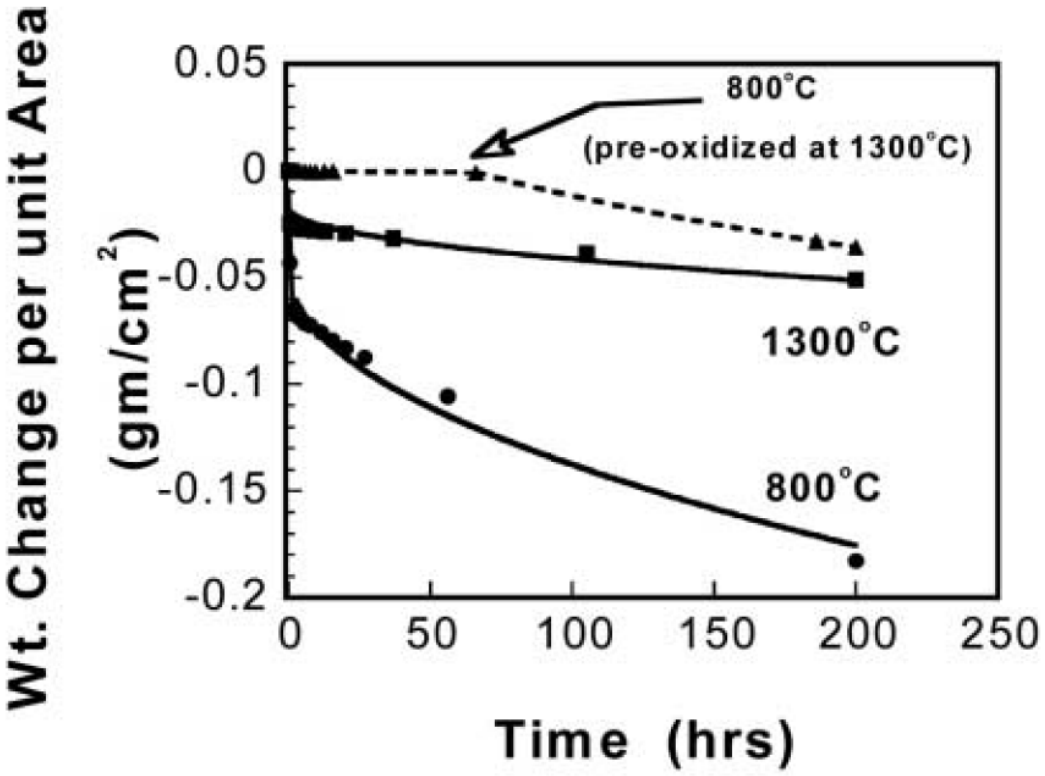


Figure 2.35: The isothermal mass loss of Mo-11Si-11B at.% samples tested at moderate (800°C) and high (1300°C) temperatures. A pre-oxidized sample was treated at 1300°C for 1 hour prior to testing at 800°C, Parthasarathy et al. [56].

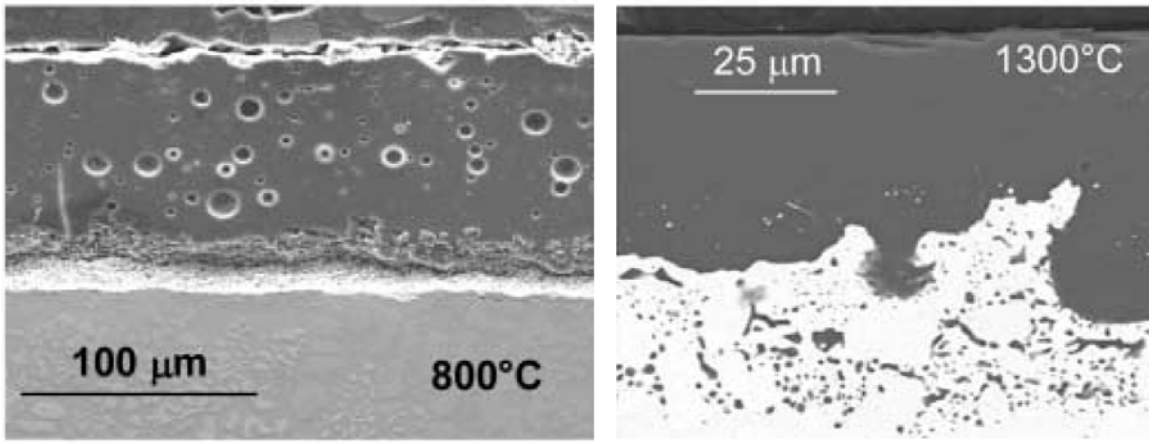


Figure 2.36: SEM image comparison of the borosilicate layer after oxidation in air at 800°C and 1300°C for 200 hours. The pores in the borosilicate layer were speculated to be due to $MoO_3$ bubbles. Note the images at different magnifications [56].

The untreated alloy had a much greater transient weight loss at 800°C than 1300°C, as well as a higher oxidation rate in the parabolic regime. In contrast, the pre-oxidized alloy showed almost zero weight loss at 800°C for up to 60 hours. The improved oxidation resistance of the pre-oxidized alloy was proposed to be due to the lower level of boron present in the glass as a result of $B_2O_3$ evaporation at the high pretreatment temperature. The rate of weight loss began to increase after a 60 hour period, presumably due to boron diffusion from the base alloy into the glass layer.

The results of Parthasarathy et al. seem contrary to those attained by Akinc and Meyer, who observed better oxidation resistance with less viscous borosilicate layers. This is due to the higher B/Si ratios investigated by Parthasarathy, which lead to a lower range of viscosities than those studied by Akinc and Meyer. The viscosity of borosilicate melts is highly dependent on the boron content. The viscosity of pure $SiO_2$ at 1000°C decreases eight orders of magnitude by the addition of 30 mol.% $B_2O_3$ [58]. Parthasarathy reported that at 700°C, the glass viscosity was $5\times10^6$ Pa·s, which is lower than the viscosity of $10^9$ Pa·s necessary to suppress bubble formation in silicate melts [56]. The combination of these findings highlight the need for the borosilicate glass to have a low enough viscosity to flow over the surface, as shown by Akinc and Meyer, but a high enough viscosity to limit permeation of oxygen and bubbling of $MoO_3$, as shown by Parthasarathy.

### 2.5.2 Oxidation Rates and Behavior of Mo-3Si-1B wt.% Alloys

The Mo-3Si-1B wt.% alloy composition is identified as having a favorable combination of mechanical properties and oxidation resistance. The oxidation rates at 1100°C measured by two different research groups are compared in Figure 2.37.

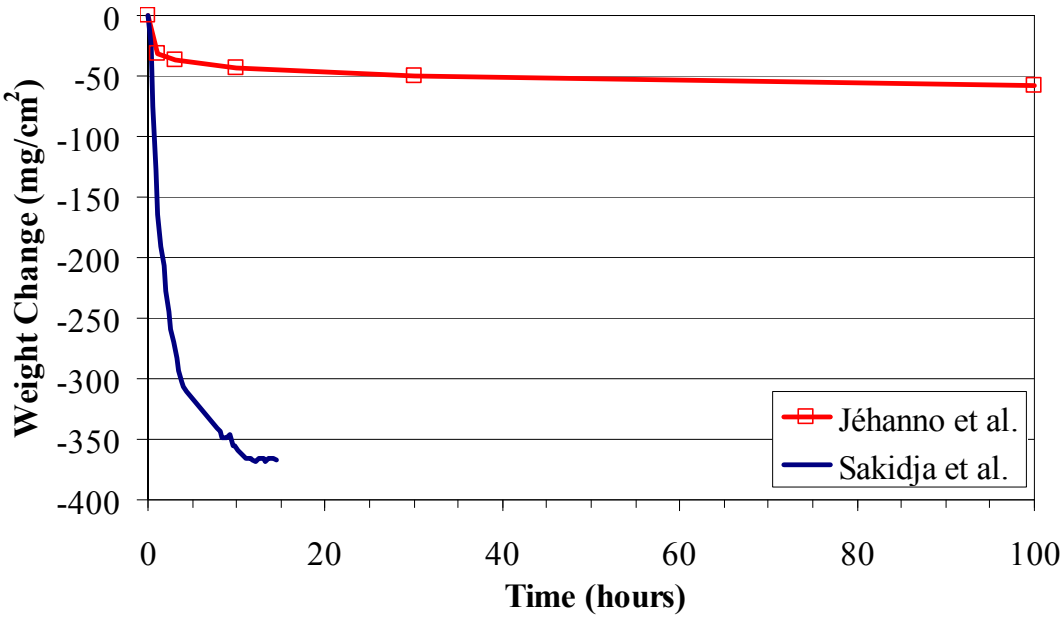

Figure 2.37: A comparison of the 1100°C oxidation rates for Mo-3Si-1B wt.% alloys prepared and tested by two different research groups [59,60]

It can be seen that the oxidation behavior varies dramatically between the two studies, even though the alloys have the same compositions. The test by Sakidja et al. had a very high transient weight loss and was ceased before reaching the diffusion controlled regime, whereas the alloy tested by Jéhanno et al. showed very little transient weight loss. It is postulated in this work that the transient oxidation behavior of Mo-Si-B alloys is a function of both the composition and microstructure. Under this assumption, alloys with a fine dispersion of the intermetallics should limit the transient weight loss, but this is difficult to verify because no systematic studies have been reported on the oxidation behavior of alloys with different degrees of microstructural coarseness. The variations in the observed oxidation behavior could also be due to other factors, including non-equilibrium silicon concentration in the $Mo_{ss}$ phase due to the melt-based processing methods used.

### 2.5.3 Improvement of Oxidation Resistance by Aluminum Addition

Aluminization of the surface of Mo-Si-B alloys by pack cementation has been shown to significantly improve oxidation resistance [59,61]. Experiments by Sakidja et al. showed near zero mass change for samples oxidized for 50 hours at temperatures ranging from 732°C -1372°C [59]. This highlights the advantage of aluminum addition, but pack cementation only affects the surface layer and it would be advantageous to have aluminum distributed throughout the material. The addition of aluminum to Mo-Si-B alloys by melt processing routes is difficult due its high volatility at the melting point of molybdenum. The powder metallurgy approach used in this project allows for the addition of aluminum. The techniques developed for aluminum addition will be discussed in Chapters 3 and 4.

Aluminum additions to Mo-Si-B alloys also have the potential of improving oxidation resistance without significantly increasing the intermetallic content of the alloy. This is due the relatively high solid solution limit of aluminum in molybdenum, 3.5 wt.% (12 at.%) at 1600°C, as illustrated in the Mo-Al phase diagram, Figure 2.38 [62]. Molybdenum and aluminum form the $Mo_3Al$ intermetallic phase, which has the A15 crystal structure and exhibits complete solubility with the $Mo_3Si$ phase.

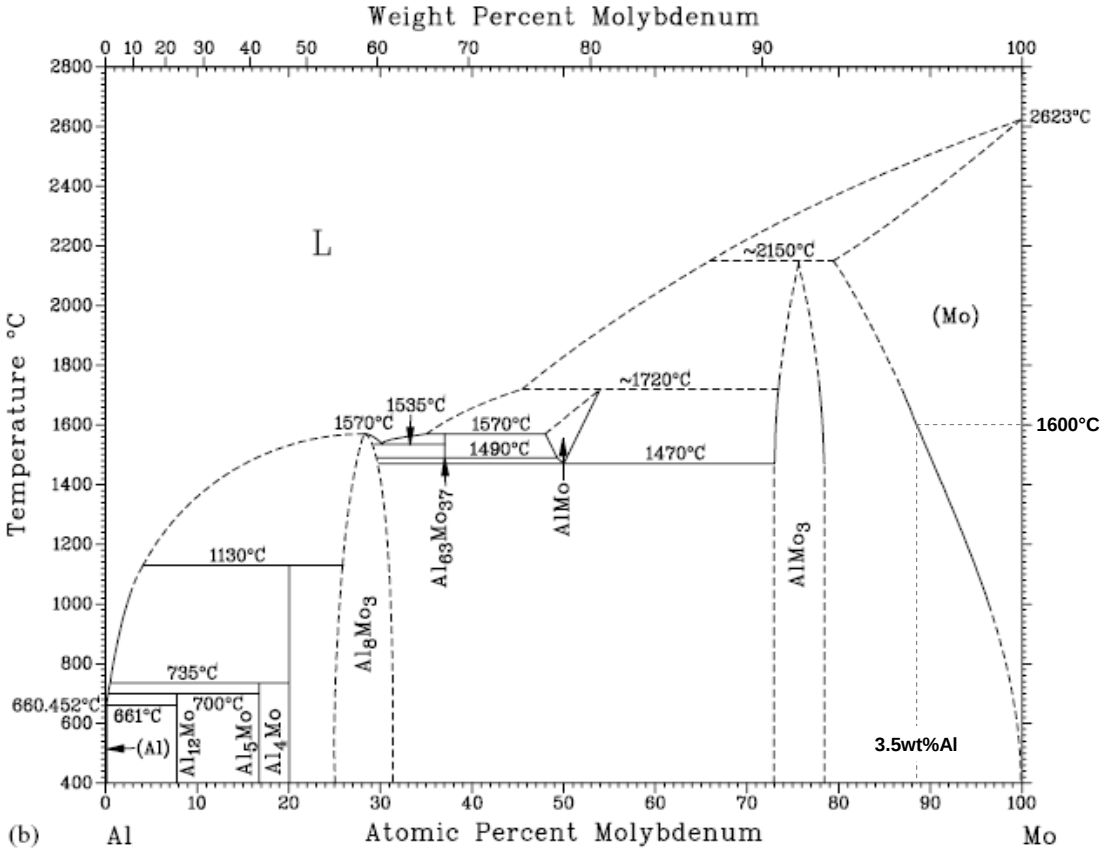


Figure 2.38: The molybdenum-aluminum binary phase diagram [62].

## 2.6 Nitride-Based Reactions for the Formation of $Mo_{ss}$-A15-T2 Alloys

It has been discussed that the Mo-Si-B alloys should have a fine dispersion of intermetallics in a continuous $Mo_{ss}$ matrix in order to achieve an acceptable compromise between oxidation resistance and mechanical properties. A number of production methods have been described, but few succeed at creating the desired microstructure. Hot-working has been shown to greatly improve the microstructures but the techniques used are costly and difficult for mass production.

One of the main objectives of this work is to demonstrate the ability to synthesize the intermetallic phases and control their dispersion using a novel powder metallurgical method. Powder metallurgy provides an opportunity for microstructure control by changes in starting materials and processing parameters. Previous efforts have produced alloys with high oxygen content, which is known to severely embrittle molybdenum alloys [63]. The oxygen impurity levels are difficult to control because elemental silicon and boron powders are prone to oxidation during processing. In the reaction synthesis method, silicon nitride ($Si_3N_4$) and boron nitride (BN) powders are used as the silicon and boron precursors and reacted with molybdenum to form Mo-Si-B intermetallic alloys. The covalent nitrides are stable in oxidizing environments up to 1000ºC which allows for fine particle processing without oxidation. This approach utilizes standard powder processing techniques and provides a means for creating Mo-Si-B alloys in a much less complex and expensive manner than previously demonstrated.

### 2.6.1 Assessment of the Formation of A15 and T2 from Mo, $Si_3N_4$ and BN

The method developed is the first attempt to form $Mo_{ss}$-A15-T2 alloys using the nitride reactants, but previous research indicates the viability of this approach. Molybdenum silicides have been reported to form at the interfaces of Mo-$Si_3N_4$ joints and Krishnarao et al. used the reaction of molybdenum and $Si_3N_4$ to produce $MoSi_2$ composites [64,65]. Benko and Wyczesany studied the interaction of molybdenum and cubic boron nitride (cBN) and reported that the two materials react to form molybdenum borides beginning at 527°C and over a wide range of nitrogen partial pressures [66].

The decomposition reactions of the nitrides are presented in Equations 2.4 and 2.5. The equilibrium partial pressure of nitrogen can be calculated from Equations 2.6 and 2.7 using the standard free energies of formation for the nitrides obtained from published thermodynamic tables:

$$Si_3N_4 \rightarrow 3Si + 2N_2 \tag{2.4}$$

$$BN \rightarrow B + \tfrac{1}{2} N_2 \tag{2.5}$$

$$\Delta G_{Si_3N_4} = -RT \ln\left(P_{N_2}{}^2\right) \tag{2.6}$$

$$\Delta G_{BN} = -RT \ln\left(P_{N_2}{}^{1/2}\right) \tag{2.7}$$

It should be noted that two different polymorphs of boron nitride have been used in this research. The initial reaction studies were completed using hexagonal boron nitride powder (hBN). Cubic boron nitride powders were also used to evaluate the effect of different powder morphologies on the distribution of intermetallics. The cubic phase was originally thought to be a metastable, high pressure polymorph, but has since been shown to be the stable form at standard conditions [67]. The free energy of the transformation from hBN to cBN, $\Delta G_{Trans.}^{hBN \rightarrow cBN}$, is plotted as a function of temperature in

Figure 2.39. The free energy of formation for the cubic boron nitride phase is not listed in the standard thermodynamic tables, but knowing the free energy of the transformation, the free energy of formation is given as:

$$\Delta G_f^{cBN} = \Delta G_f^{hBN} + \Delta G_{Trans.}^{hBN \rightarrow cBN} \tag{2.8}$$

The Gibbs free energies of formation for α-$Si_3N_4$ and the two BN phases, as well as their equilibrium nitrogen partial pressures are listed in Table 2.3 and plotted as a function of temperature in Figure 2.40 and Figure 2.41. The stability of the nitrides at low to moderate temperatures imparts oxidation resistance. At high temperatures the nitrides have high equilibrium nitrogen partial pressures and small free energies which promotes the formation of the A15 and T2 phases.

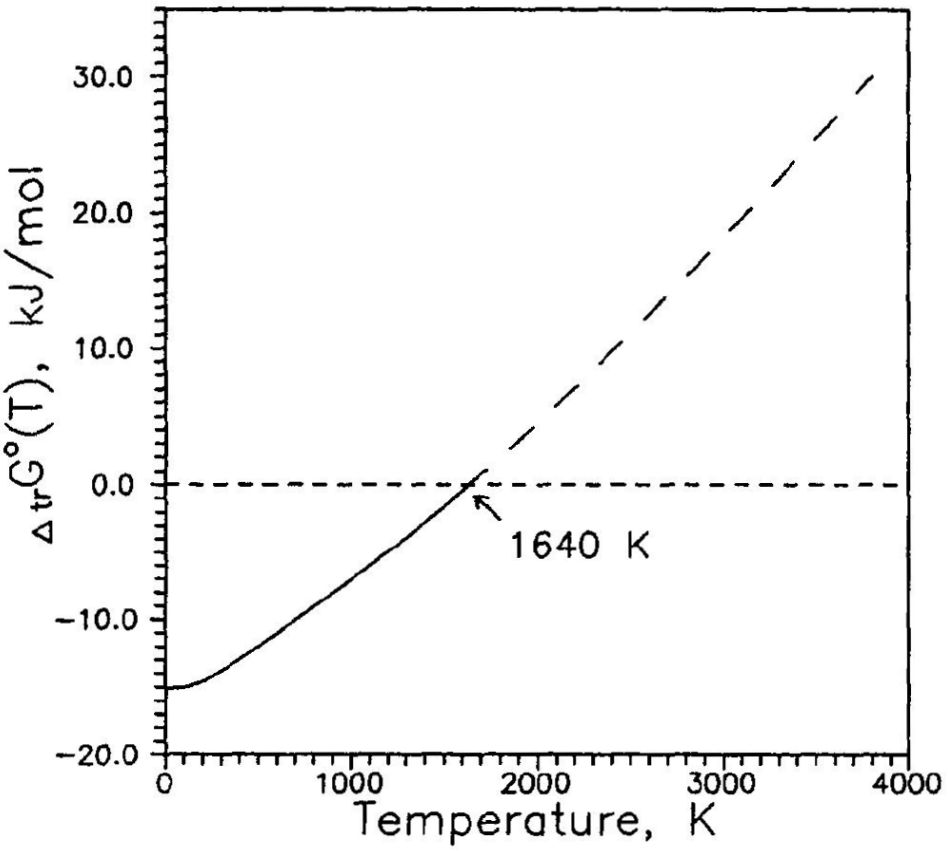


Figure 2.39: The free energy change for the transformation of hBN → cBN, Edgar [68].

Table 2.3: Gibbs free energies and equilibrium nitrogen partial pressures for the α-$Si_3N_4$, hBN and cBN reactants at various temperatures [68,69].

| | **α-$Si_3N_4$** | | **hBN** | | **cBN** | |
|---|---|---|---|---|---|---|
| Temperature (K) | $\Delta G_f$ (kJ/mol) | $P_{eq}$ $N_2$ (atm) | $\Delta G_f$ (kJ/mol) | $P_{eq}$ $N_2$ (atm) | $\Delta G_f$ (kJ/mol) | $P_{eq}$ $N_2$ (atm) |
| 1300 | -314.1 | 1.5E-16 | -139.7 | 9.1E-08 | -143.7 | 5.7E-08 |
| 1500 | -248.9 | 1.3E-11 | -122.2 | 4.6E-06 | -123.9 | 3.9E-06 |
| 1700 | -182.9 | 8.9E-08 | -104.8 | 9.1E-05 | -104.1 | 9.7E-05 |
| 1900 | -101.0 | 3.3E-04 | -87.5 | 9.6E-04 | -84.3 | 1.2E-03 |

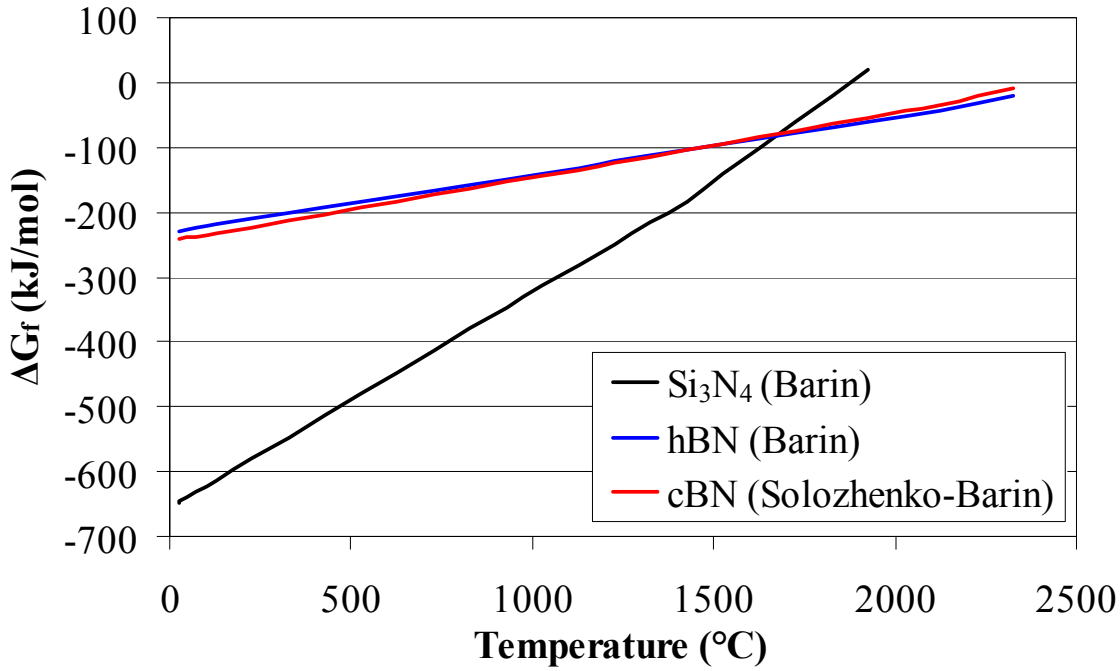


Figure 2.40: The Gibbs free energy of formation for α-$Si_3N_4$, hBN and cBN as a function of temperature [68,69].

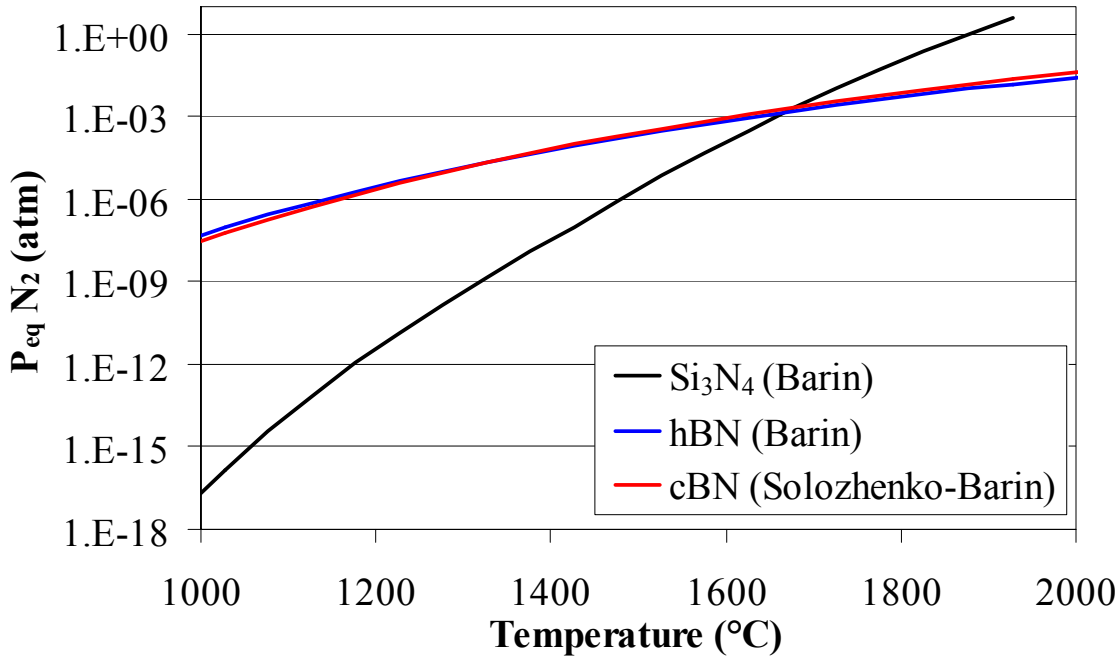


Figure 2.41: The equilibrium nitrogen partial pressure of α-$Si_3N_4$, hBN and cBN as a function of temperature [68,69].

2.6.1.1 The Reaction to Form the $Mo_3Si$ Phase

Heikinheimo et al. investigated the reactions between molybdenum and $Si_3N_4$ [70]. The phases in equilibrium with $Si_3N_4$ are plotted as a function of temperature and nitrogen partial pressure in Figure 2.42. Above 1300K molybdenum and $Si_3N_4$ only coexist over a narrow range of pressures near 10bar.

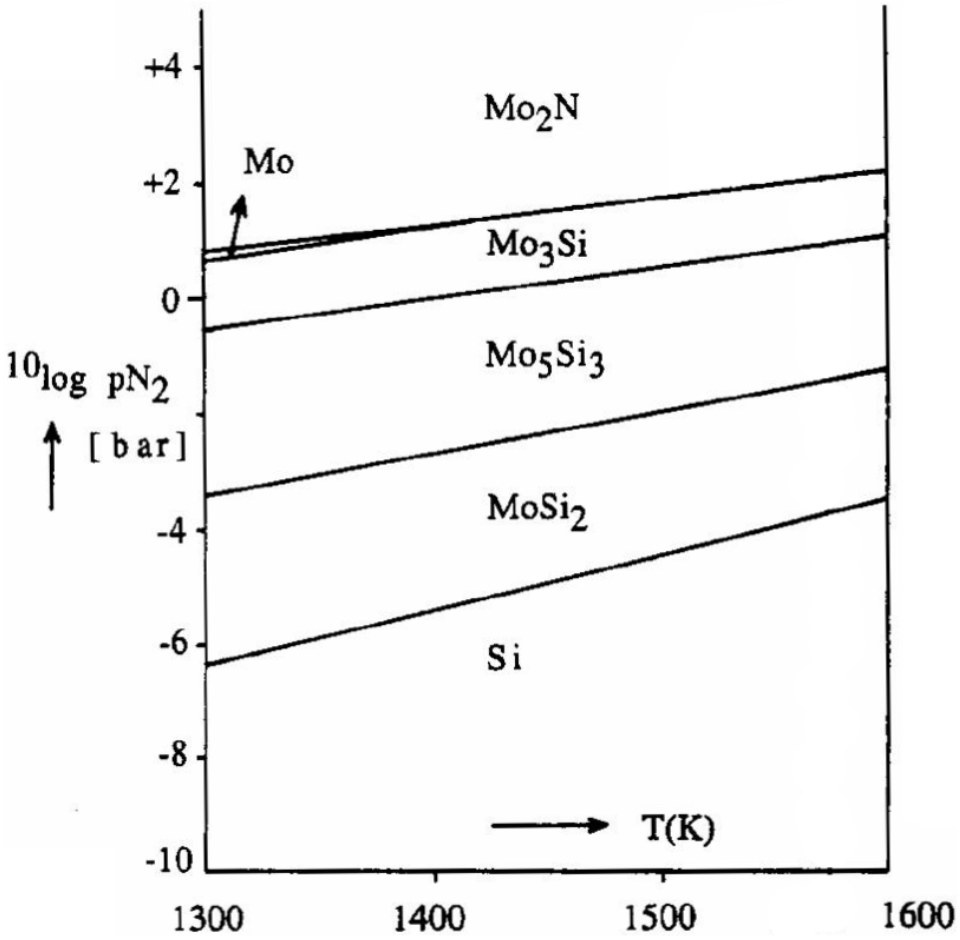


Figure 2.42: The phases in equilibrium with $Si_3N_4$ in the Mo-Si-N system as a function of temperature and nitrogen partial pressure, plotted by Heikinheimo et al. [70].

The reaction to form the A15 phase is written as:

$$3Mo + \tfrac{1}{3} Si_3N_4 \rightarrow Mo_3Si + \tfrac{2}{3} N_2 \tag{2.9}$$

and the thermodynamic driving force of the reaction, $\Delta G_{rxn}$, is given as a function of temperature by:

$$\Delta G_{rxn}^{A15}(T) = \Delta G_f^{A15}(T) - \tfrac{1}{3}\Delta G_f^{Si_3N_4}(T) \tag{2.10}$$

The free energy of formation for the A15 phase is available from standard thermodynamic tables [69]. The free energy change of the reaction between molybdenum and $Si_3N_4$ to form the A15 phase is plotted in Figure 2.43 as a function of temperature. The reaction becomes thermodynamically favorable at 1057°C.

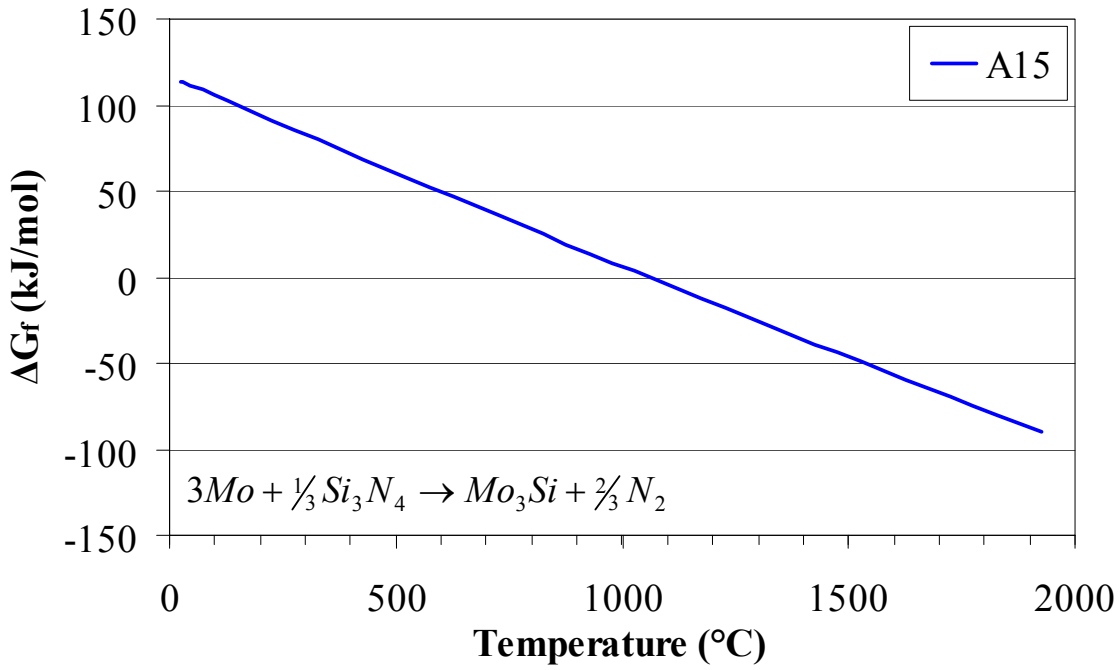


Figure 2.43: The Gibbs free energy change for the reaction of molybdenum and $Si_3N_4$ to form $Mo_3Si$ plotted as a function of temperature.

2.6.1.2 The Reaction to Form the $Mo_5SiB_2$ Phase

The reaction to form the T2 phase is written as:

$$5Mo + \tfrac{1}{3}Si_3N_4 + 2BN \rightarrow Mo_5SiB_2 + \tfrac{5}{3}N_2 \tag{2.11}$$

and the the thermodynamic driving force of the reaction, $\Delta G_{rxn}$, is given as a function of temperature by:

$$\Delta G_{rxn}^{T2}(T) = \Delta G_f^{T2}(T) - \tfrac{1}{3}\Delta G_f^{Si_3N_4}(T) - 2\Delta G_f^{BN}(T) \tag{2.12}$$

Tabulated thermodynamic properties are not available for the T2 phase; however Perepezko et al. were able to estimate the Gibbs free energy by comparing values known for the phases which coexist in equilibrium with T2 [27]. The analysis proceeds as follows: knowing that phase equilibria gives the phase fields Mo-$Mo_2B$-T2 and Mo-A15-T2, the values of the free energy are constrained such that the common tangent planes for the phase fields preclude the establishment of a $Mo_2B$-A15 phase equilibria. The analysis was repeated by comparing the other possible phase equilibria to determine the upper and lower bounds of the free energy. A mean value of -1047.30 ± 5.29 kJ/mol was determined at 1600°C. The same procedure was repeated at different temperatures and yielded the temperature dependence:

$$G \approx -100.3 - 0.505T \tag{2.13}$$

in kJ/mol, where the temperature $T$ is in Kelvin. Perepezko considered all of the intermetallic phases as stoichiometric line compounds, therefore the values calculated by this method are only a simple estimation of the free energy. More robust calculations would require an in-depth analysis including many additional factors such as the defect structures and solubility limits of the phases.

The estimated free energy values were used to determine $\Delta G_f(T2)$ and to calculate the free energy of the reaction from the nitrides, plotted in Figure 2.44 for both the hBN and cBN reactants. There is little difference in the free energy of reaction for either of the two BN reactants and the reaction becomes favorable at 1109°C with the hBN and at 1124°C with the cBN.

It can be seen from this analysis that both of the nitride-based reactions to form A15 and T2 are thermodynamically favorable and the onset of both reactions are expected to occur near 1100°C. The selection of either BN polymorph is not expected to significantly affect the temperature at which the T2 phase forms.

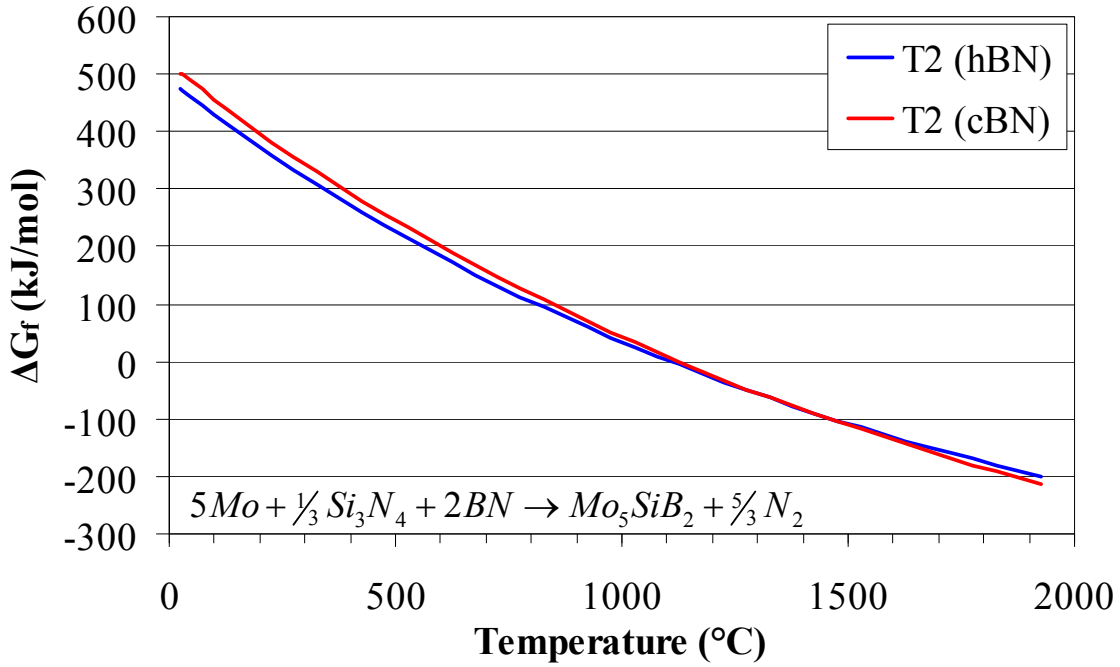


Figure 2.44: The Gibbs free energy of the reaction between molybdenum, $Si_3N_4$ and BN to form $Mo_5SiB_2$ as a function of temperature. The reaction is compared for the hBN and cBN reactants.

## 2.7 Powder Processing Purity Considerations

One of the main considerations for processing of Mo-Si-B alloys is the need to maintain low impurity contents throughout the process. This is especially a concern with powder processing methods. High surface area powders typically have high oxygen contents and organic processing additives can leave carbon residue if they do not burn out cleanly. The nitride reactants used in this research also present a source for nitrogen contamination. These impurities are all known to have detrimental effects on the mechanical properties of molybdenum alloys. Olds and Rengstorff investigated the effect of carbon, oxygen and nitrogen impurities on the ductility of arc-cast molybdenum samples using three-point bend tests [63]. The ductile-to-brittle transition temperatures are plotted in Figure 2.45, where the transition temperature was based on a 4° bend angle prior to fracture.

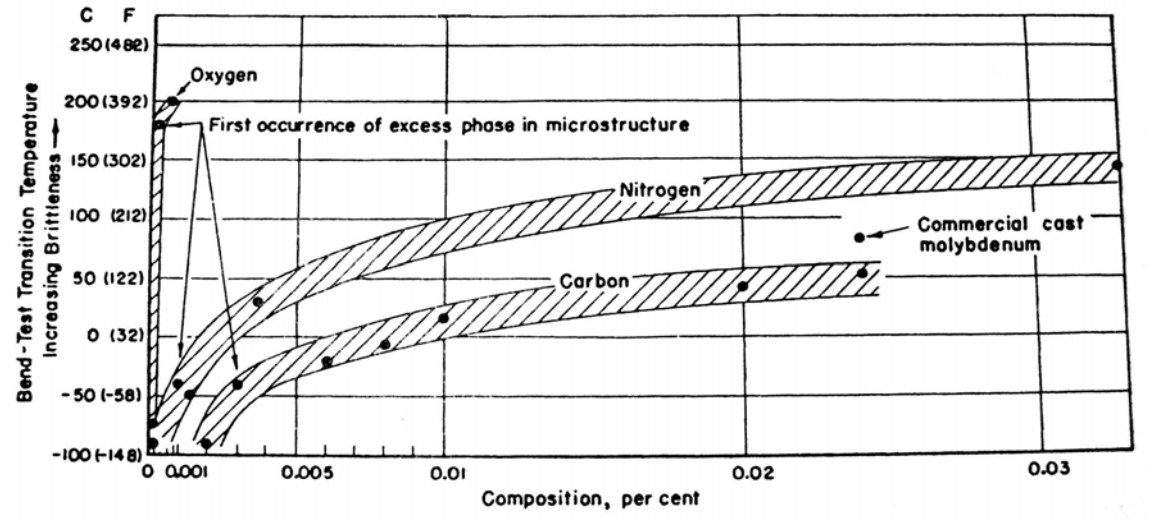


Figure 2.45: The dependence of carbon, oxygen and nitrogen contents on the DBTT of cast molybdenum, Olds and Rengstorff [63].

Oxygen dramatically affects the DBTT of pure molybdenum even at very low levels. This is due to oxygen segregation at the grain boundaries which promotes brittle, intergranular fracture [71]. It is reported to take as little as 1 ppm by weight of oxygen segregated at the grain boundaries for complete surface coverage, assuming a grain size of 100μm [45]. Kumar and Eyre have shown that the grain boundary strength declines steeply with increasing oxygen coverage at the boundaries, Figure 2.46.

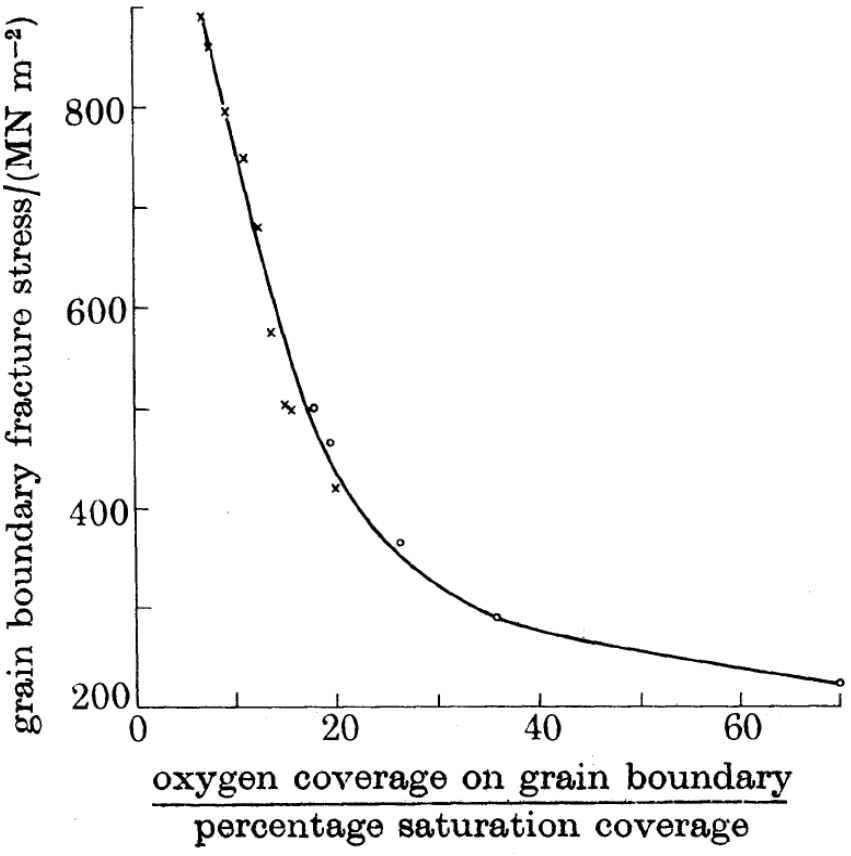


Figure 2.46: A plot of the grain boundary fracture stress of molybdenum as a function of the oxygen coverage at the boundaries, Kumar and Eyre [71].

It is important to note that although minute oxygen contents significantly harm the ductility of pure molybdenum, the effect on Mo-Si-B alloys is not entirely clear. Both silicon and boron are strong oxide formers and may getter oxygen from the grain boundaries. This could benefit the strength of the molybdenum matrix phase, but may also lead to other problems such as increased creep due to a glassy phase at the grain boundaries.

Nitrogen also has a detrimental effect on the ductility of molybdenum, although to a much lesser extent than oxygen. Nitrogen presents less of a concern during processing because it has a very low solubility in molybdenum and $Mo_2N$ begins to decompose at 680°C [72]. Jenn and Ettmayer reported that the solubility limit of nitrogen in molybdenum is given as [73]:

$$\log c_N = \frac{1}{2}\log p_{N_2} + 0.875 - \frac{4810}{T} \tag{2.14}$$

where $c_N$ is in atomic percent, $p_{N_2}$ is in atmospheres and $T$ is in Kelvin. This gives an equilibrium content of only 200ppm at 1600°C and 1atm. Furthermore, the partial pressure of nitrogen due to the decomposition of $Si_3N_4$ and BN is likely to be very low when firing in a flowing, inert atmosphere. Regardless, the presence of nitrogen in the alloys is a possible concern and the residual levels in the fired alloys should be monitored.

The work by Olds and Rengstorff indicates that carbon has a detrimental effect on ductility, Figure 2.45, although there are conflicting reports of carbon increasing the ductility of molybdenum [71,74]. Kumar and Eyre reported that carbon moderates the negative effect of oxygen by reducing the driving force of oxygen segregation to the grain boundaries [71]. A second hypothesis for the improvement is that segregation of

carbon at the grain boundaries increases the boundary strength. Counter to this explanation, Krajnikov et al. demonstrated that the formation of $Mo_2C$ platelets at the grain boundary surfaces does in fact embrittle molybdenum [75]. Suzuki et al. reconciled the two different observations by suggesting that although segregation of carbon to the grain boundaries may improve ductility, it is likely due to the elimination of the solid solution hardening effect of carbon inside the grains [74]. It can be seen from the Mo-C phase diagram that there is very little solubility of carbon in molybdenum, Figure 2.47 [76]. Rudman gives the solid solution limit of carbon in molybdenum as [77]:

$$\ln c_S = 16.78 - \frac{2.29 \times 10^4}{T} \tag{2.15}$$

with $c_S$ in ppm by weight and $T$ in Kelvin. At 1600°C, the solubility of carbon is only 95ppm and drops to essentially zero below 1000°C. Regardless of the potential benefits of carbon it can be seen that only small quantities will lead to the formation of molybdenum carbide. Therefore it is important to minimize the amount of carbon introduced during processing and ensure that any organic processing aides used burn out cleanly during firing.

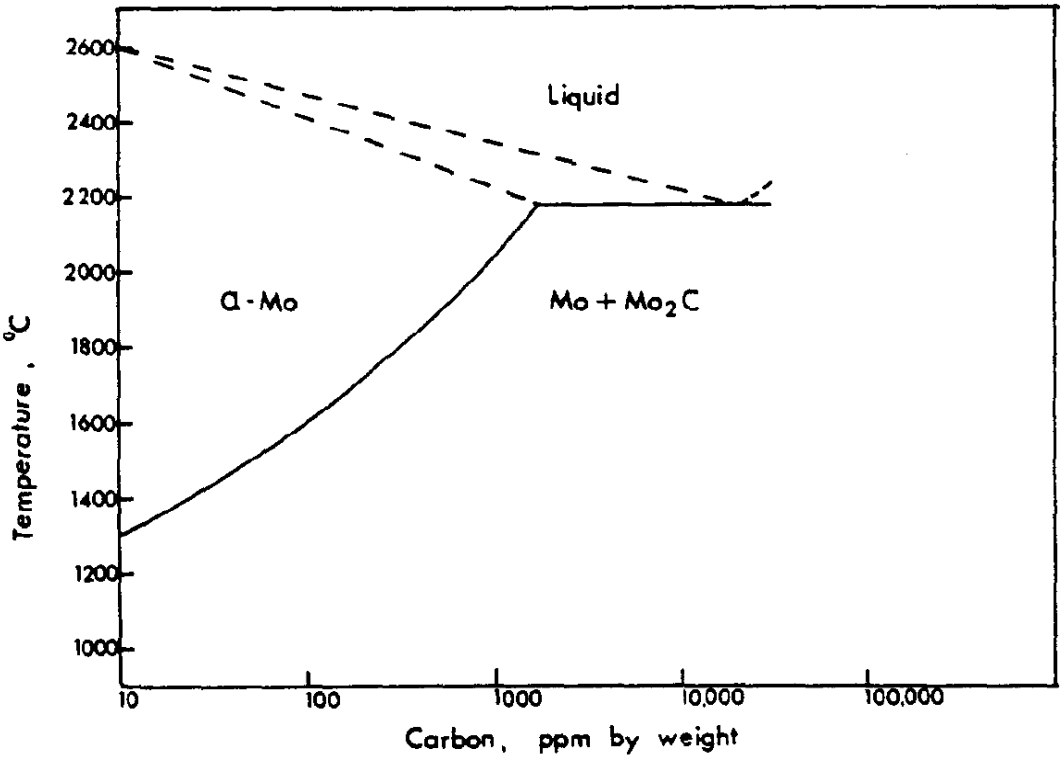


Figure 2.47: The molybdenum-carbon phase diagram [76].

# CHAPTER 3

# EXPERIMENTAL PROCEDURES

The procedures and equipment used to prepare and characterize the Mo-Si-B alloys produced by the reaction synthesis method are introduced in the following chapter. Different boron nitride reactants were selected to investigate the effects of particle size and morphology on the microstructure. The powder processing techniques have been developed to create a fine distribution of the intermetallic phases in a $Mo_{ss}$ matrix. The characterization techniques used include x-ray diffraction, scanning electron microscopy and electron backscatter diffraction imaging. The analytical methods used to quantify and interpret the microstructural parameters are described.

## 3.1 Raw Materials

Raw materials were selected on the basis of high purity and low oxygen content, as well as commercial availability in large quantities. Submicron powders were used to reduce the sintering temperatures and to maintain fine grain size after firing. Further characterization of the materials was performed to supplement the data supplied by the manufacturers. X-ray diffraction (XRD) was used to rule out the presence of impurity phases, the specific surface areas of the powders were determined by surface area analysis, the particle size distributions of the powders were measured by laser scattering, and images of the powder were obtained using scanning electron microscopy. The impurity levels of the powders were either supplied by the manufacturers or measured

from combustion analysis by Dirats Laboratories (Westfield, MS). A list of the reactant powders and an overview of the powder properties are given in Table 3.1. Further discussion of the individual powders and their properties continues in the following sections.

Table 3.1: Properties of the raw materials used in the reaction synthesis method.

| Raw Material | Grade | Purity[a] | Particle Size[a] | Surface Area ($m^2/g$) | Oxygen[b] Content |
|---|---|---|---|---|---|
| Mo (Climax) | Ultrafine | 99.95% | 100-500nm | 2.4 | 1.02 wt.% |
| $Si_3N_4$ (UBE) | SN-E03 | 99% | ~0.5μm ($d_{50}$) | 4.0 | 0.82 wt.% |
| hBN (Cerac) | B-1084 | 99.5% | 0.73μm (Fisher) | 6.7 | - |
| cBN (Advanced Abrasives) | #0.125 | - | 0.13μm ($d_{50}$) | 45.7 | - |
| | #0.5 | - | 0.54μm ($d_{50}$) | 26.5 | - |
| | #0.5 (Large Lot) | - | 0.44μm ($d_{50}$) | 11.8 | 0.92 wt.% |
| | #1 | - | 0.83μm ($d_{50}$) | 11.3 | - |

a = value supplied by the manufacturer
b = measured by Dirats Laboratories

### 3.1.1 Raw Materials – Climax Ultrafine Molybdenum Powder

Global production of molybdenum exceeds 200 million tons but less than 10% is used for the production of molybdenum-based components [15]. Molybdenum is most commonly used as an additive for strengthening of steels and nickel-based alloys. It is typically intended for addition to molten metals and relatively few suppliers produce molybdenum powder with the specific characteristics needed for powder metallurgy, namely a fine, unagglomerated powder necessary for sinter-ability at reasonable temperatures. The molybdenum used in this study was the Ultrafine grade powder produced by Climax Engineered Materials (Phoenix, AZ), which was reported by the manufacturer to have a particle size of 100-500nm. An SEM image of the powder is shown in Figure 3.1. The particle size distribution was measured using laser scattering and is plotted in Figure 3.2 as the cumulative size distribution. The cumulative distribution curve represents the percentage of particles (Y-axis), by volume percentage rather than number percentage, which are smaller than a given size (X-axis). Commonly used descriptors for the cumulative distribution are the sizes of the $10^{th}$, $50^{th}$ and $90^{th}$ percentile particles, labeled $d_{10}$, $d_{50}$ and $d_{90}$ respectively. The particle size measured by laser scattering is much larger than reported by the manufacturer. The measured surface area is $2.4 m^2/g$, which corresponds to an approximate particle size of 0.25-0.5μm. The discrepancy between the measurements is due to agglomeration of the powder, which is apparent in the SEM image. The powder is only connected by small inter-particle necks and it is possible that much of the larger size fraction will be broken down during milling.

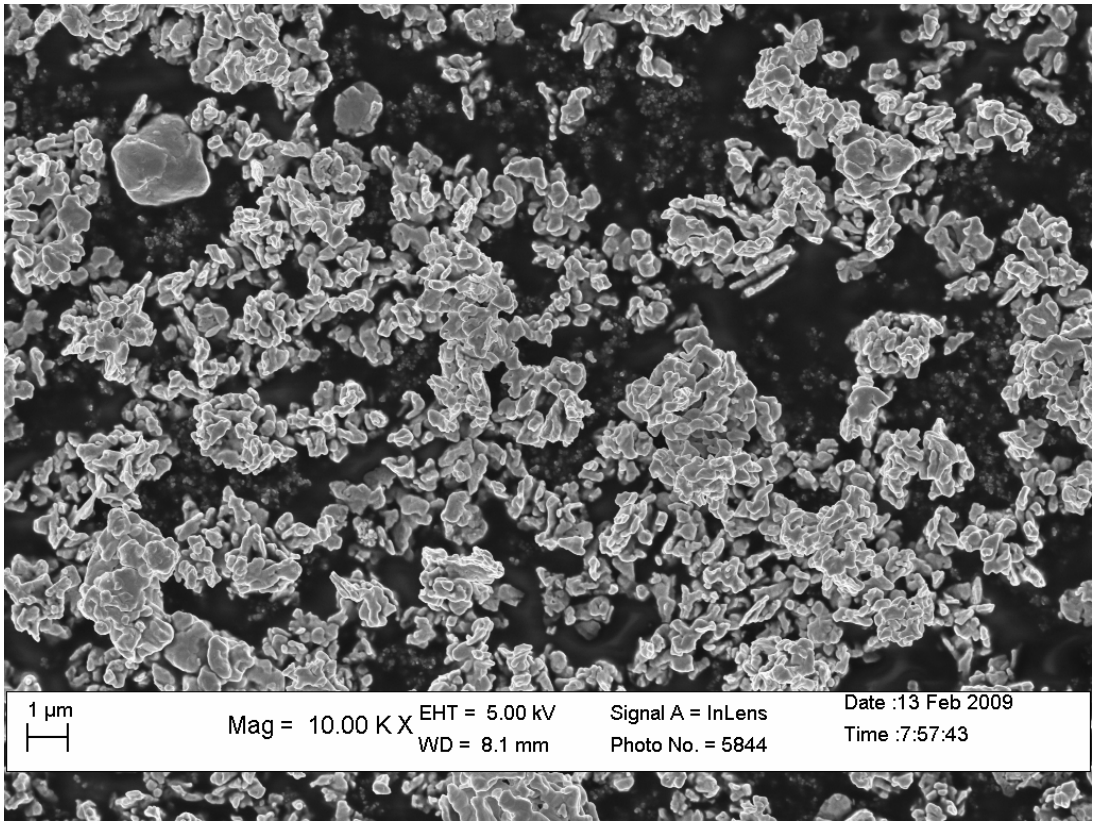

Figure 3.1: An SEM micrograph of the Climax Ultrafine molybdenum powder.

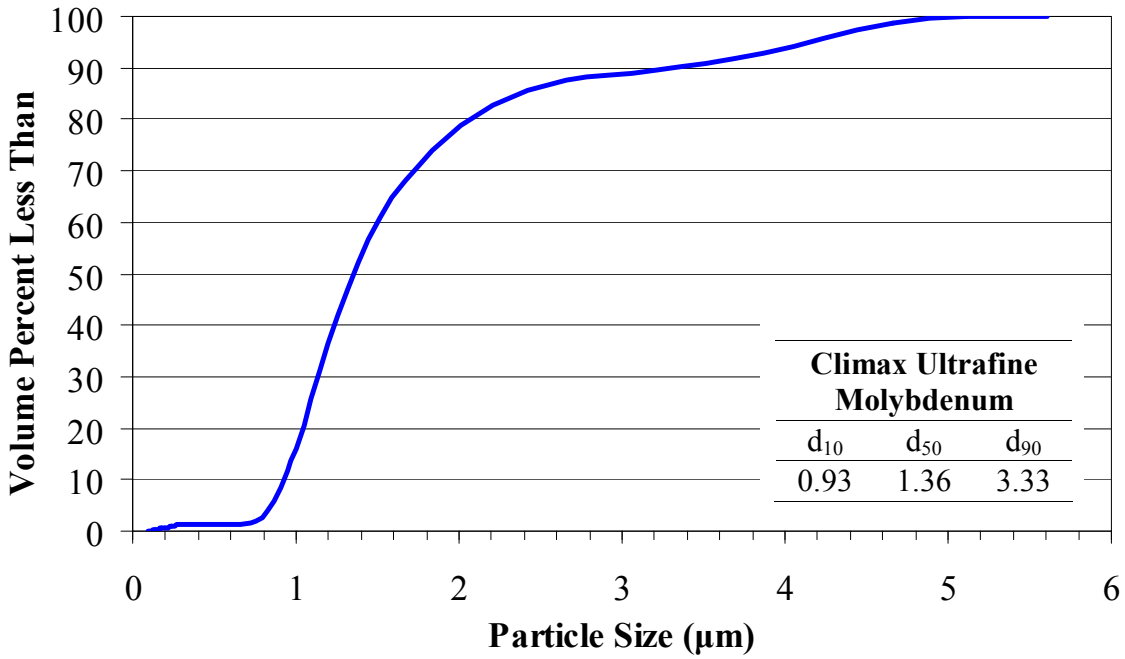

Figure 3.2: The particle size distribution of the Climax Ultrafine molybdenum powder measured by laser scattering.

The impurity levels of the molybdenum powder were supplied by the manufacturer, Table 3.2. The highest impurity contents were oxygen at 1.02 wt.% and nitrogen at 0.12 wt.%. Excluding the gaseous impurities, the remaining impurities were 500ppm.

It is worth noting that toward the completion of this project, Climax Engineered Materials discontinued the Ultrafine grade of molybdenum powder due to the high cost of production. A new grade of powder has been released using undisclosed changes in manufacturing methods meant to increase production rates and lower costs. The new powder is reported by Climax Materials to be similar to the Ultrafine grade, but at the time of this writing the new powder had yet to be evaluated.

Table 3.2: Climax Ultrafine molybdenum powder (Lot #705-1110) impurity contents on a weight basis, as supplied by the manufacturer.

| **Total Impurities Excluding Gases (ppm)** | **O (wt.%)** | **N (wt.%)** | **Fe (ppm)** | **W (ppm)** | **Ni (ppm)** | **Cr (ppm)** |
|---|---|---|---|---|---|---|
| 500 | 1.02 | 0.12 | 55 | 125 | 49 | 47 |

### 3.1.2 Silicon Nitride Powder

The silicon nitride powder used as the silicon precursor in the reaction synthesis method was a high-purity α-$Si_3N_4$ powder produced by UBE Industries (Japan). An SEM micrograph of the UBE-SNE03 powder is shown in Figure 3.3. The particle size distribution measured using laser scattering is plotted in Figure 3.4 with the $d_{10}$, $d_{50}$ and $d_{90}$ size fractions listed. The impurity contents of the powder were supplied by the manufacturer, Table 3.3.

Table 3.3: UBE-SNE03 $Si_3N_4$ powder (Lot #B85503) impurity contents on a weight basis, as supplied by the manufacturer.

| O (%) | C (%) | Cl (ppm) | Fe (ppm) | Ca (ppm) | Al (ppm) |
|---|---|---|---|---|---|
| 0.89 | <0.2 | <100 | <100 | <50 | <50 |

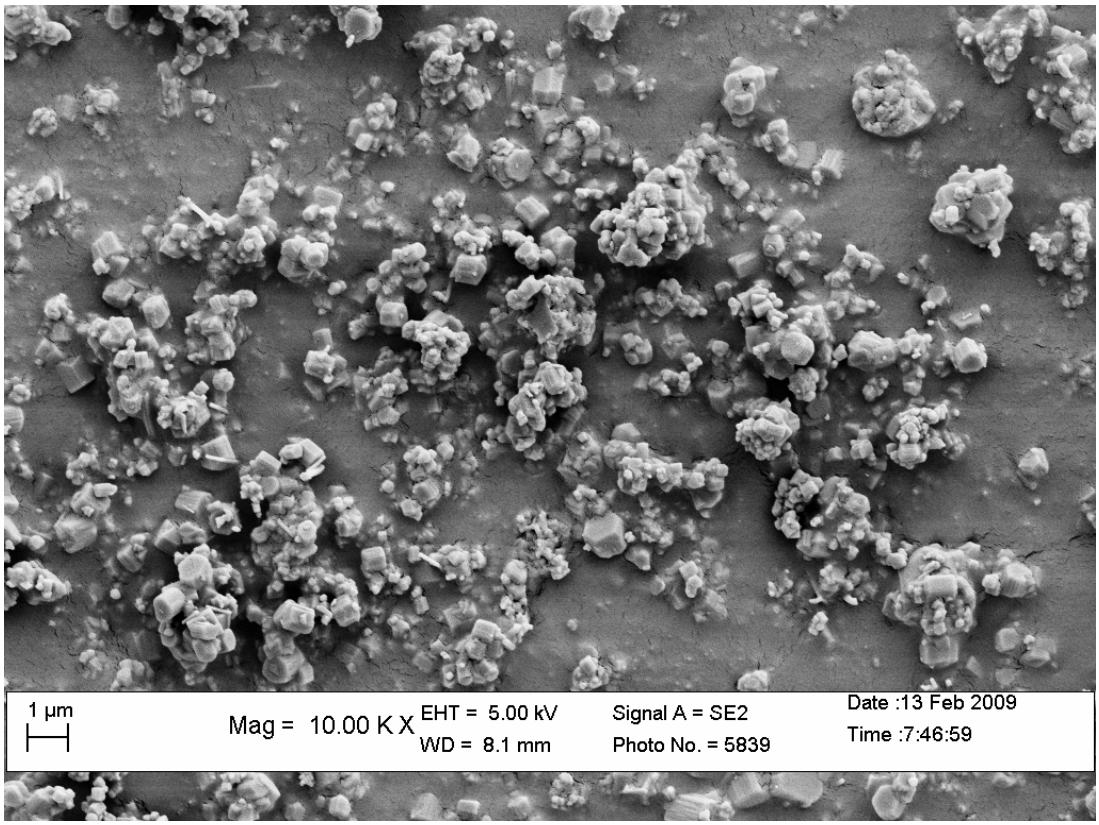


Figure 3.3: An SEM image of the UBE-SNE03 $Si_3N_4$ reactant powder.

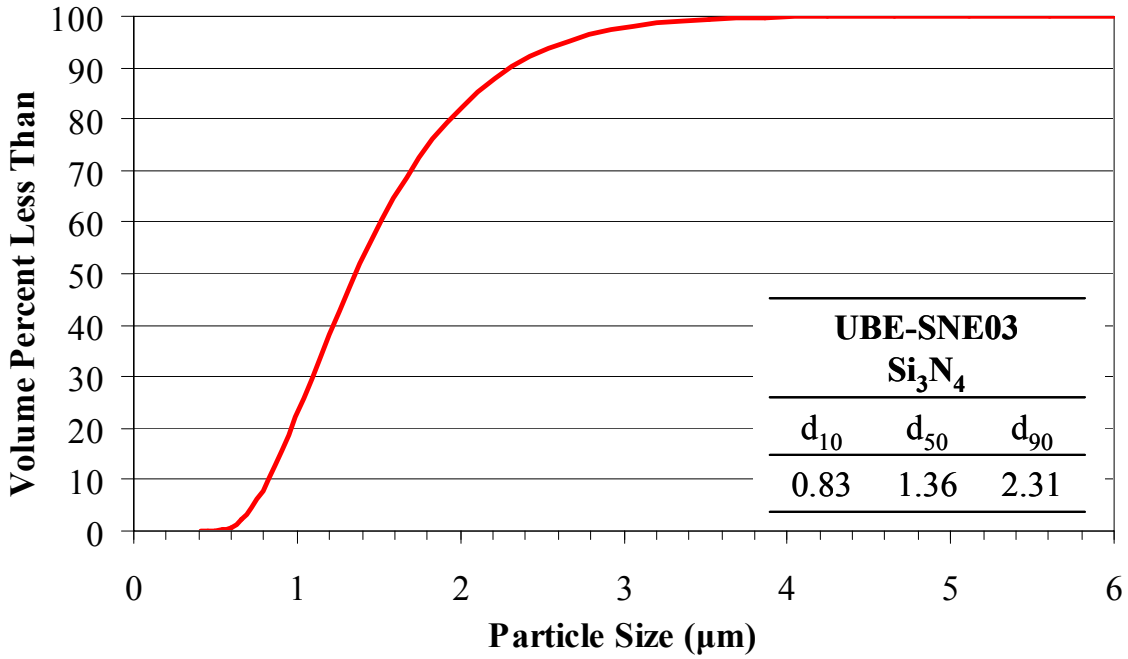


Figure 3.4: Particle size distribution of the UBE-SNE03 $Si_3N_4$ reactant powder measured by laser scattering.

### 3.1.3 Boron Nitride Powders

Hexagonal boron nitride (hBN) powder was used for the boron precursor in the initial studies of the formation of Mo-Si-B alloys by the nitride-based reactions [9,10,11]. This polymorph of boron nitride is the most commonly available and inexpensive form. It is commonly used as a dry powder lubricant and as an additive to many commercial products. The hexagonal form has a graphitic crystal structure with a highly anisotropic morphology. A high-purity hBN powder was purchased from Cerac (Milwaukee, WI). The powder was reported to have an average particle size of 0.73μm, although the particles are actually in the form of large flakes approximately 0.5μm thick and 10μm across, Figure 3.5. Further particle size analysis was not conducted on the hBN powder due to the highly anisotropic shape of the particles. The impurity contents of the powder were supplied by the manufacturer, Table 3.4.

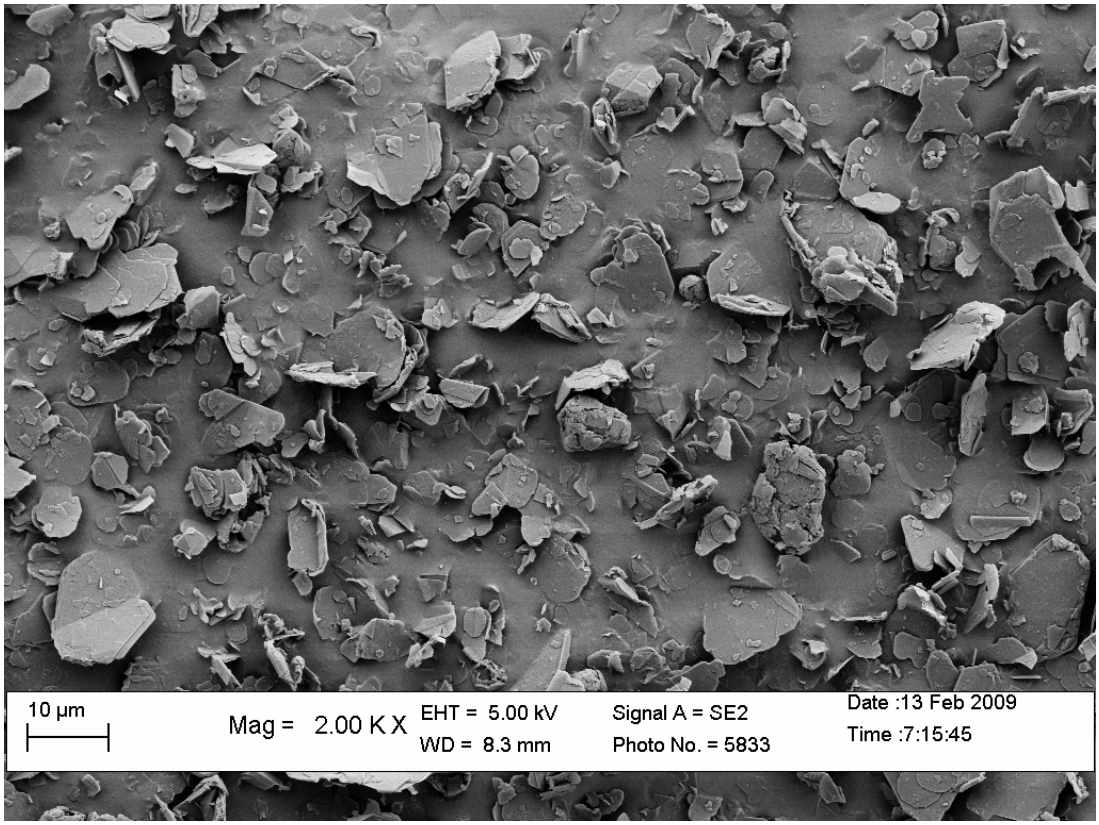


Figure 3.5: An SEM image of the hexagonal boron nitride powder illustrating the high axial ratio, with flakes measuring up to 10µm wide but only ~0.5µm thick.

Table 3.4: Cerac hBN powder (Grade B-1804, Lot #X0029881) impurity contents on a weight basis, as supplied by the manufacturer.

| **Ca (ppm)** | **Na (ppm)** | **V (ppm)** | **Al, Au, Be, Cr, Cu, Fe, Mg, Mn, Mo, Ni, Pb, Si, Sn, Ti, W, Zn, Zr** |
|---|---|---|---|
| 119 | 6 | 1 | All <1 ppm each |

It is proposed in this work that the distribution of the T2 phase in the sintered alloys is controlled by the initial distribution of the BN reactant powder. Perepezko et al. measured a growth rate constant of $9\times10^{-16}$ $m^2/s$ for the T2 phase at 1600°C, which is approximately two orders of magnitude lower than that of the A15 phase at the same temperature ($3.75\times10^{-14}$ $m^2/s$) [27]. Cubic boron nitride (cBN) powders have more isotropic morphology than hBN powder and were used to provide a more distributed and controllable dispersion of the BN reactant. The cubic polymorph of boron nitride has the zinc-blende crystal structure, similar to diamond. It is commonly used as a replacement for diamond in grinding and finishing operations and is thus available from commercial suppliers in a large variety of sizes. The cBN powder is typically more expensive than the hexagonal form, but it does not significantly increase the overall cost of raw materials due to the small amount used relative to the total weight of the alloy.

Cubic boron nitride powders in different size distributions were purchased from Advanced Abrasives (Pennsauken, NJ). This company specializes in grinding the bulk material into a variety of size fractions and following grinding, puts the powder through an acid and a base wash to remove any surface contamination from the milling operation. Air classification was used to separate the powders and to create narrow size distributions. Initially three small lots were examined with average sizes of approximately 0.125μm, 0.5μm and 1μm. SEM images of the powders are shown in Figure 3.6. It can be seen that the cBN powders are much more equiaxed and uniform in size than the hBN powder. Following initial testing, a large lot of the 0.5μm powder was purchased for the production of larger quantities of material. This second lot of 0.5μm powder had approximately the same mean particle size as the original lot, but a wider size

distribution. The particle size distributions of the four powders were measured by the manufacturer using laser scattering and are plotted in Figure 3.7. The $d_{10}$, $d_{50}$ and $d_{90}$ size fractions from the cumulative distributions are listed in Table 3.5.

The metals impurity contents were measured by the manufacturer for powder lot #80035. The contents of the other three lots should match these values as all of the powders were produced from the same starting material and only varied in the size distributions. The levels of surface impurities were measured by a surface analysis technique and the bulk impurities were measured by combustion analysis, Table 3.6. The bulk impurity levels were determined from the material remaining after combustion and are referred to as the 'ash' value. An oxygen content of 0.92 wt.% was measured by Dirats Laboratories.

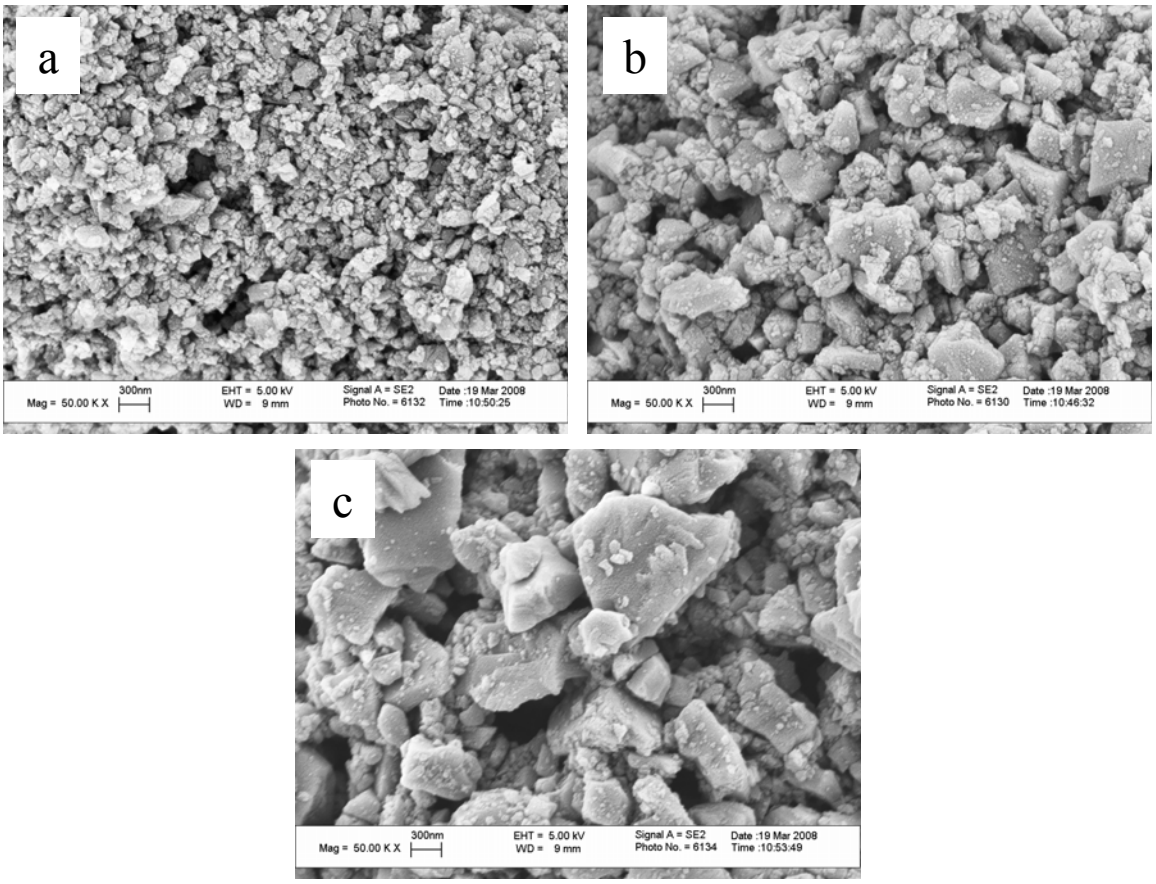


Figure 3.6: SEM images of the cBN powders; (a) 0.125µm, (b) 0.5µm and (c) 1µm.

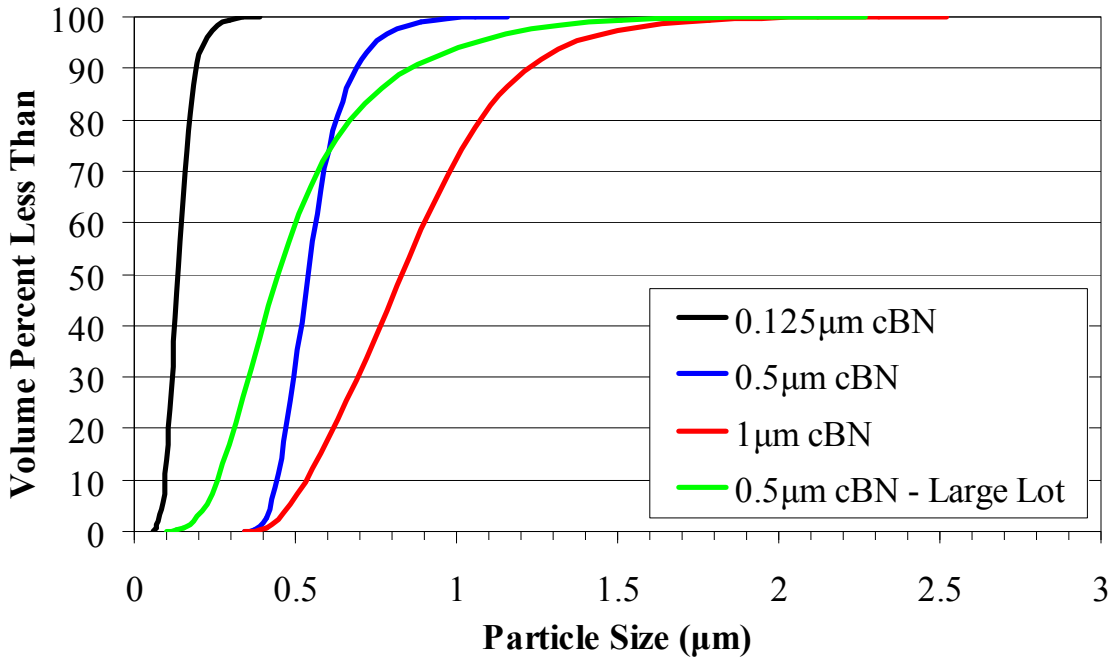


Figure 3.7: The cumulative particle size distributions of the four grades of cBN powder.

Table 3.5: Particle size distribution parameters (μm) for the four grades of cBN powder.

| **#1 (0-2) Lot #80015** | | | **#0.5 (0-1) Large Lot #80035** | | |
|---|---|---|---|---|---|
| $d_{10}$ | $d_{50}$ | $d_{90}$ | $d_{10}$ | $d_{50}$ | $d_{90}$ |
| 0.53 | 0.83 | 1.22 | 0.26 | 0.44 | 0.86 |

| **#0.5 (0-1) Lot #80027** | | | **#0.125 (0-0.25) Lot #80024** | | |
|---|---|---|---|---|---|
| $d_{10}$ | $d_{50}$ | $d_{90}$ | $d_{10}$ | $d_{50}$ | $d_{90}$ |
| 0.44 | 0.54 | 0.69 | 0.10 | 0.13 | 0.19 |

Table 3.6: Advanced Abrasives #0.5 (0-1) cBN powder (Lot #80035) metals impurity contents on an atomic basis, as supplied by the manufacturer.

| **Impurity** | **Surface Content (ppm)** | **Ash Content (ppm)** |
|---|---|---|
| Co | <5 | <10 |
| Cr | <5 | <10 |
| Fe | 29 | 60 |
| Mn | <5 | <10 |
| Na | 30 | 20 |
| Ni | <5 | <10 |
| Si | 61 | 810 |

## 3.2 Powder Processing Techniques

The nitride-based reaction synthesis method allows for the formation Mo-Si-B alloys in a less complex and expensive manner than previously demonstrated. The processing procedures were developed with consideration that the techniques used be amenable to industrial scale processes. The alloy preparation uses standard powder processing methods which are common in the powder metallurgy and ceramics industries. A significant portion of the effort was dedicated to the improvement of the powder processing procedures. An overview of the processing techniques used to create the alloys follows, and a detailed investigation of the relationship between the raw materials and the microstructures of the Mo-Si-B alloys is given in Chapter 5.

### 3.2.1 Batch Formulation

The compositions were formulated to achieve volume fractions of the $Mo_{ss}$ phase compatible with ductility. The volume fractions of the $Mo_{ss}$, A15 and T2 phases were estimated from the weight fractions of boron and silicon. Boron has negligible solubility in both the $Mo_{ss}$ and A15 phases, and it was assumed that all of the boron in the mixtures reacts to form the T2 phase. The phase fractions of $Mo_{ss}$ and A15 were determined from the remaining amount of silicon, using the solid solution limits of both phases. The stoichiometries used for the three phases were: $Mo_{0.978}Si_{0.022}$, $Mo_{76}Si_{24}$ and $Mo_5Si_{0.95}B_{1.90}$. All of the compositions are listed in relation to the weight percent of silicon and boron in the alloy following the decomposition of the nitrides.

Alloys of the composition Mo-3Si-1B wt.% have been the primary focus of research in this work. This composition is identified as having a good combination of oxidation resistance and mechanical properties and has been the focus of a number of

other research groups. The effect of higher $Mo_{ss}$ volume fractions on the dispersion of the intermetallic phases was investigated for a range of alloy compositions, all with a 3/1 Si/B ratio. Additional research was conducted on the Mo-2Si-1B wt.% composition, which is also commonly cited in the literature and provides another point of a comparison for the alloys prepared in this project.

### 3.2.2 Slurry Preparation

Molybdenum hydrolyzes in contact with water, which is especially a problem for the high-surface area Climax Ultrafine powder. Acetone-based slurries were used to limit oxidation of the reactant powders during milling. Acetone also allows spray drying to be accomplished at a much lower temperature than is used for aqueous slurries, as it has a low boiling point and heat of vaporization as compared to water.

#### 3.2.2.1 Organic Processing Additives

A low molecular weight poly-methyl methacrylate resin (PMMA) was used in slurry preparation as a dispersant (Elvacite 2008, Lucite International). The polymer adsorbs on the powder surface and disperses by stearic hindrance, which creates a homogenous dispersion of the reactants and allows for increased solid loadings. The PMMA is also used as a binder to improve the strength of the spray dried granules and the pressed powder compacts. The Elvacite resin depolymerizes upon heating and evaporates cleanly in a variety of conditions, including under vacuum and in reducing and inert atmospheres. This is important for maintaining low residual carbon levels in the fired alloys. The addition of 2 to 5 wt.% PMMA was evaluated. Stearic acid was added as a lubricant to improve the green densities and to reduce density gradients in the powder compacts. The effect of the addition of 0.3 to 0.9 wt.% was evaluated.

3.2.2.2 Milling of Powder Slurries

Milling of the slurries is necessary to break up powder agglomerates and to improve the dispersion of the nitride powders. The organic additives were fully dissolved in the acetone prior to addition of the powders. The slurries were first mixed on a rotary ball mill for 30-60 minutes and then milled for 30 minutes on a commercial paint shaker (Red Devil Model 5400, Plymouth, MN). The paint shaker imparts higher energy than rotary ball milling and provides an improved dispersion of the reactants. Milling was done in polyethylene jars using spherical milling media. Low-purity aluminum oxide media (5mm, 94% $Al_2O_3$, Performance Ceramics, Peninsula, OH) was used in early experiments but was later replaced with 3mm high-purity aluminum oxide media (99.5% $Al_2O_3$, Union Process, Akron, OH). The high-purity alumina has a higher hardness and was selected to reduce contamination.

Experiments using attrition milling were also conducted. A laboratory scale attrition mill (Union Process) was fitted with a sealed mill jar to prevent evaporation of acetone. Samples were milled using the 3mm high-purity alumina media.

**3.2.3 Spray Drying of Powder Slurries**

Spray drying is a common industrial practice used to dry powder slurries. It is often used in powdered metal and ceramic processing to create spherical agglomerates for dry pressing operations. Spherical granules flow better than the un-agglomerated powder and improve the uniformity of die fill and reduce density gradients in the pressed powder compacts. In this project spray drying gives the added benefit of locking in a uniform dispersion of the reactants.

3.2.3.1 Operation of the Büchi Laboratory Spray Dryer

Spray drying studies were conducted using a laboratory scale spray dryer (Büchi Model 190, Flawil, Switzerland), Figure 3.8. This spray dryer operates in suction mode, in which the aspirator motor draws air from the exhaust side. Fresh air is drawn in through a filtered inlet (1) and warmed by a heater coil (2). Hot air enterers the drying chamber through inlet ports spaced around the atomization nozzle (3). The nozzle is jacketed by cooling water to prevent boiling of the slurry inside the nozzle. The slurry is atomized by a two fluid, coaxial nozzle using compressed air. The slurry feed rate is controlled by a peristaltic pump and a magnetic stir bar in the fluid reservoir is used to maintain the suspension of the slurry. The dried powder is collected in two regions of the spray drier. The heaviest granules fall directly into a trap located at the bottom of the drying chamber. Smaller granules and fine particles are removed from the exhaust by a cyclonic separator (4) and caught in a second trap (8).

A variety of spray drying conditions can be modified in order to change the characteristics of the powder granules. Table 3.7 lists the dependence of the spray drying parameters on various aspects of the process. Larger granules are expected to have a more homogenous distribution of the reactants and are desired for improved flowability. The particle size of the spray dried granules is highly dependent on the concentration of the slurry. The slurries were mixed at a solids loading of 15 vol.% which was the maximum loading that could be effectively pumped by the peristaltic pump. The flow rate of the atomization air and the slurry feed rate were adjusted individually for each spray drying run to minimize overspray onto the drying chamber walls, as this represented one of the most significant losses in the spray drying process. The solvent-

based slurries were processed at a low temperature as a safety consideration. The heater setting was adjusted to maintain 40°C at the air outlet temperature probe (7) to prevent condensation of the acetone. The maximum possible temperatures that the spray dried powders are exposed to is indicated by a thermocouple at the air inlet (6). The inlet temperature was typically 80°C, but the actual temperature of the powder is between the inlet and outlet temperatures due to evaporative cooling of the droplets. The use of acetone also prevents oxidation of the starting materials by allowing for low drying temperatures. Spray drying of aqueous slurries typically requires the air inlet temperature to be in the 200-300°C range due to the high heat of vaporization of water.

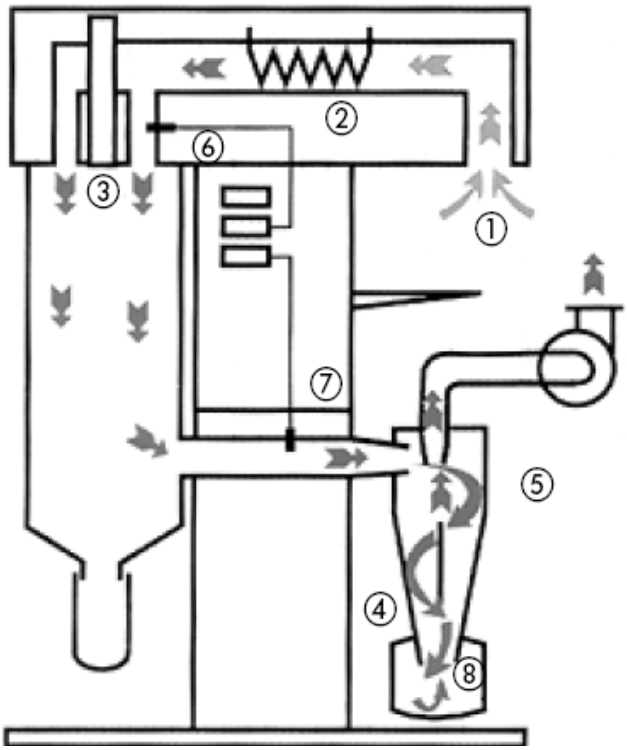


① Suction opening
② Heating
③ Flow stabilized inlet to the drying chamber
④ Cyclone, the product is separated from the air current here
⑤ Aspirator
⑥ Temperature probe air inlet
⑦ Temperature probe air outlet
⑧ Collecting vessel for the finished product

Figure 3.8: An operational diagram and picture of the Büchi laboratory spray dryer [78].

Table 3.7: The dependence of the experimental parameters on the spray drying conditions and the resulting powder characteristics [79].

| parameter / dependence | aspirator rate ↑ | air humidity ↑ | inlet temperature ↑ | spray air flow ↑ | feed rate ↑ | solvent instead of water | concentration ↑ |
|---|---|---|---|---|---|---|---|
| outlet temperature | ↑↑ less heat losses based on total inlet of energy | ↑ more energy stored in humidity | ↑↑↑ direct proportion | ↓ more cool air to be heated up | ↓↓ more solvent to be evaporated | ↑↑↑ less heat of energy of solvent | ↑↑ less water to be evaporated |
| particle size | - | - | - | ↓↓↓ more energy for fluid dispersion | (↑) more fluid to disperse | (↓) less surface tension | ↑↑↑ more remaining product |
| final humidity of product | ↑↑lower partial pressure of evaporated water | ↑↑ higher partial pressure of drying air | ↓↓ lower relative humidity in air | - | ↑↑ more water leads to higher particel pressure | ↓↓↓ no water in feed leads to very dry product | ↓ less water evaporated, lower partial pressure |
| yield | ↑↑ better separation rate in cyclone | (↓) more humidity can lead to sticking product | (↑) eventually dryer product prevent sticking | - | (↓↑) depends on application | ↑↑ no hygroscopic behaviour leads to easier dying | ↑ bigger particles lead to higher separation |

After spray drying, the powders were fully dried and then screened between 170 mesh and 400 mesh sieves (38-96μm) to recover the spherical powder granules. The +170 mesh fraction was found to be mostly agglomerates of smaller spheres and the -400 mesh fraction was a mixture of small granules and powder fines. This material can be recovered and reprocessed, but this adds an additional step and repeated processing may lead to increased oxidation of the reactants. Screening of powders using 500 mesh (25μm) and 635 mesh (20μm) sieves was attempted to improve the yield of spherical granules, but rapid clogging of the sieves prevented screening large quantities of powder.

3.2.3.2 Spray Drying Using Ultrasonic Atomization

Preparation of large quantities of powder was difficult using the Büchi spray dryer due to the low powder yields. The problem was mainly due to the atomization process. The coaxial nozzle created a wide range of droplet sizes traveling at a high velocity. The large droplets did not have time to dry before striking the walls of the drying chamber. Increasing the atomization air flow increased the overall powder yield by reducing the droplet size distribution, but a higher fraction of the powder was present as fines which were screened away from the spherical granules. In addition, the coaxial nozzle periodically became clogged during operation. Although the nozzle was easily cleared using a built in tip cleaner, the entire process required constant supervision. The labor involved in preparation of the powder using the Büchi spray dryer prevented scaling to large quantities. A different spray dryer was procured to allow for the production of quantities of powder in the 10-30 kg range. This spray dryer was a prototype unit designed by Dr. Robert Snyder (Georgia Institute of Technology, Atlanta, GA) and manufactured by Glatt Air Technologies (Ramsey, NJ), Figure 3.9. The operation of spray dryer is simple and features no mechanical parts; the slurry is simply atomized into a heated drying chamber. A chimney extends from the bottom of the chamber through the top lid of the drying chamber to vent solvent vapor and the spray dried granules are caught on a removable bottom tray.

The slurry was atomized using an ultrasonic atomization nozzle (Sono-Tek, Milton, NY). A piezoelectric crystal vibrates the nozzle a resonant frequency of 48 kHz. This forms two-dimensional standing waves, known as capillary waves, in the liquid film on the atomization surface. At a critical amplitude the waves collapse and droplets of

liquid are released. This critical amplitude is only a function of the rhealogical properties of the liquid and the resonant frequency of the nozzle, thus the droplets are formed in a narrow size distribution. For the 48 kHz nozzle, the median droplet size is 38μm and 99% of the droplets fall in the 9-150μm size range, as reported by the manufacturer for the atomization of water [80].

The droplets leave the ultrasonic atomization surface with low velocity, ~1cm/sec. The low velocity and the large 15" diameter drying chamber, as compared to the 5" chamber on the Büchi model, increased the drying time of the droplets and all but eliminated sticking to the chamber walls. An added benefit of ultrasonic atomization is that the slurry is sonicated immediately prior to drying, which may improve the dispersion of the reactants in the spray dried granules.

The ultrasonic nozzle requires a continuous, steady feed rate of slurry. Peristaltic pumps, as used with the Büchi model, are not suitable because they pulsate and cause the nozzle to drip. A dual syringe pump system was used to for fluid delivery (New Era Pump Systems, Wantagh, NY), Figure 3.10. This style of pump pushes a syringe at a controlled linear rate to provide a precise and steady flow across a wide range of rates.


Figure 3.9: The replacement spray dryer (Glatt Air Technologies, Ramsey, NJ) and ultrasonic atomization nozzle (Sono-Tek, Milton, NY).

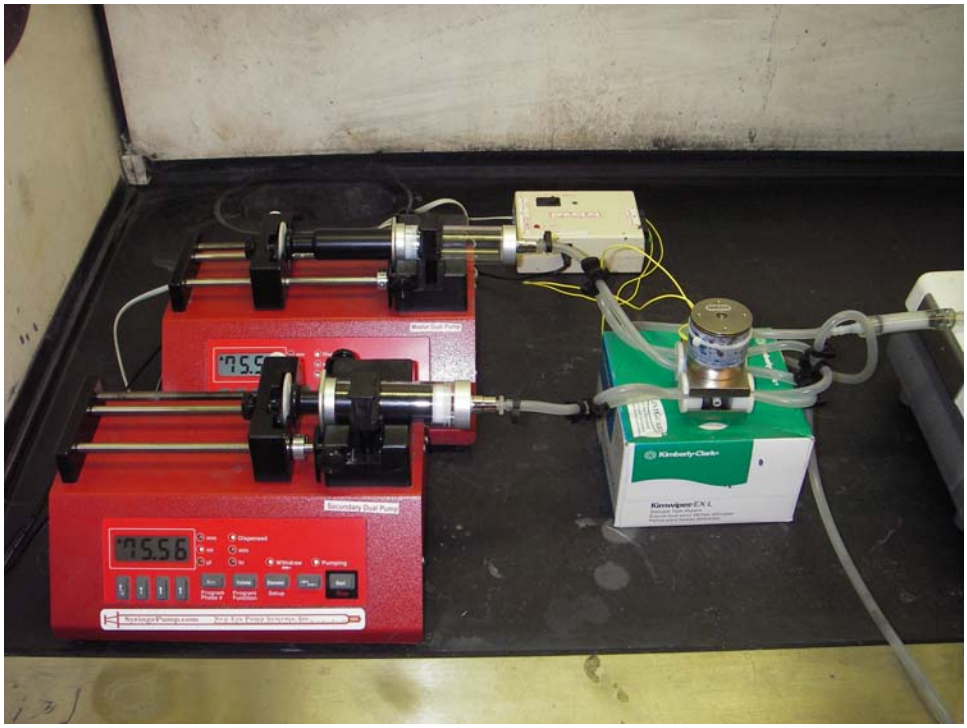

Figure 3.10: The reciprocating, dual syringe pump system used to deliver slurry to the ultrasonic atomization nozzle (New Era Pump Systems, Wantagh, NY).

The two pumps operate in tandem and are synchronized to create a continuous feed. While one pump dispenses slurry to the nozzle, the second pump withdrawes slurry from the reservoir. The system is tied into a solenoid pinch valve that switches the direction of flow from the individual pumps. The valve operates by alternatively pinching off the tubing leading to the reservoir or atomization nozzle as the direction of the syringe pumps change. The system creates a constant feed rate with less than a one second delay during switching of the pump directions. The slurry in the reservoir was kept suspended using a magnetic stir bar. The syringes were made of borosilicate glass with PTFE plungers (Hamilton, Reno, NV). This combination of atomization nozzle and feed system maintains well dispersed slurries with no significant sources of contamination.

The slurries were spray dried at rates of 350-750mL/h and the drying chamber was maintained at 65-75°C. The ultrasonic atomization nozzle does not produce any powder fines and the spray dried granules only required screening with a 100 mesh (150μm) sieve to remove large agglomerates. This spray dryer greatly reduced the labor involved with spray drying as compared to the Büchi model because the system did not require attention during operation, the powder did not require screening with fine sieves and yields of 90-95% were achieved.

### 3.2.4 Green-Body Formation

Two compaction methods were used to consolidate the powders into green-bodies; uniaxial pressing and cold-isostatic pressing (CIP). The pellets used for phase analysis, density measurements, microstructure analysis and oxidation testing were pressed using a ½" diameter, double-action die at up to 70ksi. The die walls and punch

faces were lubricated with a saturated solution of stearic acid in acetone. An automated hydraulic press was used to ensure constant loading rates and hold times.

Samples with high axial ratios, such as bars and rods, were prepared using the wet bag CIP process. A rubber mold, either urethane or latex, was filled with powder. Rigid supports were placed around the flexible molds to maintain the shape during filling and the molds were vibrated to increase the powder packing density. The molds were plugged and then sealed with a tight wrapping of latex banding tape. Air was evacuated from the molds to help prevent cracking during depressurization. The parts were isostatically pressed up to a maximum pressure of 50ksi. After a brief hold the pressure was released slowly to prevent springback.

An alternative method to form large pellets was to use a combination uniaxial pressing and CIPing. The large pellets could not be uniaxially press at high pressures due to load limitations of the press. The parts were first uniaxially pressed at a low pressure, then sealed in evacuated plastic bags and further compacted by isostatic pressing.

## 3.3 Sintering of the Mo-Si-B Alloys

The alloys were sintered in a sealed atmosphere, 2.5×24" tube furnace. The temperature was computer controlled and monitored by a B-type thermocouple placed directly above the center of the tube. The difference between the temperature measured by the control thermocouple and a second thermocouple placed inside the tube was less than 5°C, and the temperature measured across the 6" hot-zone at the center of the furnace was found to fluctuate by less than 10°C at 1600°C.

Samples were fired inside high-purity aluminum oxide tubes and combustion boats (Vesuvius-McDanel, Beaver Falls, PA). Heating and cooling rates of 3°C/min were used to protect the ceramic tubes from thermal shock. Ultra-High Purity grade gases (Airgas Products) were flowed at a rate of 150cc/min.

### 3.3.1 Furnace Atmosphere

The main advantage of using the nitrides reactants instead of elemental silicon and boron is their resistance to oxidation up to moderately high temperatures (~1000°C). This maintains low oxygen impurity levels not only during processing, but also through the initial stages of firing. The molybdenum powder is known to contain approximately 1 wt.% oxygen in the as-received condition. Despite using solvent-based processing it is probable that surface oxidation during processing further increases the oxygen content. For this reason samples were sintered in a reducing atmosphere of Ar/10% $H_2$. Molybdenum oxide reduces at approximately 700°C, a low enough temperature to avoid oxidization the $Si_3N_4$ and BN. This has been demonstrated in previous work in which $MoO_3$ was used as the molybdenum precursor [9]. After reduction of the oxide, the $Si_3N_4$ and BN still reacted to form the Mo-Si-B alloys. This illustrates that despite having high

levels of oxygen initially present in the system, the nitrides survive through the $MoO_3$ reduction stage. It is in the later stages of sintering that maintaining low oxygen levels becomes critical. As the temperature increases, the nitride reactants and intermetallic phases become susceptible to oxidation. Prior to complete densification the nitrides and, following reaction, the intermetallic phases on the interior of the samples are at risk due to interconnected porosity. The internal oxidation of silicon and boron causes the formation of silica inclusions which may harm creep resistance.

Many precautions were taken to ensure low oxygen contents during sintering. Samples were fired in a sealed-atmosphere tube furnace with a double-bubbler on the exhaust side to prevent back flow of air into the furnace. The furnace was flushed and evacuated three times prior to firing. The furnace was pumped down to below 100mTorr before the final refill to verify there were no leaks in the system. The oxygen content of the furnace exhaust was measured using an Ametek model TM-1B oxygen analyzer (Pittsburgh, PA). Even using high-purity gases, the cylinders were found to contain 45-60 ppm oxygen. A Centorr Model 2G-100-SS gettering furnace (Nashua, NH) was used to remove oxygen and water vapor impurities from the inlet gas. The gas flows over heated titanium particles inside the gettering furnace, which reacts with oxygen to form titania. The gettering furnace was operated at 800°C, above the temperature at which titanium hydride is stable, to prevent the removal of hydrogen from the inlet gas. The oxygen analyzer was periodically connected to the furnace outlet to verify the effectiveness of gettering furnace. The gettering furnace was shown to drop the oxygen content in the gas stream from the baseline value in the cylinders down to 0.0ppm.

### 3.3.2 Hot-Isostatic Pressing

Complete densification of the Mo-Si-B samples did not occur at the maximum furnace temperature of 1600°C. Hot-isostatic pressing (HIP) was used to further densify the Mo-Si-B samples with the goal of achieving full theoretical density and eliminating residual porosity. The reaction synthesis alloys require pre-firing because the evolution of nitrogen gas during the decomposition of the nitride powders. HIP treatments were performed between 1300°C and 1500°C at 200 MPa by American Isostatic Presses (Columbus, OH).

For samples with no interconnected porosity, the HIP treatment can simply be conducted on the samples in the as-fired state. This condition typically occurs at samples densities of approximately 94% T.D. or higher. If there is surface connected porosity extending into the sample, the pressure exerted by the HIP equalizes inside the pores and cancels out the external pressure. In this case the samples must be encapsulated in evacuated and sealed vessels. The encapsulation material must be deformable at the HIP temperature to effectively transmit the external pressure to the part.

#### 3.3.2.1 Encapsulation of Hot-Isostatically Pressed Samples

Three different encapsulation materials were investigated for HIPing at different temperatures. The first encapsulation method tested was to seal the parts in either fused silica or Vycor (Corning Inc., Corning, NY). Vycor is a borosilicate glass with 96% silica and has the advantage of a lower glass transition temperature than pure silica. Ampoules were made from tubing by technical glass blower Don Woodyard (Georgia Institute of Technology, Atlanta, GA). The parts were surrounded with 280 mesh alumina grit inside the ampoules to prevent the glass from infiltrating the pores during the

HIP treatment. This also prevented shifting of the parts and protected the encapsulation during shipping. The ampoules were evacuated using a mechanical vacuum pump and then necked down and sealed under vacuum. HIP treatments using the glass encapsulation were tested at 1400°C and 1500°C.

Encapsulation in metal tubes was also investigated. Tubes slightly larger than the diameter of the parts were crimped at one end and welded to a ¼" evacuation tube. The parts were packed in the alumina grit to prevent contact of the samples with the encapsulant. The other end of the tube was then crimped and welded. A gas fitting with a ball valve was swaged onto the evacuation tube and the encapsulations were pressure checked for leaks. The tubes were flushed with argon gas three times before the final evacuation to 100mTorr, and then sealed under vacuum using the ball valves. The evacuated tubes were heated with a torch, crimped three to four times and then hermetically welded across one of the crimps. Low carbon steel (ASTM 1010) was used for HIP treatments up to 1300°C and titanium (CP-Grade 2) was used up to 1500°C.

After the HIP treatments, the integrity of the encapsulation was evident based on deformation around the part. Any pinholes in the welds allowed the pressure to equalize inside the encapsulation and prevented it from transmitting pressure to the parts inside. The encapsulant was cut away and the aluminum oxide barrier layer was ground from of the surface of the parts. Because grinding of the surface changed the sample dimensions, shrinkage measurement were not obtained for encapsulated parts but the density measurements and other characterization techniques were completed as with the pressureless sintered parts.

### 3.4 Aluminum Addition to Mo-Si-B Alloys

Powder metallurgical processing allows for the addition of aluminum to the Mo-Si-B alloy, which is not possible using melt-based processing. Preliminary attempts to add aluminum to the alloys via reaction with aluminum nitride were unsuccessful. Further literature review revealed that aluminum nitride is stable in molybdenum up to 1800°C [81]. Aluminum was then added to the alloys in its elemental form. A high-purity aluminum powder, 99.9%, was obtained from American Elements (Grade AL-M-O3-P, Los Angeles, CA). The average powder size is reported to be 1-3μm. An SEM image of the powder is shown in Figure 3.11.

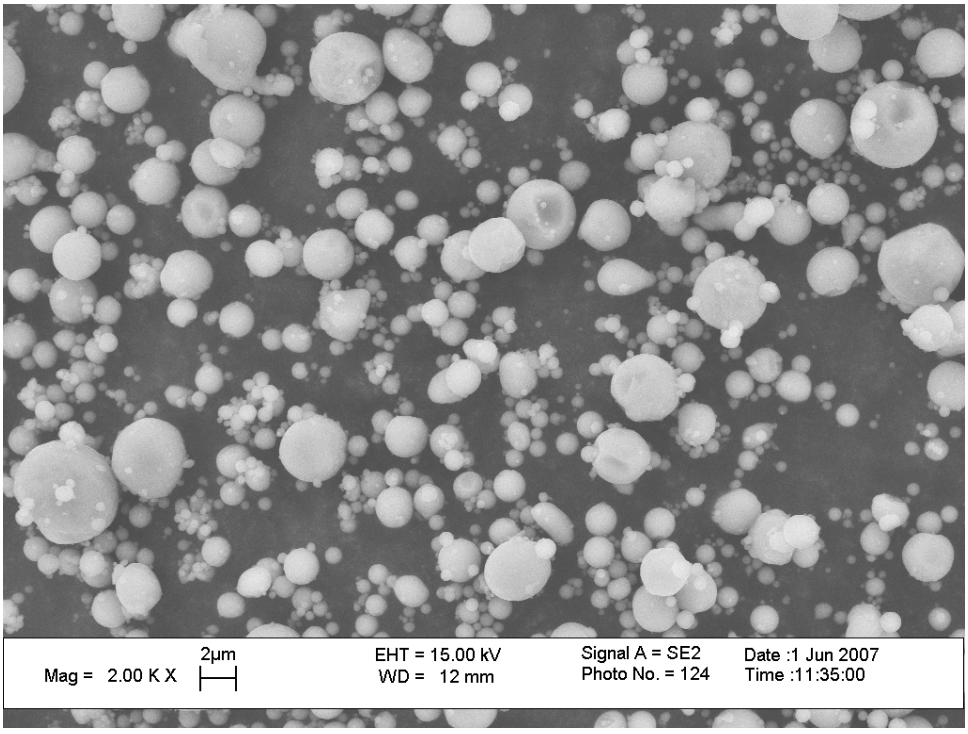


Figure 3.11: An SEM micrograph of the American Elements aluminum powder used in the reactions to form Mo-Al-Si-B alloys.

Small batches of aluminum containing alloys were prepared by mixing the powders using a mortar and pestle. Slurry preparation and spray drying were avoided in the preliminary investigations to prevent the formation of $Al_2O_3$. Reaction between molybdenum and aluminum at 600°C was resulted in a large volume expansion of the material. To prevent swelling of the powder compacts the molybdenum and aluminum powders were pre-reacted at 900°C for 2 hours, creating a Mo-$Mo_3Al$ mixture which was then dry ball milled with the $Si_3N_4$ and BN powders to form the Mo-Al-Si-B alloys.

## 3.5 Characterization Techniques

A variety of techniques were used to characterize the materials, study the reactions which form the intermetallic phases, and to investigate the effect of the processing parameters on the distribution of the phases in the alloys.

### 3.5.1 Powder Characterization

The specific surface areas of powder samples were calculated using the Brunauer, Emmett and Teller (BET) method which measures the surface area by nitrogen gas adsorption. Measurements were made using a Coulter SA3100 surface area analyzer (Beckman Coulter, Inc. Fullerton, CA).

Particle size distributions were measured using a Beckman Coulter LS 13 320 laser diffraction particle size analyzer (Beckman Coulter, Inc. Fullerton, CA). The powders were dispersed in deionized water using an ultrasonic probe prior to analysis. Each material was analyzed two times and the tests were averaged. The measurement of particle size by laser diffraction requires knowledge of the refractive indices for the materials which were obtained from the Handbook of Optical Constants of Solids (Palik and Ghosh, 1998) [82].

### 3.5.2 Thermal Analysis

A combination of differential thermal analysis (DTA) and thermo-gravimetric analysis (TGA) was used examine the reactions. Weight loss is observed for the nitride-based reactions due to the evolution of nitrogen gas. Simultaneous TGA/DTA measurements were made using a Netzsch Model 449 C thermal analyzer (Selb, Germany). A high purity alumina powder was used as the reference standard for the DTA measurements. The reference powder was pre-fired at 1600°C in air to remove any volatile compounds which may have affected the TGA results. Measurements were made at a heating rate of 3°C/min in flowing Ar/5% $H_2$ to match the firing conditions used for sintering.

### 3.5.3 X-Ray Diffraction Analysis

X-ray diffraction (XRD) analysis was used to identify the phases present in the alloys. The diffraction patterns were measured with a PANanalytical X'Pert PRO diffactometer using $Cu_{K_\alpha}$ radiation. An incident beam monochromater was used to eliminate secondary diffraction peaks due to $K_{\alpha_2}$ and $K_\beta$ radiation. The phase identification program Jade (v. 7, Materials Data, Inc., Livermore, CA) was used to match the XRD patterns of the phases present to the corresponding powder diffraction files (PDF) obtained from the ICDD PDF-4+ database (International Centre for Diffraction Data, Newtown Square, PA). Molybdenum, A15 and T2 were matched to PDF numbers 00-042-1120, 00-051-0764 and 01-072-6779, respectively.

3.5.3.1 Quantitative Phase Analysis

The fractions of the different phases in the alloys were estimated from the $Mo_{ss}$-A15-T2 phase triangle at 1600°C for the purpose of developing batches [3]. When studying the mechanical properties and oxidation resistance of the different compositions, it is important to know the exact volume fractions of the molybdenum matrix and the ratios of the A15 and T2 phases following reaction. The volume fractions of the phases were determined by quantitative XRD phase analysis using the program MAUD (Materials Analysis Using Diffraction) [83]. The software calculates the relative fractions of each phase using Rietveld refinement. In the Rietveld method, a theoretical XRD pattern is generated and compared to the measured pattern. The calculated pattern is modified by adjusting the parameters related to the background, peak profiles and crystal structures. The pattern is refined using a least-squares approach until it matches the measured pattern and the relative phase fractions are calculated [84]. This method is especially useful for analyzing diffraction patterns with strongly overlapping peaks, as is observed with for the three phases in the Mo-Si-B alloys.

Rietveld refinement requires knowledge of the crystal structure data for all of the phases in the measurement. This information was taken from the crystallographic information files (CIF) found in the Inorganic Crystal Structure Database. The CIFs used for the Mo, A15 and T2 phases were; 76147, 35755 and 44454, respectively. High resolution XRD measurements were made for Rietveld analysis. The samples were scanned between 24 and 80° 2θ with a step size of 0.02°. The ratio between the maximum peak intensity, molybdenum (110), and background intensities in the scans was greater than 100:1.

### 3.5.4 Density and Shrinkage Measurements

The densities of the samples were measured from both dimensional measurements and Archimedes method. The green densities of the powder compacts were calculated using the following equation:

$$\rho_{Bulk} = M / V \tag{3.1}$$

where $M$ is the mass of the pellet and $V$ is the volume. Sample dimensions were measured before and after sintering. The shrinkage of the samples is given as:

$$\%Shrinkage = \frac{\Delta l}{l_0} * 100 \tag{3.2}$$

Inaccuracies in the measured volume can occur due to cupping and warping of the fired samples. More accurate values are obtained using Archimedes method, which compares the weight of the dry sample ($W_{Dry}$), the weight suspended in water ($W_{Susp}$) and the weight of the sample with all of the open porosity saturated with water ($W_{Sat}$). To ensure the open porosity was fully saturated, the samples placed in a bell jar and held under vacuum for thirty minutes. While still under vacuum, the samples were immersed in water and held under vacuum for an additional thirty minutes. The typical procedure for saturating the porosity is to immerse the samples in boiling water. Because many of the density measurements were taken at an intermediate stage prior to hot-isostatic pressing, exposure to boiling water was avoided to limit surface oxidation of internal pores. The bulk density of a sample is given as:

$$\rho_{Bulk} = \frac{W_{Dry}}{W_{Sat} - W_{Susp}} \tag{3.3}$$

The percentage of open porosity of the sample is calculated as:

$$\%O.P. = \frac{W_{Sat} - W_{Dry}}{W_{Sat} - W_{Susp}} * 100 \tag{3.4}$$

which corresponds to the volume of surface connected porosity.

### 3.5.5 Electron Microscopy

Imaging specimens was done using both Leo 1530 and Leo 1550 field emission scanning electron microscopes (SEM). Microstructural imaging with the Leo 1530 microscope was done in back-scatter mode. Electron backscatter images show phase contrast as a function of the average atomic number of a phase. The molybdenum phase appears as the brightest phase in Mo-Si-B alloys due to its higher average atomic number. The A15 and T2 phases appear darker but there is not enough phase contrast to differentiate between the individual intermetallics. The Leo 1550 microscope was not equipped with a back-scatter detector but it was found at high accelerating voltages (20kEV) that there was enough contrast in secondary-electron mode to differentiate between the molybdenum and intermetallic phases. Both microscopes were equipped with energy-dispersive spectroscopy (EDS) which was used for elemental analysis.

Microstructure cross-sections of sintered alloys were prepared by mounting the samples in a polymer resin and polishing with a series of diamond polishing solutions. The final polishing step was the Struers OP-S colloidal silica solution (Struers, Westlake, OH) which has a slight chemical etching effect in addition to the mechanical polishing. Powder samples were mounted on conductive carbon tape and non-conductive samples were sputter coated with gold.

3.5.5.1 Electron Back-Scatter Diffraction (EBSD) Imaging

Microstructural analysis of Mo-Si-B alloys by BSE imaging is difficult due to the low level of attainable contrast. Electron backscatter diffraction (EBSD) imaging was used to create high-quality microstructure maps suitable for automated image analysis. The technique is also commonly referred to as orientation imaging microscopy (OIM). In this technique the sample is mounted in an SEM at approximately a 70° angle to the beam. A three-dimensional electron diffraction pattern called the Kikuchi pattern forms and is captured by a phosphor camera located to the side of the sample. An example of the diffraction pattern is shown in Figure 3.12. The lines in the image, called Kikuchi bands, are characteristic of the crystal structure and its specific orientation in space. Automated analysis software is used to identify the phase and determine its crystallographic orientation in relation to the sample. The beam is moved in a step-wise pattern and the phase and orientation at each location are recorded. If the orientations between neighboring pixels of the same phase are below a minimum misorientation angle, the points are assigned to the same grain. This information is used to form microstructure images which include both the phase and grain boundaries. EBSD precisely maps the distribution of all three phases and make automated image analysis possible. This technique also provides accurate measurement of the grain sizes and volume fractions of the phases.

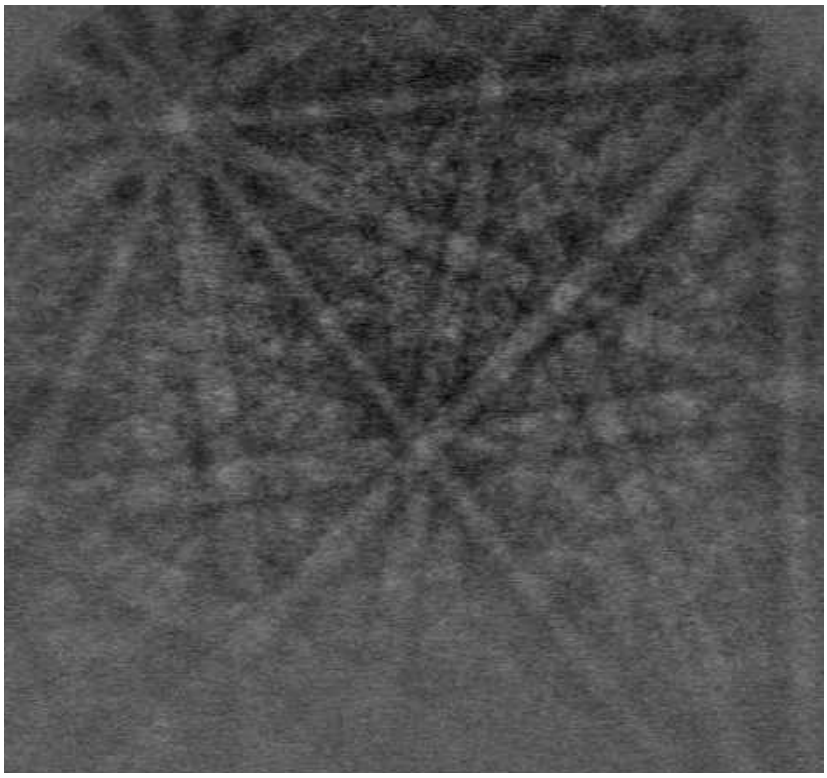

Figure 3.12: An example electron diffraction Kikuchi pattern used in EBSD analysis.

EBSD data collection was performed by Ron Witt of EBSD Analytical (Lehi, UT). Scans were taken over a 300×300μm region using a 300nm step size. Identification of the electron diffraction patterns requires prior knowledge of the crystal structures for all of the phases included in the measurement. This information was obtained from the same crystallographic information files used for Rietveld analysis. Simultaneous EDS data was collected and used to improve the confidence of fit for the indexing between the molybdenum and A15 phase, both of which have body-centered cubic crystal structures. The EDS data for oxygen was used to detect the presence of silica inclusions in the microstructures. Individual pixels with an oxygen signature of greater than 25% of full scale were assigned as silica. Analysis of the EBSD data was completed using the software program OIM Analysis (v. 5.2, EDAX Inc., Mahwah, NJ).

## 3.6 Microstructural Quantification of the Phase Distributions

The properties of Mo-Si-B alloys are highly dependent on microstructure and it is important to understand how changes in materials selection, processing and firing schedules affect the microstructures of the alloys. Quantitative stereology techniques have been used to investigate how changes in processing parameters affect the size, morphology and distribution of the intermetallic phases. Microstructural parameters of the reaction sintered Mo-Si-B alloys were determined using a number of techniques, ranging from simple line counting methods to calculation of the two-point correlation functions. The microstructural parameters were measured from the EBSD phase maps which allowed for quantification of the individual intermetallic phases. The overall distribution of intermetallics in the molybdenum matrix was examined, as well as the distributions of the individual A15 and T2 phases. Parameters measured from two-dimensional planes of polish can be taken as a universal value assuming the microstructure is isotropic in all three dimensions [87]. This was found to be the case for the reaction sintered Mo-Si-B alloys and evidence supporting this assertion is given in Chapter 5.

### 3.6.1 Phase Region Size Measurement

EBSD analysis was used to measure the grain size distributions of the individual phases, but in most cases the intermetallic regions were composed of multiple grains and often incorporated other phases. The continuous area that a single phase occupied was denoted the 'phase region'. The size distributions of the phase regions were measured for A15 and T2 to better understand the relationship between processing parameters and the dispersion of the intermetallics. EBSD maps were created for the individual phases and

the sizes of the discrete phase regions were measured using the program ImageJ [85]. The areas of each of the phase regions were converted to an equivalent diameter and the size distributions were measured, Figure 3.13.

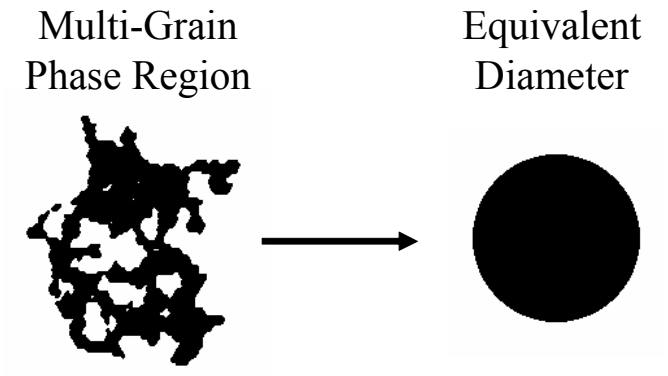


Figure 3.13: Schematic for determining the size of the 'phase region'. The area of the region was measured and converted to an equivalent diameter.

### 3.6.2 Mean Free Distance of the Intermetallic Phases

A parameter used to describe the distribution of particles in a matrix is the mean-free distance, which is the mean edge-to-edge spacing between particles and represents the uninterrupted distance in the matrix phase of the microstructure. The spacing of the intermetallics is believed to affect the oxidation resistance of Mo-Si-B alloys and one-half of the mean free distance can be seen as the average distance the glass phase must spread to cover the $Mo_{ss}$ matrix regions and create a continuous surface oxide. The measurements were made from EBSD phase maps of the individual phases. A 3×3 test grid with 80μm squares was superimposed on the image and the number of particles intersected by the test lines was counted to give the number of particles per unit length of

test line, $N_L$. A count of ½ was given for instances where the test line was tangent to or ended in a particle. The mean free path, $\lambda$, is in the unit of length and defined as [86]:

$$\lambda = \frac{1 - (V_V)_\alpha}{N_L} \tag{3.6}$$

where $(V_V)_\alpha$ is the volume fraction of the particulate phase $\alpha$.

### 3.6.3 Two-Point Correlation Functions

A set of statistical descriptors called two-point correlation functions were used to describe the distribution of the intermetallic phase regions. Two-point correlation functions are used to quantify the spatial arrangements (clustering, etc.) of a particulate phase and to identify anisotropy of the microstructure [87]. A schematic describing the correlation functions is illustrated for a two-phase mixture in Figure 3.14. When considering a multi-phase microstructure the two-point correlation function [$P_{ii}(r)$] is defined as the average probability that both endpoints of a randomly oriented line of length $r$ are located in phase $i$. Similarly, the probability that the first point is located in phase $i$ and the second point is located in phase $j$ is [$P_{ij}(r)$]. The correlation functions are measured between all of the phases in the microstructure yielding nine functions for a three-phase system, but because [$P_{ij}(r)$] = [$P_{ji}(r)$], the number is reduced to six independent functions.

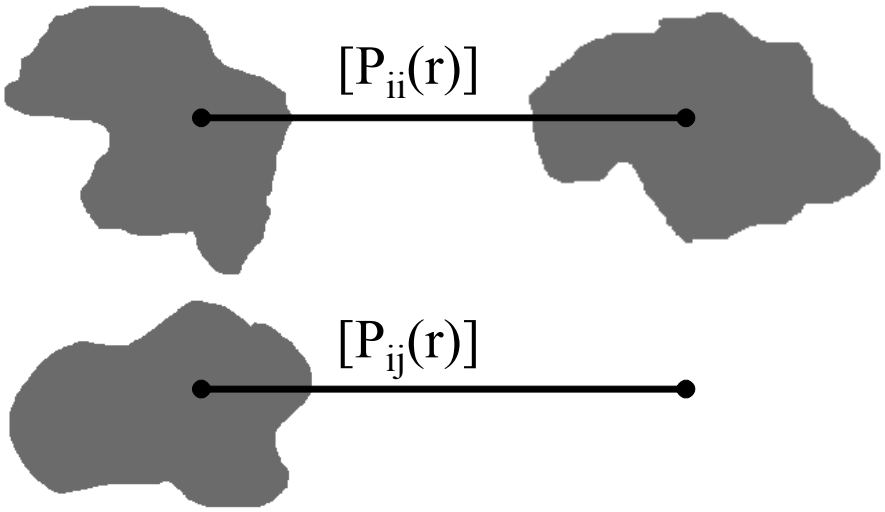


Figure 3.14: Depiction of the two-point correlation functions for a two-phase mixture, a particulate phase *i* and the matrix phase *j*.

The correlation functions are plotted as the average probability $[P_{ii}(r)]$ with respect to the test line length. The values of the correlation functions at either extreme of the plot are uniquely fixed by the volume fraction $V_f$ as [87]:

$$\lim_{r\to 0}\left[P_{ii}(r)\right] = V_{f,i} \tag{3.8}$$

$$\lim_{r\to \infty}\left[P_{ii}(r)\right] = \left(V_{f,i}\right)^2 \tag{3.9}$$

The two-point correlation functions were measured from EBSD phase maps of the Mo-Si-B alloys by Dr. Arun Gokhale (Georgia Institute of Technology, Atlanta, GA) using proprietary in-house software. The program first defines the test area and a virtual box is placed inside the image with sides spaced at the maximum test line length, $l_m$, from the edge of the image. The first end of the test line is placed randomly inside the virtual box and then the second end of the test line is placed at length *r* away from the first point, in a randomly oriented direction. The purpose of the virtual box is to create a measurement frame which ensures that both ends of the test line fall inside the image.

The orientation of the line and the phases present at the endpoints are recorded and the measurement is repeated many times for each test line length. The process is repeated for line length $r$ increasing from zero to $l_m$. The correlation functions were measured for the $Mo_{ss}$ phase, [$P_{Mo\text{-}Mo}(r)$], the combined intermetallic phases [$P_{Int\text{-}Int}(r)$], and the individual intermetallic phases [$P_{A15\text{-}A15}(r)$] and [$P_{T2\text{-}T2}(r)$]. The direction dependent two-point correlation functions [$P_{ij}(r,\theta)$] were also measured in the $X$ and $Y$-directions to determine if the microstructural features were isotropic.

## 3.7 Measurement of Material Properties

### 3.7.1 High Temperature Tensile Testing

High-temperature mechanical testing of Mo-2Si-1B and Mo-3Si-1B wt.% alloys was conducted for batches prepared with hBN powder. Bars of approximately 15×15×60mm were formed by cold-isostatic pressing and fired at 1600°C for 6 hours. The sintered bars were encapsulated in titanium tubes and hot-isostatically pressed at 1500°C and 30ksi for 6 hours. Tensile test specimens of the dog-bone geometry were cut from the bars using electro-discharge machining and the flat surfaces were polished with progressively finer SiC paper, finishing with 1μm diamond paste. The gauge sections of the samples were approximately 1.5×2.5×27 mm, Figure 3.15. Testing was conducted by Dr. Sharvan Kumar (Brown University, Providence, RI). Stress-strain curves were measured at 100°C increments between 900-1300°C. The tests were conducted in a vacuum chamber to prevent oxidation of the samples. The fracture surfaces were examined by SEM to identify whether the samples had failed by transgranular or intergranular fracture and look for signs of ductile deformation.

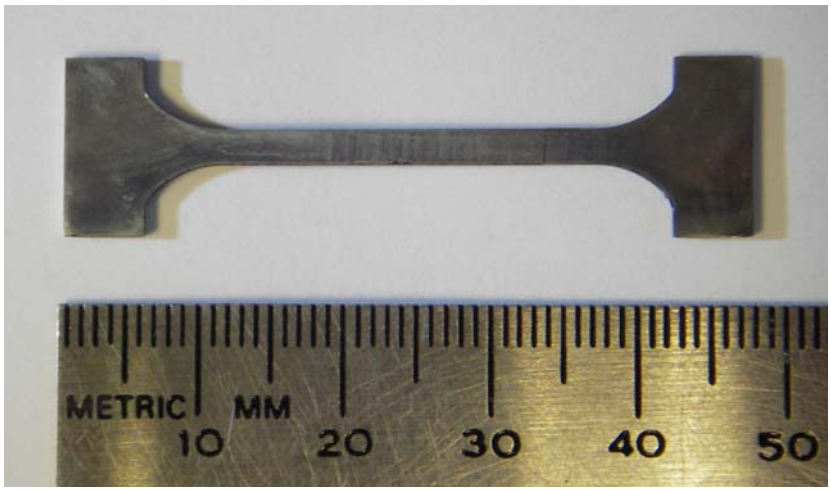


Figure 3.15: The dog-bone geometry tensile test specimens used for high-temperature testing of the Mo-Si-B alloys.

### 3.7.2 Oxidation Testing

3.7.2.1 Oxidation in One Atmosphere Air

The oxidation resistance of the Mo-Si-B alloys was tested at 1000°C and 1100°C in air. The samples were polished with 1200 grit SiC sandpaper prior to testing to remove any surface variation in the samples. Isothermal oxidation tests were conducted in a box furnace. The samples were removed from the furnace and weighed at periodic intervals to plot the weight loss as a function of time. The characteristics and thicknesses of the oxide layers were examined from polished cross-sections oxide surface.

3.7.2.2 Pre-Oxidation in Low Oxygen Atmospheres

Helmick et al. [55] studied the formation of borosilicate layers on Mo-3Si-1B wt.% alloys. It was found that much of the initial transient weight loss of the samples is due to channels formed during the early stages of oxidation that extend to the alloy surface. They were able to eliminate these channels by slowing the initial rate of

oxidation by controlling the oxygen partial pressure and flow rate. Following this work, a pre-oxidation procedure was developed. Mo-3Si-1B wt.% alloys were oxidized in a sealed tube furnace with a mixture of Ar-0.1% $O_2$ over a variety of flow rates, temperatures and hold times. The samples were heated and cooled in pure argon and exposed to the oxygen mixture only at the temperature and time period being investigated. Using low oxygen contents gives control over the oxidation rate and allows for the study of the early stages of oxide formation. Pre-oxidation was also used to form continuous glass layers on samples prior to further testing in air. This was done to minimize the transient weight loss in order to better observe oxidation in the diffusion controlled regime.

# CHAPTER 4

# PREPARATION OF Mo-Si-B ALLOY FROM REACTION SYNTHESIS

The formation of Mo-Si-B alloys produced by the nitride-based reaction synthesis method is discussed in the following chapter. The characterization of reactions to form the intermetallics, investigations to improve the processing procedures and the sintering of the alloys are reviewed and discussed.

## 4.1 Nitride-Based Reactions

The reactions of the nitrides with molybdenum were studied for the formation of the individual intermetallic compounds in the molybdenum-rich corner of the Mo-Si-B phase diagram and for three-phase mixtures of $Mo_{ss}$-A15-T2. The experiments were conducted using the Climax molybdenum, UBE $Si_3N_4$ and Cerac hBN powders. The formation of the desired phases was confirmed by x-ray diffraction. Simultaneous TGA/DTA measurements were used to determine the onset of the reactions which form the intermetallics phases. The formation of Mo-Al intermetallics and potential routes to incorporate aluminum into the alloys were also investigated.

### 4.1.1 Formation of the Intermetallic Compounds in the Mo-Si-B System

The intermetallic compounds found in the molybdenum-rich corner of the Mo-Si-B phase diagram were prepared by the reaction of molybdenum, $Si_3N_4$ and hBN. Three powder mixtures were prepared to give the stoichiometric ratios of $Mo_3Si$, $Mo_5SiB_2$ and $Mo_2B$ after reaction. A mixture of the molybdenum-silicon solid solution was also

prepared at the 1600°C solid solution limit of 0.675 wt.% silicon. The powder mixtures were pressed into pellets and fired at 1600°C for 2h in Ar/10% $H_2$ and then cooled at 10°C/min.

X-ray diffraction was used to verify the formation of the phases, Figure 4.1 to Figure 4.3. Single phase compounds were achieved for both the A15 and $Mo_2B$ mixtures. The T2 mixture had a minor fraction of molybdenum present, as marked in the diffraction pattern, Figure 4.2. The T2 phase has a relatively wide composition range, but the stoichiometric composition is very close to the two-phase $Mo_{ss}$-T2 region of the phase diagram. A slight error in the formulation of the mixture could explain the presence of the molybdenum. Sakidja et al. have observed that molybdenum precipitates inside the T2 phase during cooling due to a slight shift in the phase stability at lower temperatures, which could also explain the presence of the molybdenum phase [88].

Trace peaks corresponding to the A15 phase were observed in the $Mo_{ss}$ mixture after firing and could be the result of incomplete dissolution of silicon. The A15 could also be precipitating from the solution during cooling due to the reduced solubility of silicon at lower temperatures. A test was conducted to determine if the A15 phase was precipitating at the cooling rates used. The sample was reheated to 1600°C for one hour and cooled at a slower rate of 1°C/min, Figure 4.4. The trace A15 peaks were not observed after the second firing, illustrating that the original observation was due to incomplete dissolution of silicon. This is significant as it demonstrates that the phase assemblage observed at room temperature will not differ greatly from that given by the phase diagram at 1600°C, for the cooling rates used.

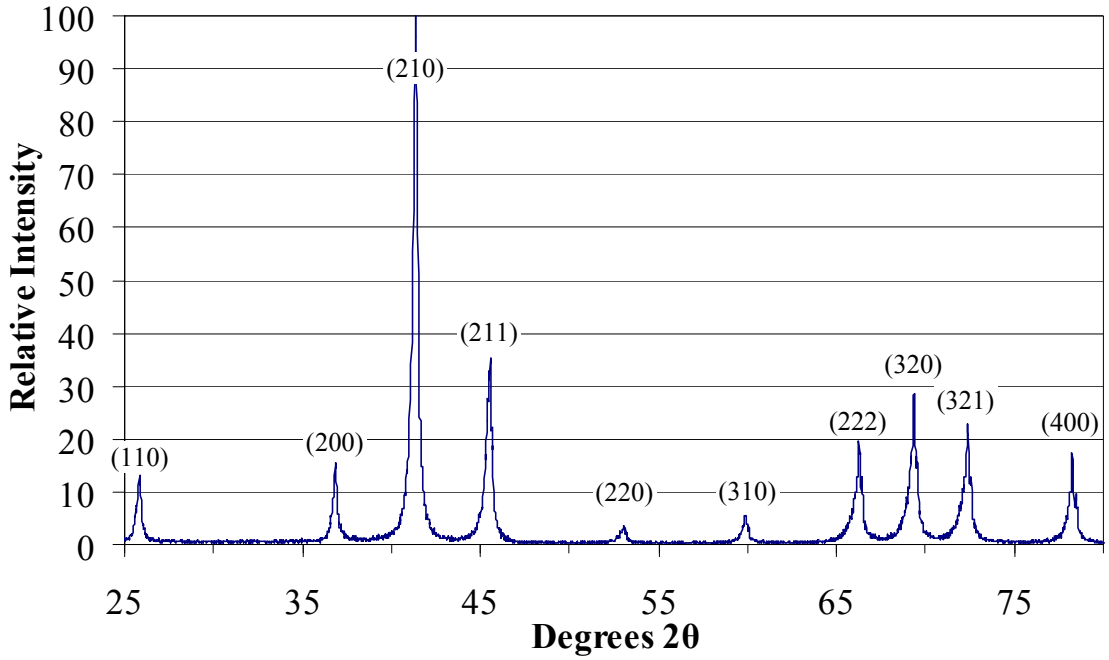


Figure 4.1: XRD pattern of the pure phase A15 mixture formed by reaction synthesis, sintered at 1600°C for 2 hours.

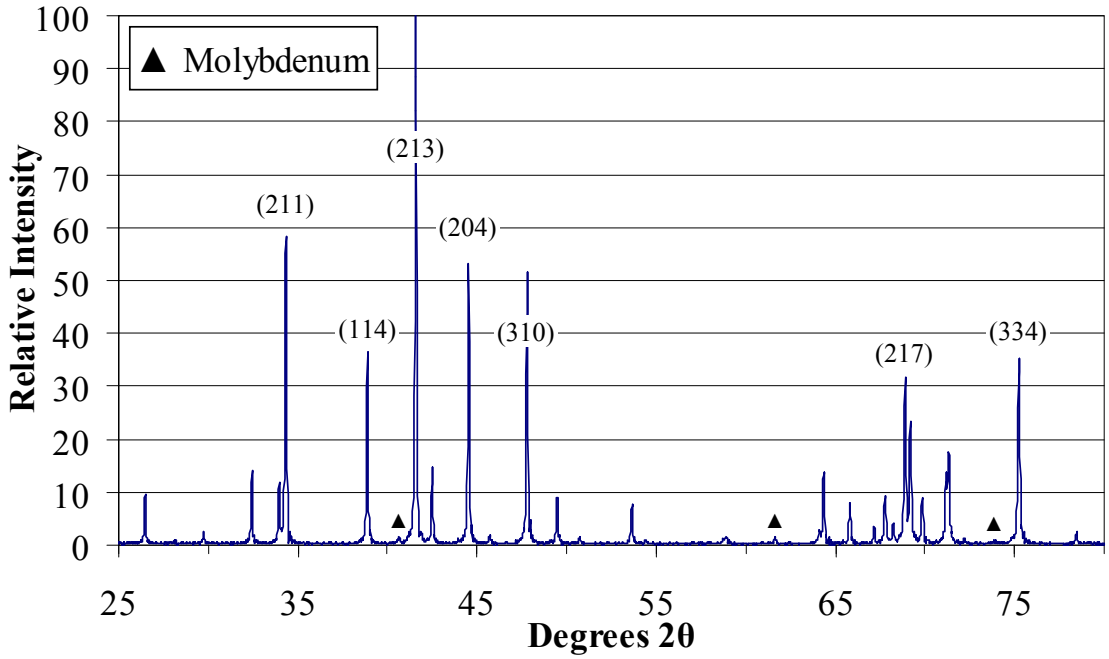


Figure 4.2: XRD pattern of T2 mixture formed by reaction synthesis, sintered at 1600°C for 2 hours. The peaks due to a minority amount of the molybdenum phase are indicated.

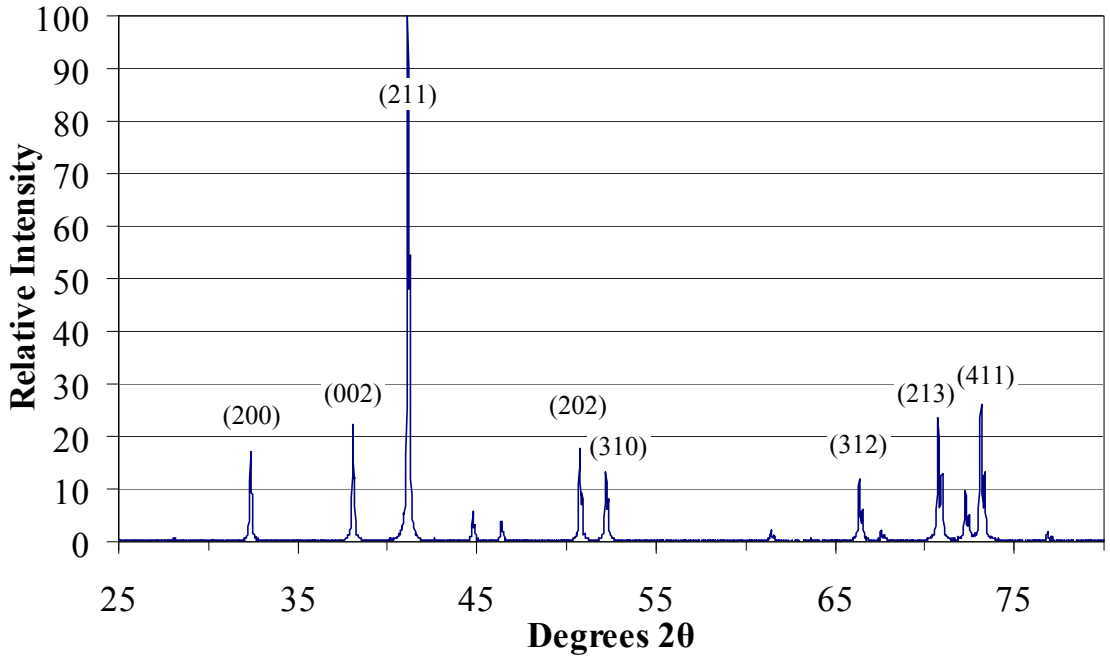


Figure 4.3: XRD pattern of the pure phase $Mo_2B$ mixture formed by reaction synthesis, sintered at 1600°C for 2 hours.

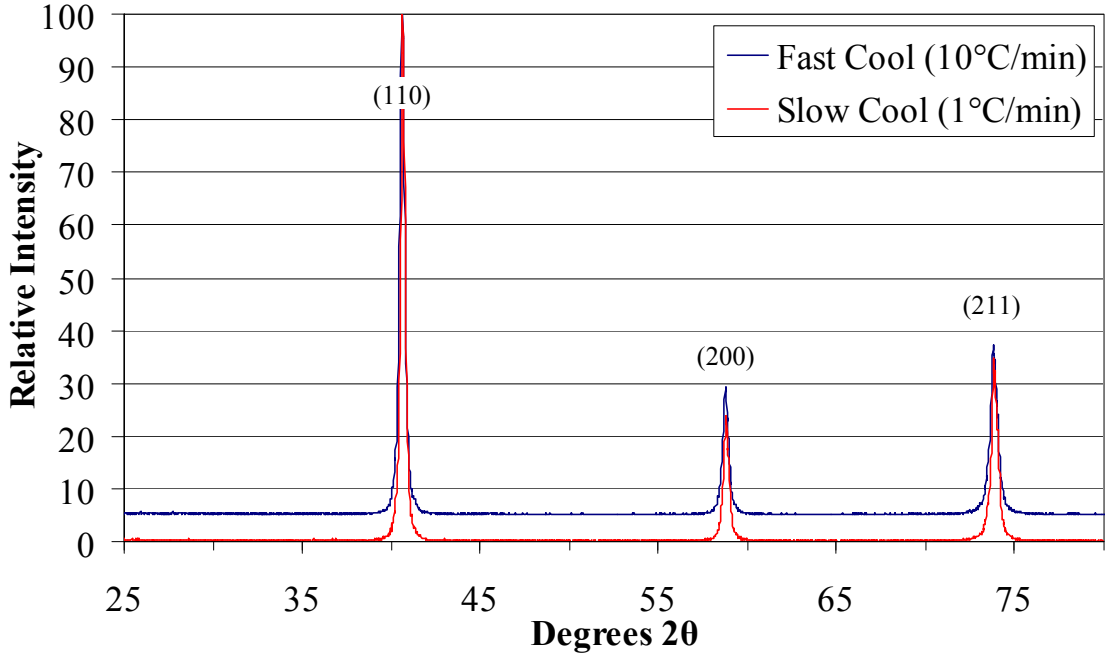


Figure 4.4: XRD patterns of the $Mo_{ss}$ mixture fired at 1600°C, after cooling at 1°C/min and 10°C/min. Once dissolved, the A15 phase was not observed at either cooling rate.

TGA measurements were used to determine the onset of the reactions between molybdenum and the nitrides to form the A15 and T2 phases. The stoichiometric powder mixtures were tested in Ar/5% $H_2$ and heated at 3°C/min to match the firing conditions used to sinter the alloys. The weight change is plotted as a function of temperature for the two mixtures, Figure 4.5. There was an initial period of weight loss up to 885°C due either to the evaporation or reduction of $MoO_3$. This was followed by a second period of weight loss due to the evolution of nitrogen, which marks the onset of the reaction. The T2 precursor mixture began reacting at 1140°C and the A15 precursor mixture began reacting at 1193°C, which are close to the thermodynamic predictions of 1109°C and 1057°C. It can be seen from the TGA measurements that the reactions proceed rapidly. The weight losses due to the evolution of nitrogen were 5.2 wt.% for the A15 mixture and 6.4 wt.% for the T2 mixture. By the end of the measurements at 1400°C, the decomposition of the nitrides was 93.2% complete for the A15 mixture and 79.0% complete for the T2 mixture.

The densities of the pellets used for XRD analysis were measured by Archimedes method, Table 4.1. The molybdenum-silicon solid solution and A15 phase both sintered to high relative densities (91-98% T.D.). The boron containing compounds underwent little densification and had high levels of open porosity. This observation corresponds well with diffusion couple measurements by Perepezko et al. that demonstrated the growth rate of the T2 phase is two orders of magnitude slower than the A15 phase [27]. From these results it appears that boron may hinder the densification of Mo-Si-B alloys, although more work needs to be completed to understand its effect on the sintering of the $Mo_{ss}$ phase.

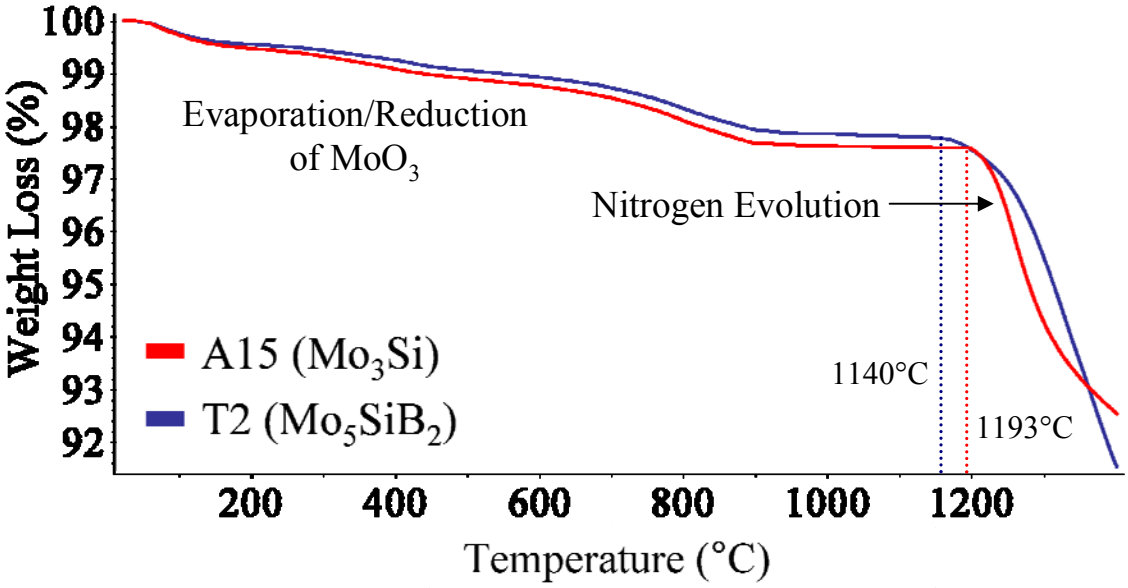


Figure 4.5: TGA traces for the A15 and T2 precursor mixtures heated at 3ºC/min in Ar/5% $H_2$. The onset of the reaction is indicated by the evolution of nitrogen gas.

Table 4.1: The Archimedes densities of the pure phase Mo-Si-B compounds after firing at 1600°C for 2 hours.

| | **Bulk Density (g/cc)** | **Relative Density (% T.D.)** | **Open Porosity (%)** |
|---|---|---|---|
| $Mo_{ss}$ | 9.86 | 98.1 | 0.4 |
| A15 | 8.15 | 90.9 | 1.7 |
| T2 | 4.18 | 47.4 | 33.1 |
| $Mo_2B$ | 5.16 | 55.9 | 33.4 |

### 4.1.2 Formation of $Mo_{ss}$-A15-T2 Alloys by Reaction Synthesis

The combined formation of the A15 and T2 intermetallic phases in $Mo_{ss}$-A15-T2 alloys was studied for the Mo-3Si-1B wt.% composition. A TGA trace was measured at 3°C/min to 1400°C in a mixture of flowing Ar/5% $H_2$, Figure 4.6. The behavior was similar to that observed for the individual intermetallic mixtures. An initial period of weight loss due to elimination of $MoO_3$ was followed by a second period of weight loss due to the evolution of nitrogen. The reaction began at 1140°C, the same temperature observed for the T2 powder mixture. The total weight loss observed in the measurement due to the evolution of nitrogen was 2.3 wt.%, indicating that the decomposition of the nitrides was 72.2% complete by 1400°C.

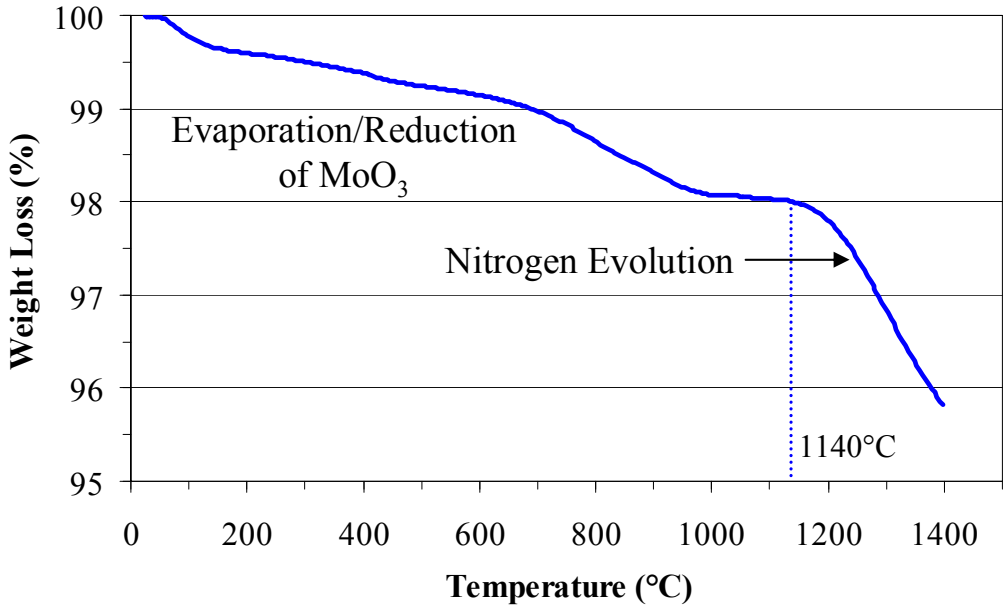


Figure 4.6: TGA trace for a Mo-3Si-1B wt.% precursor mixture heated at 3ºC/min in Ar/5% $H_2$. The onset of the reaction is indicated by the evolution of nitrogen gas.

The weight loss observed in the TGA traces indicates the temperature where the nitrides begin to react, but gives no information as to which phases are formed. In the prior discussion of the TGA measurements it was assumed that molybdenum and the nitrides react to form the A15 and T2 phases, but it is possible that other intermediate molybdenum silicides and borides are formed. The products of the nitride-based reactions were investigated for the $Mo_{ss}$-A15-T2 phase field using isothermal firings and subsequent phase identification by XRD. Mo-3Si-1B wt.% pellets were fired at different temperatures in Ar/10% $H_2$ with a 6 hour hold at each temperature, Figure 4.7. An XRD scan of the unfired mixture shows the peak locations of the reactant powders. After firing at 1100°C for 6 hours, the nitride peaks are no longer observed and the formation of a small amount of T2 is apparent. This temperature is slightly lower than predicted by the thermodynamics of the reaction, but it is important to note that the free energy of formation of the T2 phase used in the calculations was only an estimated value. The discrepancy between the predicted and observed temperature of the reaction is within the margins of error for the estimated free energy value and the accuracy of the furnace. Both the A15 and T2 phases were detected by 1200°C (pattern not shown). The relative peak heights in the diffraction patterns appear unchanged between the 1300°C and 1500°C firings, indicating that the reactions are complete after six hours at 1300°C. This is supported by the observation that the decomposition of the nitrides had progressed to 72% completion by 1400°C with zero hold time.

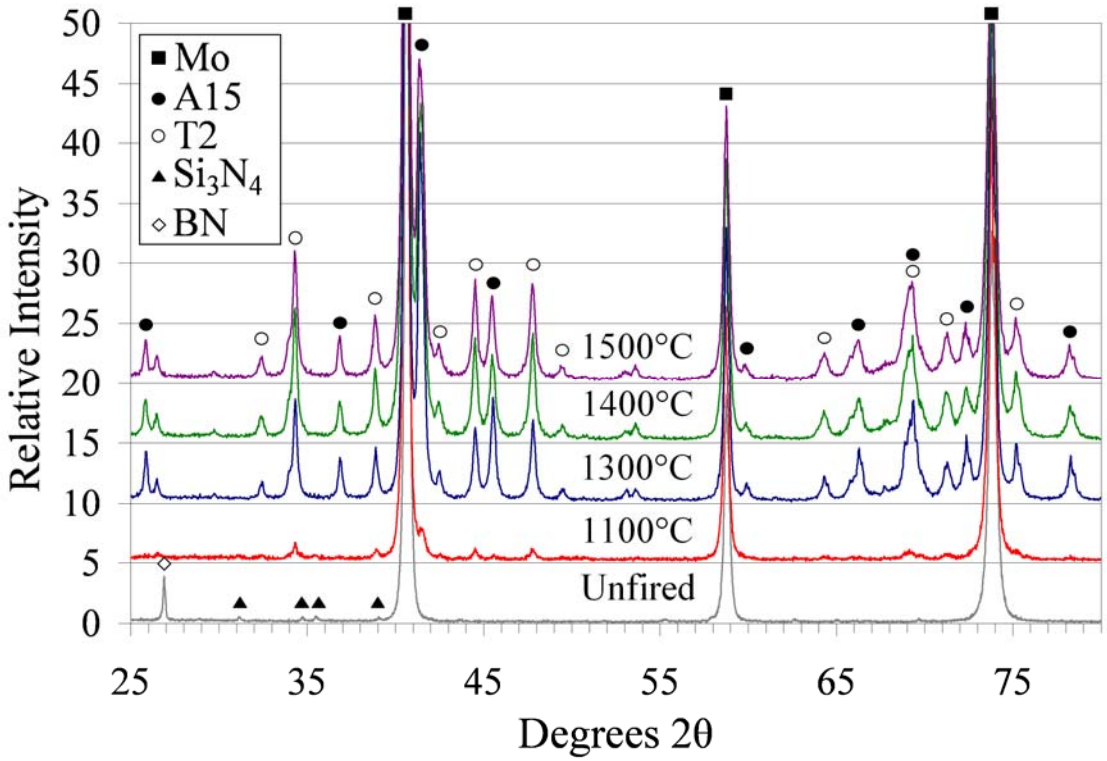


Figure 4.7: Comparison of the XRD patterns of samples fired in Ar/10% $H_2$ between 1100°C and 1500°C with a 6 hour hold at each temperature. Almost no change in the peak heights was observed between 1300°C and 1500°C, indicating completion of the reactions.

### 4.1.3 Impurity Considerations for the Reaction Synthesis Method

It was discussed in Chapter 2 that nitrogen harms the ductility of molybdenum, creating a potential concern for alloys processed by the reaction synthesis method, due to the $Si_3N_4$ and BN reactants. Early investigations of the reaction synthesis method have alleviated this concern. The reactions to form the intermetallic phases were first examined by TGA/DTA under an atmosphere of $N_2$/5% $H_2$ and the experiment demonstrated that the stable temperature field for $Mo_2N$ is well below the temperature at which the nitrides react. A Mo-3Si-1B wt.% sample was heated at 5°C/min to 1400°C, Figure 4.8. Beginning at 700°C there was a large weight gain due to the formation of $Mo_2N$. At 875°C the sample began to lose weight due to the decomposition of the $Mo_2N$. This was confirmed by the corresponding DTA trace which shows an endotherm due to the evolution of nitrogen. Based on this observation it can be concluded that the use of the nitride reactants will not lead to the formation of $Mo_2N$, but other problems occur as a result of sintering in nitrogen. The presence of nitrogen stabilized the nitride reactants and drove the temperature of the decomposition reaction to approximately 1300°C. A volume increase also accompanies the formation of the $Mo_2N$ which will reduce the density of the samples. Finally, the equilibrium concentration of nitrogen in molybdenum is dependent on the partial pressure of nitrogen in the atmosphere. For a partial pressure of 1atm, the equilibrium concentration at 1600°C is 30 wppm [73]. To avoid the problems caused by firing in nitrogen, all of the alloys were sintered in an $Ar/H_2$ atmosphere. Because the samples were fired in a flowing gas mixture, the partial pressure of nitrogen over the samples due to the decomposition of the nitrides was assumed to be very low.

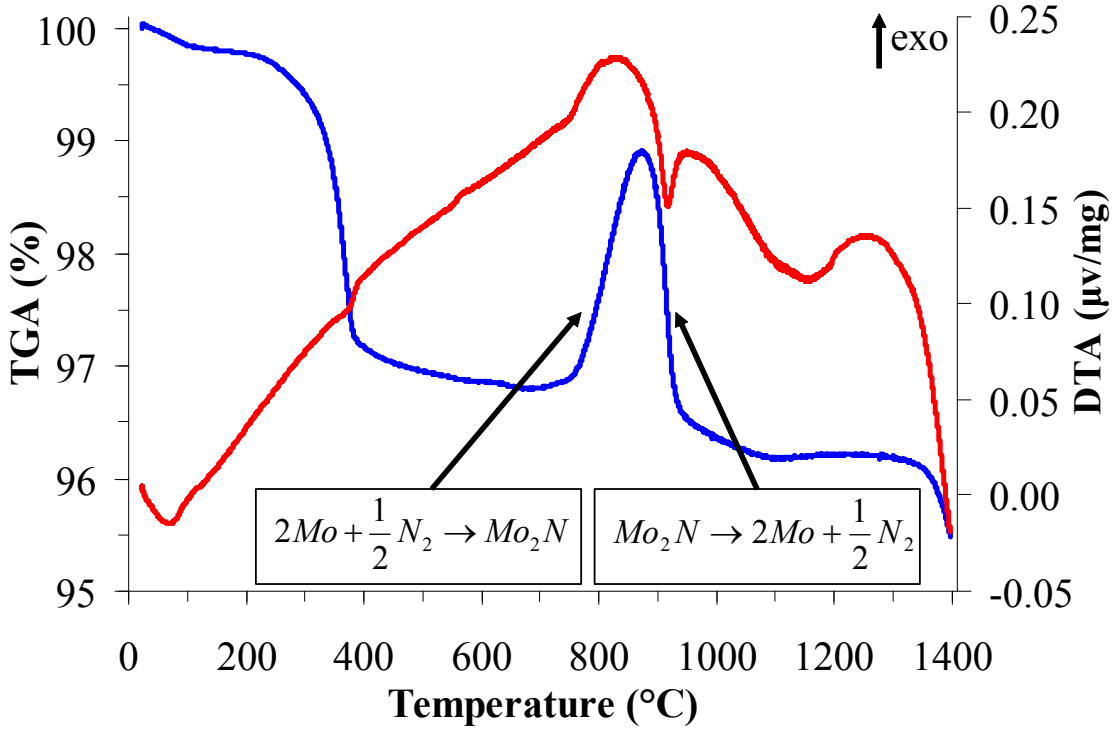


Figure 4.8: Combined TGA/DTA traces of a Mo-3Si-1B wt.% sample heated at 5°C/min in an atmosphere of $N_2$/5% $H_2$. The formation and decomposition of $Mo_2N$ are indicated.

Another potential concern with powder processing is that despite efforts to limit the oxygen impurity levels throughout the process, the initial molybdenum powders already contain a relatively high level of oxygen. The as-received powder contains approximately 1 wt.% oxygen and additional surface oxidation likely occurs during processing. Molybdenum oxide is reduced in hydrogen at approximately 600-700°C and in this work it is claimed that the $Si_3N_4$ and BN precursors prevent the formation of silicon and boron oxides through the reduction stage. This has been verified in previous work in which $MoO_3$ powder was used as a molybdenum precursor in the reaction synthesis method [9]. $MoO_3$, $Si_3N_4$ and hBN powders were mixed in a ratio to give the

composition Mo-3Si-1B wt.% after the reduction of the oxide and decomposition of the nitrides. Powder compacts were fired in a reducing atmosphere with an extended hold at 700°C to reduce the $MoO_3$ powder, and then sintered at 1600°C. XRD analysis of the sintered samples confirmed the formation of the A15 and T2 phases. The initial powder mixture had more than a sufficient amount of oxygen present in the $MoO_3$ powder to completely consume the nitride reactants, and the intermetallic phases would not have formed if the nitrides were oxidized,. This experiment illustrates the main benefit of using the nitride reactants. The ability to create alloys with low oxygen levels represents a significant development in the powder processing Mo-Si-B alloys.

### 4.1.4 Addition of Aluminum to Mo-Si-B Alloys

The addition of aluminum to Mo-Si-B alloys has the potential to greatly improve oxidation resistance, although the high vapor pressure of aluminum at the melting point of molybdenum prevents its addition through melt-based processes. Paswan et al. attempted to add aluminum to Mo-Si-B alloys using powder processing methods but the aluminum was oxidized to form $Al_2O_3$ rather than incorporated into the alloy [8]. In this work, the formation Mo-Al-Si-B alloys has been accomplished through careful control of the processing and firing conditions.

In an initial attempt aluminum powder was mixed into a Mo-Si-B batch and fired, but there was not a simple means to verify that aluminum was actually incorporated into the alloy and had not oxidized to form $Al_2O_3$. The detection of minor levels of alumina in the Mo-Si-B alloys by XRD is difficult due to the high x-ray scattering cross-section of molybdenum. The minor alumina peaks were hidden in the background of the scans despite extended collection times. Furthermore, the $Mo_3Al$ phase is isomorphous with

$Mo_3Si$ and is not detected as a separate phase. To circumvent these difficulties the reaction of aluminum and molybdenum was first investigated for a two-phase mixture in the Mo-$Mo_3Al$ phase field. Molybdenum powder was dry ball milled with 7 wt.% aluminum powder, pressed into pellets and fired at 1600°C for 6h. The samples underwent an approximately 50% increase in size and gained 3.2 wt.% due to partial oxidation of the aluminum, although if complete oxidation of the aluminum had occurred a weight gain of 6.2% would have been expected. XRD analysis revealed peaks corresponding to molybdenum and $Al_2O_3$, along with a large number of unidentified peaks possibly due to various Mo-Al or Mo-Al-O compounds. A second firing of the Mo-7Al wt.% mixture was conducted using improved gettering of the inlet gas. The resulting XRD pattern showed peaks corresponding to both molybdenum and $Mo_3Al$, with only small peaks for aluminum oxide. The large increase in dimension was observed again and assumed to be due to the melting of aluminum prior to reaction. An attempt was then made to react the mixture below the melting point of aluminum in order to avoid the large volume expansion. A compact of the Mo-7Al wt.% mixture was fired at 600°C for 6h. The mixture reacted to form a combination of molybdenum and $MoAl_3$, Figure 4.9, but the large dimensional increase occurred despite being fired below the melting point of aluminum. The sample was crushed using a mortar and pestle, pressed in a pellet and refired to 1600°C for 6h to complete the reaction to form Mo-$Mo_3Al$. The resulting diffraction pattern is shown in Figure 4.9. Only molybdenum and the $Mo_3Al$ phase were present and no $Al_2O_3$ was detected.

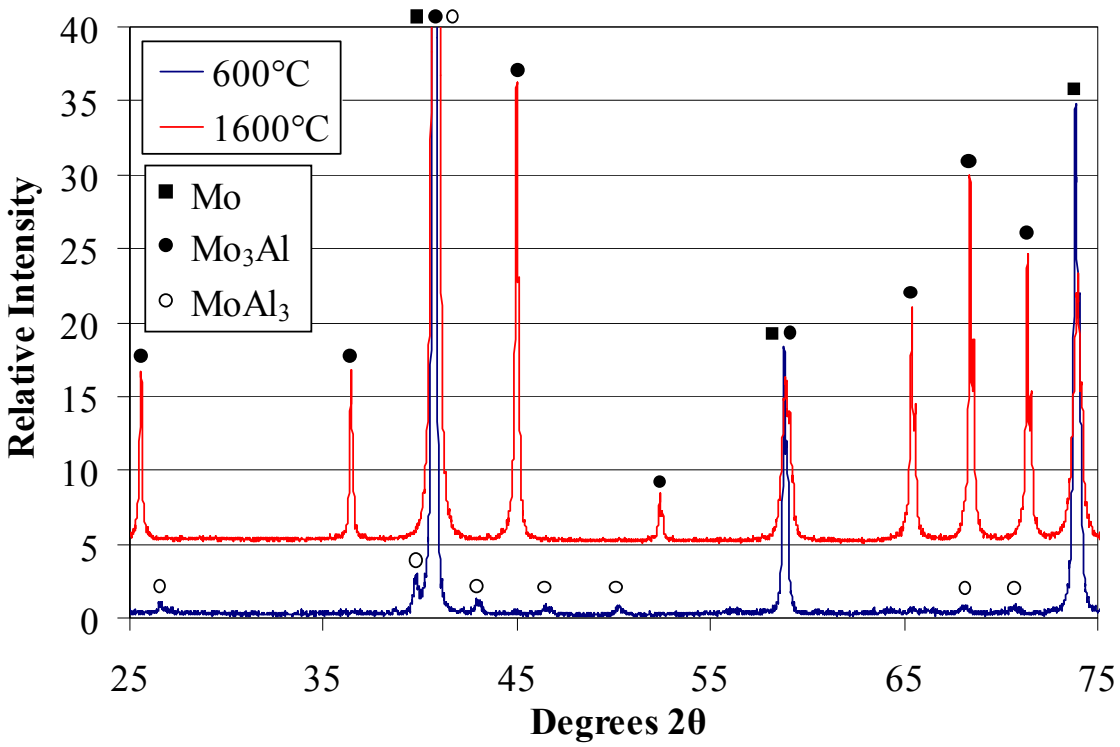


Figure 4.9: XRD scans for the Mo-7Al wt.% mixture. Mo-$MoAl_3$ was formed after pre-reaction at 600°C and Mo-$Mo_3Al$ was formed after further reaction at 1600°C.

A combination of TGA and DTA measurements was used to determine the temperature at which aluminum and molybdenum react and to investigate the cause of the large volume expansion, Figure 4.10. There was a strong exothermic peak beginning at 625°C which indicates the start of the reaction. The DTA trace returned to a baseline level by 655°C, slightly before the melting point of aluminum at 660°C. The exothermic reaction may heat the sample above the melting point of aluminum and cause the formation of a transient liquid phase would explain the volume increase, but an endotherm. This would also be expected due to the enthalpy of melting. A possible explanation is that the exothermic peak is large enough to counter the endotherm due to melting. A continual increase in weight also began at the same temperature as the

exothermic peak. This was due to oxidation of the sample because the inlet gas of the TGA/DTA was not gettered. Aluminum is protected by a surface oxide layer, but further oxidation occurred after the oxide layer was disrupted by the reaction.

Building on the previous findings, the addition of aluminum to the $Mo_{ss}$-A15-T2 alloy was attempted again. A Mo-5Al wt.% mixture was pre-reacted at 900°C for 2 hours to create the Mo-$Mo_3Al$ mixture, Figure 4.11. The mixture remained friable after firing and was dry ball milled with $Si_3N_4$ and hBN powders. The composition Mo-5Al-1Si-1B wt.% was selected because the formation of the A15 phase is dependent on aluminum being incorporated into the alloy. If all of the aluminum is oxidized, the composition will form a two-phase $Mo_{ss}$-T2 mixture. Powder compacts were fired to 1600°C for 6 hours and XRD analysis showed a combination of molybdenum, A15 and T2, with no $Al_2O_3$ detected, Figure 4.11. The presence of the A15 phase is evidence that the aluminum was not oxidized and had been incorporated into the alloy. The aluminum and silicon based A15 phases also have different lattice parameters and the observed A15 peaks are shifted away from those for $Mo_3Si$ and towards the $Mo_3Al$ lattice parameter.

This work illustrates that powder processing methods can be used to create Mo-Al-Si-B alloys. Using pre-reacted mixtures of molybdenum and aluminum provides a means to circumvent the large volume expansion in the powder compacts. Further work needs to be completed to refine the process and increase the reliability of the methods developed.

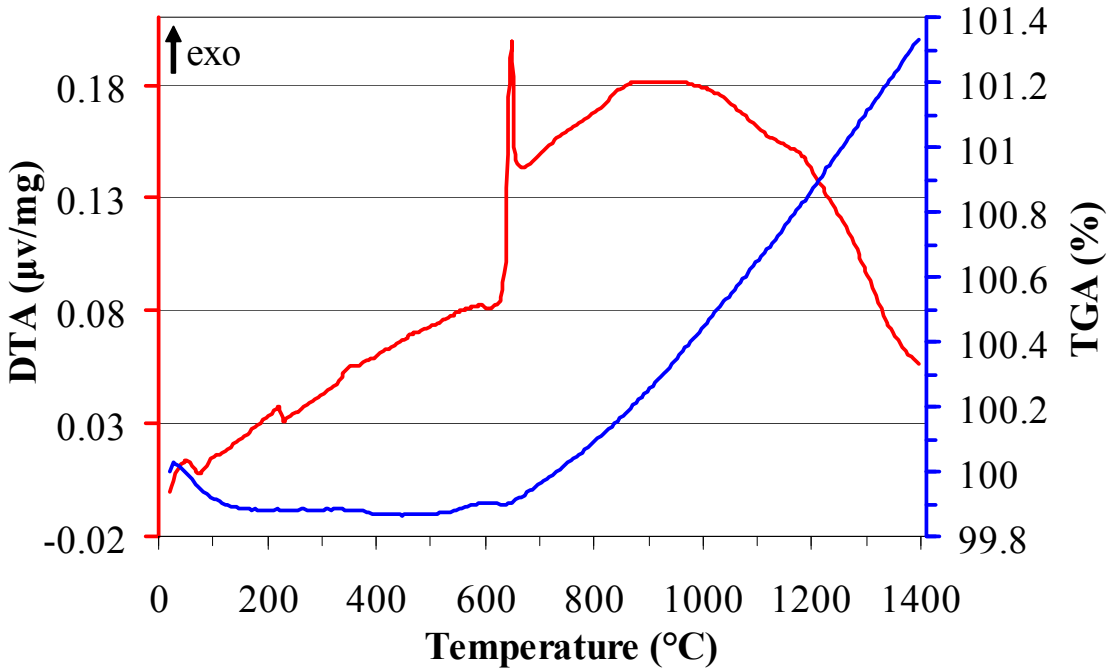


Figure 4.10: Combined TGA/DTA traces for the Mo-7Al wt.% mixture heated at 3°C/min in Ar/5% $H_2$. The reaction is indicated by an exothermic peak at 625°C.

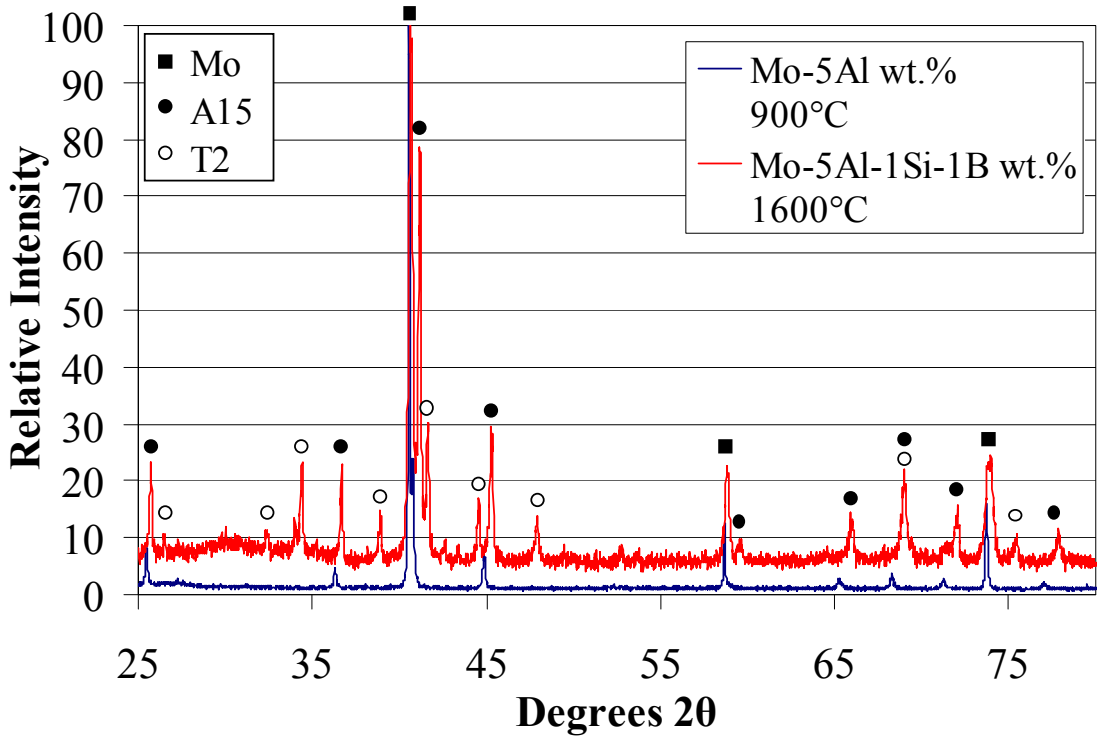


Figure 4.11: XRD patterns for the Mo-5Al wt.% mixture pre-reacted at 900°C and for the Mo-5Al-1Si-1B wt.% alloy after sintering at 1600°C.

## 4.2 Powder Processing Studies

Fabrication of Mo-Si-B alloys by powder metallurgy eliminates many of the problems associated with melt-based processing, namely the formation of non-equilibrium phases, coarse microstructures and the intermetallic matrix phase. Nevertheless there are issues associated with powder processing that must be addressed for this method of production to be successful. Impurity contents and residual porosity must be minimized. The production techniques developed should also be amenable to industrial processes, which introduces factors that are not always addressed at the laboratory scale such as yield and scalability to large production volumes. The objective of the experiments detailed in this section were to optimize the powder processing methods to improve the quality of the alloys and to develop processing parameters that can be transferred to industrial scale production of Mo-Si-B alloys.

### 4.2.1 Spray Drying

Spray drying is a common industrial practice used to dry powder slurries and is often used in powdered metal and ceramic processing to create spherical agglomerates for pressing operations. It is a critical step in the reaction synthesis method and is used to lock in the dispersion of the $Si_3N_4$ and BN reactants following milling. The qualities of the spray dried powders were evaluated as a function of the binder content and resulting oxygen, carbon and nitrogen impurity levels were measured.

#### 4.2.1.1 Dispersant/Binder Selection

Dispersants are used in powder processing to allow higher solids loading in the slurries and to create a more homogenous dispersion. A variety of solvents and dispersants were tested and the combination of acetone and polymethyl methacrylate

(PMMA) was selected. Acetone evaporates quickly and limits oxidation of the molybdenum powder during processing. The PMMA also acts as a binder and improves the strength of the spray dried granules and the pressed compacts. Elvacite grade 2008 PMMA resin was selected because it is known to burn out cleanly in a variety of conditions, including under vacuum and in reducing and inert atmospheres. Upon heating the polymer breaks down to the monomer and evaporates. The exact temperature range for burnout was determined by TGA analysis. A sample of the resin was tested under the conditions used to sinter the Mo-Si-B alloys, 3°C/min in Ar/5% $H_2$, Figure 4.12. The polymer began to break down at 250°C and completely evaporated by 420°C.

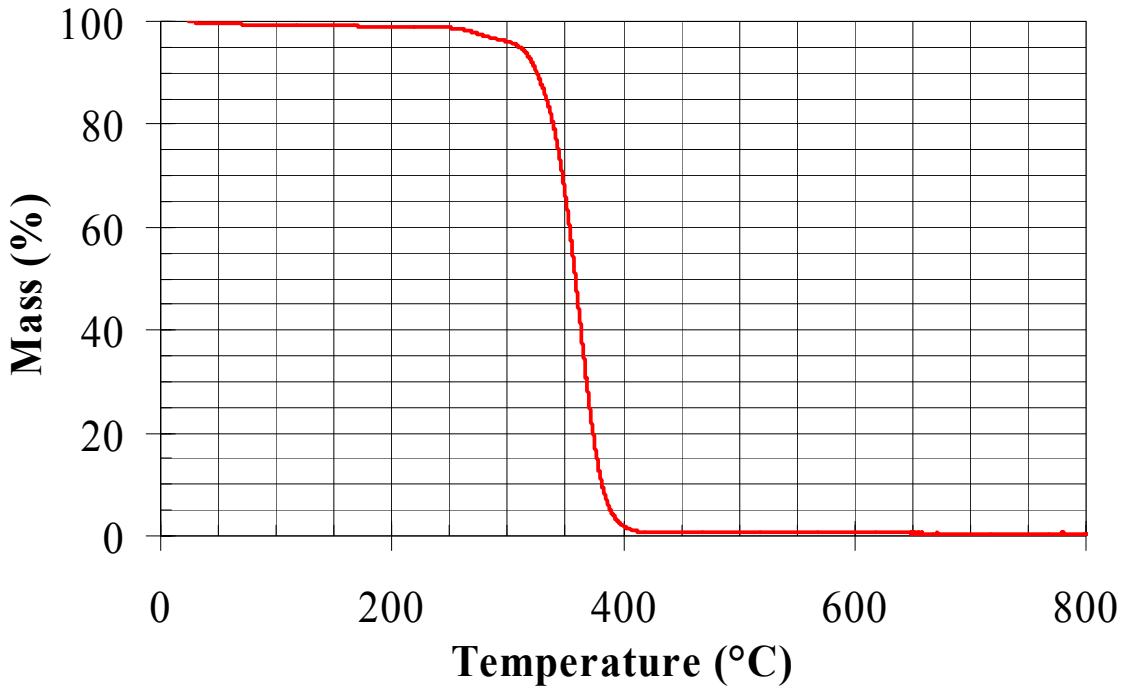


Figure 4.12: TGA trace for the Elvacite 2008 PMMA heated at 3°C/min in Ar/5% $H_2$.

After evaporation the depolymerized resin condenses as a liquid in the downstream regions of the furnace system and it is desirable to minimize the amount of binder used. The yield, size distribution and morphology of the spray dried granules were investigated as a function of the PMMA content. Note that the additions of the organic additives are reported as weight percentages of the reactant powders. Experiments were conducted using the Büchi spray dryer. Although the tests were conducted on a small scale, many of the issues encountered with the laboratory scale spray dryers are relevant to large industrial dryers.

4.1.1.2 Binder Content and Spray Drying Yield

A significant fraction of the powder slurry was not recovered as granules when using the Büchi spray dryer, mostly due to liquid droplets hitting the walls of the drying chamber. Moreover, much of the spray dried material was present as powder fines. The fines interstitially pack between larger particles and reduce the ability of the granules to flow. After spray drying the powders were screened between 170 and 400 mesh (38-90μm) sieves to separate out the spherical granules which provide uniform die fill and reduced density gradients in dry pressing operations. The larger granules also have a more homogenous composition between individual granules. As the size of the granules approached the size of the reactant powders, inhomogeneity became an issue. This was especially a problem with the hBN reactant, as illustrated in Figure 4.13.

The majority of the powder was below 400 mesh and only a small fraction of the powder recovered was in the form of granules in the desired 170-400 mesh size range. An SEM image of the -400 mesh size fraction reveals that a significant portion is present as spherical agglomerates, Figure 4.14. Attempts were made to recover the additional

spheres using 500 (25µm) and 635 (20µm) mesh sieves, but the fine sieves clogged quickly and the effort required to screen large amounts of powder was prohibitive.

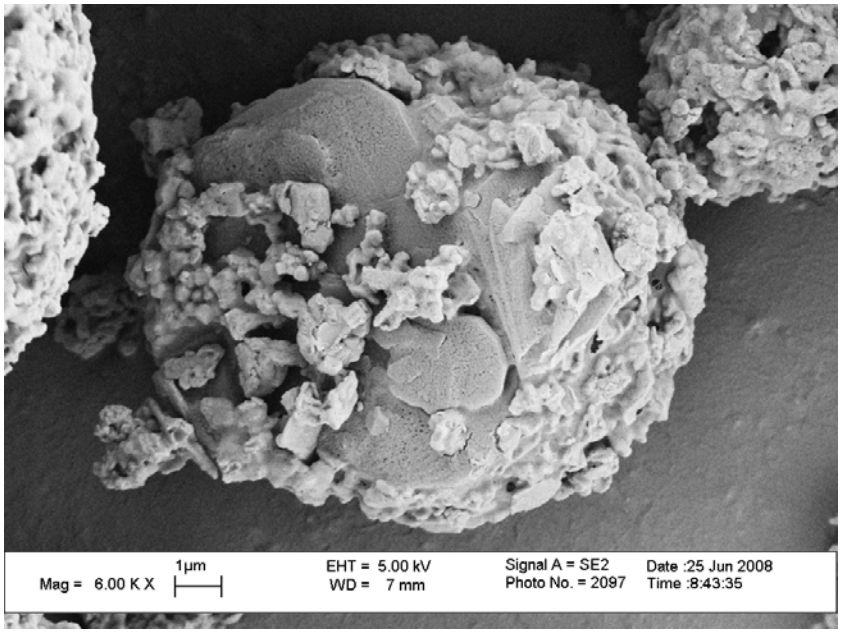


Figure 4.13: A spray dried agglomerate which illustrates the inhomogeneity of the powder fines.

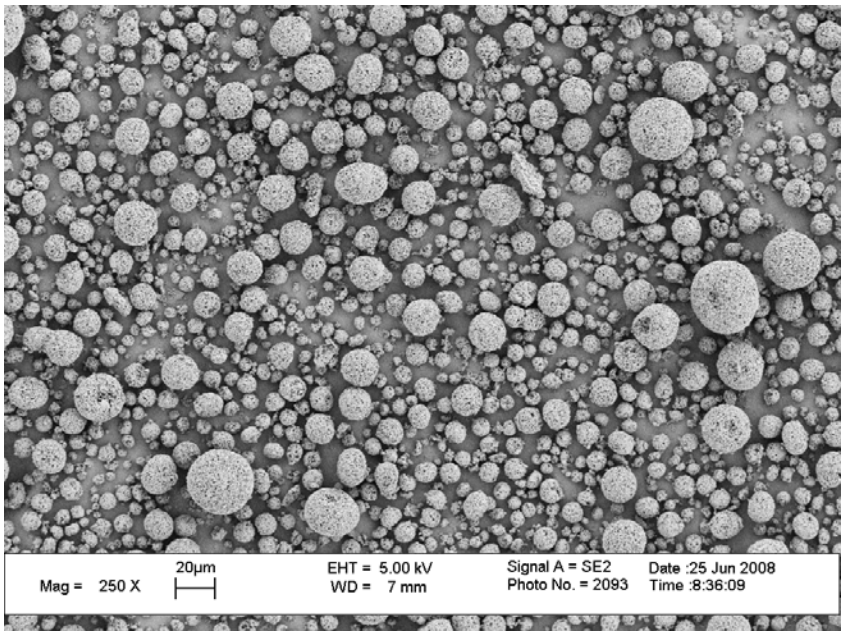


Figure 4.14: The -400 mesh powder fraction from the Büchi spray dryer.

The effect of the PMMA content on the yield of the granules was investigated. Four Mo-3Si-1B wt.% slurries were prepared with PMMA additions of 2, 3, 4 and 5 wt.%. The spray dryer settings were kept constant for each of the slurries to maintain consistency. The total powder yield increased with PMMA content, as did the percentage of granules in the 170-400 mesh size range, Figure 4.15. This was likely due to faster formation of a polymer shell which would prevent the slurry droplet from sticking to the spray dryer walls. The granules with higher PMMA content were also stronger and less prone to breaking in the separation cyclone of the spray dryer.

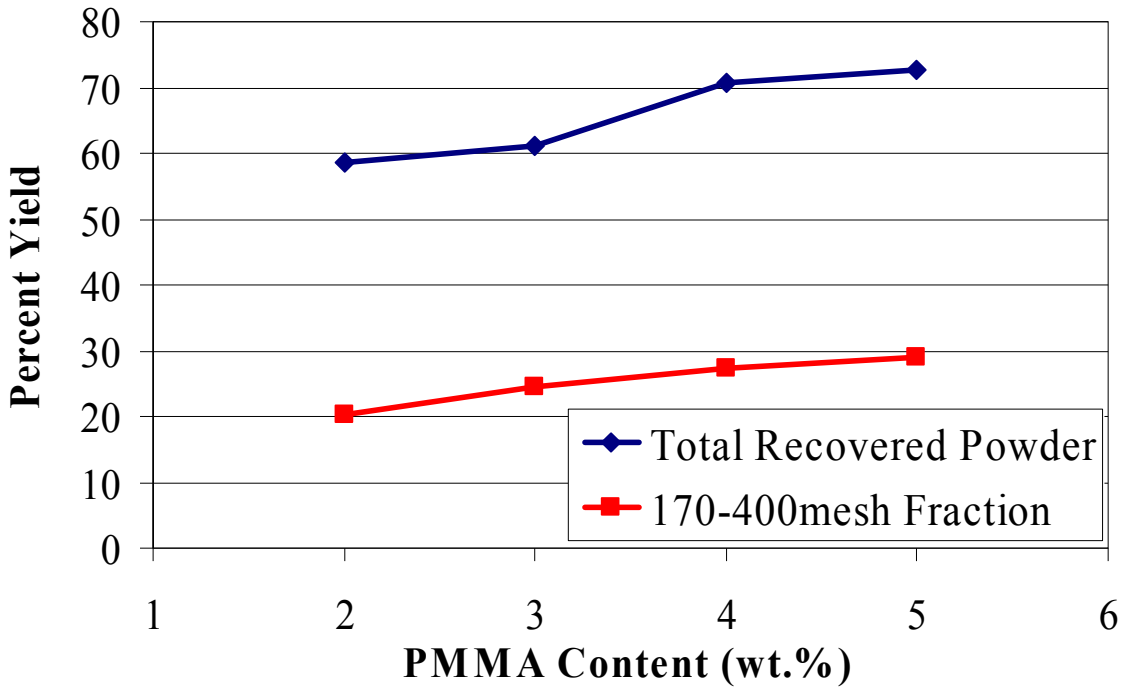


Figure 4.15: Yield of the spray dried powders as a function of the PMMA binder content, using the Büchi spray dryer.

4.2.1.3 Binder Content and Impurity Levels

The relationship between the binder content and the interstitial impurity levels of the sintered samples was investigated. Spray dried granules from the four batches were fired together in Ar/10% $H_2$ to 1600°C with a 6 hour hold. Samples from each batch of the sintered granules were sent to two independent labs for measurement of the oxygen, carbon and nitrogen levels, Dirats Labs (Westfield, MA) and H.C. Starck (Coldwater, MI). The samples sent to each facility were taken from the same powder batches and firing runs to ensure consistency. Additional firings of the 3 and 5 wt.% PMMA powders were conducted to corroborate the measurements. The complete set of carbon and oxygen levels measured by the two laboratories are plotted together in Figure 4.16. The measured impurity levels are also listed in Table 4.2. The nitrogen levels were low, typically in the 10-20 ppm range, and varied little between the different samples and measurements. There was some discrepancy in the oxygen and carbon levels measured by the two different laboratories and there was also a variation in the interstitial levels between different trials, but overall there was little dependence between the carbon and oxygen levels and the PMMA content used. The typical oxygen contents of 200-500 ppm are lower than reported previously for Mo-Si-B alloys produced using powder metallurgy. Low oxygen levels are important for limiting silica inclusions in the microstructure and to reduce the DBTT of molybdenum.

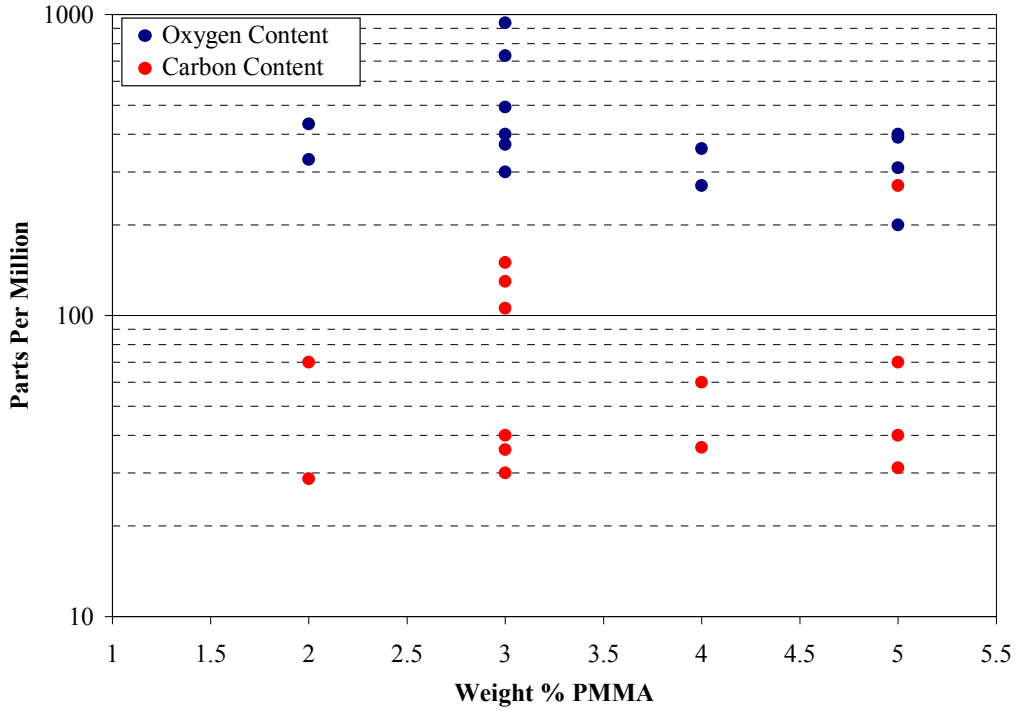


Figure 4.16: Oxygen and carbon impurity levels of Mo-3Si-1B wt.% alloys fired at 1600°C for 6 hours, produced with varying levels of PMMA. The data is combined from measurements from H.C. Starck and Dirats Labs.

Table 4.2: Oxygen, nitrogen and carbon impurity levels of Mo-3Si-1B wt.% alloys fired at 1600°C for 6 hours, produced with varying levels of PMMA binder.

| Measured By | PMMA Content (wt.%) | Oxygen (ppm) | Nitrogen (ppm) | Carbon (ppm) |
|---|---|---|---|---|
| Dirats | 3 | 300 | 20 | 150 |
| Dirats | 5 | 400 | 10 | 40 |
| Dirats | 3 | 400 | 10 | 40 |
| Dirats | 5 | 200 | 20 | 270 |
| Dirats | 2 | 330 | 20 | 70 |
| H.C. Starck | 2 | 433 | 39 | 28.7 |
| Dirats | 3 | 730 | 20 | 130 |
| H.C. Starck | 3 | 938 | 13 | 105.7 |
| Dirats | 4 | 270 | 20 | 60 |
| H.C. Starck | 4 | 359 | 9 | 36.5 |
| Dirats | 5 | 310 | 10 | 70 |
| H.C. Starck | 5 | 391 | 5 | 31.2 |
| Dirats | 3 | 370 | <10 | 30 |
| H.C. Starck | 3 | 493 | 24 | 35.9 |

A relatively small fraction of the spray dried slurry was recovered from the Büchi spray dryer as granules in the desired size range, although up to 90% recovery of the original material was possible by recovering the dried slurry from the drying chamber and the milling media, as well as the coarse and fine fractions screened away from the spherical granules. This material can be reprocessed and spray dried again, but repeated processing may increase the impurity levels. A test was conducted to determine if reprocessing the powder affects the interstitial levels. The fine powder left over after screening was reconstituted with acetone, milled and spray dried again. This powder was fired at 1600°C for 6 hours with a sample of the original spray dried powder and the impurity levels of the two samples were compared, Table 4.3.

There was an increase in the residual oxygen levels as a result of reprocessing. This does not preclude the use of the reprocessed powder, but does underscore the importance of achieving a high powder yield with each spray drying run.

Table 4.3: Impurity contents measured for the 1st run spray dried powders and the reprocessed powders, fired at 1600°C for 6 hours.

| Processing Condition | Oxygen (wt.%) | Carbon (wt.%) | Nitrogen (wt.%) |
|---|---|---|---|
| 1st Run Powder | 0.06 | 0.01 | 0.001 |
| Reprocessed Powder | 0.08 | 0.01 | 0.001 |

4.2.1.4 Final Binder Content Selection

It is important to note that while PMMA represent only a small fraction of the total batch weight, it occupies a large percentage of the material volume. For 2 and 5 wt.%, the PMMA represents 13% and 27% of the spray dried powder volume. Polymeric binders swell during heating and the decomposed monomer creates internal pressure if there is no path to escape. The binder content should be limited to prevent cracking of the powder compacts, but the granules must also be robust enough to survive the cyclonic separator of the Büchi spray dryer. Examination of the powder spray dried with 2 wt.% binder revealed a large number of broken spheres. A binder content of 3 wt.% produced satisfactory granules and was selected for future spray drying. This gave a lower yield than the batches spray dried with 5 wt.% PMMA, but it was deemed more important to minimize the amount of binder necessary to burnout.

**4.2.2 Spray Drying Using Ultrasonic Atomization**

Due to the low yields of the Büchi spray dryer, spray drying based on ultrasonic atomization was evaluated as discussed in Chapter 3.2. The ultrasonic atomization nozzle is reported by the manufacturer to create a narrow size distribution of droplets based on the resonant frequency of the nozzle, although the distribution varies with the viscosity of the fluid. The size distribution of the spray dried spheres produced by the ultrasonic nozzle was investigated for slurries with two different viscosities. Slurries of the Mo-3Si-1B wt.% composition were prepared with 3 wt.% PMMA at 15 and 20 vol.% solids loading. The temperature of the drying chamber was maintained at 75°C and the slurry was atomized at 500mL/hr. The size distributions of the spray dried granules were measured by sieve analysis, Figure 4.17.

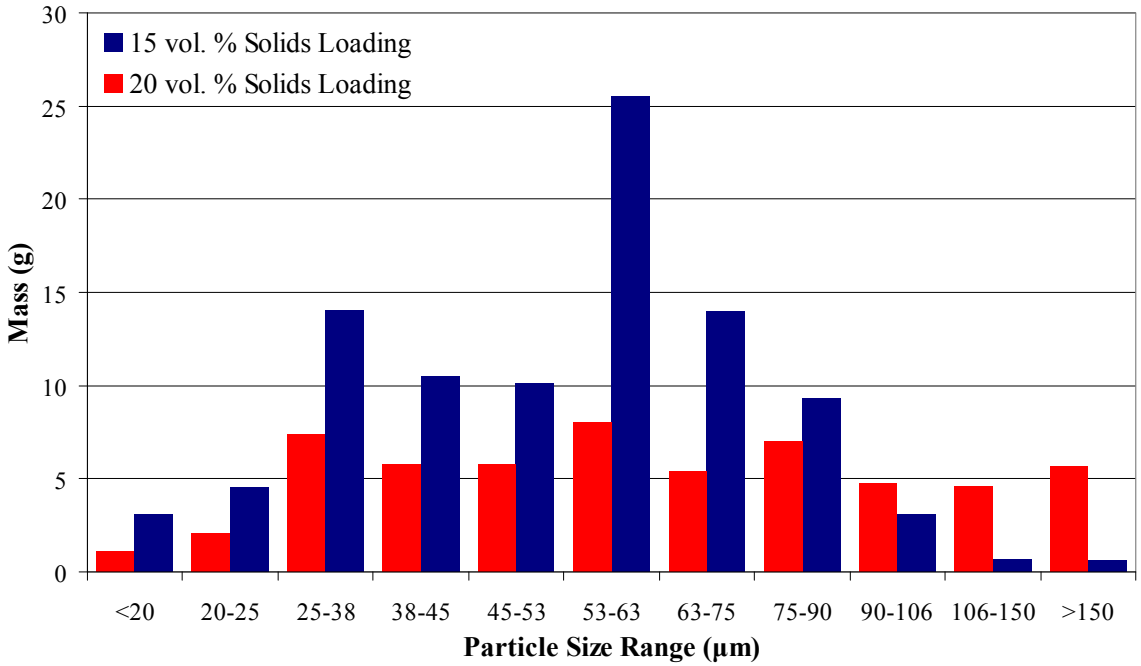


Figure 4.17: Size distributions of granules spray dried from 15 and 20 vol.% slurries using ultrasonic atomization, as determined by sieve analysis.

Higher solids loading increases the rate at which powder is produced, but it lead to a broad size distribution of the spray dried granules. This was due to the high viscosity of the 20 vol.% slurry which inhibited the atomization process. Broad size distributions allow for interstitial packing of the smaller granules and create non-uniform die fill. The 15 vol.% slurry gave a narrower granule size distribution, with an average size of approximately 55µm. An added benefit of the process was that the powder only required screening below 100 mesh (150 µm) prior to use. The powder fines produced by the coaxial nozzle were not present in the ultrasonically atomized powder, Figure 4.18. The ultrasonic spray dryer also significantly increased the powder yield. Over a series of experiments approximately 5kg of powder was spray dried and 90% was recovered as spherical granules in the first pass.

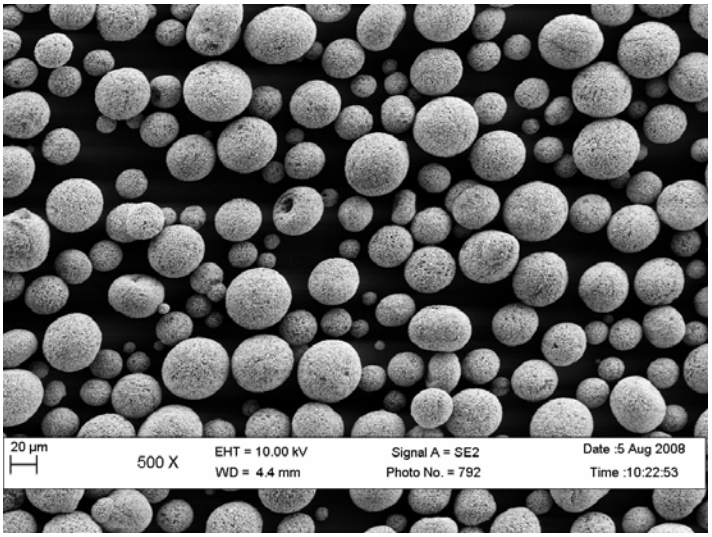

Figure 4.18: Spray dried granules (-100mesh) produced using ultrasonic atomization. No fines are evident in the powder.

### 4.2.3 Investigation of Stearic Acid Lubricant Addition

Stearic acid is commonly used in powder processing as a dry pressing lubricant to improve the green density of powder compacts and to reduce density gradients. The effect of stearic acid addition on green density was investigated for Mo-3Si-1B wt.% powders made with the Cerac HBN powders. Four powder batches were spray dried with 3 wt.% PMMA and different levels of stearic acid addition; 0, 0.3, 0.6 and 0.9 wt.%. Pellets were uniaxially pressed in a ½" die at increasing loads. The volumes of the samples were determined using geometric measurements. Note that the weight of the organic additives has been subtracted from the sample weights so that the calculated densities reflect only the contribution of the reactant powders. Two pellets of each powder were pressed for each pressure and the average green density was plotted as a function of compaction pressure, Figure 4.19. A previous study indicated that the increase in green density as a function of pressure leveled off between 70 and 80ksi. In further studies, 70ksi was set as the upper pressure limit to prevent die breakage.

It can be seen from the comparison of the compaction curves that there was not a consistent trend between the green density and the level of stearic acid addition. The scatter in the data lies mainly within the standard deviation of the individual data points. As no definitive conclusion could be gained from the uniaxially pressed pellets, the effect of stearic acid addition on green density was studied for parts made using cold-isostatic pressing. Two of the powder batches were compared, with 0 and 0.3 wt.% stearic acid. Cylindrical rods of approximately 0.25" diameter were formed in a latex mold. The sample volumes were measured using geometric measurements. After CIPing, the pressed rods were slightly out of round due to the flexible mold. To account for the error, a range of the maximum and minimum possible densities for each sample have been plotted, Figure 4.20.

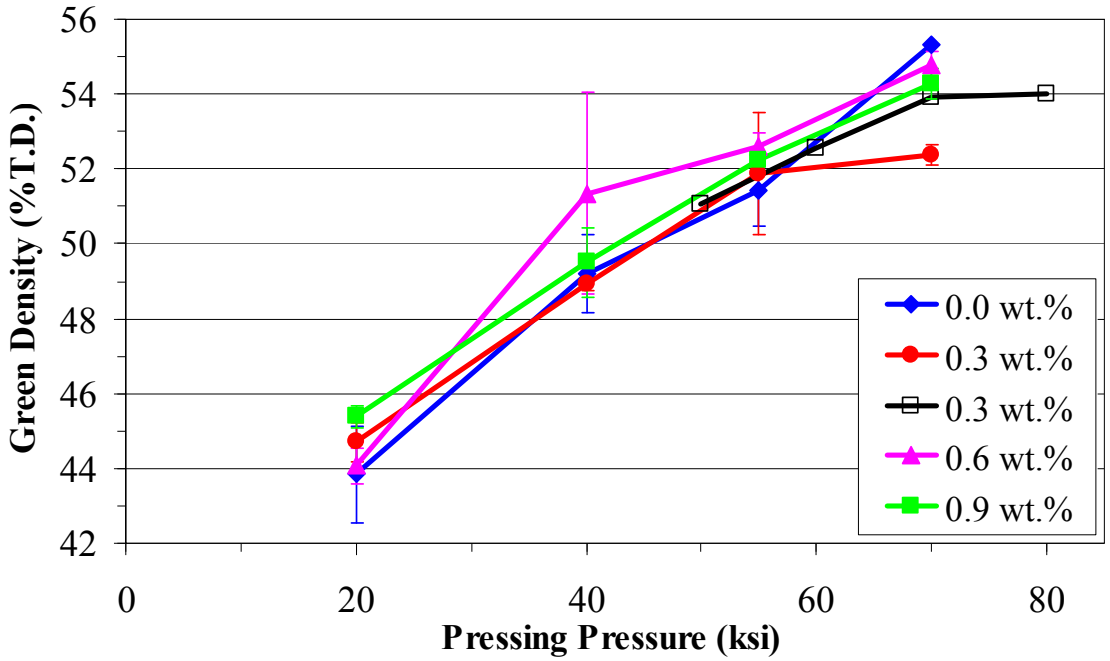


Figure 4.19: Green density comparison for uniaxially pressed pellets with varying levels of stearic acid addition.

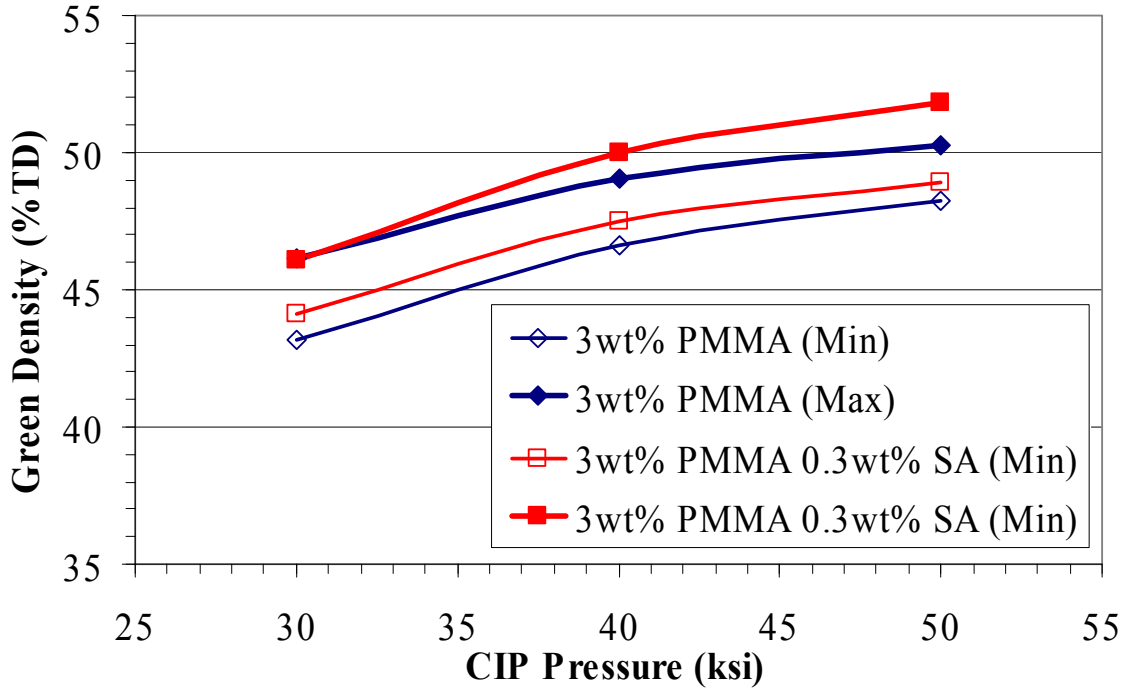


Figure 4.20: Green density comparison of CIPed powders containing 3 wt.% PMMA with and without the addition of 0.3wt.% stearic acid (SA). The curves indicate the possible high and low limits of the densities.

For the CIPed samples, the addition of stearic acid provided a slight improvement in density. The effect of stearic acid addition on the residual oxygen, carbon and nitrogen contents was also examined. Spray dried powders from the four batches were fired together at 1600°C for 6h in Ar/10% $H_2$ and the impurity levels were measured, Table 4.4. The residual oxygen content was found to dramatically increase with increasing stearic acid levels. In light of the modest improvements in green density and the increased oxygen contents, the use of stearic acid as a powder lubricant was discontinued.

Table 4.4: Oxygen, nitrogen and carbon impurity levels of sintered Mo-Si-B alloys produced with varying levels of stearic acid addition.

| Stearic Acid wt.% | Oxygen wt.% | Carbon wt.% | Nitrogen wt.% |
|---|---|---|---|
| 0 | 0.06 | 0.01 | 0.001 |
| 0.3 | 0.33 | 0.01 | 0.002 |
| 0.6 | 0.23 | 0.01 | 0.001 |
| 0.9 | 0.47 | 0.01 | 0.002 |

### 4.2.4 Firing Hold Times and Oxygen Impurity Contents

The effect of the firing schedule on the oxygen impurity content of Mo-3Si-1B wt.% alloys was investigated. The majority of the oxygen in the unfired powder mixture is due to the 1 wt.% present in the molybdenum powder, but molybdenum oxide is reduced at 600-700°C in the Ar/10% $H_2$ sintering atmosphere used. It was discussed in Section 4.1.3 that the nitrides are resistant oxidization though this reduction stage. After heating to ~700°C, the remaining oxygen content in the alloys is from impurities in the nitride powders, which contribute 600ppm oxygen to the system in the form of $SiO_2$ and $B_2O_3$. This value also neglects any oxidation that may have occurred during processing. Despite the high levels, it has been shown that the oxygen levels can be reduced to as low as 200ppm after firing at 1600°C for 6 hours. At high temperatures $B_2O_3$ has a high vapor pressure, and in sufficiently low oxygen partial pressures $SiO_2$ will decompose and evaporate as SiO.

A study was conducted to investigate using long hold times to reduce the oxygen impurity levels. A relatively low temperature was selected for the experiment to limit sintering and prevent the alloy from sealing the borosilicate inclusions from contact with the firing atmosphere. Spray dried powders were fired at 1300°C with up to a 24 hour hold and the residual oxygen levels were measured by Dirats Laboratories, Figure 4.21. Two powders were compared, one prepared with the hBN powder and the other with the 0.5µm cBN powder.

It is evident that the longer hold times effectively reduced the oxygen impurity levels, although much lower levels were achieved at 1600°C due to the higher vapor pressures of $B_2O_3$ and SiO. Continued effort should be completed to optimize firing schedules in order to minimize the residual oxygen levels.

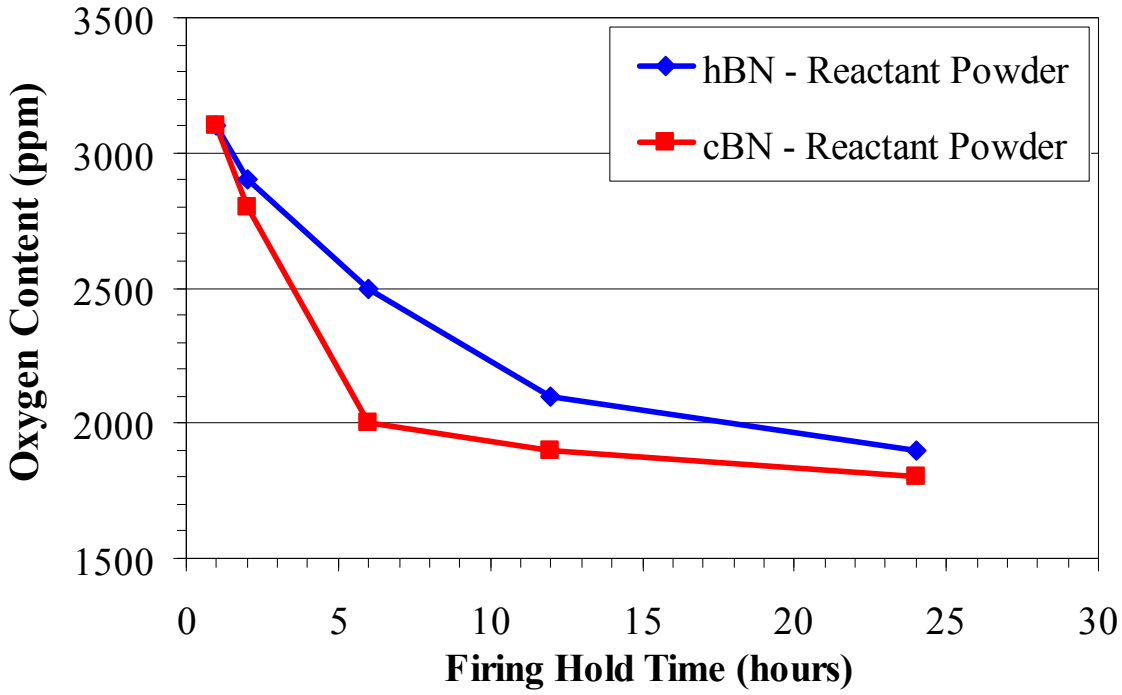


Figure 4.21: Oxygen content of Mo-3Si-1B wt.% alloys as a function of hold time at 1300°C.

### 4.2.5 Complex Shape Formation

The possibility exists to produce Mo-Si-B alloys in near final geometry using the reaction synthesis method and the powder processing techniques presented here. This would reduce the machining necessary to make components and significantly lower production costs. Cold-isostatic pressing of powders can be used to produce complex shapes and techniques exist for producing components with internal geometries using sacrificial cores.

An attempt was made to demonstrate complex shape formation using the CIP method. A latex bag mold modeled after a turbine blade was use as the test article (Trexler Rubber, Ravenna, OH). The mold was filled with spray dried Mo-3Si-1B wt.% powder, CIPed at 50ksi and then fired to 1600°C for 6 hours. The sintered turbine blade is shown in Figure 4.22. The blade was formed and sintered with little distortion. The sharp corners present on the original model were maintained on the Mo-Si-B blade. The magnified image demonstrates that fine details are preserved during the formation process. Small, ~1mm lettering present in the latex mold was transferred to the CIPed part. This was only a simple proof of concept test piece, but it demonstrates the complexity of the parts that could be formed by this method.

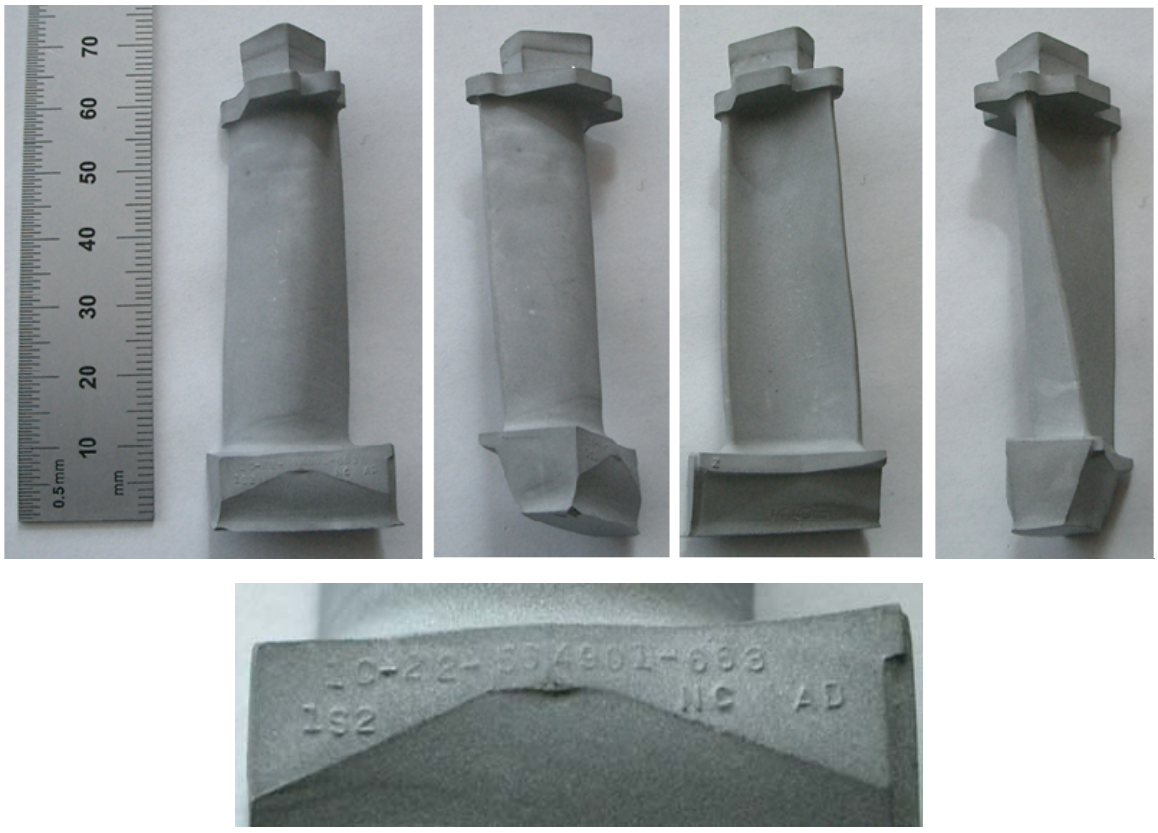


Figure 4.22: A Mo-3Si-1B wt.% alloy turbine blade produced by cold-isostatic pressing.

## 4.3 Sintering of Mo-Si-B Alloys

### 4.3.1 Pressureless Sintering

The densification of Mo-Si-B alloys produced by the reaction synthesis method was compared for the compositions Mo-3Si-1B wt.% (~ 57 vol.% $Mo_{ss}$) and Mo-2.2Si-0.74B wt.% (~ 70 vol.% $Mo_{ss}$). All of the alloys in this section were prepared with the hBN powder. Pellets were uniaxially pressed at 70ksi in a 0.5" die and fired between 1200°C and 1600°C with 6 hour holds at each set point. The densities of the fired samples were measured using Archimedes method. Two samples of each composition were fired for every temperature and the average values are plotted in Figure 4.23. The standard deviations of the densities fall within the data points marked on the plot.

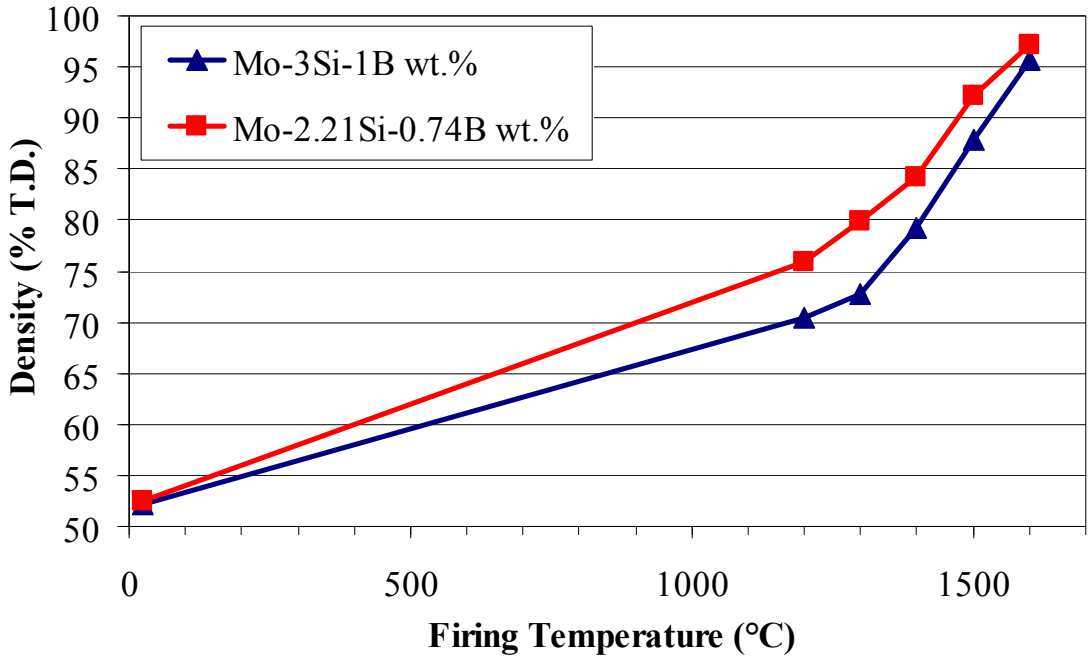


Figure 4.23: Densities of Mo-3Si-1B wt.% and Mo-2.21Si-0.74B wt.% alloys fired in Ar/10% $H_2$ with a 6 hour hold at each temperature. The standard deviations of the measurements fall within the data points on the plot.

The composition with higher $Mo_{ss}$ fraction consistently achieved higher densities at each temperature. This indicates that densification is inhibited by the presence of the intermetallic phases. This is to be expected given the poor sintering observed for the intermetallic phases, the T2 phase in particular. Ultimately both compositions achieved relative densities above 95% of theoretical at the maximum furnace temperature of 1600°C. The sintering curves have not leveled off and increasing the firing temperature would result in higher densities, however this would also increase grain growth.

A BSE image for the Mo-3Si-1B wt.% alloy fired at 1600°C for 6 hours is shown in Figure 4.24. The $Mo_{ss}$ phase as lighter than the intermetallic phases but there is not enough contrast to distinguish between A15 and T2. Porosity and silica inclusions appear black. It can be seen from the micrograph that the reaction synthesis method creates a fine dispersion of intermetallics in a mostly contiguous $Mo_{ss}$ matrix.

Hot-isostatic pressing was used to fully densify the alloys while maintaining the fine grain size. Two specimens of composition Mo-3Si-1B wt.% were pre-fired at 1600°C for 6 hours. The specimens were HIPed without encapsulation at 1400°C and 30ksi for six hours and achieved near theoretical density. Encapsulation is only required for samples with continuous open porosity. The surface connected porosity in sintered compacts typically becomes discontinuous at approximately 94% T.D. The densities before and after HIPing are compared in Table 4.5.

Table 4.5: Density improvements from HIPing at 1400°C and 30ksi for 6 hours, for samples pre-fired at 1600°C for 6 hours.

| **Sintered 1600°C, 6h** | | **HIP 1400°C, 30ksi, 6h** | |
|---|---|---|---|
| Density (g/cc) | Open Porosity (%) | Density (g/cc) | Open Porosity (%) |
| 93.9 | 0.6 | 99.8 | 0.0 |
| 94.2 | 0.0 | 99.1 | 0.0 |

The microstructure of the HIPed Mo-3Si-1B wt.% alloy is shown in Figure 4.25. The few fine black spots present were identified as silica inclusions by EDS analysis. The residual porosity has been eliminated and there does not appear to be any significant grain growth due to HIPing. The ability to achieve full theoretical density through the powder processing route opens the possibility of complex shape formation. Furthermore, the microstructure of the alloy continues uninterrupted to the edge of the sample which reduces the need for machining operations, Figure 4.26. This is a significant improvement over samples produced in the early development of the reaction synthesis process where an approximately 100μm thick 'skin' was observed on the surface of the samples, Figure 4.27 [9]. The skin formation was found to be the result of oxygen impurities in the firing atmosphere. When the Mo-Si-B alloys are dense they form a layer which protects against oxidation, but open porosity present during the early stages of sintering allows for internal oxidation of the nitrides and intermetallic phases. This illustrates the importance of maintaining very low oxygen contents during firing.

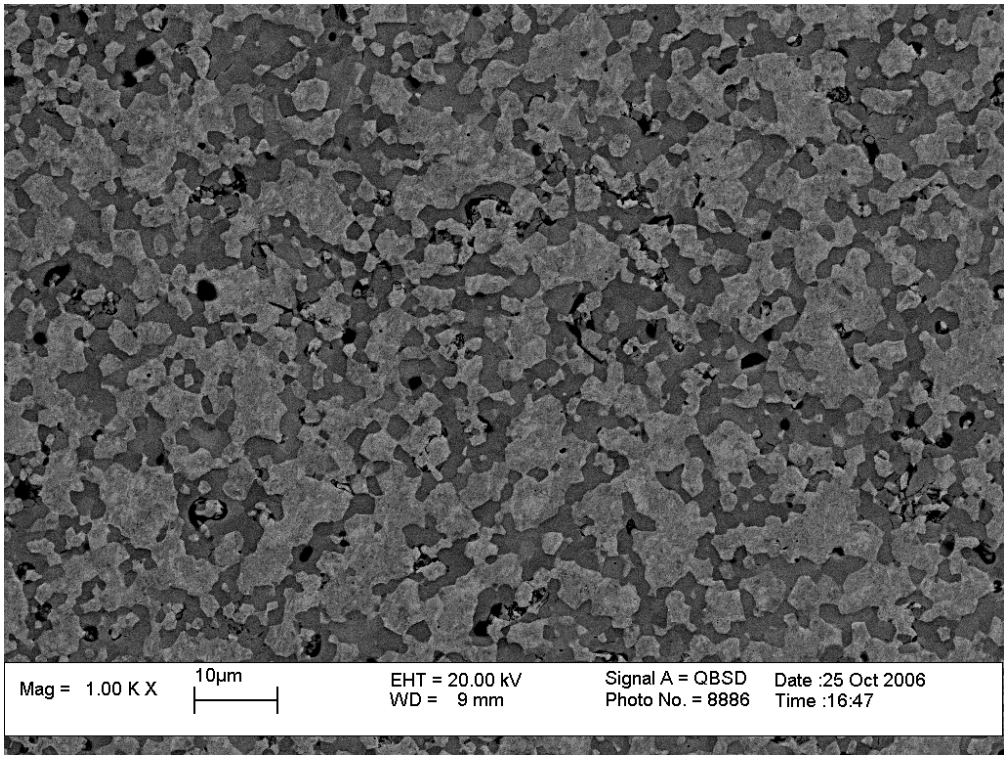

Figure 4.24: Microstructure of a Mo-3Si-1B wt.% alloy fired at 1600°C for 6 hours.

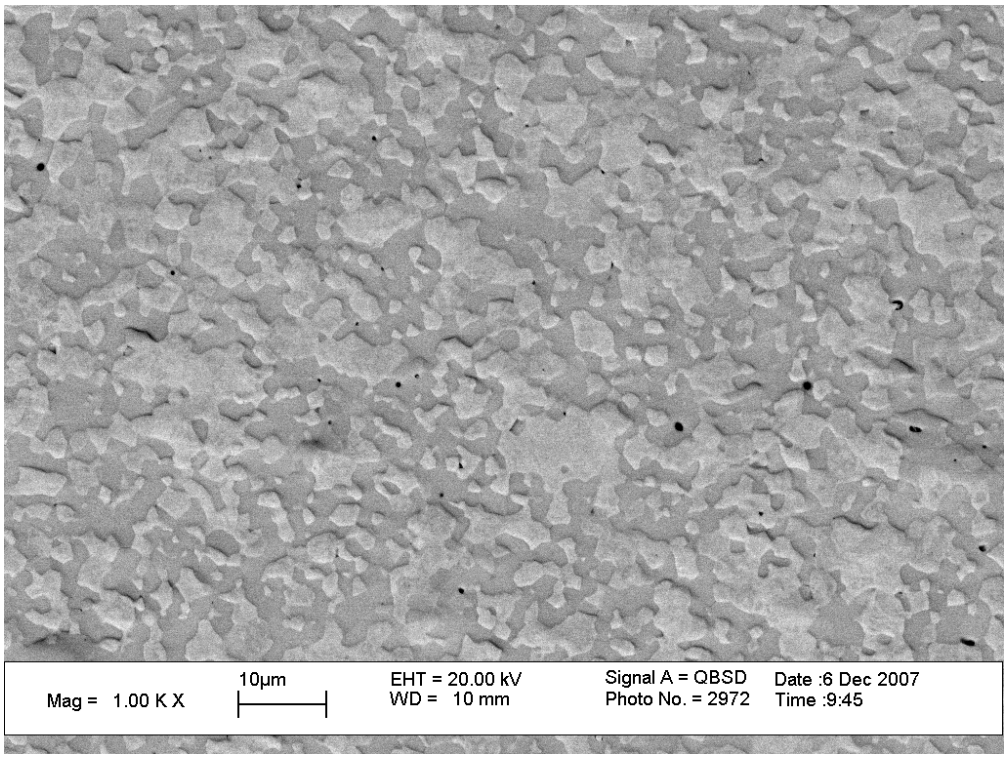

Figure 4.25: Microstructure of a Mo-3Si-1B wt.% alloy fired at 1600°C for 6 hours, and hot-isostatically pressed at 1400°C and 30ksi for 6 hours.

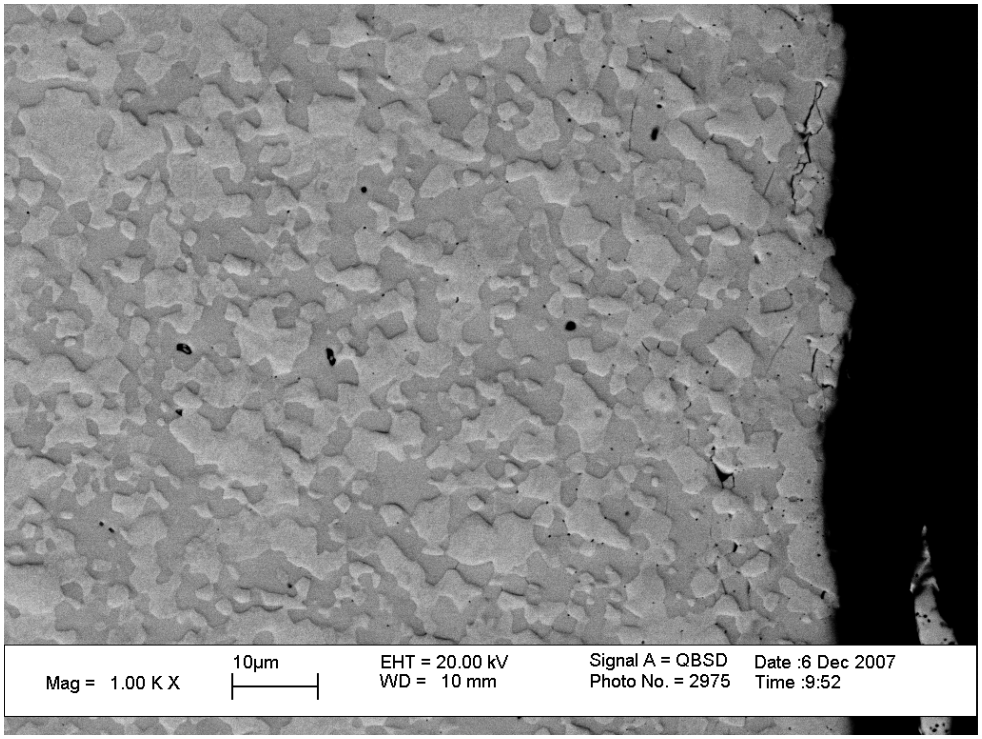


Figure 4.26: Surface of a Mo-3Si-1B wt.% alloy fired at 1600°C for 6 hours, and hot-isostatically pressed at 1400°C and 30ksi for 6 hours.

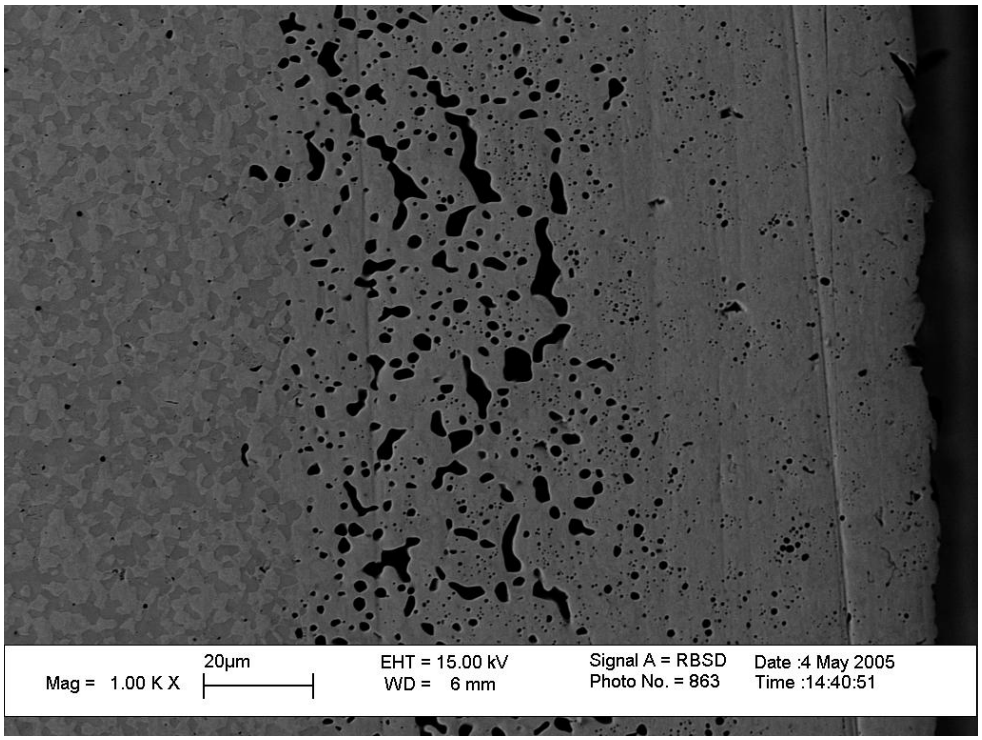


Figure 4.27: An example of the 'skin' formed on sample surfaces due to sintering with trace amounts of oxygen present in the firing atmosphere.

4.3.1.1 Low-Temperature Sintering to Reduce Grain Growth

A review of the literature reveals that the reaction synthesis approach creates Mo-Si-B alloys with finer grained microstructures than nearly all previously reported methods. The typical firing schedule used in this project was 3°C/min to 1600°C with a 6 hour hold. The ability to complete the reactions at temperatures as low as 1300°C presents an opportunity to create even finer microstructures. Sintering at various temperatures and hold times was investigated for the Mo-3Si-1B wt.% alloy in an attempt to identify firing schedules that would minimize grain growth while still achieving discontinuous porosity. Avoiding encapsulation for HIPing aids the transition from simple geometries to complex shapes. It was previously demonstrated that the reactions to form the intermetallic phases are complete after 6 hours at 1300°C. Further investigation revealed that the reactions could be completed in only 2 hours. Sintering curves were compiled for samples fired with 2 and 24 hour holds between 1300°C to 1600°C and compared to the previous firings with 6 hour holds. Two samples were fired for each temperature and hold time and the average densities are plotted in Figure 4.28. The standard deviation of the densities fall within the data points marked on the plot.

There was not a change in the density of the samples at 1300°C between the 2 and 24 hours. This indicates that the densification observed between the green state and 1300°C is likely due to the reaction of the nitrides. It is apparent from this study that sintering at 1600°C is required to achieve the ~94% density required for HIPing without encapsulation. The microstructures of the samples fired with 2 hour hold times are compared in Figure 4.29. The 1300°C, 2 hour firing resulted in very fine intermetallics which are close in size to the original starting materials. A comparison of the samples

fired with 6 and 24 hour holds reveals significant grain growth, Figure 4.30. Qualitatively, the grain sizes of the samples held at temperature for 24 hours appear roughly equivalent to those fired at 100°C higher for only 6 hours. It was concluded that hold times longer than 6 hours resulted in significant grain growth without much benefit to the density. Based on this initial examination it appears that in order to densify the alloys while limiting grain growth, firing at higher temperatures with short hold times is preferable to extended low temperature firings.

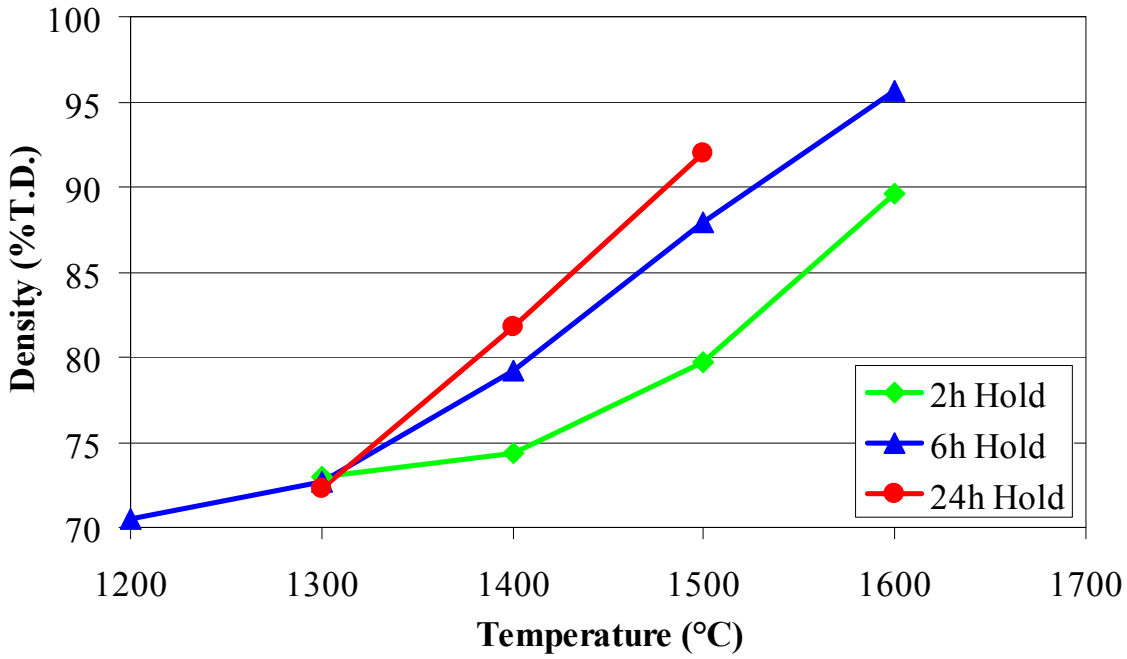


Figure 4.28: Densities of the Mo-3Si-1B wt.% alloy fired in Ar/10% $H_2$ with 2, 6 and 24 hour holds at each temperature. The standard deviations of the measurements fall within the data points on the plot.

1300°C – 2h Hold

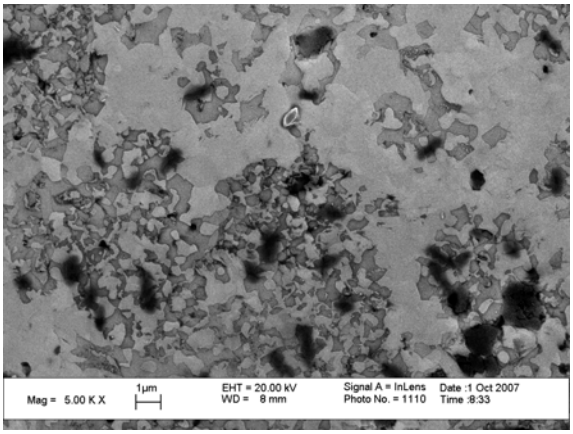


1400°C – 2h Hold

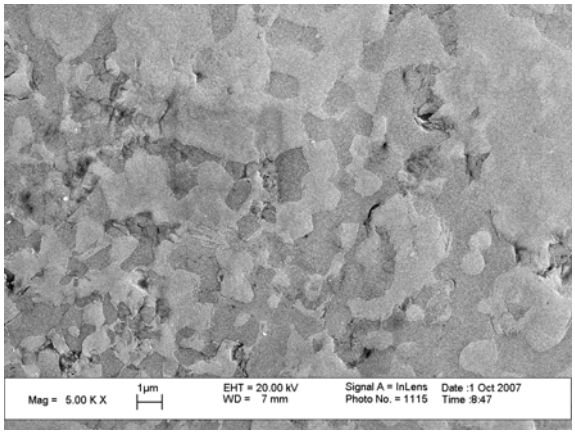


1500°C – 2h Hold

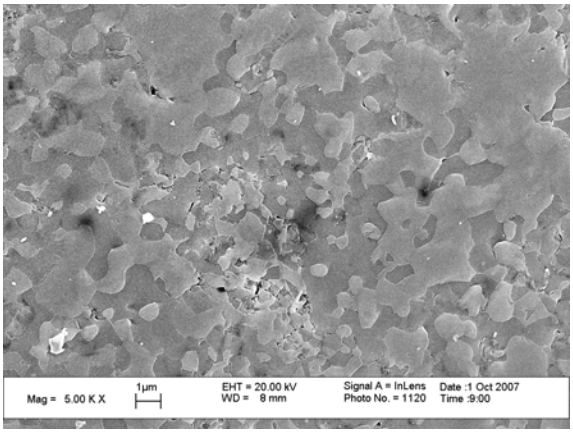


1600°C – 2h Hold

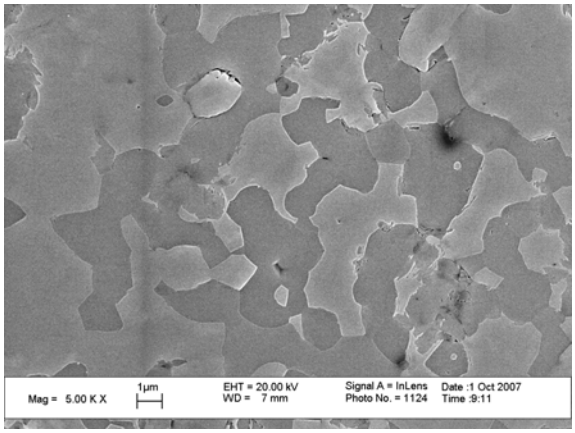


Figure 4.29: Microstructure comparison of Mo-3Si-1B wt.% samples fired between 1200°C and 1600°C with 2 hour hold times.

1300°C – 6h Hold

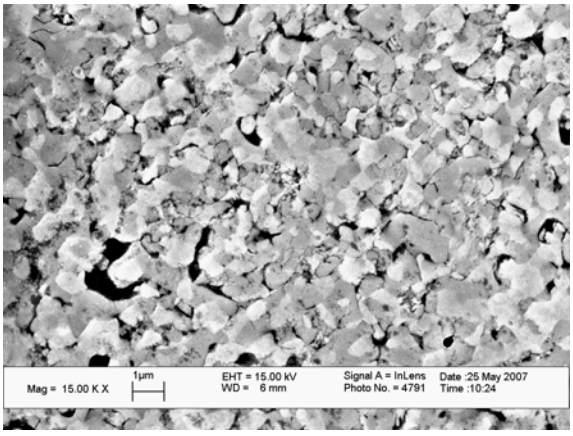


1300°C – 24h Hold

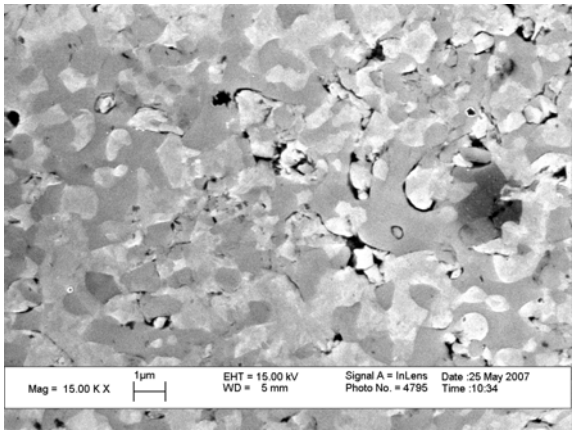


1400°C – 6h Hold

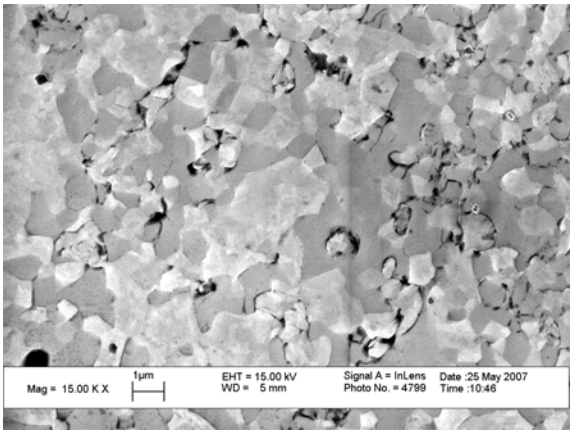


1400°C – 24h Hold

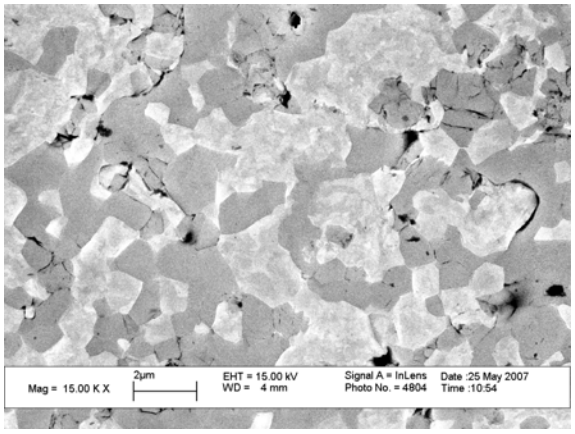


1500°C – 6h Hold

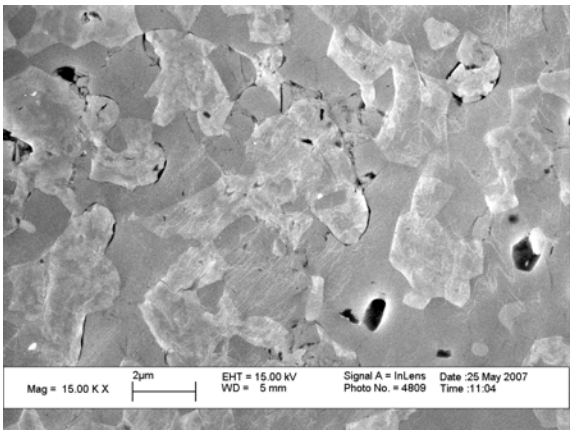


1500°C – 24h Hold

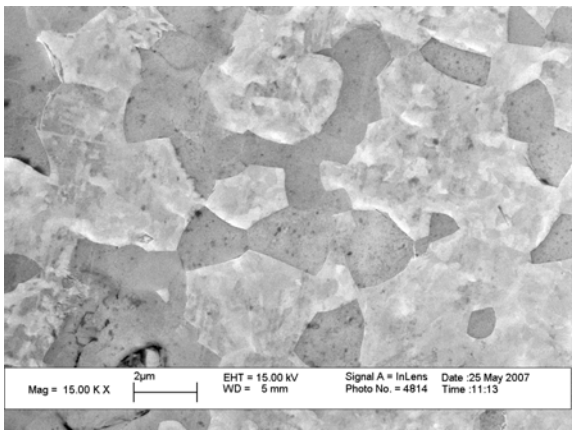


Figure 4.30: Microstructure comparison of Mo-3Si-1B wt.% samples fired between 1300°C and 1500°C with 6 and 24 hour hold times.

### 4.3.2 Grain Size and HIP Temperature

It was previously demonstrated that hot-isostatic pressing at 1400°C is sufficient to achieve theoretical density, Table 4.5. A trial was conducted to determine if the alloys could be consolidated by HIPing at even lower temperatures to minimize the grain size. Samples of composition Mo-3Si-1B and Mo-2Si-1B wt.% were pre-fired at 1300°C for 2 hours which produced intermetallic regions in the 0.5-1μm range, Figure 4.29. Encapsulation of the samples was required due to the high level of open porosity. The samples were sealed in evacuated low-carbon steel canisters and HIPed at 1300°C and 30ksi for 6 hours. A coarse aluminum oxide powder was used to prevent contact between the samples and the canister. The resulting alloys had very fine microstructures as compared to corresponding samples fired at 1600°C, Figure 4.31 and Figure 4.32. Some residual porosity was present, but it is possible that full density could be achieved with slightly higher temperatures, higher pressures or longer hold-times.

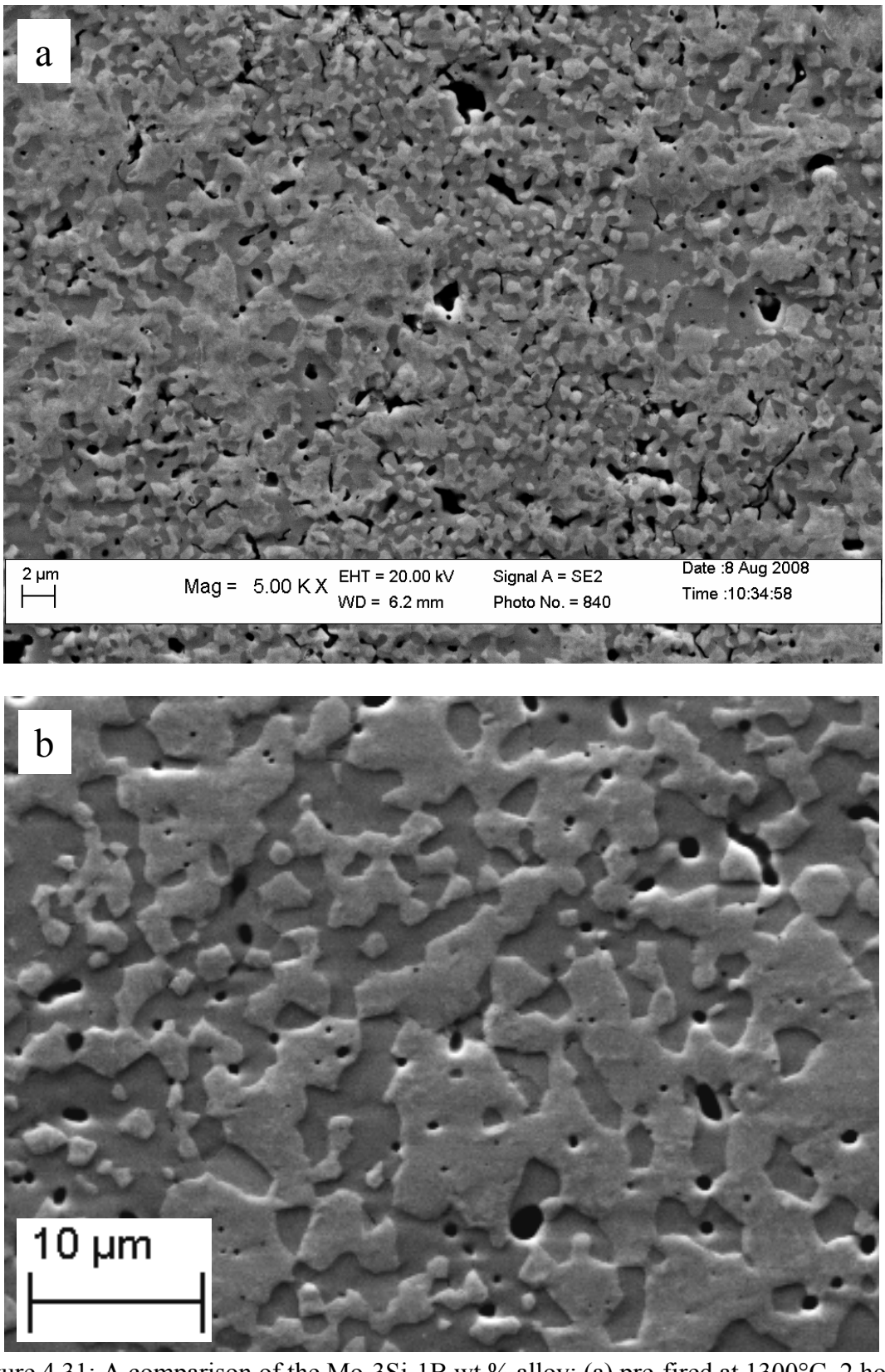


Figure 4.31: A comparison of the Mo-3Si-1B wt.% alloy: (a) pre-fired at 1300°C, 2 hours and HIPed at 1300°C, 6 hours and (b) pre-fired at 1600°C, 6 hours and HIPed at 1500°C.

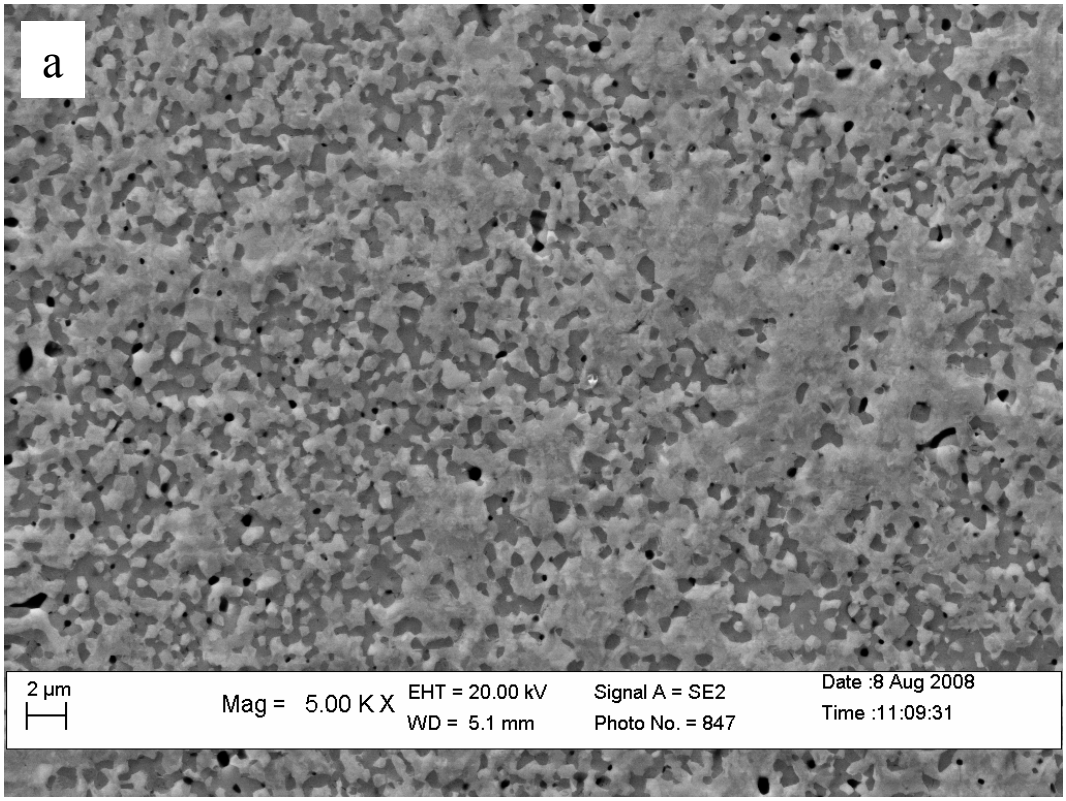


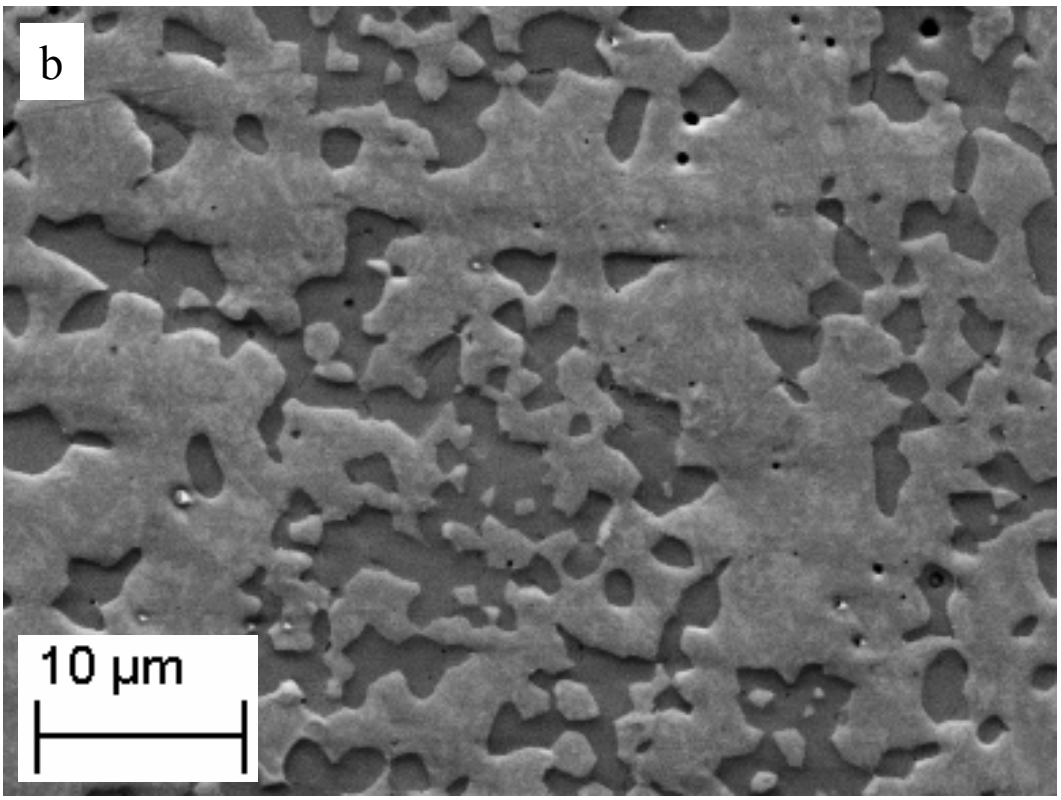


Figure 4.32: A comparison of the Mo-2Si-1B wt.% alloy: (a) pre-fired at 1300°C, 2 hours and HIPed at 1300°C, 6 hours and (b) pre-fired at 1600°C, 6 hours and HIPed at 1500°C.

### 4.3.3 Variation of Intermetallic Content

The properties of Mo-Si-B alloys are highly dependent on microstructure and the selection of an alloy composition for a given use will be a compromise between the mechanical properties and the service life of the component. High intermetallic contents improve oxidation resistance, but at the expense of toughness. It has been shown that the processing route developed creates a mostly contiguous $Mo_{ss}$ matrix, even for the Mo-3Si-1B wt.% alloy with only ~57 vol.% $Mo_{ss}$. An investigation was conducted on alloys with increasing $Mo_{ss}$ content to determine if the intermetallics remain present as a fine dispersion, which may be necessary for good oxidation resistance.

Five Mo-Si-B compositions were prepared with varying silicon and boron contents, ranging from 1.91 to 3 wt.% Si and 0.64 to 1 wt.% B. The silicon to boron ratio was kept at a constant 3:1 ratio in all of the compositions and the $Mo_{ss}$ matrix phase contents were varied from 57-75 vol.%, as estimated from the phase diagram. Powder slurries for the five compositions were prepared and processed in an identical manner to eliminate possible variations in microstructure due to processing. The slurries were mixed on the paint shaker for 30 minutes and immediately spray dried. Half inch pellets were uniaxially pressed at 70ksi. The samples were fired together at 1600°C with a 6 hour hold in Ar/10%$H_2$, followed by a post-sintering HIP step at 1500°C and 30ksi for 6 hours. The densities of the samples were measured before and after HIPing using Archimedes method. After the intial firing almost zero open porosity was detected, allowing the samples to be HIPed without encapsulation. Figure 4.33 plots the densities of the samples after both pressureless sintering and HIPing. The occurrence of values slightly greater than 100% of theoretical density is the result of either slight errors in the

calculation of the theoretical densities or variations from the expected phase fractions. The shrinkages of the samples from the green to the fully dense state were found to be mostly independent of the composition, Figure 4.34.

The microstructures of the five compositions were observed using BSE imaging, Figure 4.35. It can be seen from the micrographs that the reaction synthesis method creates a fine dispersion of intermetallics over the range of compositions, with the matrix continuity increasing with the molybdenum content.

The volume fractions of the constituent phases were measured by quantitative XRD phase analysis using the program MAUD. The software determines the relative phase fractions using the Rietveld method, which is a least-squares approach that refines a theoretical profile until it matches the measured profile. The volume percentages measured for the five compositions are compared to those estimated from the phase diagram in Table 4.6. The quantities *sigma* and $R_w$ are indicators used to describe the quality of the fit between the calculated and measured diffraction profiles. It has been suggested by the developer of MAUD that values of *sigma*<2 and $R_w$<15 are appropriate. Relatively good fits were achieved for each of the refinements and there is a close match between the phase contents estimated from the phase diagram and those measured by the Rietveld refinements, with the values differing by less than 3%. The best way to evaluate the quality of the refinement is to simply compare the measured and calculated XRD patterns from the quantitative XRD analysis, Figure 4.36. The two patterns are overlaid and compared in a difference plot, which show only small differences between the two profiles. This comparison is from the analysis of the Mo-3Si-1B wt.% composition, but the quality of the fit is representative of those achieved for the other compositions.

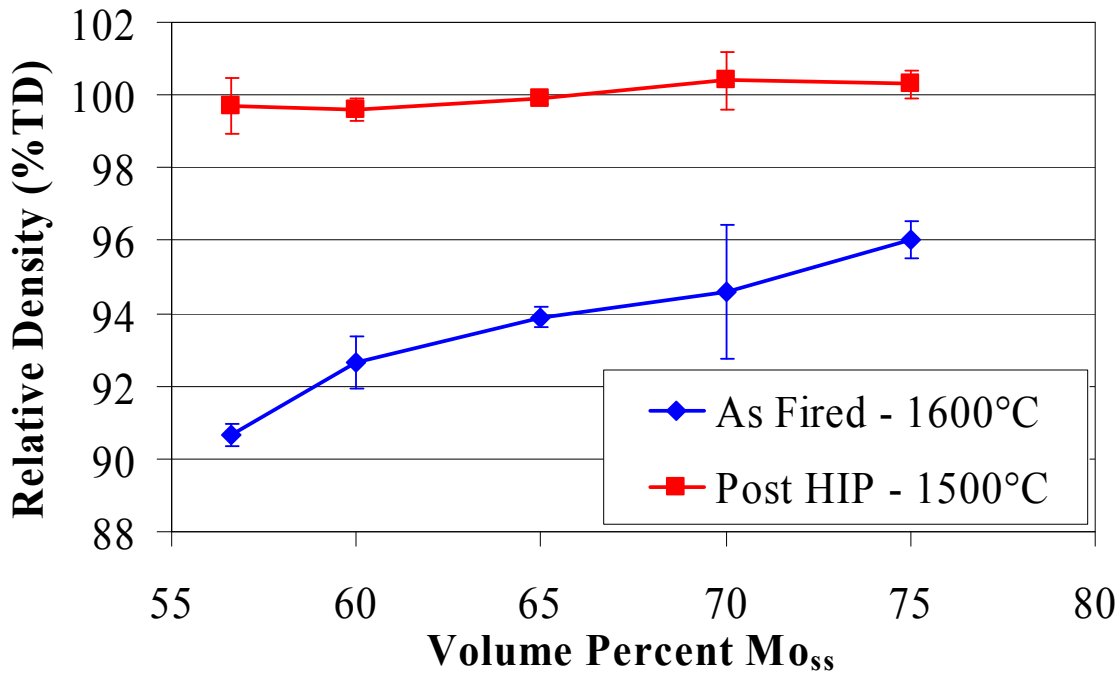


Figure 4.33: Comparison of the densities achieved for Mo-Si-B samples with a varying fraction of $Mo_{ss}$, after pressureless sintering (1600°C, 6h) and after a post-sinter HIP cycle (1500°C, 30ksi, 6h).

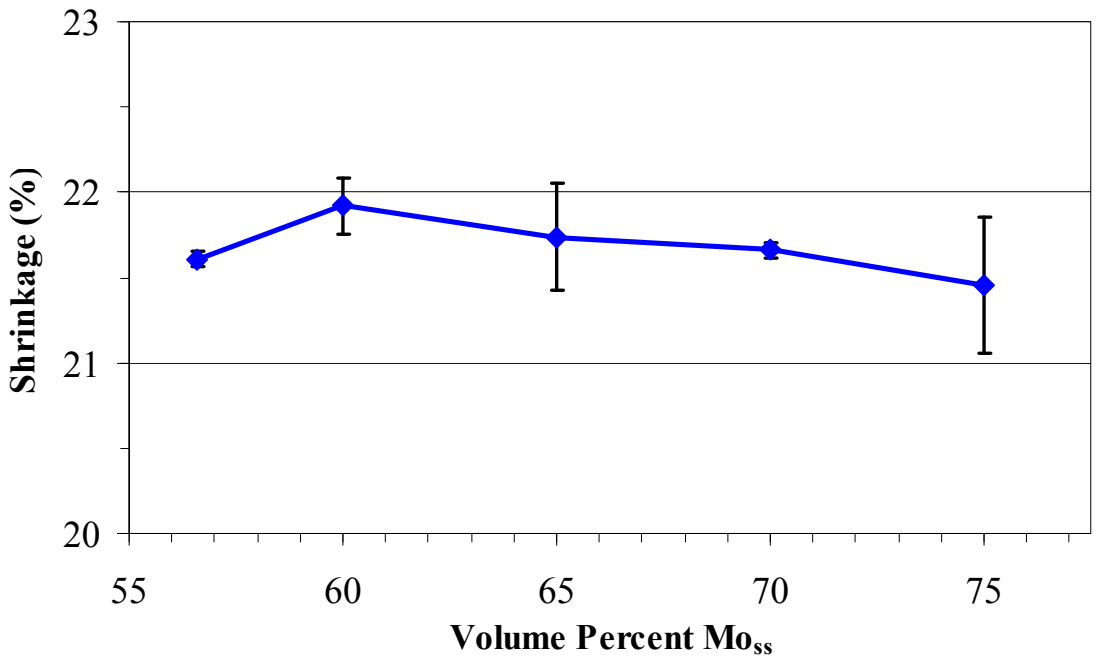


Figure 4.34: The total shrinkage of Mo-Si-B samples with a varying fraction of $Mo_{ss}$, measured from the green to fully densified states.

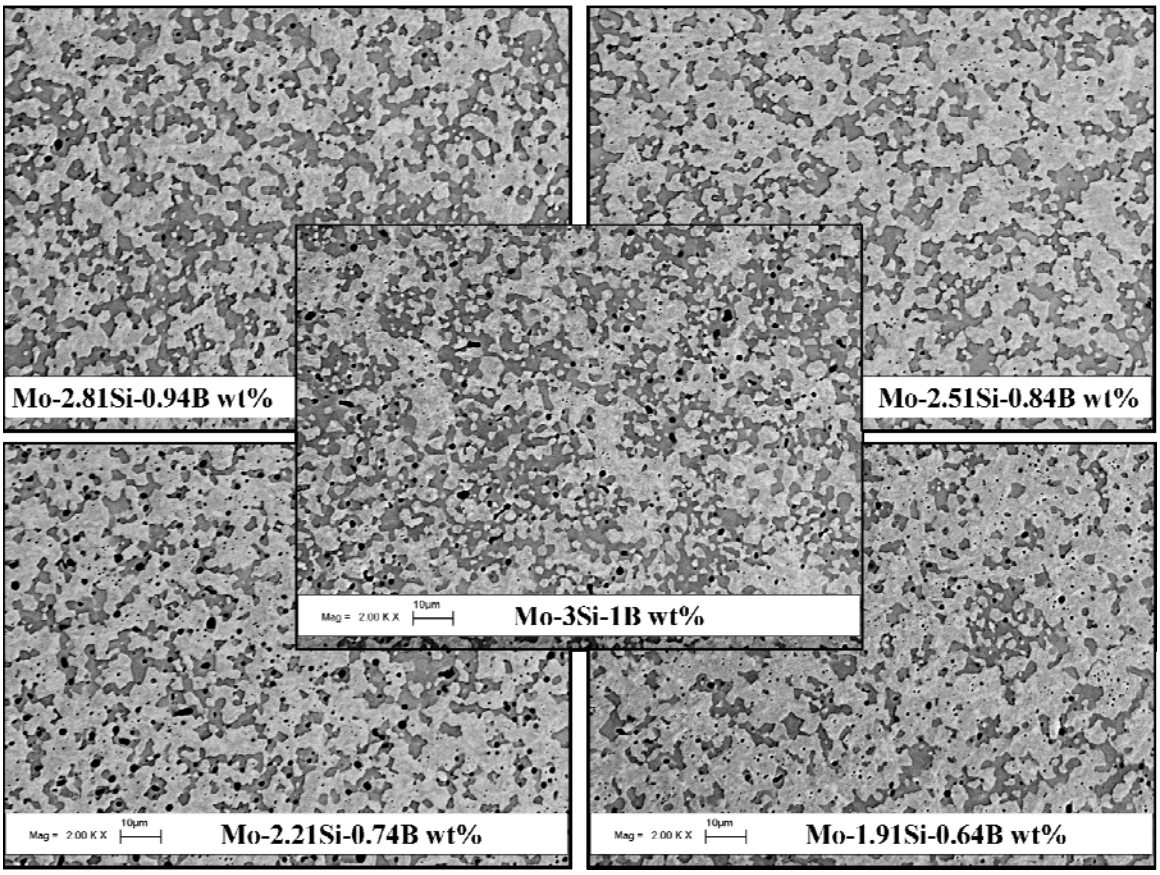

Figure 4.35: SEM backscatter images of Mo-Si-B alloys with a constant 3:1 silicon to boron weight ratio, varying in composition from 1.91 to 3 wt.% Si and 0.64 to 1 wt.% B.

The solubility limits at 1600°C for the three constituent phases were factored into the calculations of the phase fractions from the phase diagram, but the stoichiometric compositions of Mo, $Mo_3Si$ and $Mo_5SiB_2$ were used in the Rietveld refinements because modeling the solid solutions requires more in depth knowledge of the lattice substitution sites. Continued work should completed to improve the crystallographic models used for Rietveld refinement to achieve more accurate quantitative data; however at the current level of analysis there was good agreement between the phase fractions calculated from the phase diagram compatibility triangle and the quantitative XRD analysis.

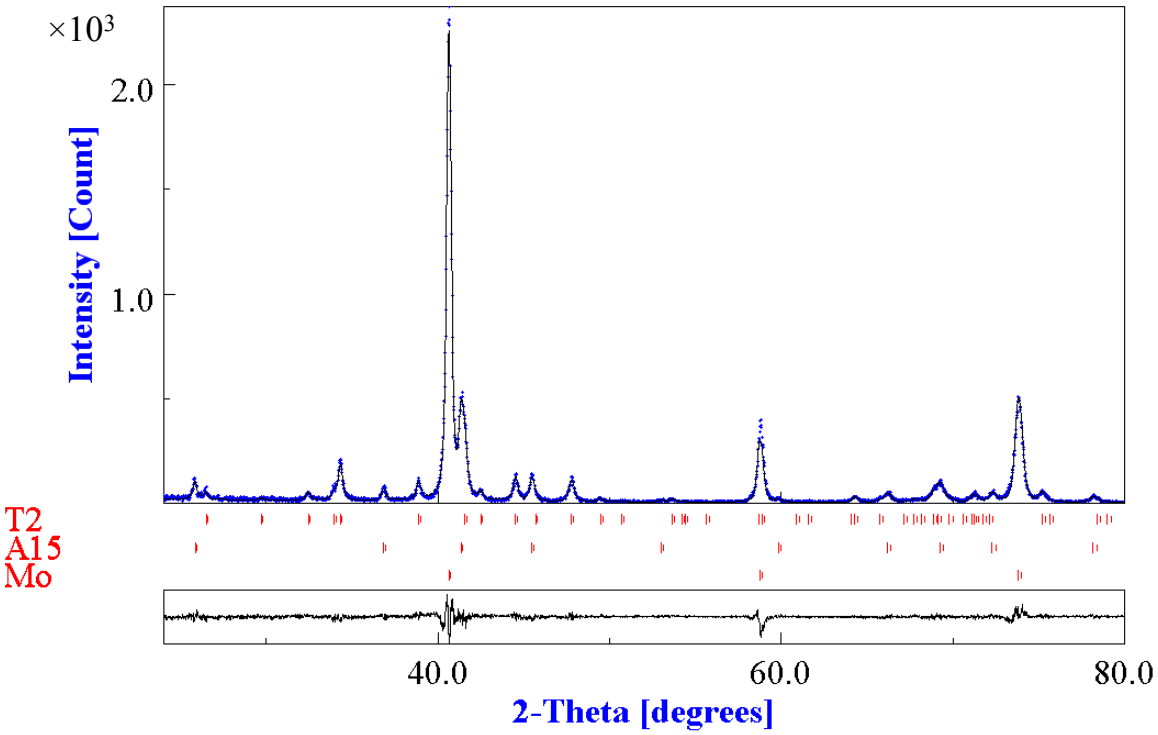


Figure 4.36: Rietveld refinement screenshot from MAUD with the measured (blue) and calculated (black) diffraction profiles overlaid and compared in a difference plot. The peak locations are indicated.

Table 4.6: Comparison of the phase contents calculated from the phase diagram to those measured using quantitative XRD analysis. Low *sigma* and $R_w$ values indicate good fits were achieved between the experimental and calculated diffraction patterns.

| Mo-3Si-1B wt.% | | | | |
|---|---|---|---|---|
| | **Phase Diagram Vol.%** | **Rietveld Vol.%** | **Sigma** | **$R_w$ (%)** |
| **$Mo_{ss}$** | 56.8 | 55.9 | | |
| **A15** | 16.0 | 17.9 | 1.1 | 16.1 |
| **T2** | 27.2 | 26.2 | | |

| Mo-2.81Si-0.94B wt.% | | | | |
|---|---|---|---|---|
| | **Phase Diagram Vol.%** | **Rietveld Vol.%** | **Sigma** | **$R_w$ (%)** |
| **$Mo_{ss}$** | 59.9 | 60.0 | | |
| **A15** | 14.6 | 17.2 | 1.2 | 16.0 |
| **T2** | 25.6 | 22.8 | | |

| Mo-2.51Si-0.84B wt.% | | | | |
|---|---|---|---|---|
| | **Phase Diagram Vol.%** | **Rietveld Vol.%** | **Sigma** | **$R_w$ (%)** |
| **$Mo_{ss}$** | 64.8 | 66.2 | | |
| **A15** | 12.2 | 12.8 | 1.2 | 16.3 |
| **T2** | 23.0 | 21.0 | | |

| Mo-2.21Si-0.74B wt.% | | | | |
|---|---|---|---|---|
| | **Phase Diagram Vol.%** | **Rietveld Vol.%** | **Sigma** | **$R_w$ (%)** |
| **$Mo_{ss}$** | 69.8 | 70.9 | | |
| **A15** | 9.8 | 7.6 | 1.2 | 16.6 |
| **T2** | 20.4 | 21.5 | | |

| Mo-1.91Si-0.64B wt.% | | | | |
|---|---|---|---|---|
| | **Phase Diagram Vol.%** | **Rietveld Vol.%** | **Sigma** | **$R_w$ (%)** |
| **$Mo_{ss}$** | 74.9 | 76.2 | | |
| **A15** | 7.4 | 5.4 | 1.2 | 17.1 |
| **T2** | 17.7 | 18.4 | | |

# CHAPTER 5

# MICROSTRUCTURAL MANIPULATION AND EVALUATION

The powder metallurgy approach developed creates an opportunity to optimize microstructural features through changes in starting materials and processing conditions. Investigations were made to understand the relationships between processing parameters and the achieved microstructures. The effect of the size and morphology of the boron nitride reactant powder on the dispersion of the T2 phase was examined. The microstructures of alloys with varying intermetallic contents were also investigated. EBSD imaging was used to elucidate the distributions of the individual intermetallic phases and to create high-quality microstructure maps suitable for automated image analysis. A variety of methods were used to quantify the distribution of the phases.

## 5.1 Electron Backscatter Diffraction Imaging

BSE imaging provides a simple means to investigate the microstructure of Mo-Si-B alloys, but does not provide adequate contrast to differentiate between the A15 and T2 phases. The lack of contrast also prevents the use of automated image analysis. Attempts were made to quantify the microstructures in terms of a two-phase mixture of the $Mo_{ss}$ and intermetallics regions. The separation of the phases is visually apparent, but the image must be converted to binary form for use with image analysis software. Using the imaging software package ImageJ, it was not possible to adjust the threshold values of the brightness and contrast to create binary images which accurately represented the

microstructures. The grain boundaries are also not visible in the BSE images, which prevents determination of the grain sizes. Electron backscatter diffraction (EBSD) imaging was used to avoid the ambiguity of the BSE micrographs. EBSD analysis identifies the phase and the crystallographic orientation at each point in the microstructure and accurately plots the phase and grain boundaries of all three phases. This eliminates the difficulties with thresholding the BSE images and simplifies image analysis. EBSD analysis was also used to measure the volume fractions and grain size distributions of the three individual phases.

Phase maps of the microstructures were produced using a combination of EBSD and energy-dispersive spectroscopy (EDS), performed by EBSD Analytical (Lehi, UT). The EDS data was used to improve the confidence of fit for the indexing between the BCC molybdenum and A15 phases. An EBSD phase map for the Mo-3Si-1B wt.% alloy processed with the hBN powder and fired to 1600°C for 6 hours is shown in Figure 5.1. The EBSD technique clearly reveals the boundaries between the three phases and allows for examination of the dispersion of the individual intermetallic phases. It is evident that the intermetallic regions observed in the BSE images are combinations of the A15 and T2 phases, an observation which can not be obtained from the BSE images. It should be noted that the grain boundaries are not plotted in Figure 5.1 and that many of the phase regions are actually an accumulation of smaller grains. The grain boundaries are plotted on the phase map in Figure 5.2. It can be seen that this technique allows for detailed examination of how processing and materials selection affect the final microstructure.

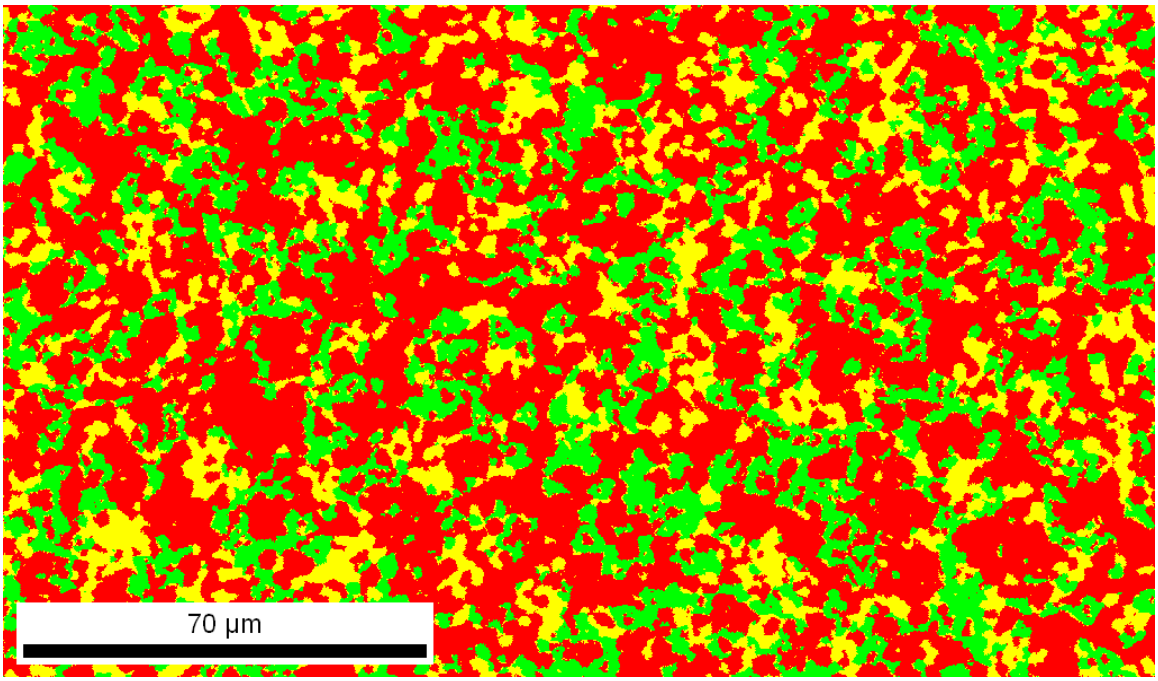

Figure 5.1: An EBSD phase map of the Mo-3Si-1B wt.% alloy processed with hBN powder and sintered at 1600°C for 6 hours.

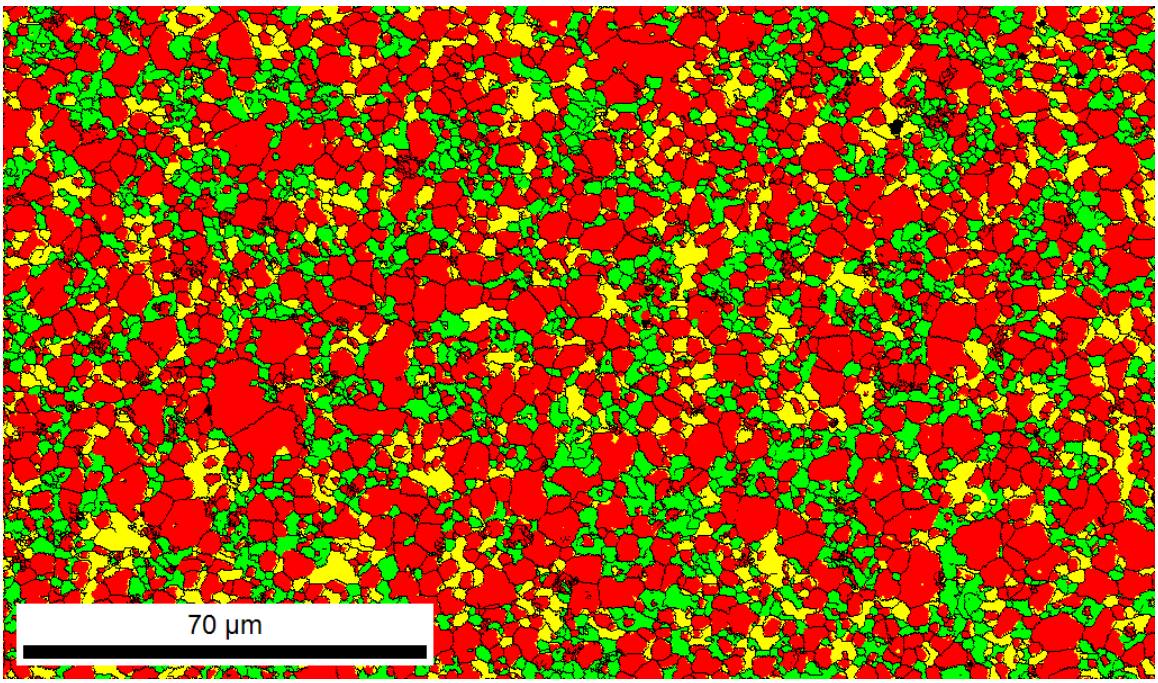

Figure 5.2: The EBSD map of the Mo-3Si-1B wt.% alloy processed with hBN powder and sintered at 1600°C for 6 hours, with the grain boundaries plotted.

The volume fractions of the three phases determined from EBSD analysis were compared to those calculated from the ternary phase diagram and measured by Rietveld analysis, Table 5.1. The values determined from the three techniques closely match, differing by 3% at the most.

Table 5.1: A comparison of the phase contents (vol.%) of the Mo-3Si-1B wt.% alloy calculated from the phase diagram and measured by Rietveld and EBSD analysis.

| | **Phase Diagram** | **Rietveld Analysis** | **EBSD Analysis** |
|---|---|---|---|
| **$Mo_{ss}$** | 56.8 | 55.9 | 57.5 |
| **A15** | 16.0 | 17.9 | 18.3 |
| **T2** | 27.2 | 26.2 | 24.2 |

The EBSD analysis software compares the crystallographic orientations of the phases measured at each pixel and assigns grain boundaries for misorientation angles greater than two degrees. This is a precise method of defining grains which does not rely on being able to visually observe the grain boundaries. The EBSD technique calculates the grain size distributions from the entire region imaged. Hand measurement techniques such as line counting rely on a sample set of the grains and are typically used to determine only an average grain size. The analysis software was used to calculate the grain size distributions of the three phases, plotted in terms of the area fraction in Figure 5.3. An alternative plot gives the cumulative grain size distributions, Figure 5.4. The $d_{10}$, $d_{50}$ and $d_{90}$ grain size parameters are listed in Table 5.2 for the three phases.

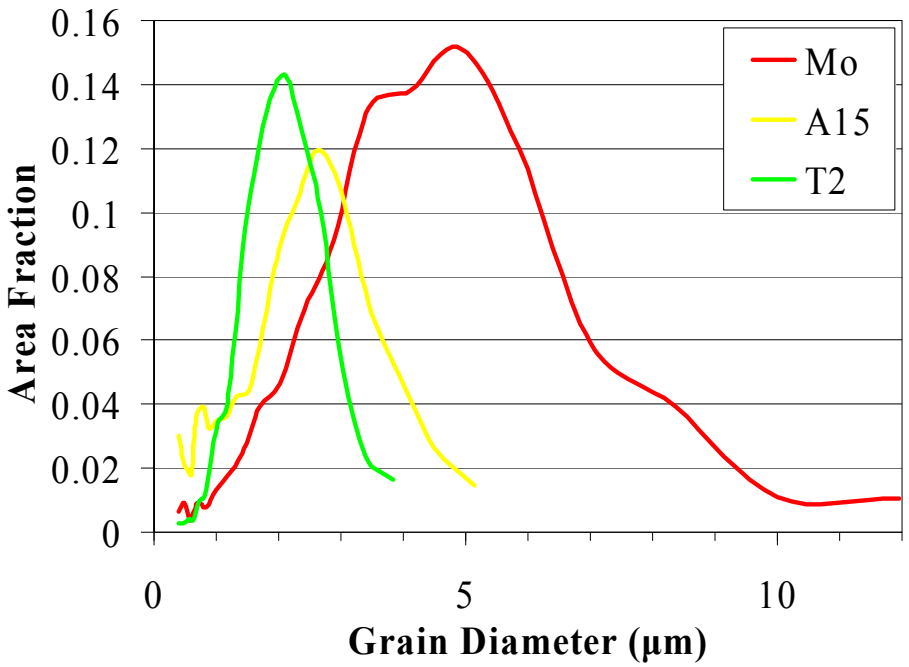


Figure 5.3: The grain size distributions of the three phases in the Mo-3Si-1B wt.% alloy processed with hBN and sintered at 1600°C for 6 hours.

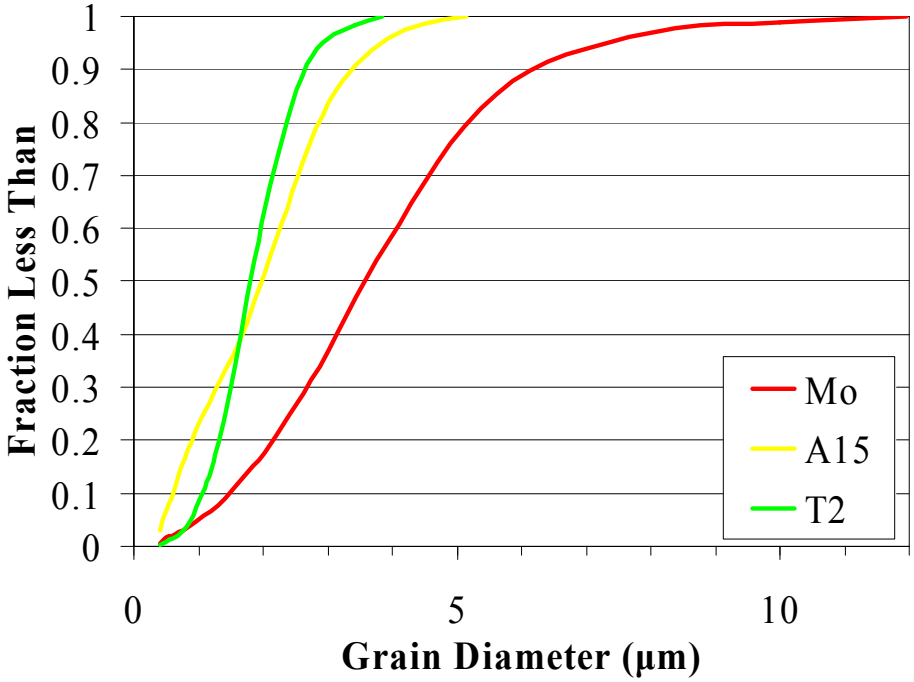


Figure 5.4: The cumulative grain size distributions of the three phases in the Mo-3Si-1B wt.% alloy processed with hBN and sintered at 1600°C for 6 hours.

Table 5.2: The $d_{10}$, $d_{50}$ and $d_{90}$ parameters from the cumulative grain size distributions for the Mo-3Si-1B wt.% alloy processed with hBN and fired at 1600°C for 6h.

| | $d_{10}$ (µm) | $d_{50}$ (µm) | $d_{90}$ (µm) |
|---|---|---|---|
| **$Mo_{ss}$** | 1.5 | 3.6 | 6.1 |
| **A15** | 0.6 | 2.0 | 3.4 |
| **T2** | 1.1 | 1.8 | 2.6 |

Accurate measurement of grain sizes and other microstructural parameters from two-dimensional cross-sections requires that the sample microstructures are isotropic. This can be ensured by examining microstructure cross-sections taken perpendicular to the three axes. This is best avoided due if possible due to the cost and time required for EBSD analysis. An indication of the microstructure isotropy is to observe if there is any crystallographic texture present. Texture occurs when a high proportion of grains are aligned in the same crystallographic direction. Texture can be represented by pole figure plots which are stereographic projections that plot the orientation of a given crystallographic direction in relation to the sample. The pole figures for the [001], [110] and [111] crystallographic directions are plotted for the BCC molybdenum and A15 phases in Figure 5.5 and Figure 5.6. The [001], [100] and [110] directions are plotted for the tetragonal T2 phase in Figure 5.7. The common labeling convention for pole figures is in relation to the rolling direction (RD) and the transverse direction (TD). The EBSD data was measured from cylindrical pressed pellets and these directions are arbitrary. The normal direction at the origin of the plot is parallel to the axial direction of the samples. The scales of the contours are in terms of intensity normalized to the random value.

Texture is indicated by patterns of high density in the pole figure contour plots which are often present as concentric rings about the normal direction. It can be seen that the pole figure plots of all three phases appear random. In addition, the maximum intensity observed is approximately two, i.e. two times random, which is a low value and indicates there is no significant texture in any of the phases.

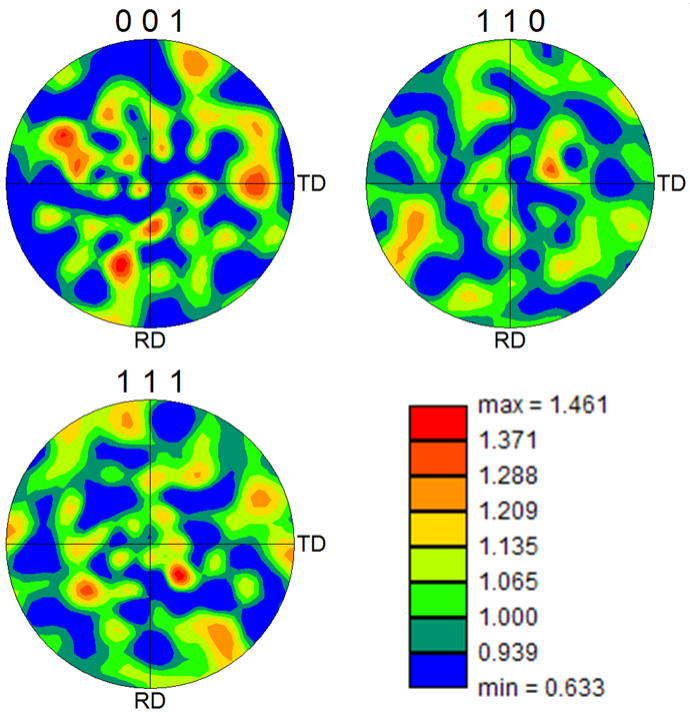


Figure 5.5: Pole figure plots measured by EBSD for the $Mo_{ss}$ phase in the Mo-3Si-1B wt.% sample, prepared with hBN and fired at 1600°C for 6 hours.

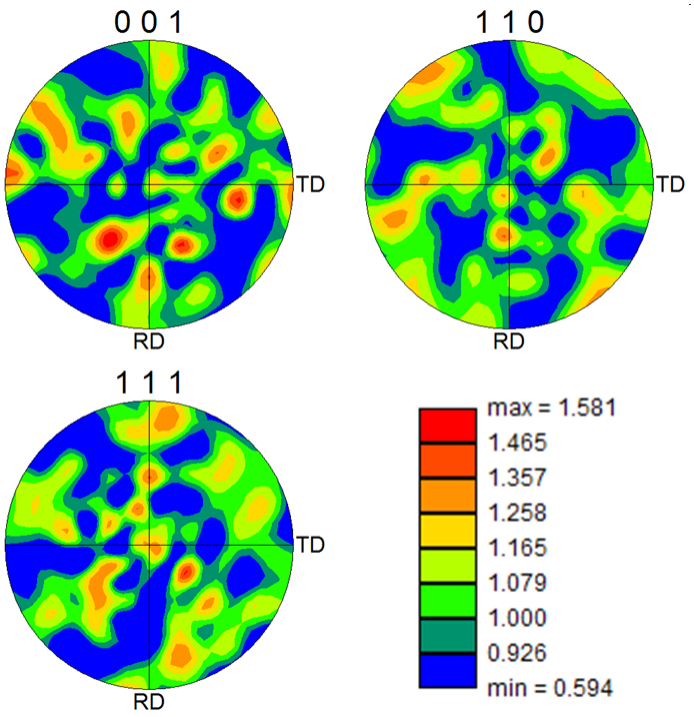


Figure 5.6: Pole figure plots measured by EBSD for the A15 phase in the Mo-3Si-1B wt.% sample, prepared with hBN and fired at 1600°C for 6 hours.

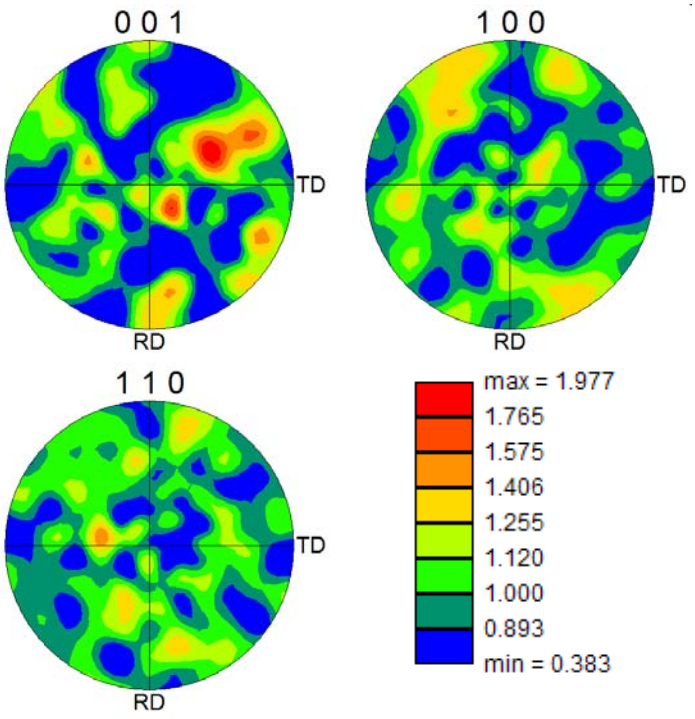


Figure 5.7: Pole figure plots measured by EBSD for the T2 phase in the Mo-3Si-1B wt.% sample, prepared with hBN and fired at 1600°C for 6 hours.

## 5.2 Effect of the Boron Nitride Powder on the Dispersion of Intermetallics

The microstructural characteristics of a given Mo-Si-B composition vary greatly as a result of processing. Melt processing yields discrete molybdenum regions while the nitride-based powder metallurgy method produces a dispersion of intermetallics in a molybdenum matrix. Studies were conducted to determine the effect of the size and morphology of the BN reactant powders on the distribution of intermetallic phases and the continuity of the molybdenum matrix. Boron diffusion in molybdenum is slow and it is proposed that the dispersion of the T2 phase is related to the initial dispersion of the boron nitride powder in the greenbodies. The microstructures presented so far have all been produced using hexagonal boron nitride powder. The powder is highly anisotropic with flakes measuring approximately 0.5μm thick and up to 10μm across. A fracture surface of an unfired powder compact reveals that the hBN flakes are not significantly broken up during milling of the slurry, Figure 5.8.

The radial dimension of the hBN flakes is an order of magnitude larger than the other powders in the mixture. This leads to a high degree of heterogeneity in the initial dispersion of boron in the microstructure. The starting size and morphology of the BN powder has been varied to study changes in the dispersion of the T2 phase in the fired microstructures. Alloys were produced using the three different cubic boron nitride powders described in Chapter 3, with approximately 0.125μm, 0.5μm and 1μm average particle sizes. The cBN powders have isotropic morphologies and narrow size distributions which are more on scale with the sizes of the molybdenum and $Si_3N_4$ powders.

Mo-3Si-1B wt.% slurry batches prepared with the four BN powders were mixed on the paint shaker for 30 minutes and spray dried with the Büchi spray dryer. Pellets were uniaxially pressed at 70ksi and fired together at 1600°C for 6h in Ar/10% $H_2$. The fired pellets had near zero open porosity and were hot-isostatically pressed without encapsulation at 1500°C and 30ksi for 6h. The densities of the pellets were measured before and after HIPing and did show any significant difference as a result of the BN powder used, Figure 5.9.

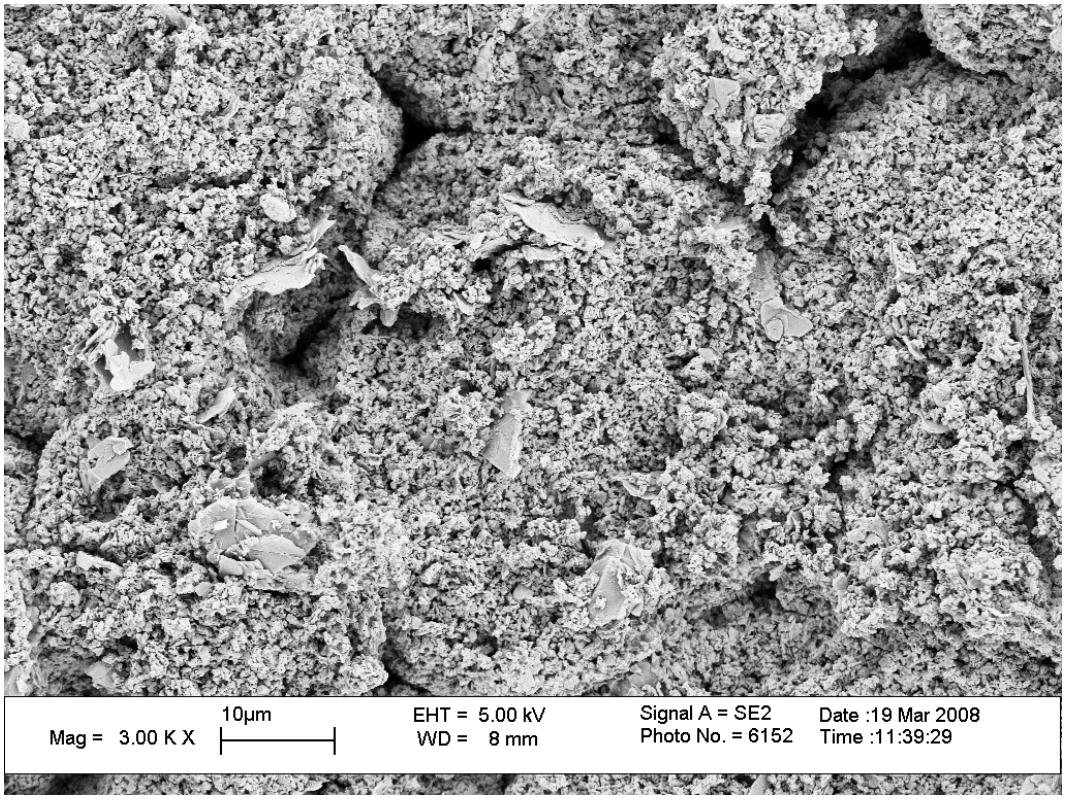

Figure 5.8: The fracture cross-section of an unfired Mo-Si-B greenbody produced with hBN. It is apparent that the large hBN flakes are not broken up during miling.

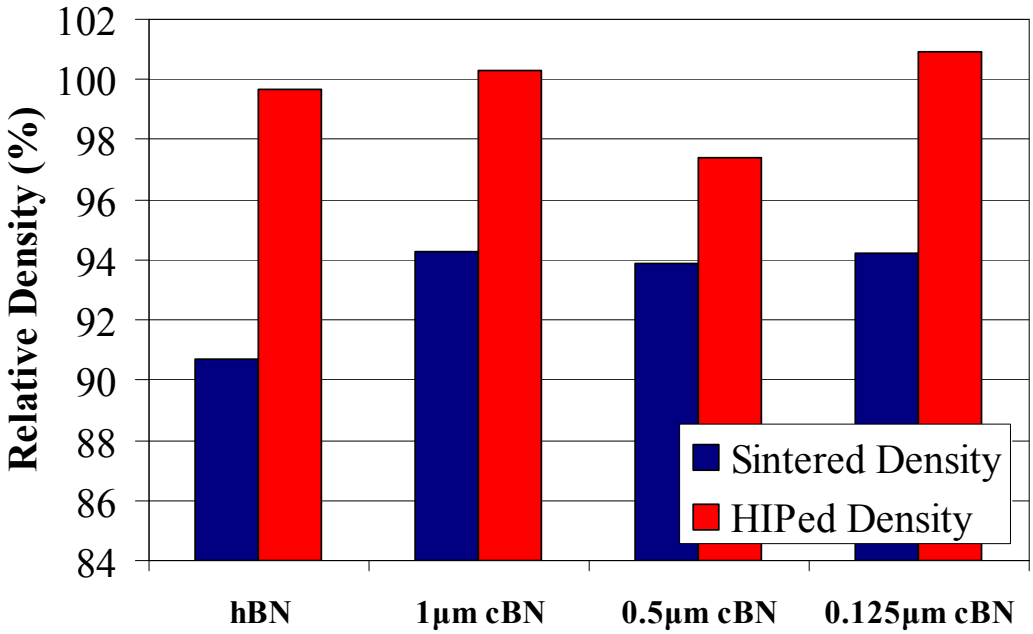


Figure 5.9: Density comparison of the Mo-3Si-1B wt.% samples made with different BN reactant powders, in the as-fired condition (1600°C, 6h) and after a post-sinter HIP cycle (1500°C, 30ksi, 6h).

The samples were imaged by EBSD and microstructural parameters were measured as a function of the BN powder used. Phase maps were created over a 300×300µm region using a 300nm step size. Enlarged portions of the phase maps are compared in Figure 5.10. The measurement parameters of the EBSD scans were expanded to include the oxygen EDS data which was used to identify the presence of silica inclusions in the microstructures. A data partition was created in which the regions with high oxygen levels were assigned as silica and removed from the calculations of the phase volumes and grain sizes. The silica inclusions are shown in the images as black and amount to less than 0.5% of the sample volumes. The volume fractions of the phases determined from the EBSD analysis are compared in Table 5.3.

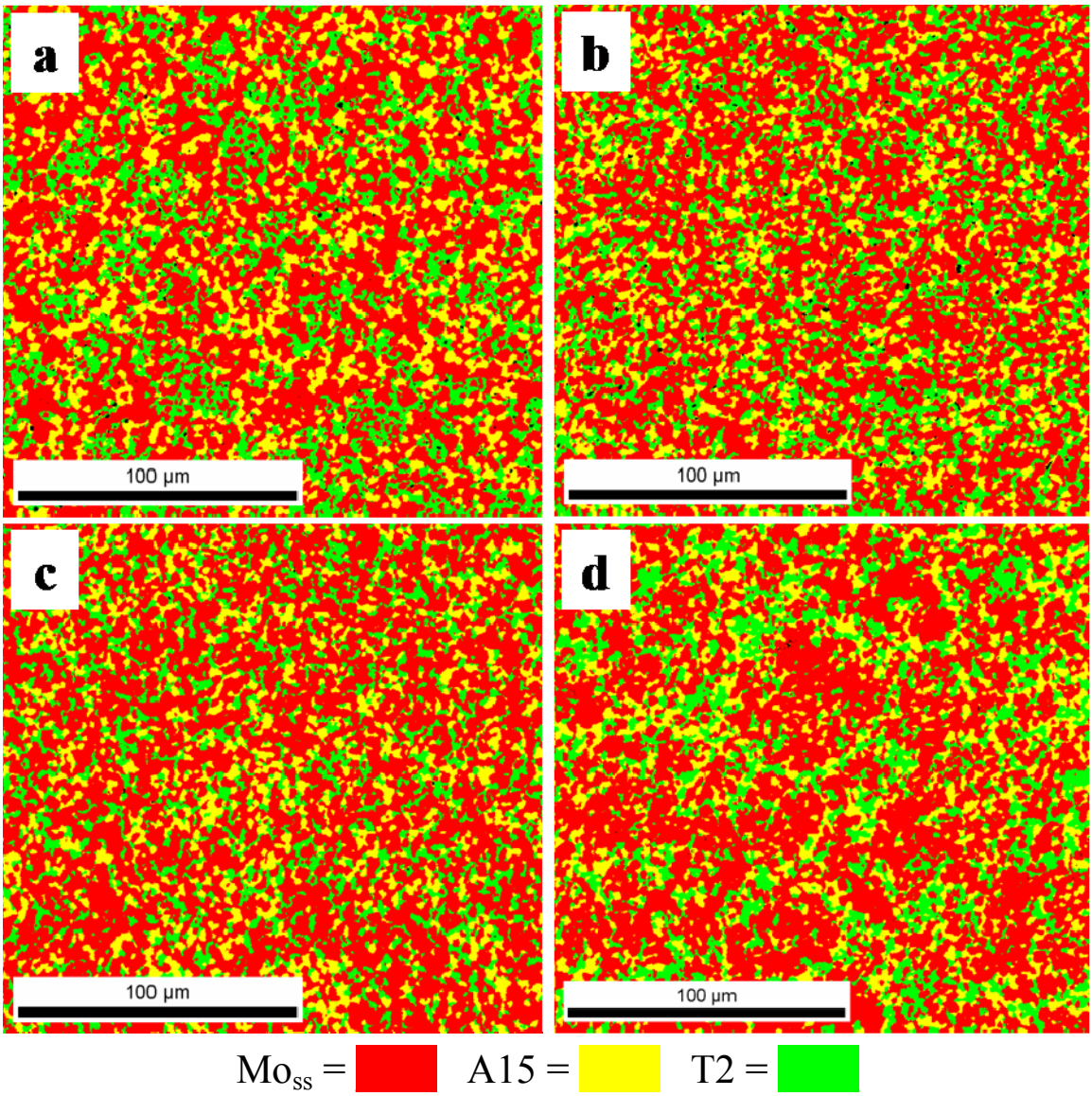


Figure 5.10: EBSD phase maps for Mo-3Si-1B wt.% alloys processed with different sized boron nitride reactants: (a) hBN, (b) 1µm cBN, (c) 0.5µm cBN and (d) 0.125µm cBN. The small fraction of silica inclusions (<0.5 vol.%) in the alloys is shown in black.

Table 5.3: The phase contents (vol.%) measured by EBSD analysis for Mo-3Si-1B wt.% alloys produced with different BN reactant powders.

| **BN Powder** | **Mo$_{ss}$** | **A15** | **T2** |
|---|---|---|---|
| hBN | 56.9 | 20.3 | 22.6 |
| 1µm cBN | 59.6 | 19.5 | 20.9 |
| 0.5µm cBN | 62.9 | 18.5 | 18.6 |
| 0.125µm cBN | 59.8 | 20.0 | 20.2 |

Comparing the microstructures qualitatively, it can be seen that the spacing and clustering of the intermetallic phases changed as a result of the different BN reactant powders. The large flakes of the hBN powder lead to clustered regions of the T2 phase which were likely the location of the original powder particles. The T2 phase was well dispersed in the alloys prepared with the 0.5μm and 1μm cBN powder, but there was a high level of clustering of the intermetallics in the alloy prepared with the 0.125μm powder. These qualitative observations are reflected in the size distributions measured for the intermetallic phases. The grain size distributions of the A15 and T2 phases were obtained from the EBSD analysis, but it should again be noted that the single phase areas observed in the microstructures are typically comprised of many smaller grains. The continuous area that a single phase occupies has been denoted the 'phase region', which represents the cluster size of the interconnected grains. The area of each individual phase region was measured using the image analysis software ImageJ and converted to an equivalent diameter. The complete details of the phase region measurement are given in Chapter 3.6. The grain and phase region size distributions for the A15 and T2 phases are compared in Figure 5.11 and Figure 5.12. The $d_{10}$, $d_{50}$ and $d_{90}$ parameters are listed in Table 5.4 for the phase region size distributions and Table 5.5 for the grain size distributions.

The grain size distributions for both A15 and T2 varied little with the size or morphology of the BN powder used. A more significant effect was observed in the size distributions of the phase regions. It has been proposed that the dispersion of the T2 phase is directly related to the dispersion of the BN reactant powder, thus it was assumed that the size of the T2 clusters would be proportional to the size of the powder. This was

observed for the hBN powder which creates the largest T2 cluster sizes due to the large flakes (0.5×10μm) which persisted through milling. The 0.5μm and 1μm cBN powders both produced fine size distributions of the T2 phase, but the 0.125μm cBN powder resulted in significant clustering. The envisioned scenario is dependent on the BN powders being fully dispersed in the powder compacts. Clustering of the T2 phase in the 0.125μm cBN sample was likely a result of poor dispersion of the reactant powder. The small grain size and high surface area of the powder may cause agglomeration during processing, which was translated to the final microstructure. The 0.125μm cBN powder has a high specific surface area of 45.7$m^2$/g and for fine, high surface area powders, the Van der Waals force becomes the predominant force and makes dispersion difficult. It is possible that higher energy milling or sonication of the slurry would improve dispersion.

The BN nitride powder was selected as the variable in these experiments due to the slow diffusion of boron in molybdenum. Silicon diffuses much faster and the A15 distribution was presumed to be less influenced by the initial dispersion of $Si_3N_4$, however there does appear to be a correlation between the phase region size distributions of the A15 and T2 phases. Future work should be completed to investigate the cause of the relationship between the distributions of the two phases and to determine the effects of different sized $Si_3N_4$ reactant powders.

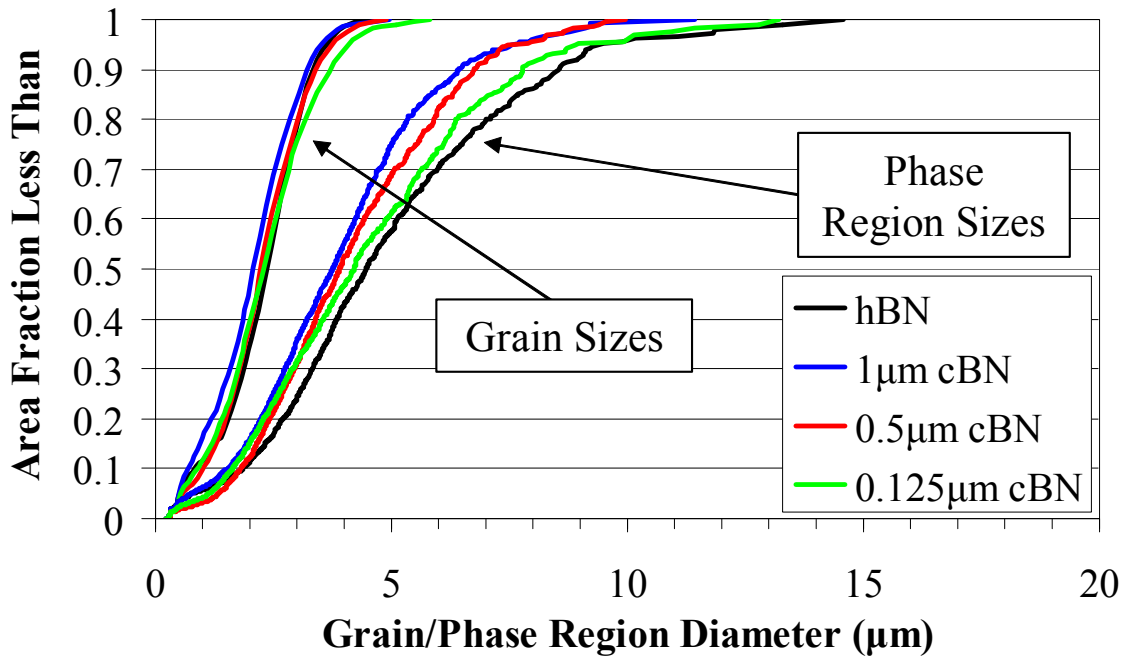


Figure 5.11: The cumulative 'phase region' and grain size distributions of the A15 phase, measured for Mo-3Si-1B wt.% alloys produced with different BN reactant powders (1600°C, 6 hours).

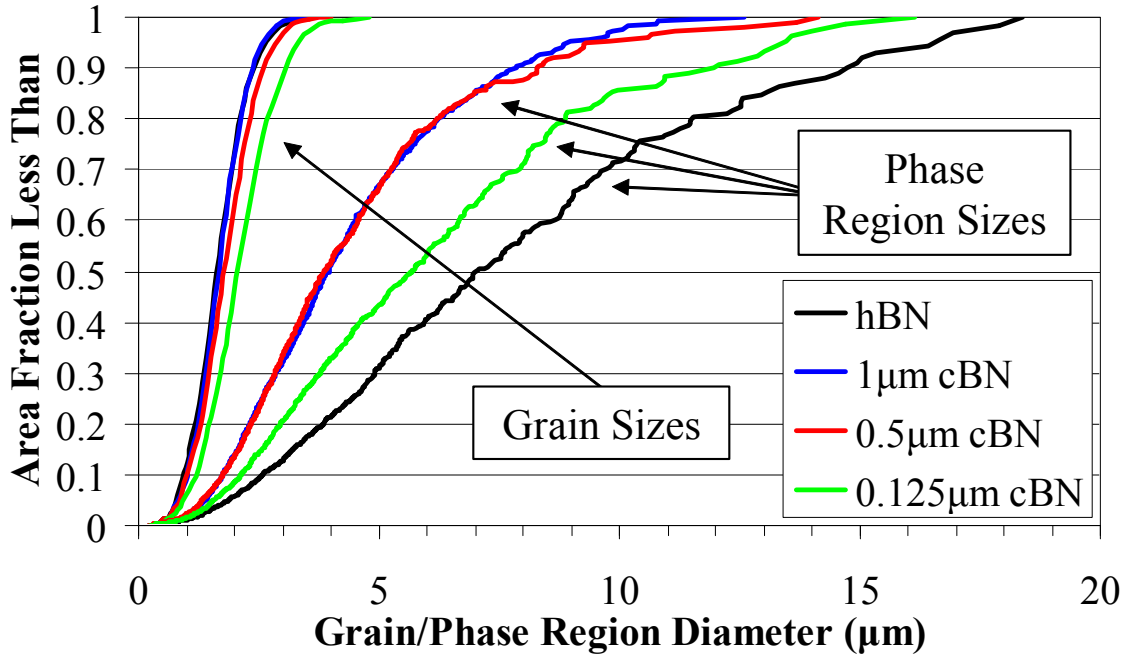


Figure 5.12: The cumulative 'phase region' and grain size distributions of the T2 phase, measured for Mo-3Si-1B wt.% alloys produced with different BN reactant powders (1600°C, 6 hours).

Table 5.4: The $d_{10}$, $d_{50}$ and $d_{90}$ parameters of the 'phase region' size distributions for Mo-3Si-1B wt.% alloys produced with different BN reactant powders (1600°C, 6 hours).

| | A15 Phase | | | T2 Phase | | |
|---|---|---|---|---|---|---|
| BN Powder | $d_{10}$ (μm) | $d_{50}$ (μm) | $d_{90}$ (μm) | $d_{10}$ (μm) | $d_{50}$ (μm) | $d_{90}$ (μm) |
| hBN | 1.8 | 4.5 | 8.6 | 2.6 | 7.0 | 14.7 |
| 1μm cBN | 1.5 | 3.8 | 6.4 | 1.8 | 4.0 | 7.8 |
| 0.5μm cBN | 1.8 | 3.9 | 6.8 | 1.8 | 3.9 | 8.3 |
| 0.125μm cBN | 1.6 | 4.2 | 7.8 | 2.1 | 5.7 | 12.0 |

Table 5.5: The $d_{10}$, $d_{50}$ and $d_{90}$ parameters of the grain size distributions for Mo-3Si-1B wt.% alloys produced with different BN reactant powders (1600°C, 6 hours).

| | A15 Phase | | | T2 Phase | | |
|---|---|---|---|---|---|---|
| BN Powder | $d_{10}$ (μm) | $d_{50}$ (μm) | $d_{90}$ (μm) | $d_{10}$ (μm) | $d_{50}$ (μm) | $d_{90}$ (μm) |
| hBN | 0.8 | 2.3 | 3.4 | 0.9 | 1.6 | 2.4 |
| 1μm cBN | 0.7 | 2.1 | 3.2 | 1.0 | 1.7 | 2.4 |
| 0.5μm cBN | 1.0 | 2.2 | 3.3 | 1.0 | 1.7 | 2.6 |
| 0.125μm cBN | 0.9 | 2.3 | 3.6 | 1.2 | 2.1 | 3.1 |

### 5.2.1 Two-Point Correlation Functions – Direction Dependence

Two-point correlation functions capture information on microstructural features such as spatial arrangements (clustering, etc.) and anisotropy. They were measured to further examine the relationship between the raw material selection and the distributions of intermetallic phases in the $Mo_{ss}$ matrix. The calculation of three-dimensional microstructure parameters by two-point correlation functions requires examining cross-sections perpendicular to all three axes, but the analysis of one plane is sufficient if the correlation functions are independent of direction [87]. The two-point correlation functions measured in the *X* and *Y*-directions were compared for the three phases in the Mo-3Si-1B wt.% alloy produced with hBN powder, Figure 5.13 - Figure 5.15. The

correlation functions of all three phases were nearly identical in the perpendicular directions. This combined with the previous observation that there was no microstructural texture indicates the samples have an isotropic morphology and that the observation of a single plane of polish will be sufficient to estimate the microstructural properties in three dimensions.

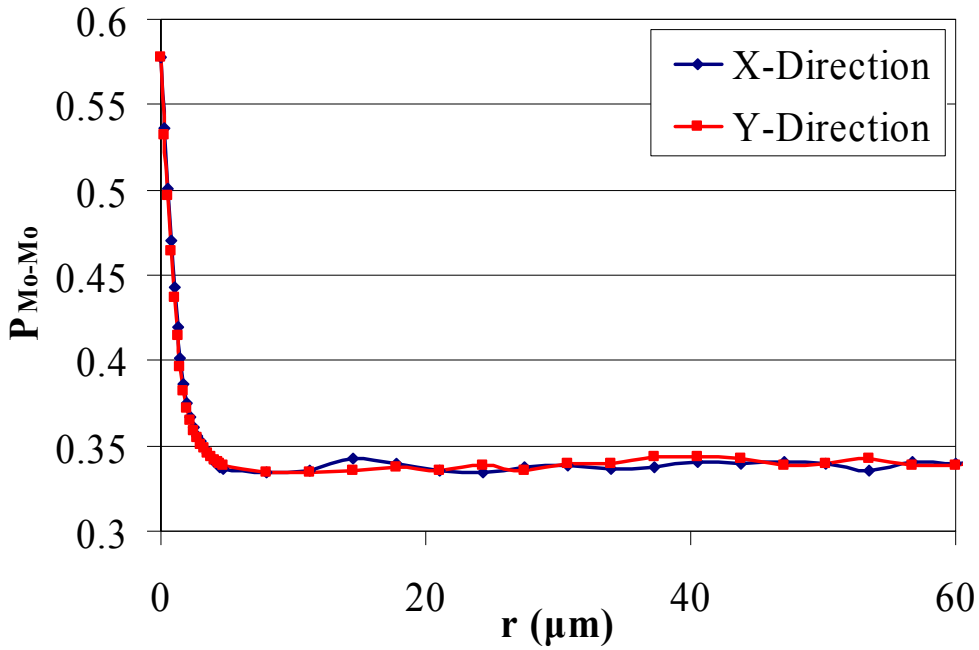


Figure 5.13: The direction dependent two-point correlation functions for the $Mo_{ss}$ phase, [$P_{Mo\text{-}Mo}(r)$], in the Mo-3Si-1B wt.% alloy (1600°C, 6 hours) compared for the *X* and *Y*-directions.

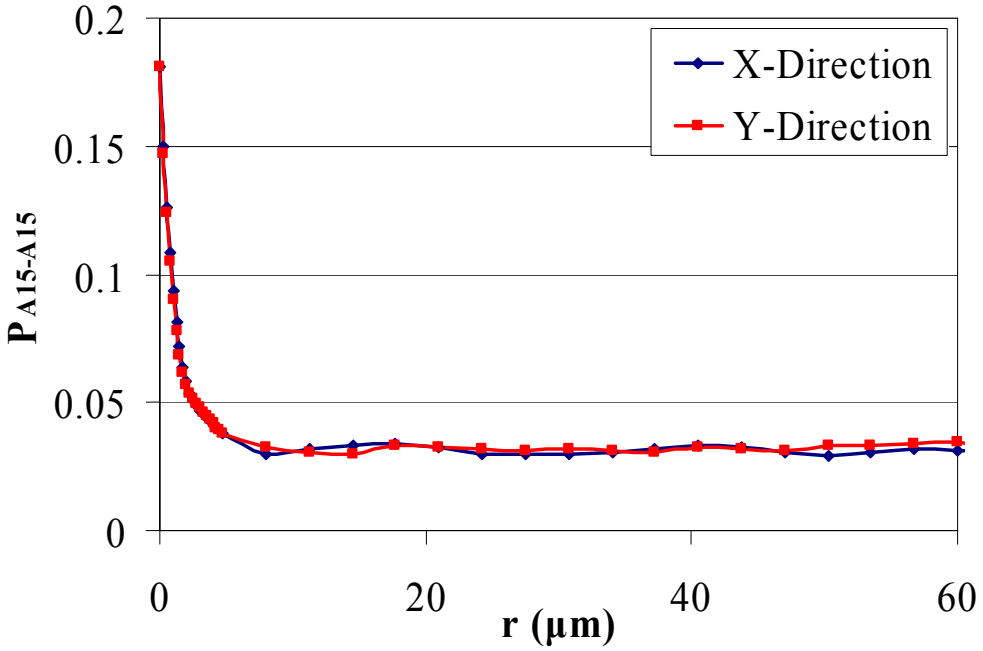


Figure 5.14: The direction dependent two-point correlation functions for the A15 phase, [$P_{A15\text{-}A15}(r)$], in the Mo-3Si-1B wt.% alloy (1600°C, 6 hours) compared for the *X* and *Y*-directions.

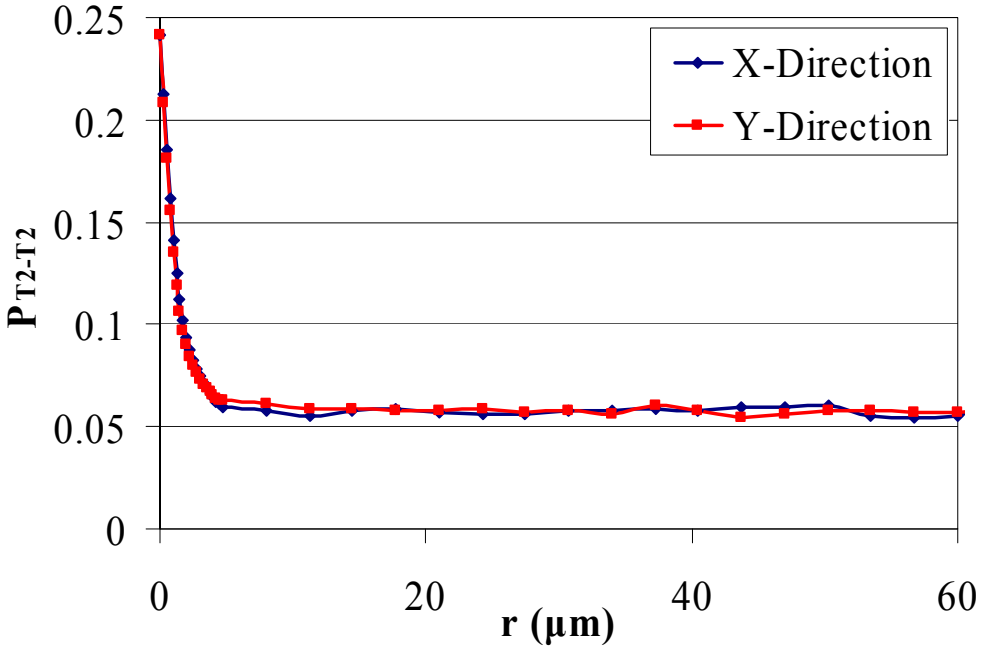


Figure 5.15: The direction dependent two-point correlation functions for the T2 phase, [$P_{T2\text{-}T2}(r)$], in the Mo-3Si-1B wt.% alloy (1600°C, 6 hours) compared for the *X* and *Y*-directions.

### 5.2.2 Two-Point Correlation Functions – Dependence on the BN Reactant Powder

The two-point correlation functions were compared for the alloys produced with the four different BN powders. Measurements were made for the three phases, as well as for the distribution of the combined intermetallics. The functions [$P_{Mo\text{-}Mo}(r)$], [$P_{Int.\text{-}Int.}(r)$], [$P_{A15\text{-}A15}(r)$] and [$P_{T2\text{-}T2}(r)$] were normalized by the volume fraction squared, $f^2$, and are compared in Figure 5.16 - Figure 5.19. The functions are bounded by two limits; for a test line length of zero, the value of the two-point correlation function is determined by the volume fraction of the phase. For an infinite test line length, the probability of both endpoints being in the same phase is equal to the volume fraction squared, $f^2$, thus the normalized function approaches one as the length $r$ increases. The two-point correlation functions are useful for describing the distribution of a particulate phase and two features from the curves are associated with heterogeneity of the microstructure, $L_o$ and $L_\infty$. The definitions of these values stem from research on particle reinforced composite microstructures, where $L_o$ reflects the average size of the particles and $L_\infty$ is the average size of the particle clusters [87]. The parameter $L_o$ is defined as the distance at which the slope of the curve has decreased to one-tenth of its initial value, and in this work can be seen as the 'effective' particle size of the intermetallics. Past this length, the normalized correlation functions depend on the heterogeneity of the microstructure and clustering of the particles. The cluster size $L_\infty$ is defined by the distance at which the normalized two-point correlation function first reaches within 2% of 1.0 (i.e. 1.02). The values of $L_o$ and $L_\infty$ are compared for the four microstructures in Table 5.6.

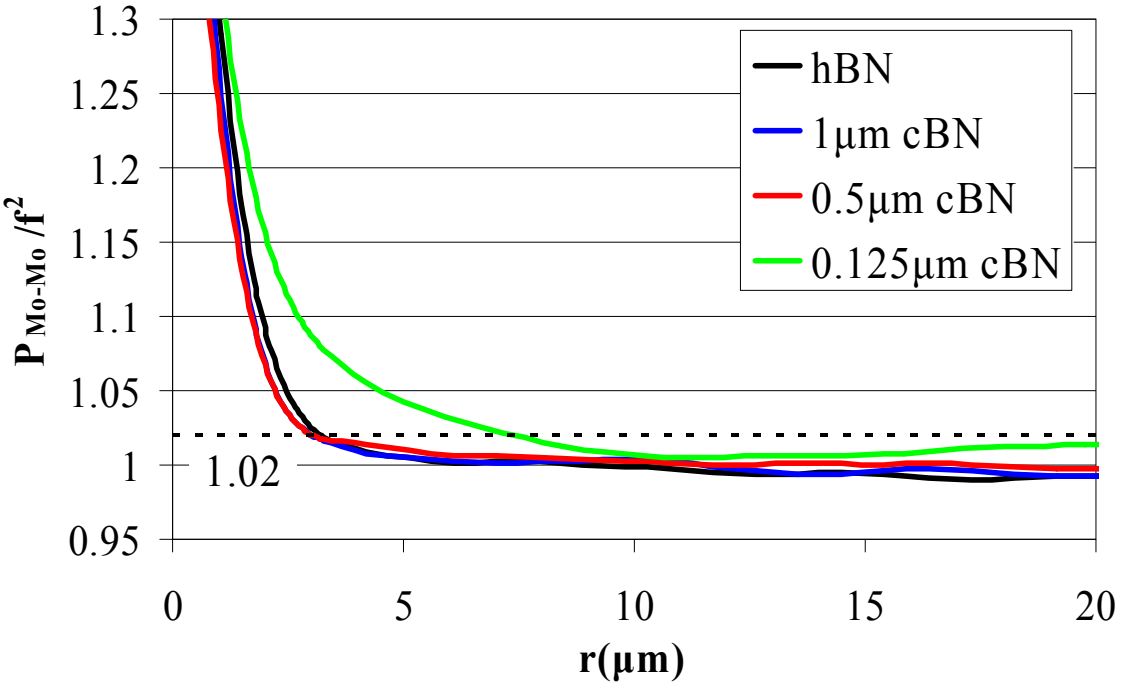


Figure 5.16: Two-point correlation functions, [$P_{Mo\text{-}Mo}(r)$], for alloys produced using different BN reactant powders (normalized by the $Mo_{ss}$ volume fraction squared, $f^2$).

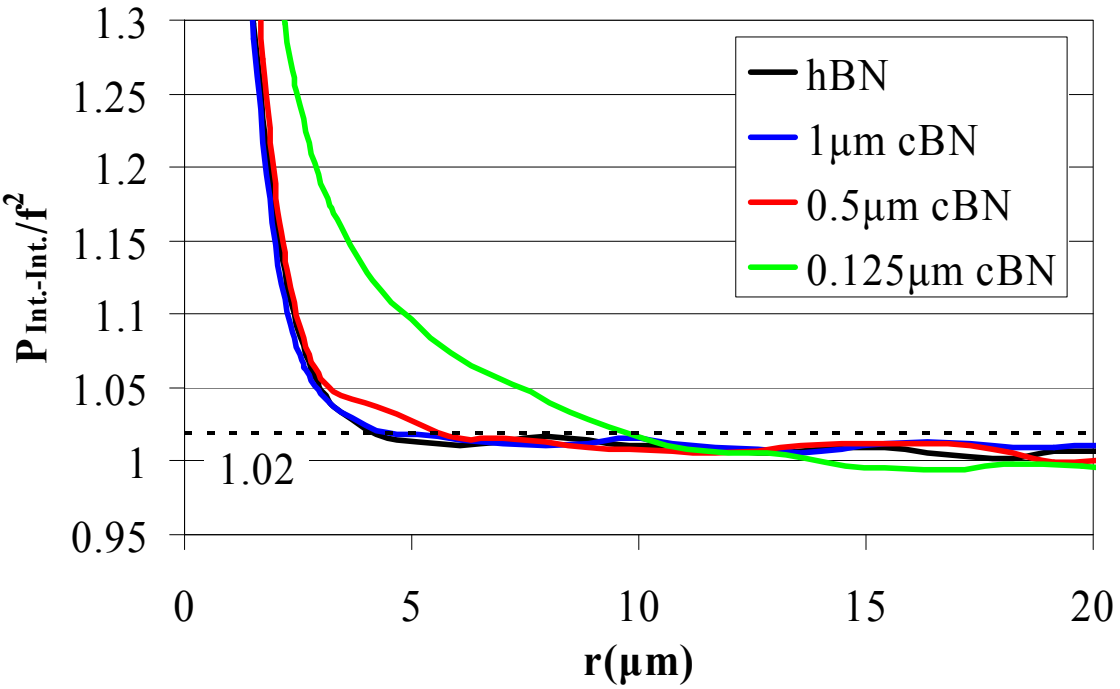


Figure 5.17: Two-point correlation functions, [$P_{Int.\text{-}Int.}(r)$], for alloys produced using different BN reactant powders (norm. by the intermetallic volume fraction squared, $f^2$).

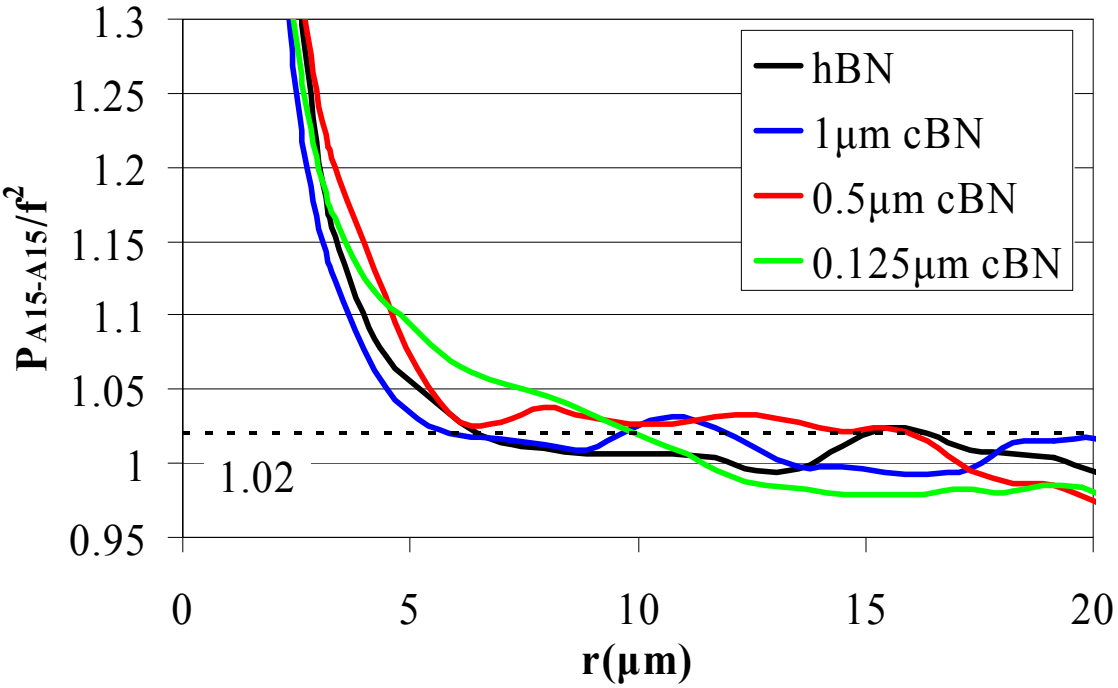


Figure 5.18: Two-point correlation functions, [$P_{A15\text{-}A15}(r)$], for alloys produced using different BN reactant powders (normalized by the A15 volume fraction squared, $f^2$).

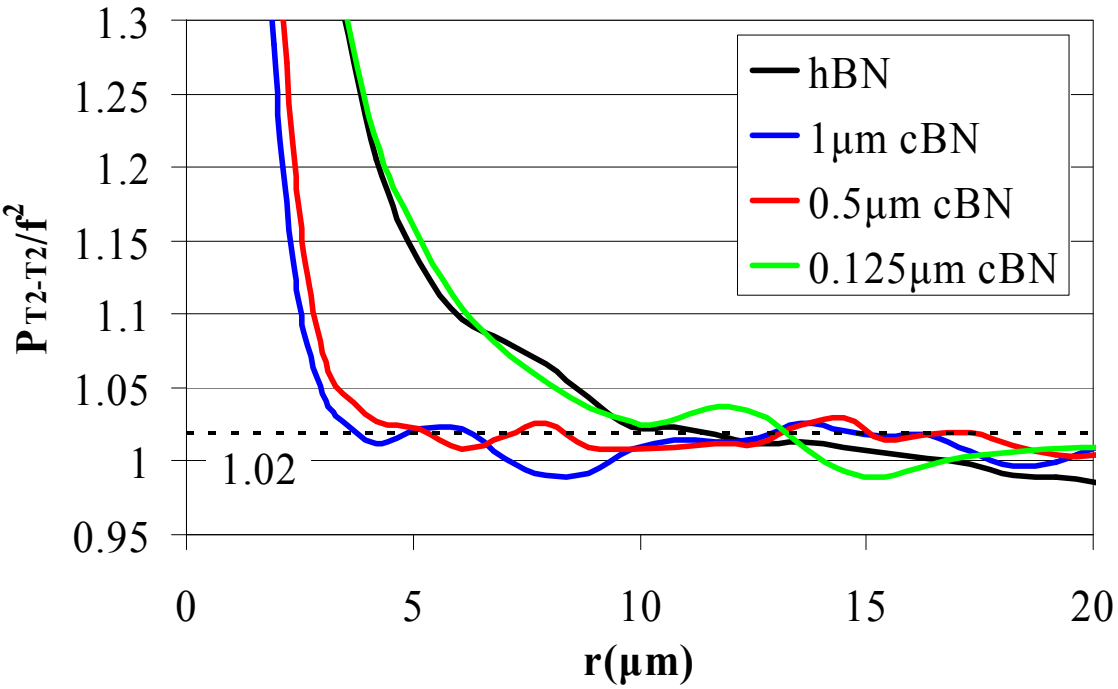


Figure 5.19: Two-point correlation functions, [$P_{T2\text{-}T2}(r)$], for alloys produced using different BN reactant powders (normalized by the T2 volume fraction squared, $f^2$).

Table 5.6: Microstructural length scale parameters measured from the two-point correlation functions for alloys produced using different BN reactant powders.

| | $L_o$ (µm) | | | | $L_\infty$ (µm) | | | |
|---|---|---|---|---|---|---|---|---|
| BN Powder | $Mo_{ss}$ | A15 | T2 | A15+T2 | $Mo_{ss}$ | A15 | T2 | A15+T2 |
| hBN | 2.4 | 2.5 | 2.4 | 2.4 | 3.2 | 6.5 | 11.3 | 4.1 |
| 1µm cBN | 2.3 | 2.1 | 2.1 | 2.3 | 3.0 | 5.9 | 3.7 | 4.4 |
| 0.5µm cBN | 2.4 | 2.4 | 2.1 | 2.4 | 3.0 | 6.4* | 5.3 | 5.6 |
| 0.125µm cBN | 2.8 | 2.1 | 2.7 | 2.7 | 7.4 | 10.0 | 13.2 | 9.7 |

*value has been adjusted to the point that the correlation function first approached and became approximately tangent to the defining limit for $L_\infty$.

There is little difference in the effective particles sizes, $L_o$, of the four specimens and the differences in the microstructures were mainly due to the different cluster sizes, $L_\infty$. The correlation functions for the $Mo_{ss}$ phase were relatively independent of the BN powder used, with the exception of the 0.125µm cBN based sample. The high $L_\infty$ value indicates large molybdenum regions, which is also evident from the micrographs. The same observation is made from the overall distribution of the intermetallic phases in the $Mo_{ss}$ matrix. Comparing the values of $L_\infty$, it can be seen that the $Mo_{ss}$ and intermetallic clusters in the 0.125µm cBN sample are approximately twice as large as those in the other samples.

Examining the individual intermetallics, it can be seen that the A15 cluster size is relatively independent of the BN powder, again with the exception of the 0.125µm cBN. The fine 0.125µm cBN may also be agglomerating with the $Si_3N_4$ powder during slurry processing. The relationships between the BN powder and the T2 cluster sizes are similar to those observed for the phase region size measurements. The large hBN flakes lead to large T2 clusters, as does the agglomeration of the 0.125µm cBN powder. The

measurements from the two-point correlation functions demonstrate that although the phase region sizes of the intermetallics in the 0.125μm cBN specimen are smaller than in the hBN specimen, the 0.125μm cBN powder actually results in the largest clusters of the A15 and T2 phases. The two techniques used to describe the clustering of the intermetallic phases are compared in Table 5.7. It was observed that the effective particle size determined from the two-point correlation measurements was approximately equal to the average grain size of the phase. It was also observed that the cluster size $L_\infty$ was approximately equal to the $d_{90}$ size parameter of the phase region size distributions.

It is clear from this study that changing the size and morphology of the BN reactant powder is an effective means to alter the dispersion of the T2 phase in the sintered alloys. The 0.5μm and 1μm cBN powders significantly improved the dispersion of T2 as compared to the hBN powder, although the high surface area of the 0.125μm cBN powder lead to agglomeration of the nitride reactants during processing and resulted in the most clustering. Changes were also observed in the dispersion of the A15 phase and future work should be completed to investigate the relationship between the distributions of the two phases. The ability to precisely control the microstructure through materials selection and changes in processing conditions will be an important step in the development of Mo-Si-B alloys.

Table 5.7: Comparison of the size parameters measured from the phase distributions and from two-point correlation analysis for alloys produced with different BN powders.

| | **Phase Distribution Measurements** | | | |
|---|---|---|---|---|
| | Grain Size ($d_{50}$) (μm) | | Phase Region Size ($d_{90}$) (μm) | |
| BN Powder | A15 | T2 | A15 | T2 |
| hBN | 2.3 | 1.6 | 8.6 | 14.7 |
| 1μm cBN | 2.1 | 1.7 | 6.4 | 7.8 |
| 0.5μm cBN | 2.2 | 1.7 | 6.8 | 8.3 |
| 0.125μm cBN | 2.3 | 2.1 | 7.8 | 12.0 |

| | **Two-Point Correlation Measurements** | | | |
|---|---|---|---|---|
| | Effective Particle Size ($L_o$) (μm) | | Cluster Size ($L_\infty$) (μm) | |
| BN Powder | A15 | T2 | A15 | T2 |
| hBN | 2.5 | 2.4 | 6.5 | 11.3 |
| 1μm cBN | 2.1 | 2.1 | 5.9 | 3.7 |
| 0.5μm cBN | 2.4 | 2.1 | 6.4 | 5.3 |
| 0.125μm cBN | 2.1 | 2.7 | 10.0 | 13.2 |

### 5.3 Effect of the $Mo_{ss}$ Volume Fraction on the Dispersion of Intermetallics

The distribution of the intermetallic phases was studied as a function of the volume fraction of the $Mo_{ss}$ matrix. Alloys of composition Mo-2.51Si-0.84B and Mo-2.21Si-0.74B wt.% were compared to the Mo-3Si-1B wt.% analyzed in Section 5.2. This study was conducted prior to the investigation of the cBN powders and the samples were prepared with the hBN powder. The complete details of the sample preparation are given in Chapter 4.3. The EBSD phase map for the Mo-3Si-1B wt.% alloy was shown in Figure 5.10a, and the phase maps of the two additional alloys are shown in Figure 5.20 and Figure 5.21. The volume fractions of the phases determined from EBSD analysis

were compared to those calculated from the ternary phase diagram and measured by Rietveld analysis, Table 5.8. The values measured for the $Mo_{ss}$ phase match closely but there is a discrepancy in the A15/T2 ratio measured from EBSD. The phase region size distributions for A15 and T2 are compared to the grain size distributions in Figure 5.22 and Figure 5.23. The $d_{10}$, $d_{50}$ and $d_{90}$ parameters are listed in Table 5.9 for the phase region size distributions and Table 5.10 for the grain size distributions.

Table 5.8: The phase contents (vol.%) of different alloy compositions as calculated from the phase diagram and measured by Rietveld and EBSD analysis.

| **Mo-3Si-1B wt.%** | | | |
|---|---|---|---|
| | **Phase Diagram** | **Rietveld Analysis** | **EBSD Analysis** |
| **$Mo_{ss}$** | 56.8 | 55.9 | 56.9 |
| **A15** | 16.0 | 17.9 | 20.3 |
| **T2** | 27.2 | 26.2 | 22.6 |

| **Mo-2.51Si-0.84B wt.%** | | | |
|---|---|---|---|
| | **Phase Diagram** | **Rietveld Analysis** | **EBSD Analysis** |
| **$Mo_{ss}$** | 64.8 | 66.2 | 66.1 |
| **A15** | 12.2 | 12.8 | 17.2 |
| **T2** | 23.0 | 21.0 | 16.7 |

| **Mo-2.21Si-0.74B wt.%** | | | |
|---|---|---|---|
| | **Phase Diagram** | **Rietveld Analysis** | **EBSD Analysis** |
| **$Mo_{ss}$** | 69.8 | 70.9 | 71.5 |
| **A15** | 9.8 | 7.6 | 13.6 |
| **T2** | 20.4 | 21.5 | 14.9 |

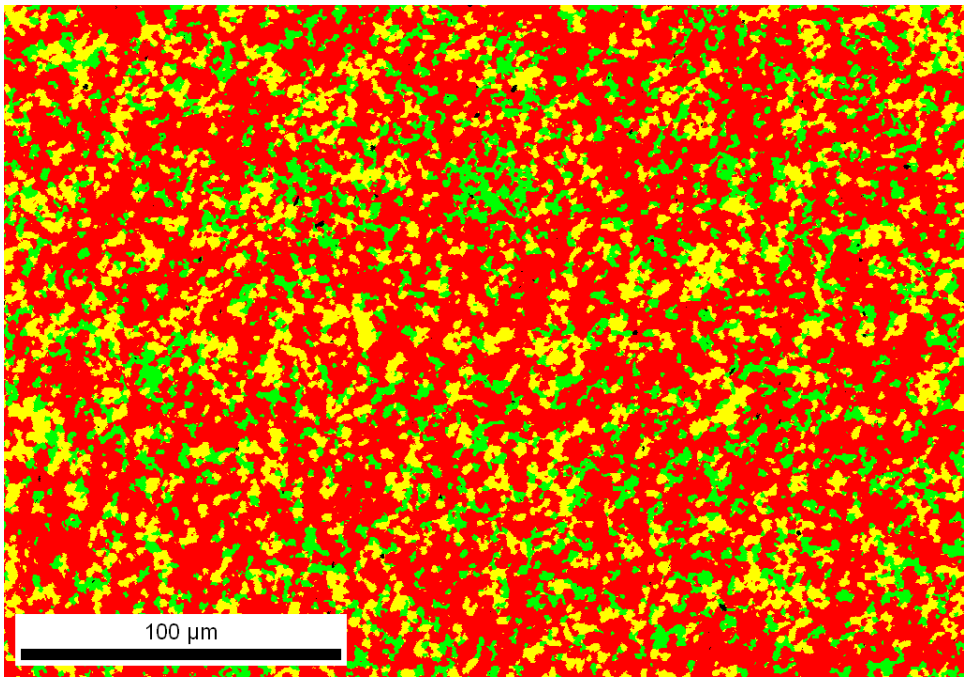


Figure 5.20: EBSD phase map of the Mo-2.51Si-0.84B wt.% alloy with 66.1 vol.% Mo$_{ss}$, processed with hBN powder (1600°C, 6 hours).

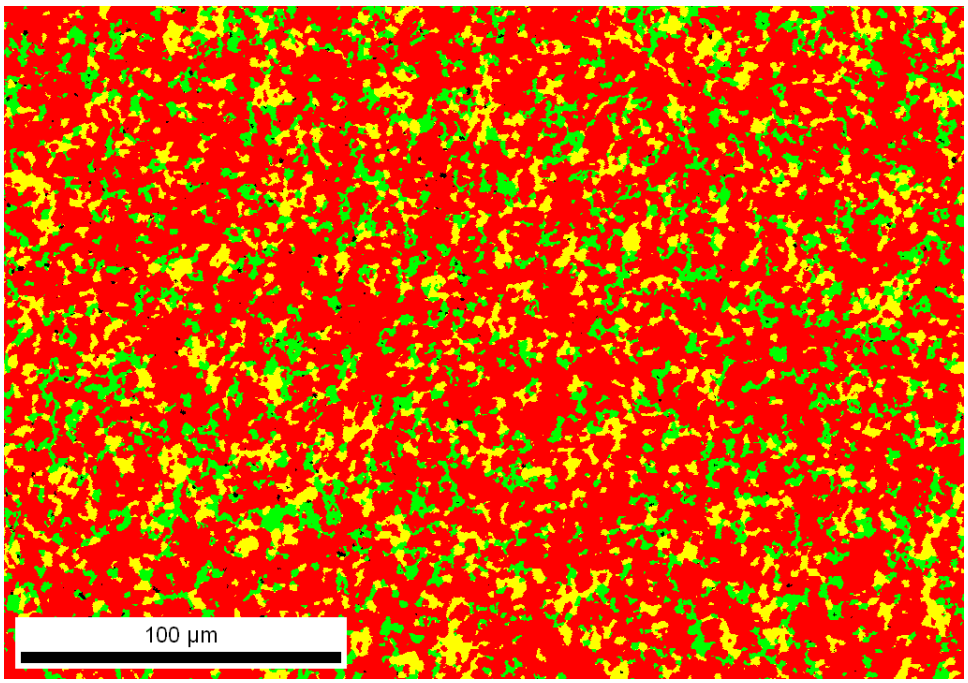


Figure 5.21: EBSD phase map of the Mo-2.21Si-0.74B wt.% alloy with 71.5 vol.% Mo$_{ss}$, processed with hBN powder (1600°C, 6 hours).

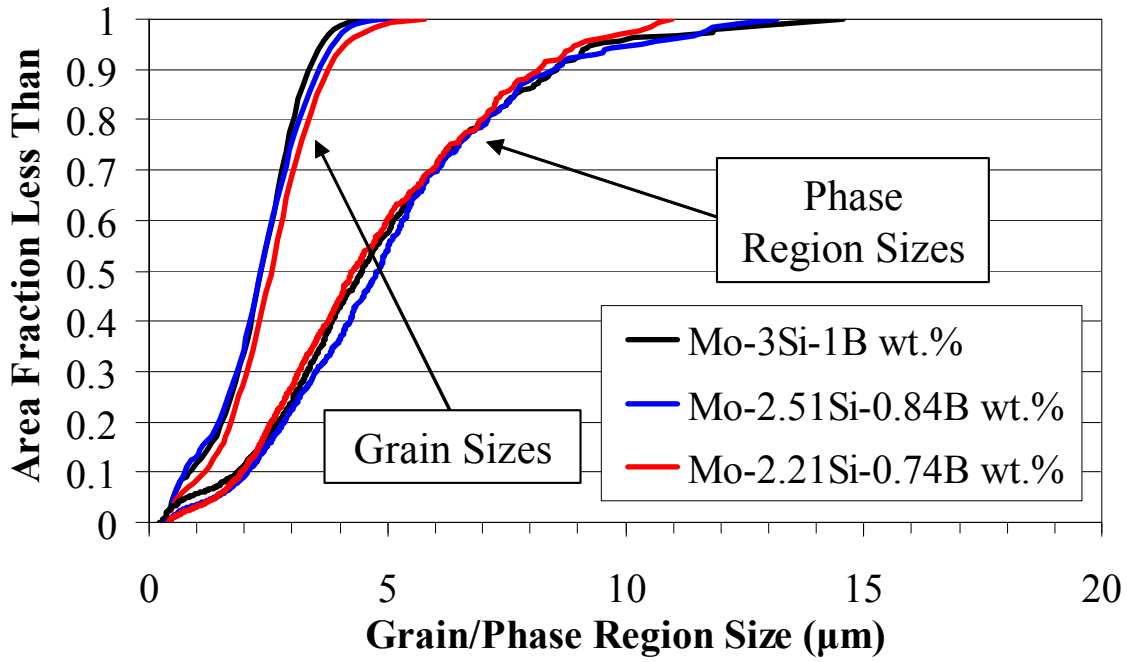


Figure 5.22: The cumulative 'phase region' and grain size distributions of the A15 phase, measured for alloys of different composition, processed with hBN reactant powder (1600°C, 6 hours).

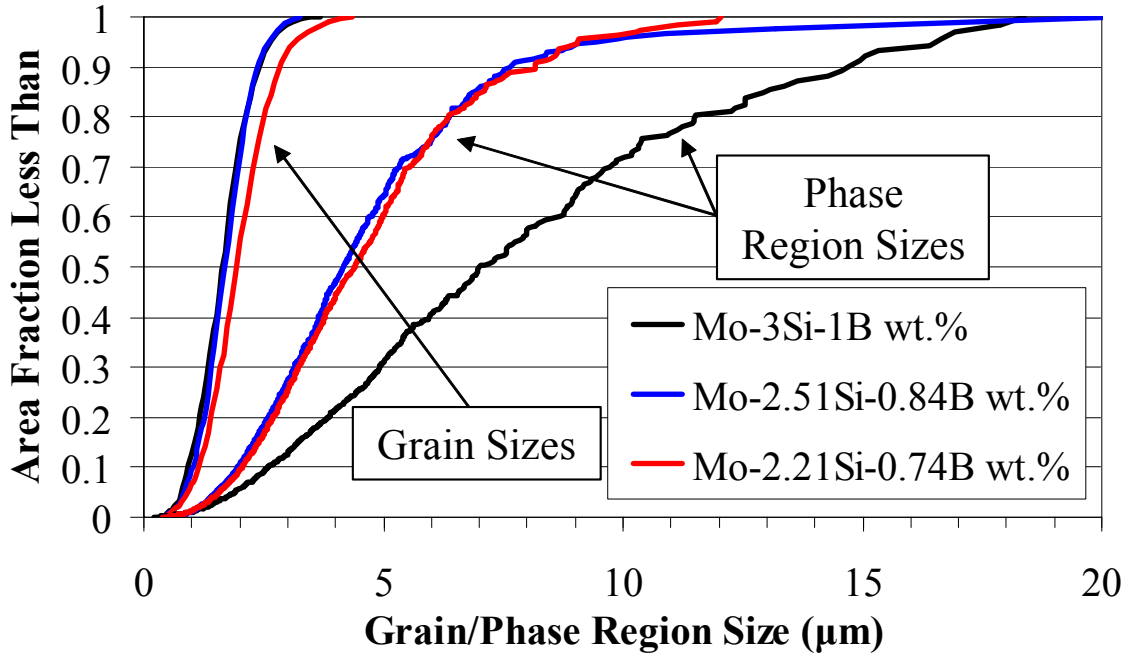


Figure 5.23: The cumulative 'phase region' and grain size distributions of the T2 phase, measured for alloys of different composition, processed with hBN reactant powder (1600°C, 6 hours).

Table 5.9: The $d_{10}$, $d_{50}$ and $d_{90}$ parameters from the 'phase region' size distributions for alloys of different composition, processed with hBN reactant powder (1600°C, 6 hours).

| | A15 Phase | | | T2 Phase | | |
|---|---|---|---|---|---|---|
| Composition | $d_{10}$ (μm) | $d_{50}$ (μm) | $d_{90}$ (μm) | $d_{10}$ (μm) | $d_{50}$ (μm) | $d_{90}$ (μm) |
| Mo-3Si-1B | 1.8 | 4.5 | 8.6 | 2.6 | 7.0 | 14.7 |
| Mo-2.51Si-0.84B | 2.1 | 4.8 | 8.5 | 2.0 | 4.2 | 7.7 |
| Mo-2.21Si-0.74B | 1.9 | 4.3 | 8.2 | 2.1 | 4.4 | 8.2 |

Table 5.10: The $d_{10}$, $d_{50}$ and $d_{90}$ parameters from the grain size distributions for alloys of different composition, processed with hBN reactant powder (1600°C, 6 hours).

| | A15 Phase | | | T2 Phase | | |
|---|---|---|---|---|---|---|
| Composition | $d_{10}$ (μm) | $d_{50}$ (μm) | $d_{90}$ (μm) | $d_{10}$ (μm) | $d_{50}$ (μm) | $d_{90}$ (μm) |
| Mo-3Si-1B | 0.8 | 2.3 | 3.4 | 0.9 | 1.6 | 2.4 |
| Mo-2.51Si-0.84B | 0.7 | 2.3 | 3.6 | 1.0 | 1.7 | 2.4 |
| Mo-2.21Si-0.74B | 1.2 | 2.6 | 3.8 | 1.1 | 1.9 | 2.8 |

For the three alloys, both the A15 grain size and phase region size distributions were independent of the composition. The T2 grain sizes were also relatively independent of the composition, as were the phase region sizes for the Mo-2.51Si-0.84B and Mo-2.21Si-0.74B wt.% alloys. The observation that the sizes of the clusters were not dependent on the volume fraction of the phase indicates that they are instead controlled by the original dispersion of the reactant powder. This was not observed for T2 in the Mo-3Si-1B wt.% alloy, but the large T2 phase regions may be the result of smaller clusters impinging on each other due to the higher fraction of the phase.

Qualitatively, it is observed that the $Mo_{ss}$ matrix becomes more continuous and the intermetallics are more dispersed with decreasing intermetallic content. The spacing of the intermetallics is proposed to affect the oxidation resistance of Mo-Si-B alloys. A

stereological parameter called the mean free path, described in Chapter 3, was used to quantify the spacing of the intermetallic phases for the three different compositions, Figure 5.24. This parameter is the average edge-to-edge spacing of the intermetallics and represents the uninterrupted distance in the $Mo_{ss}$ matrix phase. One-half of the mean free distance can be seen as the average distance the glass phase must spread to cover the $Mo_{ss}$ matrix regions in order to create a continuous surface oxide. Increasing the $Mo_{ss}$ content from 57 to 72 vol.% resulted in an over 50% increase in the mean free path for both intermetallic phases. This expected to hinder the ability to quickly form a continuous oxide layer during the transient oxidation stage, but it will also be shown in Chapter 6 that the onset of ductility is reduced for lower intermetallic contents. The development of Mo-Si-B alloys for a given application will be dependent on finding a favorable compromise between mechanical properties and oxidation resistance.

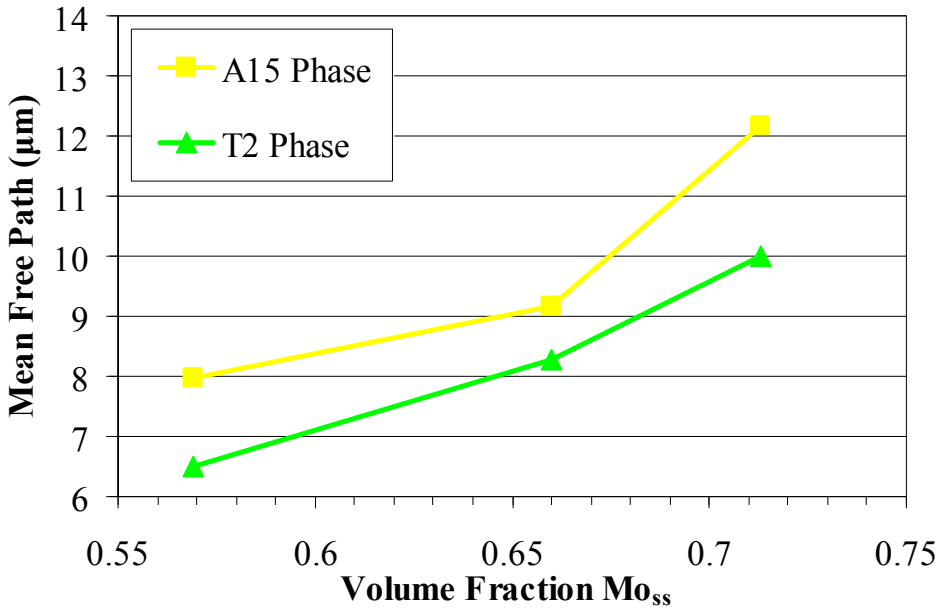


Figure 5.24: The mean free path, $\lambda$, of the A15 and T2 phases as a function of $Mo_{ss}$ volume fraction, for alloys processed with hBN powder (1600°C, 6 hours).

## 5.4 Microstructure Refinement by Hot-Isostatic Pressing at Low Temperatures

Refining the microstructural scale of the Mo-Si-B alloys may improve strength according to the Hall-Petch relationship and it has also been established that a close spacing of intermetallic phases reduces the level of transient weight loss during oxidation. It was discussed in Chapter 4.3 that the reactions to form A15 and T2 are complete after two hours at 1300°C. This presents the opportunity to densify the alloys by hot-isostatic pressing at low temperatures to minimize grain growth.

### 5.4.1 Hot-Isostatic Pressing – 1300°C

Low temperature sintering was discussed in Chapter 4.3 for the Mo-3Si-1B wt.% alloys prepared with hBN powder. A sample was pre-fired at 1300°C for 2 hours, sealed in an evacuated steel canister and HIPed at 1300°C and 30ksi for 6 hours. The resulting alloy had a very fine microstructure as compared to corresponding samples fired to 1600°C. The EBSD phase map is shown in Figure 5.25. The scan was taken over a 150×150μm region and the step size was reduced to 150nm due to the fine grain size.

It can be seen that there is significant clustering of the T2 phase. This is further illustrated in Figure 5.26, which compares the EBSD phase maps of the T2 phase for the alloys processed at 1300°C and 1600°C. The lower diffusion rates at 1300°C limited the grain growth and redistribution of the T2 phase. This example further illustrates that the dispersion of the T2 phase is dependent on the original dispersion of the BN powder.

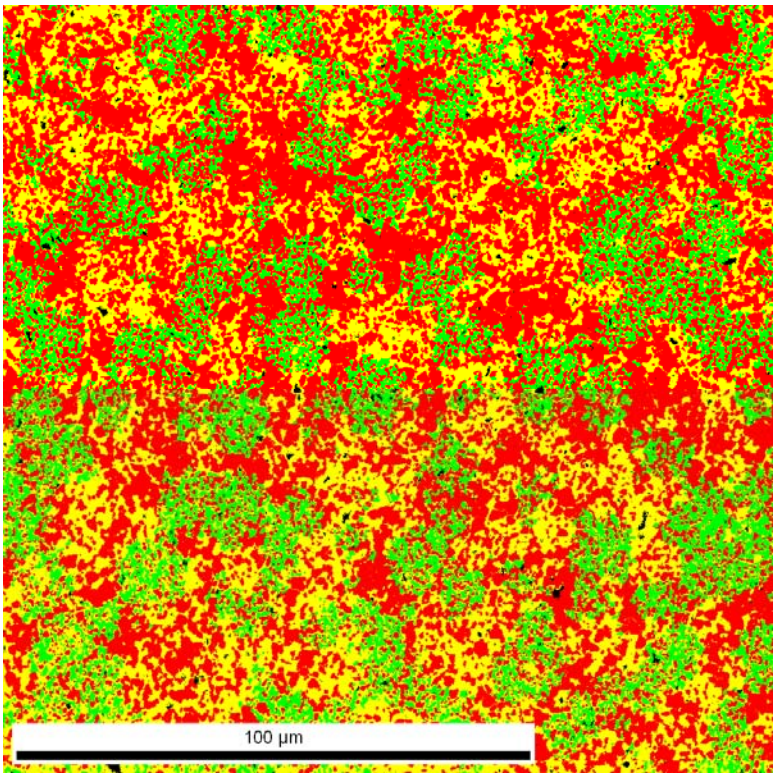


$Mo_{ss}$ = A15 = T2 =

Figure 5.25: EBSD phase map of a Mo-3Si-1B wt.% alloy produced with hBN powder and consolidated at 1300°C, measured with a 150nm step size.

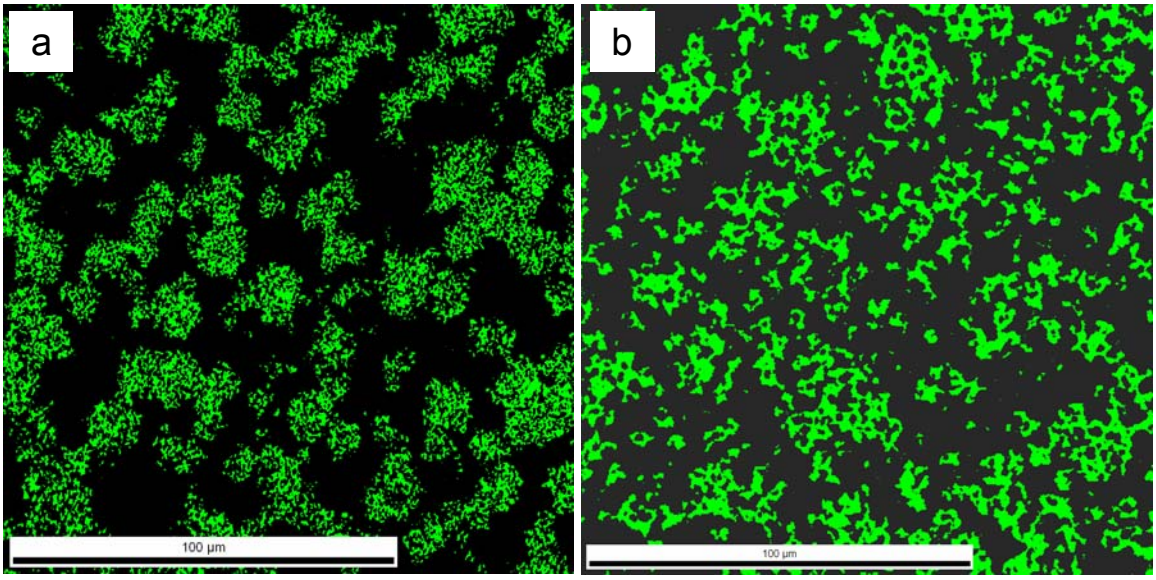


Figure 5.26: T2 phase maps for the Mo-3Si-1B wt.% alloy produced with hBN powder, processed at: (a) 1300°C and (b) 1600°C.

The phase contents measured by EBSD for specimens HIPed at 1300°C are listed in Table 5.11. The contents measured from analyses using two different step sizes are compared to those predicted from the 1600°C phase diagram. There is a discrepancy in the measured phase volumes between the 300nm and 150nm step sizes. During the EBSD data acquisition, EDS data was used to help differentiate between the molybdenum and A15 phases which both have a BCC crystal structure. The interaction volume of the EDS measurement may have exceeded the 150nm step size and compromised the ability to accurately distinguish the $Mo_{ss}$ and A15 phases. The net result was a reduction in $Mo_{ss}$ (7.5%) and an increase in A15 (11.1%) for the 150nm step size. The T2 phase has a tetragonal crystal structure and its identification is based solely on the EBSD identification which has a smaller interaction volume and is less likely to be compromised by the 150nm step size. Further analysis will be conducted to determine the resolution limit of the EBSD/EDS technique for the Mo-Si-B alloys.

The grain sizes for the alloy HIPed at 1300°C are compared to those of the corresponding alloy pressureless sintered at 1600°C for 6 hours, Figure 5.27 and the $d_{10}$, $d_{50}$ and $d_{90}$ parameters are listed in Table 5.12. Lowering the sintering temperature from 1600°C to 1300°C reduced the grain sizes of all three phases by over a factor of two.

Table 5.11: The phase contents (vol.%) measured by EBSD analysis for the Mo-3Si-1B wt.% alloy densified at 1300°C, compared to the 1600°C equilibrium composition.

| | **Phase Diagram (1600°C)** | **EBSD Analysis 300nm Step Size (1300°C)** | **EBSD Analysis 150nm Step Size (1300°C)** |
|---|---|---|---|
| **$Mo_{ss}$** | 56.8 | 55.4 | 47.8 |
| **A15** | 16.0 | 22.3 | 33.4 |
| **T2** | 27.2 | 22.3 | 18.8 |

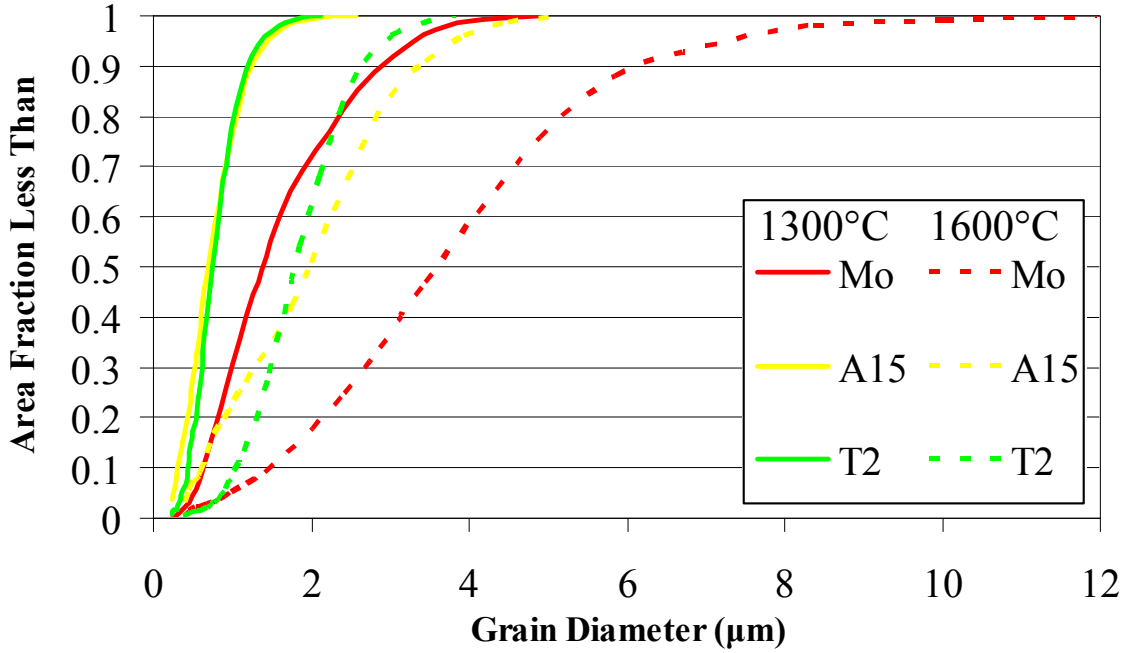


Figure 5.27: The grain size distributions of the phases in the Mo-3Si-1B wt.% alloy processed with hBN powder, for samples densified at 1300°C and 1600°C.

Table 5.12: The $d_{10}$, $d_{50}$ and $d_{90}$ parameters of the grain size distributions for Mo-3Si-1B wt.% alloys densified at 1300°C and 1600°C.

| | **1300°C, 2h (PS) 1300°C, 6h (HIP)** | | | **1600°C, 6h (PS)** | | |
|---|---|---|---|---|---|---|
| | $d_{10}$ (µm) | $d_{50}$ (µm) | $d_{90}$ (µm) | $d_{10}$ (µm) | $d_{50}$ (µm) | $d_{90}$ (µm) |
| **$Mo_{ss}$** | 0.6 | 1.4 | 2.9 | 1.5 | 3.6 | 6.1 |
| **A15** | 0.3 | 0.7 | 1.2 | 0.6 | 2.0 | 3.4 |
| **T2** | 0.4 | 0.7 | 1.2 | 1.1 | 1.8 | 2.6 |

### 5.4.2 Hot-Isostatic Pressing – 1300°C - Attrition Milled Powder

The Mo-3Si-1B wt.% sample sintered and HIPed at 1300°C had a significant degree of clustering of the T2 phase. The powder used to produce the alloy was attrition milling for one hour to break up agglomerates and improve the dispersion of the reactants. The BET surface area of the powder mixture was measured after 30 and 60 minutes of attrition milling, Table 5.13. Even for the relatively short milling time, the surface area was increased 28%.

A sample of the attrition milled alloy powder was uniaxially pressed, pre-fired at 1300°C for 2 hours, sealed in an evacuated steel canister and then HIPed at 1300°C and 30ksi for 6 hours. EBSD analysis was conducted using a step size of 300nm, Figure 5.28. The measured phase contents are given in Table 5.11. The phase map of the T2 phase is compared to the non-attrition milled sample in Figure 5.29. The grain sizes appear larger for the attrition milled sample because of the larger step size (300nm) that was used for the EBSD analysis, but it can be seen that even one hour of attrition milling significantly improved the dispersion of the T2 phase. The regions void of T2 are fewer and smaller than in the non-attrition milled sample.

Table 5.13: The specific surface areas measured for the Mo-$Si_3N_4$-hBN powder mixture after attrition milling.

| **Mill Time (minutes)** | **Surface Area ($m^2/g$)** |
|---|---|
| 0 | 2.32 |
| 30 | 2.52 |
| 60 | 2.98 |

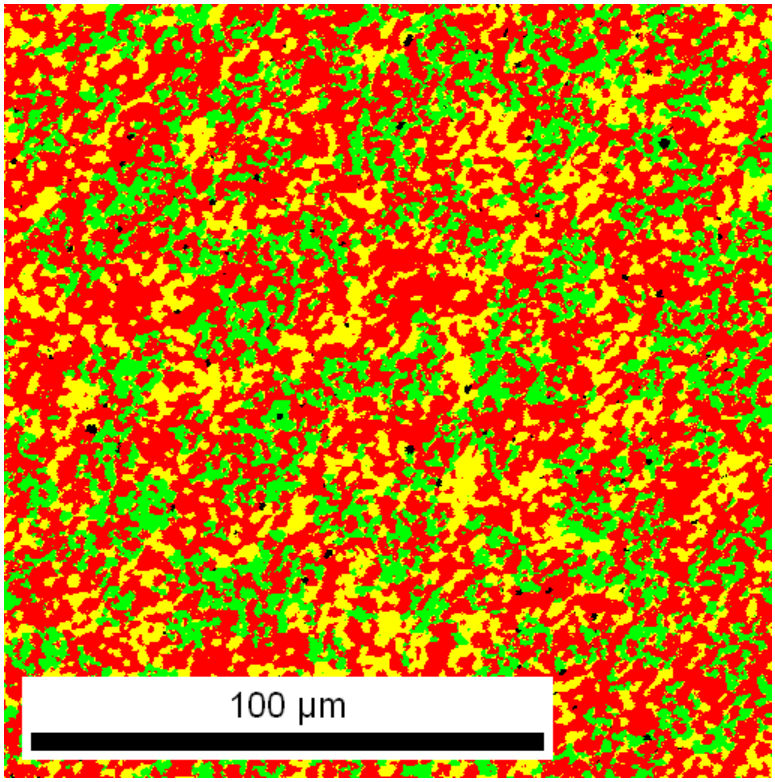

Figure 5.28: EBSD phase map of the Mo-3Si-1B wt.% alloy prepared from attrition milled powder and consolidated at 1300°C, measured with a 300nm step size.

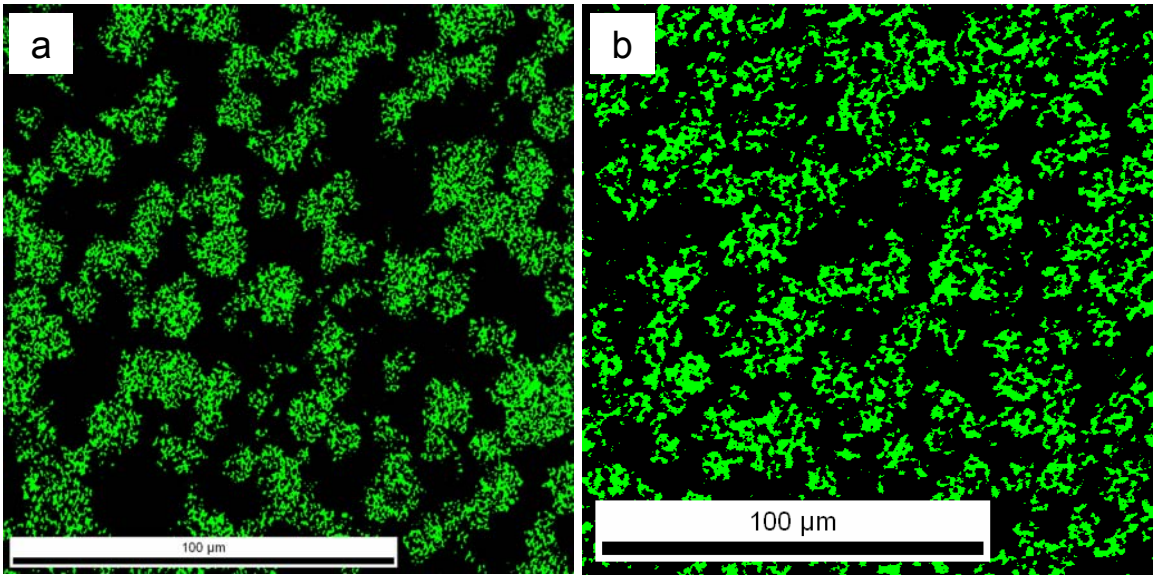

Figure 5.29: T2 phase distribution for Mo-3Si-1B wt.% alloys produced with hBN powder: (a) 1300°C and (b) 1300°C with attrition milled powder.

# CHAPTER 6

# MECHANICAL TESTING

High-temperature tensile tests were conducted on Mo-3Si-1B and Mo-2Si-1B wt.% alloys prepared with the Cerac hBN powder. Bars of the material were formed by cold-isostatic pressing, sintered at 1600°C for 6 hours, then encapsulated and HIPed at 1500°C and 30ksi for 6 hours. The 15×15×60mm HIPed bars were given to Dr. Sharvan Kumar at Brown University for mechanical testing. Dog-bone geometry specimens were prepared by electro-discharge machining and the flat surfaces were polished to a 1μm finish. Tests were conducted under vacuum at an initial strain rate of $10^{-4}$ $s^{-1}$ and the engineering stress-strain curves were measured as a function of temperature.

## 6.1 Tensile Testing of the Mo-3Si-1B wt.% Alloy

The Mo-3Si-1B wt.% alloy achieved a density of 99.4% T.D. A portion of the bar was examined by SEM and the fraction of silica inclusions was measured to be 0.8 vol.% by area analysis. A representative EBSD phase map for the alloy is shown in Figure 6.1. The complete analysis of the Mo-3Si-1B wt.% alloy prepared with hBN was given in Chapter 5.

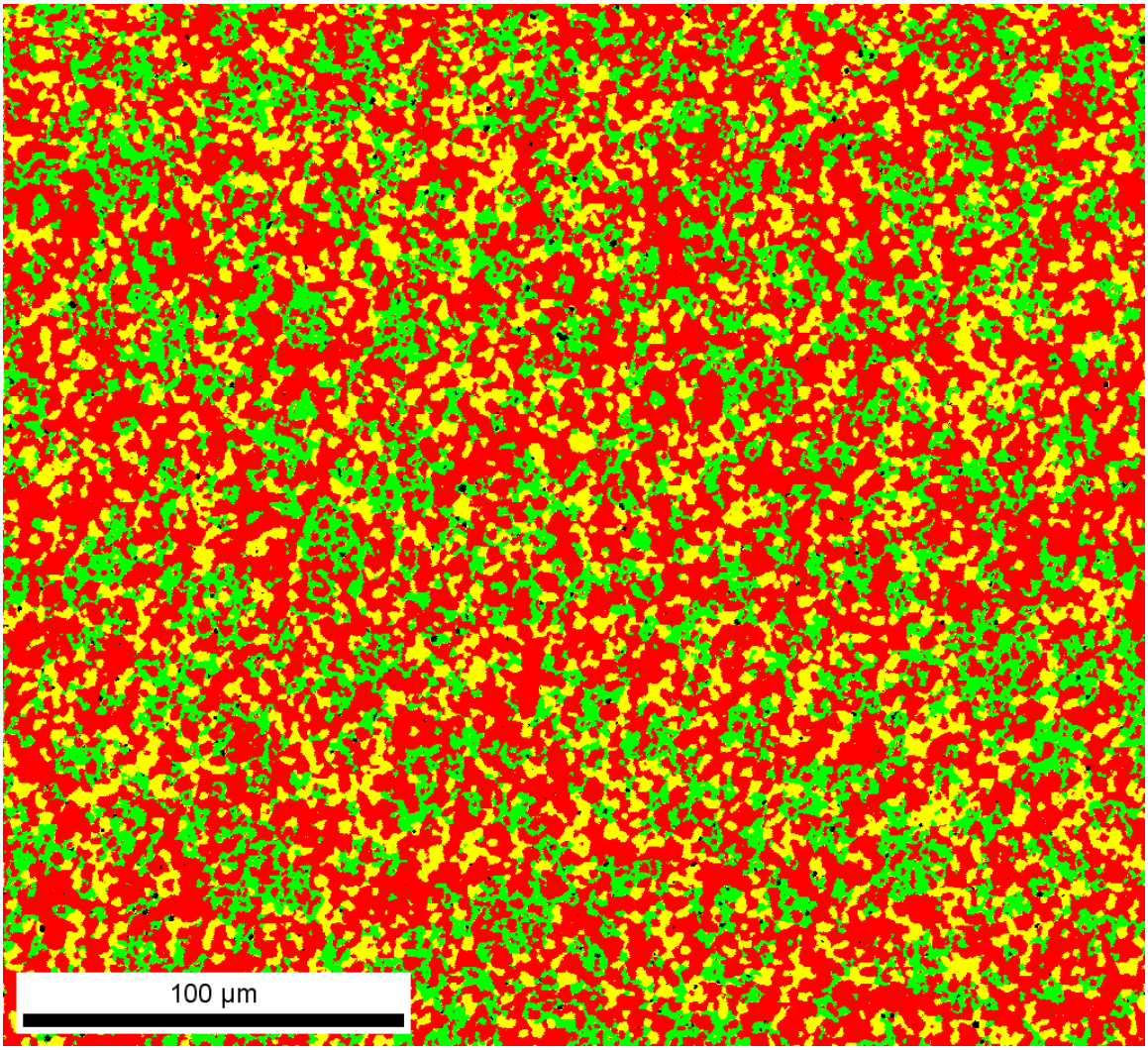


$Mo_{ss}$ = A15 = T2 =

Figure 6.1: A representative EBSD phase map of the Mo-3Si-1B wt.% alloy used for high-temperature tensile testing. The alloy was prepared with hBN powder and sintered at 1600°C for 6 hours, followed HIPing at 1500°C and 30ksi for 6 hours.

Tensile tests were performed at 100°C increments between 900 and 1300°C, Figure 6.2. Only one sample was tested at each temperature due to limited access to the high temperature mechanical tester. The 0.2% yield stress (YS), the ultimate tensile strength (UTS), the total elongation-to-failure and the plastic strain for the five tests are listed in Table 6.1. The 0.2% yield stress is defined as the stress at which 0.2% plastic strain is observed. The modulus of elasticity could not be determined from the stress-strain curves in these experiments because the compliance of the test fixture was not calibrated.

The specimen tested at 900°C failed in a completely brittle manner and no plastic deformation was observed. Failure occurred at a low load and the sample appears to have fractured prematurely. Flaws dictate the strength of brittle materials and premature fracture is often due to internal defects in the material or surface damage introduced by machining. The source of the failure is typically indicated by the presence of a 'fracture mirror', which is a smooth, circular region emanating from origin of the fracture [89]. An SEM image of the fracture surface clearly shows a fracture mirror in the shape of a quarter circle emanating from a corner of the sample, which is a likely location for cracks to form during machining, Figure 6.3.

A high strength value was measured at 1000°C but no plastic strain was observed. Plastic strain began to occur in the alloy at 1100°C. At 1200°C the stress-strain curve reached a plateau before fracture, indicating the onset of ductile behavior. At 1300°C the alloy reached an ultimate tensile strength, followed by significant plastic flow. Analysis of the fracture surfaces shows that all of the samples failed by intergranular fracture, Figure 6.4 to Figure 6.7. The fracture surfaces up to 1100°C indicate failure in a

completely brittle manner. At 1200°C there was some evidence of ductility and at 1300°C significant plastic deformation was observed. A high magnification image of the 1300°C fracture surface shows pullout of the molybdenum grains, Figure 6.8.

There is little tensile data for Mo-Si-B alloys in the literature for comparison. Jéhanno et al. conducted tensile tests of Mo-3Si-1B wt.% alloys, as discussed in Chapter 2.4. The alloys were formed by inert gas atomization, consolidated by hot-isostatic pressing and extruded to break up the intermetallic matrix. Tensile testing was only conducted up to 1100°C. Both the reported values of the 0.2% YS and UTS are approximately 20MPa lower than measured for the reaction synthesis alloy, although the reported elongation of 21.5% indicates a lower DBTT. It has been demonstrated that the DBTT temperature can be decreased as much as 150°C by transitioning from an intermetallic matrix to a continuous $Mo_{ss}$ matrix [43]. Continued effort should be directed at improving the processing techniques to yield a more continuous $Mo_{ss}$ matrix.

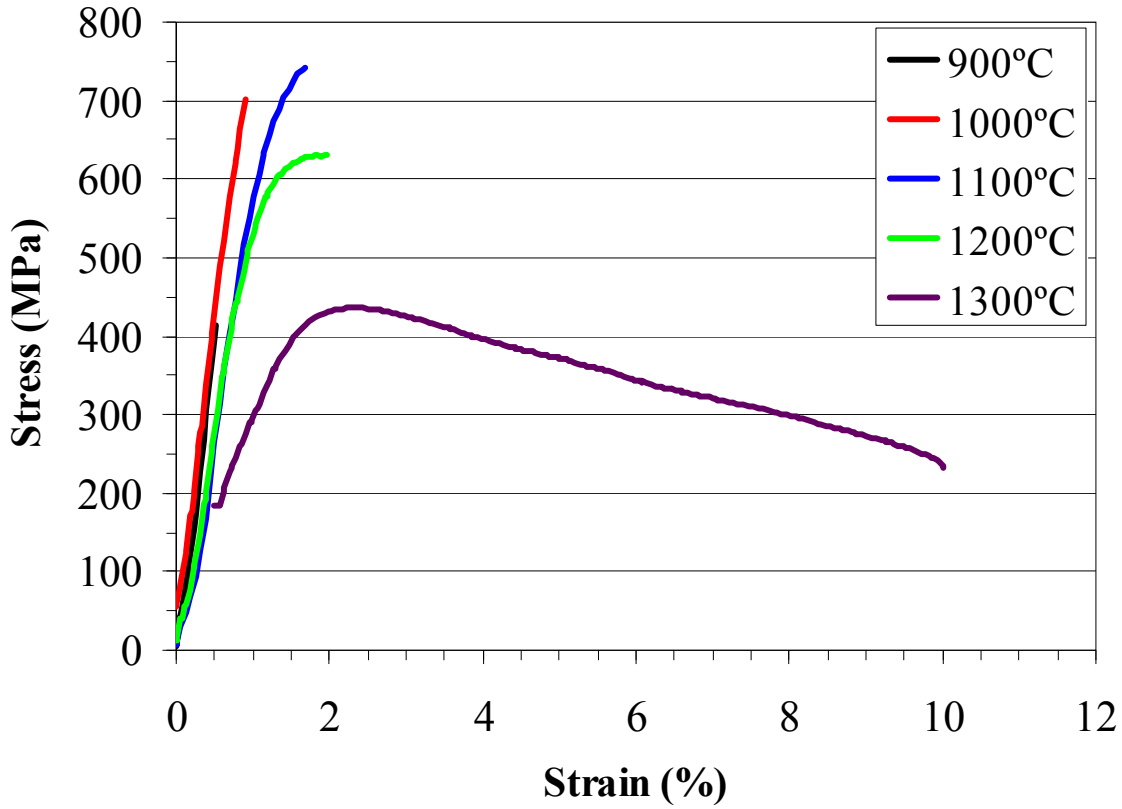


Figure 6.2: Stress-strain curves for the Mo-3Si-1B wt.% alloy, measured by tensile testing at a strain rate of $10^{-4}$ $s^{-1}$.

Table 6.1: The 0.2% yield stress, ultimate tensile strength and elongation-to-failure for the Mo-3Si-1B wt.% samples tested at a strain rate of $10^{-4}$ $s^{-1}$.

| Temperature (°C) | 0.2% YS (MPa) | UTS (MPa) | Elongation-to-Failure (%) | Plastic Strain (%) |
|---|---|---|---|---|
| 900 | - | 415 | 0.5 | - |
| 1000 | - | 702 | 0.9 | - |
| 1100 | 683 | 742 | 1.7 | 0.5 |
| 1200 | 577 | 630 | 2.0 | 0.9 |
| 1300 | 419 | 436 | 10.0 | 9.3 |

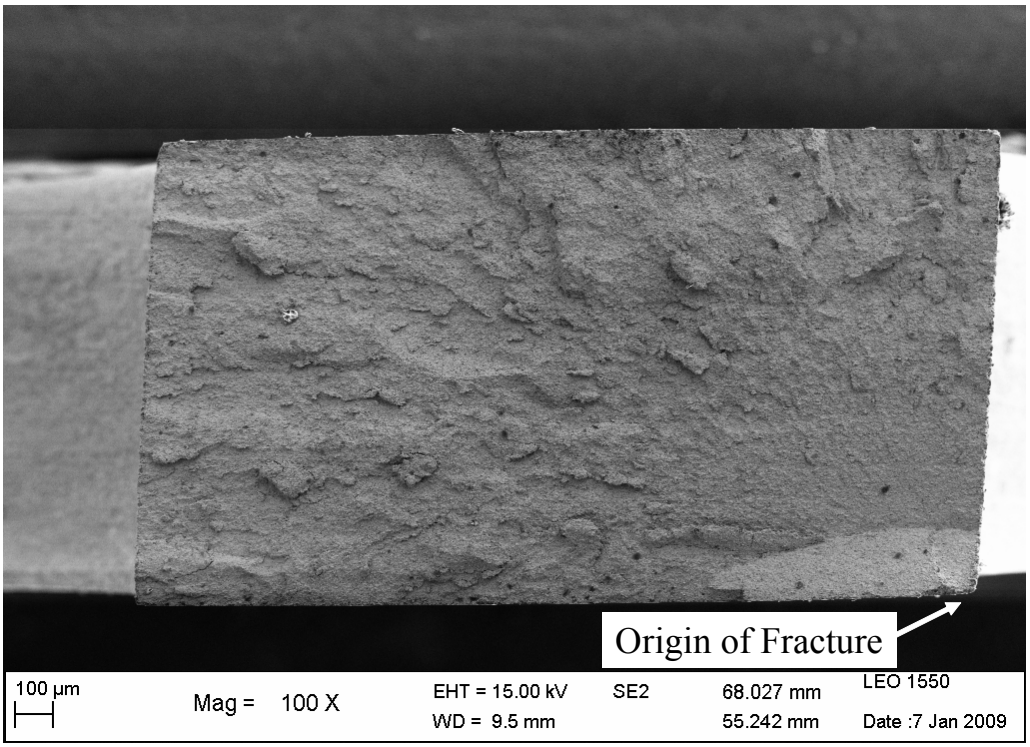


Figure 6.3: The fracture surface of the Mo-3Si-1B wt.% alloy tested at 900°C, with the likely origin of fracture indicated.

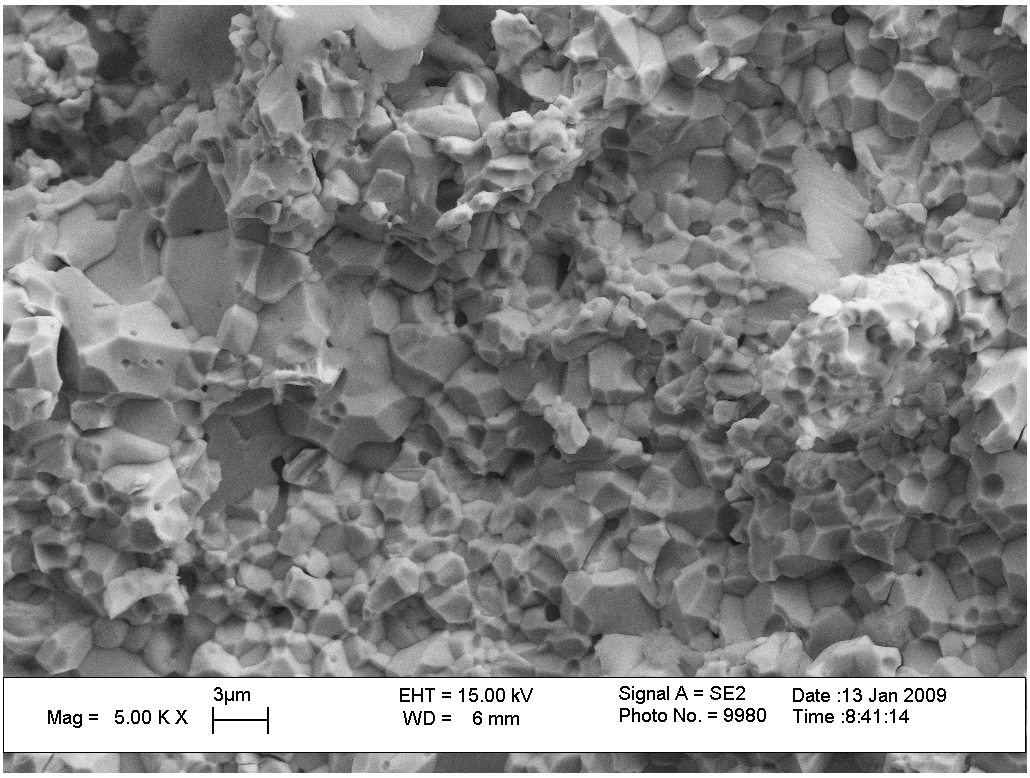


Figure 6.4: The fracture surface of the Mo-3Si-1B wt.% alloy tested at 1000°C.

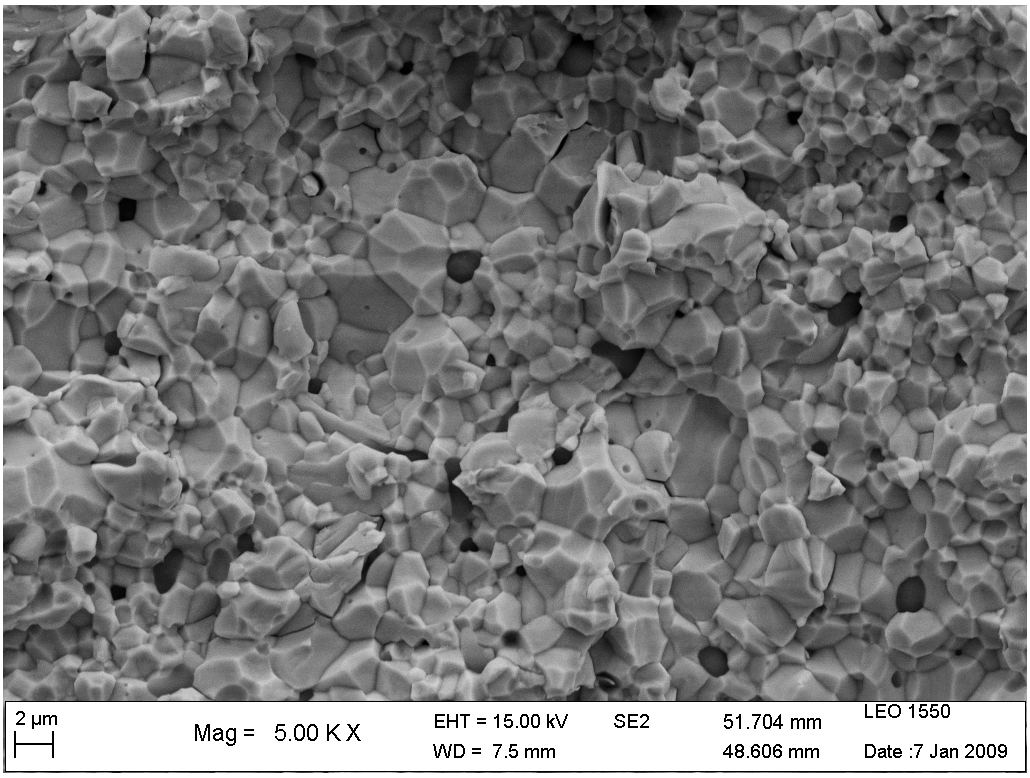

Figure 6.5: The fracture surface of the Mo-3Si-1B wt.% alloy tested at 1100°C.

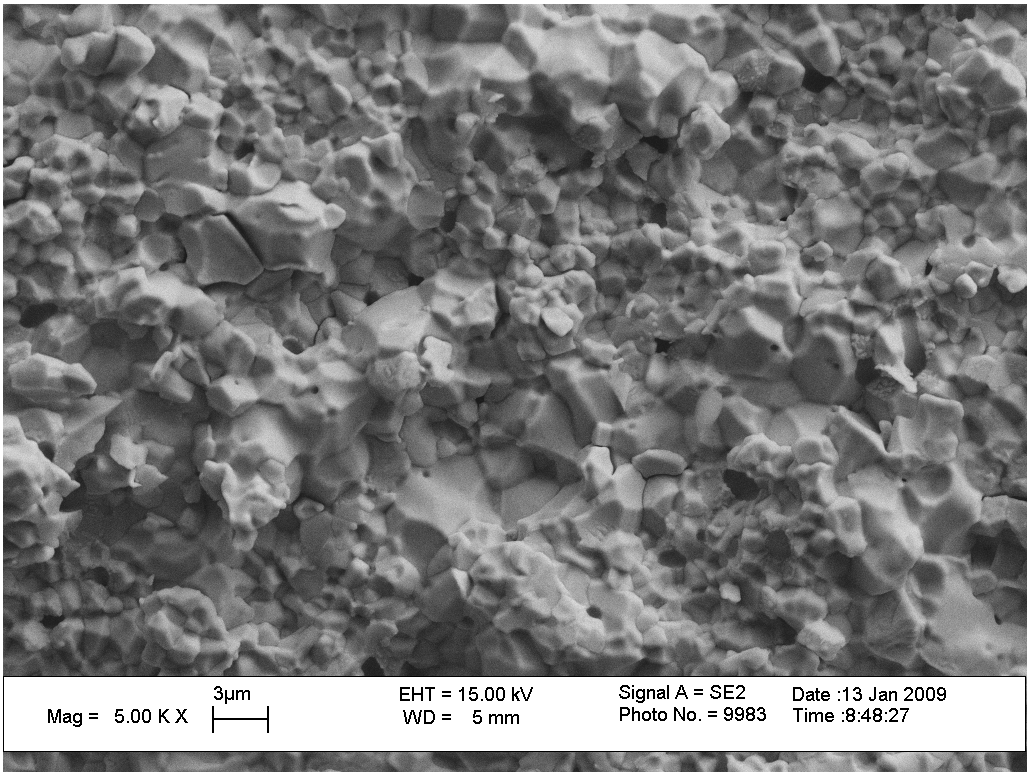

Figure 6.6: The fracture surface of the Mo-3Si-1B wt.% alloy tested at 1200°C.

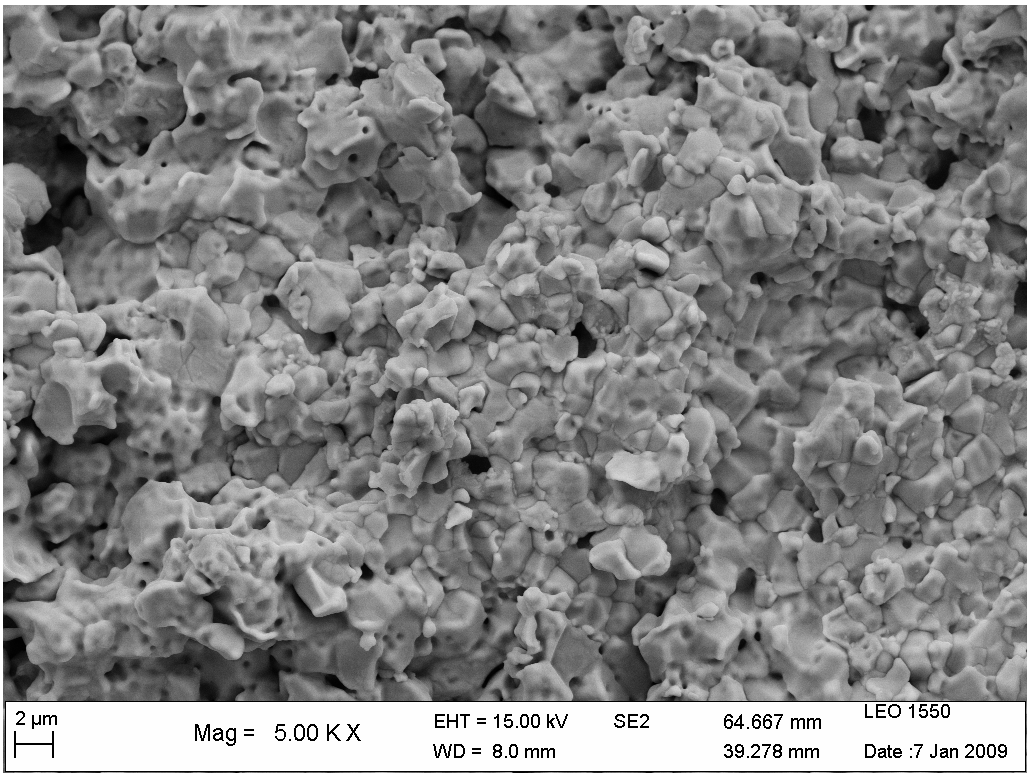

Figure 6.7: The fracture surface of the Mo-3Si-1B wt.% alloy tested at 1300°C.

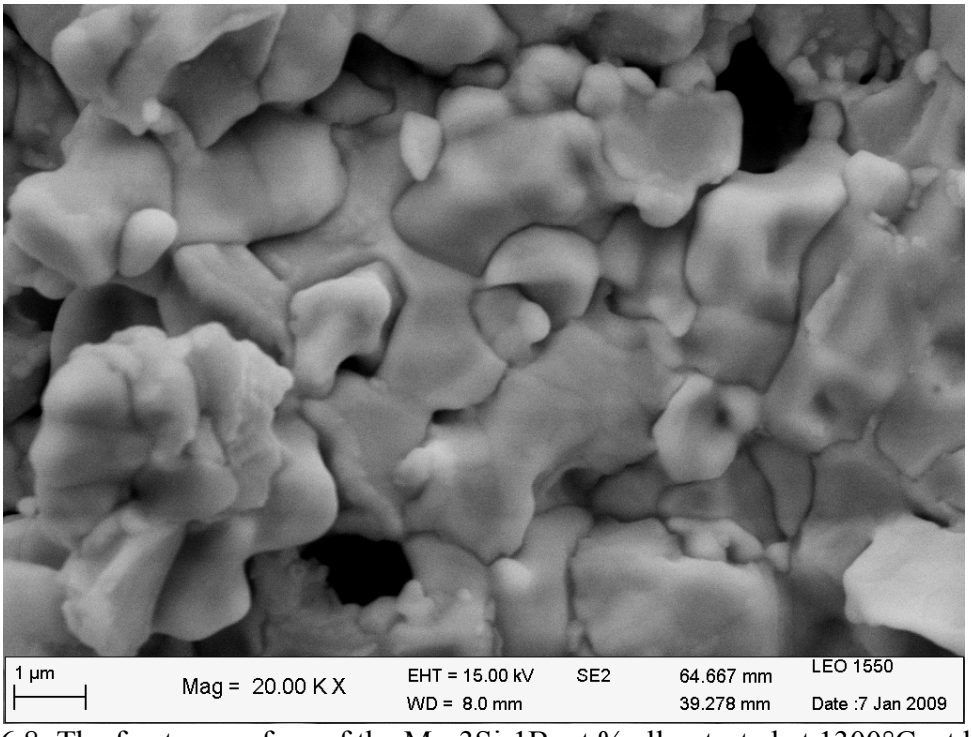

Figure 6.8: The fracture surface of the Mo-3Si-1B wt.% alloy tested at 1300°C, at high magnification.

### 6.2 Tensile Testing of the Mo-2Si-1B wt.% Alloy

A HIPed bar of composition Mo-2Si-1B wt.% was prepared by the nitride reactions for comparison to previous studies conducted by Kumar [37,38]. The procedure for preparing the alloy and the dog-bone tensile specimens was the same as previously discussed. After hot-isostatic pressing, the sample achieved a density of 99.8% of theoretical. A portion of the bar was examined by SEM and the volume fraction of silica inclusions was measured by area analysis as 0.03 vol.%. An EBSD phase map of the HIPed alloy is shown in Figure 6.9. This composition was reported by Kumar to be a two-phase alloy of $Mo_{ss}$-T2 with approximately 38 vol.% of the T2 phase. The volume fractions of the phases determined from EBSD analysis were compared to those calculated from the ternary phase diagram and measured by Rietveld analysis, Table 6.2. It can be seen that the Mo-2Si-1B wt.% alloy contains a small fraction of the A15 phase and is actually in the three-phase field. The grain size distributions of A15 and T2 phases were measured from EBSD analysis and are compared to the phase region size distributions, Figure 6.10. The $d_{10}$, $d_{50}$ and $d_{90}$ size parameters for the distributions are given in Table 6.3.

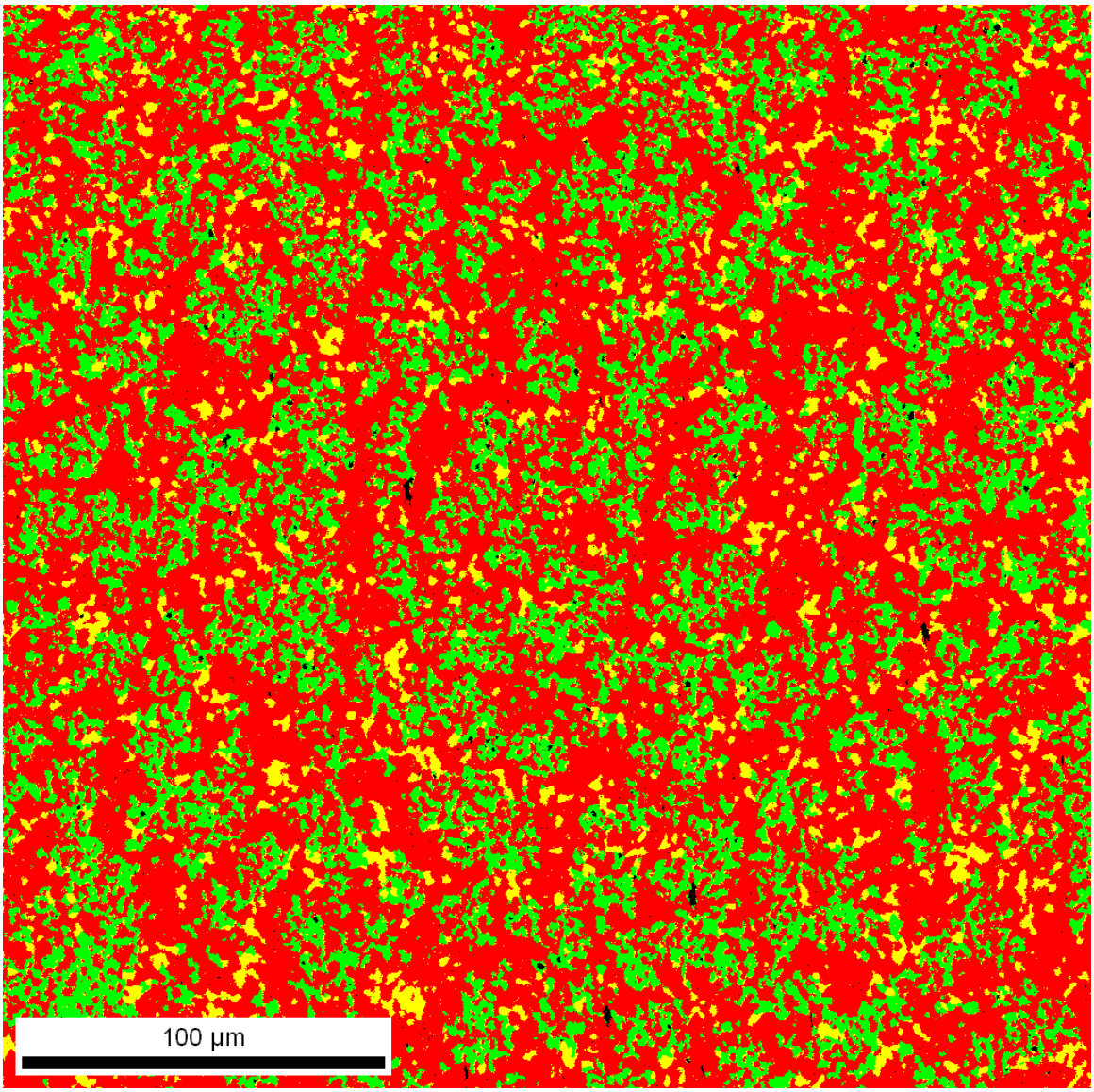


Figure 6.9: An EBSD phase map measured from a portion of the Mo-2Si-1B wt.% alloy used for high-temperature tensile testing. The alloy was prepared with hBN powder and sintered at 1600°C for 6 hours, followed HIPing at 1500°C and 30ksi for 6 hours.

Table 6.2: A comparison of the phase contents (vol.%) of the Mo-2Si-1B wt.% alloy calculated from the phase diagram and measured by Rietveld and EBSD analysis.

| | **Phase Diagram** | **Rietveld Analysis** | **EBSD Analysis** |
|---|---|---|---|
| **Mo$_{ss}$** | 69.5 | 64.7 | 67.2 |
| **A15** | 2.8 | 4.6 | 9.2 |
| **T2** | 27.6 | 30.6 | 23.7 |

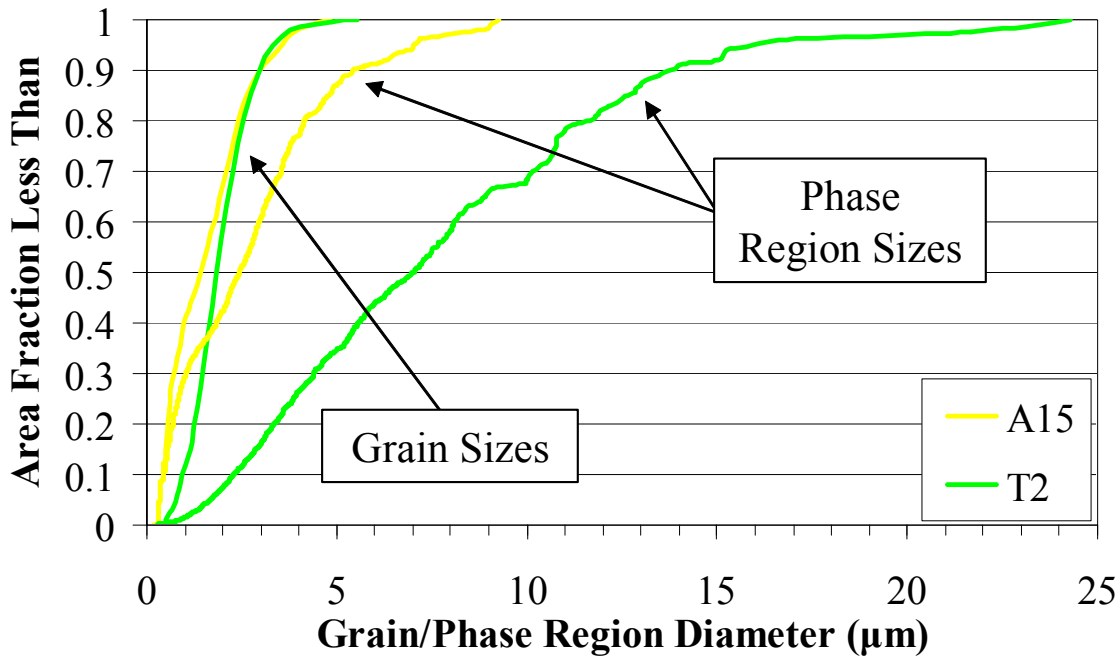


Figure 6.10: The grain size and phase size distributions for the intermetallic phases in the Mo-2Si-1B wt.% alloy used for high-temperature tensile testing.

Table 6.3: The $d_{10}$, $d_{50}$ and $d_{90}$ parameters for the grain size and phase size distributions for the Mo-2Si-1B wt.% alloy processed with hBN and fired at 1600°C for 6h.

| | **A15 Phase** | | | **T2 Phase** | | |
|---|---|---|---|---|---|---|
| | $d_{10}$ (µm) | $d_{50}$ (µm) | $d_{90}$ (µm) | $d_{10}$ (µm) | $d_{50}$ (µm) | $d_{90}$ (µm) |
| **Grain Size** | 0.5 | 1.4 | 3.0 | 1.0 | 1.9 | 2.9 |
| **Phase Region Size** | 0.5 | 2.4 | 5.4 | 2.3 | 7.0 | 13.8 |

High-temperature tensile tests were performed between 1000°C and 1200°C, Figure 6.11. The 0.2% yield stress, ultimate tensile strength, total elongation-to-failure and plastic strain are listed in Table 6.4. Both specimens tested at 1000°C fractured in a brittle manner and failed outside of the gauge sections, Figure 6.12. This was probably due to cross loading of the specimens and indicates the strengths measured are depressed from the actual values. The plateau of the stress-strain at 1100°C curve indicates the

onset of ductility, although ductile behavior was not evident in the fracture image, Figure 6.13. At 1200°C there was significant elongation and ductile failure was evident from the fracture surface, Figure 6.14. An image of the necked region of the specimen reveals that the specimen sustained a high level of damage before failure, Figure 6.15.

No comparative tensile test data was found in the literature for the Mo-2Si-1B wt.% alloy. The only strength values reported were compressive strengths measured by Kumar for alloys formed by isothermal forging, Chapter 2, Figure 2.19 [37]. The compressive strengths measured for Mo-Si-B alloys will be higher than the tensile strengths because differences in the coefficient of thermal expansion ($\alpha_{Mo} < \alpha_{A15,T2}$) cause residual stresses during cooling that lead to premature failure in tension [60]. Compression testing also tends to inflate the strength values because is it less dependent on flaws in the material. A yield stress of 790 MPa was measured at 1000°C, but the 1200°C yield stress was only 400MPa. The reaction synthesis alloy has superior high-temperature mechanical properties with a yield strength of 480 MPa at 1200°C in tension.

The UTS of the Mo-2Si-1B wt.% alloy was about 100 MPa lower at each temperature than the Mo-3Si-1B wt.% alloy, but the onset of ductility for the Mo-3Si-1B wt.% alloy is 100°C higher. The strengths of the alloys are expected to decrease with an increasing fraction of the $Mo_{ss}$ matrix. Jain and Kumar tested the tensile strength of the saturated $Mo_{ss}$ alloy and measured yield strengths of only 360MPa at 1000°C and 110MPa at 1200°C [90]. High strength appears to come at the expense of ductility, but these tests only represent the initial effort in determining the microstructure-properties relationships. The compromise in mechanical properties can likely be reduced by improved dispersion of the intermetallic particles and increased molybdenum continuity.

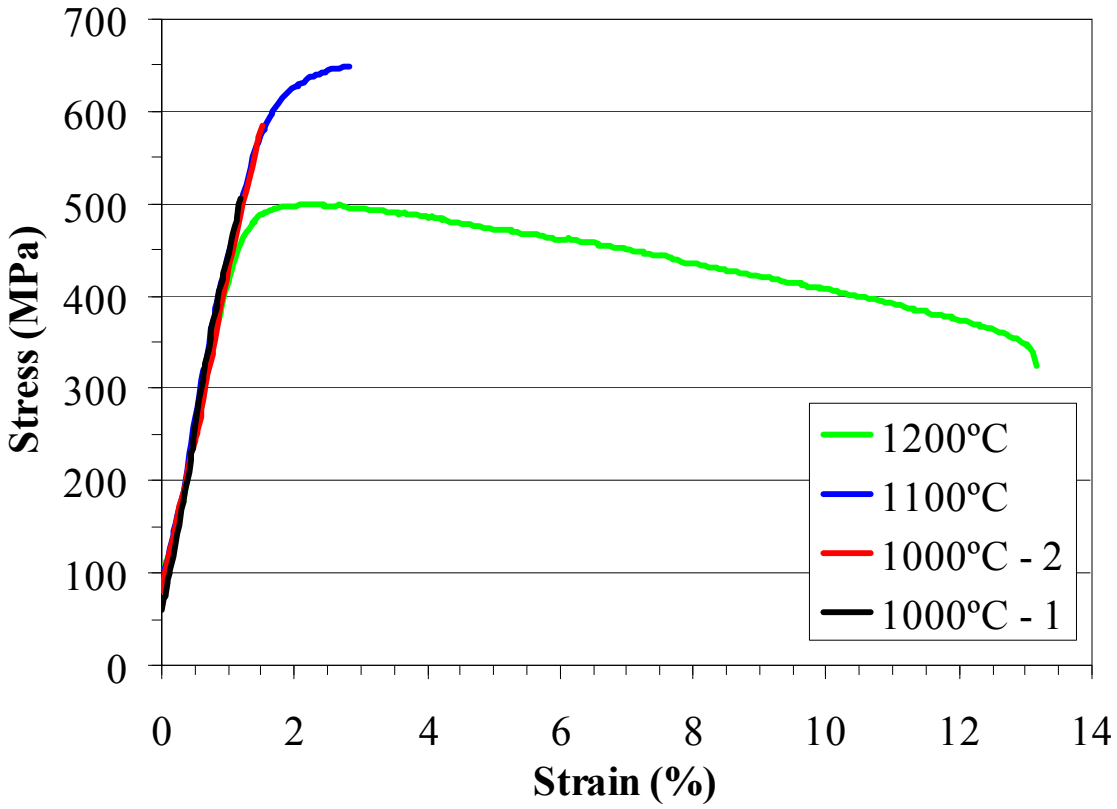


Figure 6.11: Stress-strain curves for the Mo-2Si-1B wt.% alloy, measured by tensile testing at a strain rate of $10^{-4}$ $s^{-1}$.

Table 6.4: The 0.2% yield stress, UTS and elongation-to-failure for the Mo-2Si-1B wt.% samples tested at a strain rate of $10^{-4}$ $s^{-1}$.

| Temperature (°C) | 0.2% YS (MPa) | UTS (MPa) | Elongation-to-Failure (%) | Plastic Strain (%) |
|---|---|---|---|---|
| 1000 - 1 | - | 507 | 1.2 | - |
| 1000 - 2 | - | 585 | 1.5 | - |
| 1100 | 579 | 649 | 2.8 | 1.3 |
| 1200 | 477 | 499 | 13.2 | 12.5 |

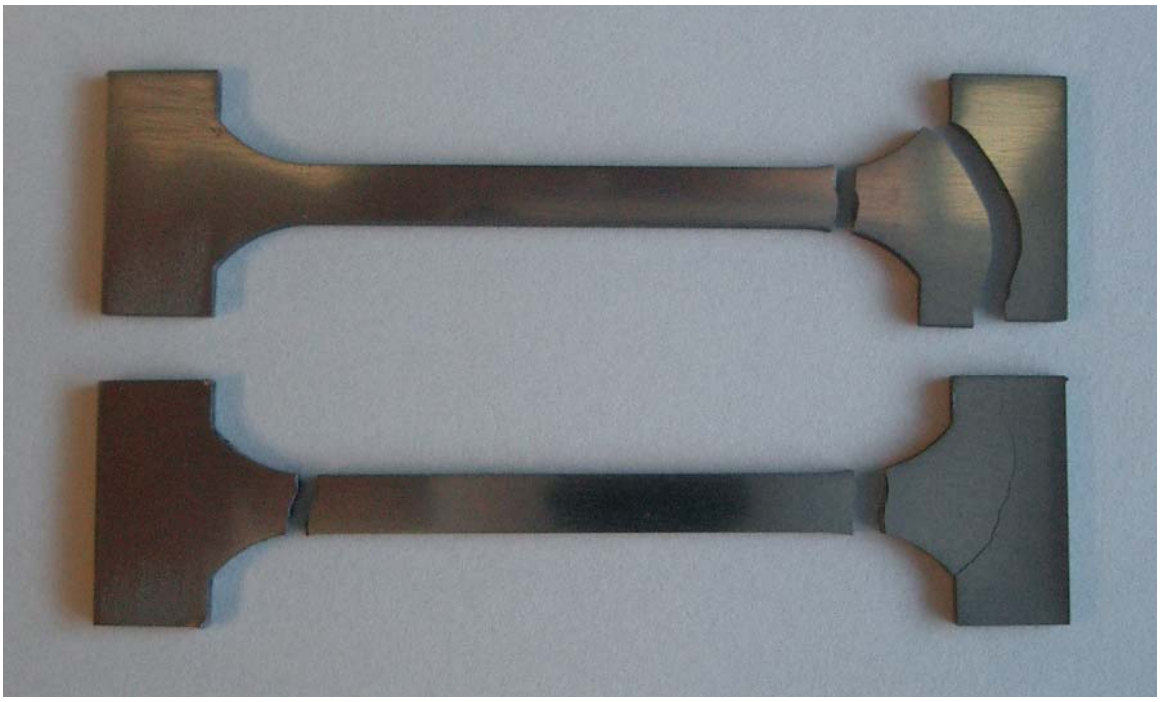

Figure 6.12: Image of the Mo-2Si-1B wt.% tensile specimens tested at 1000°C. Premature fracture occurred in the grip sections, possibly due to cross-loading.

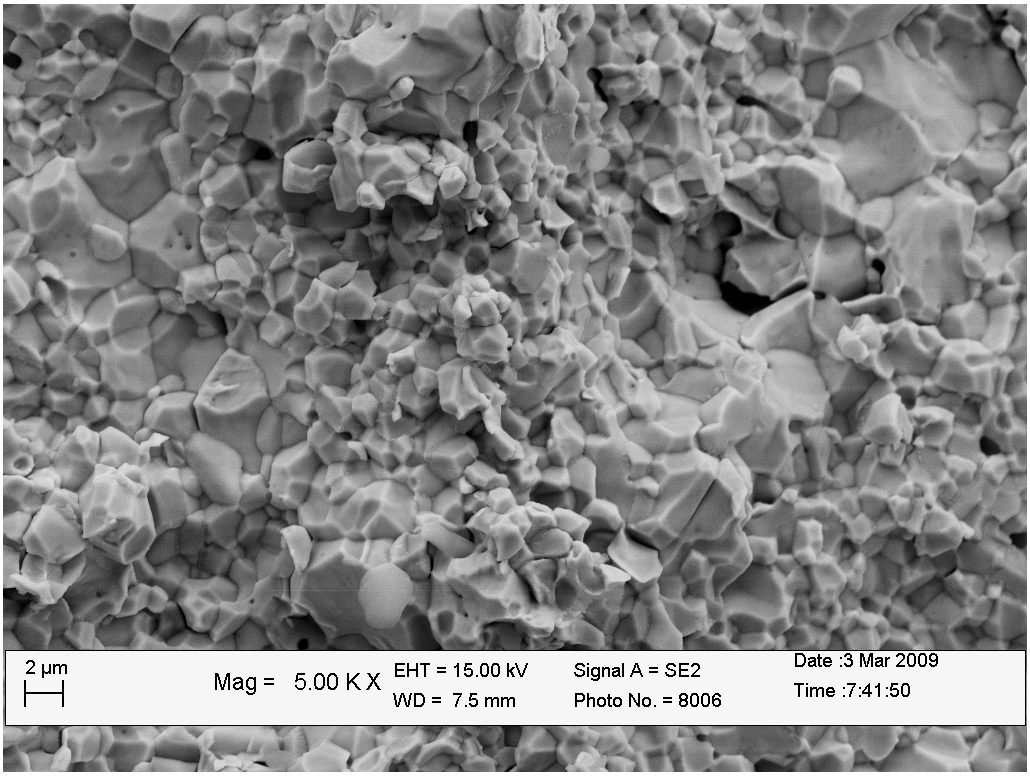


Figure 6.13: The fracture surface of the Mo-2Si-1B wt.% alloy tested at 1100°C.

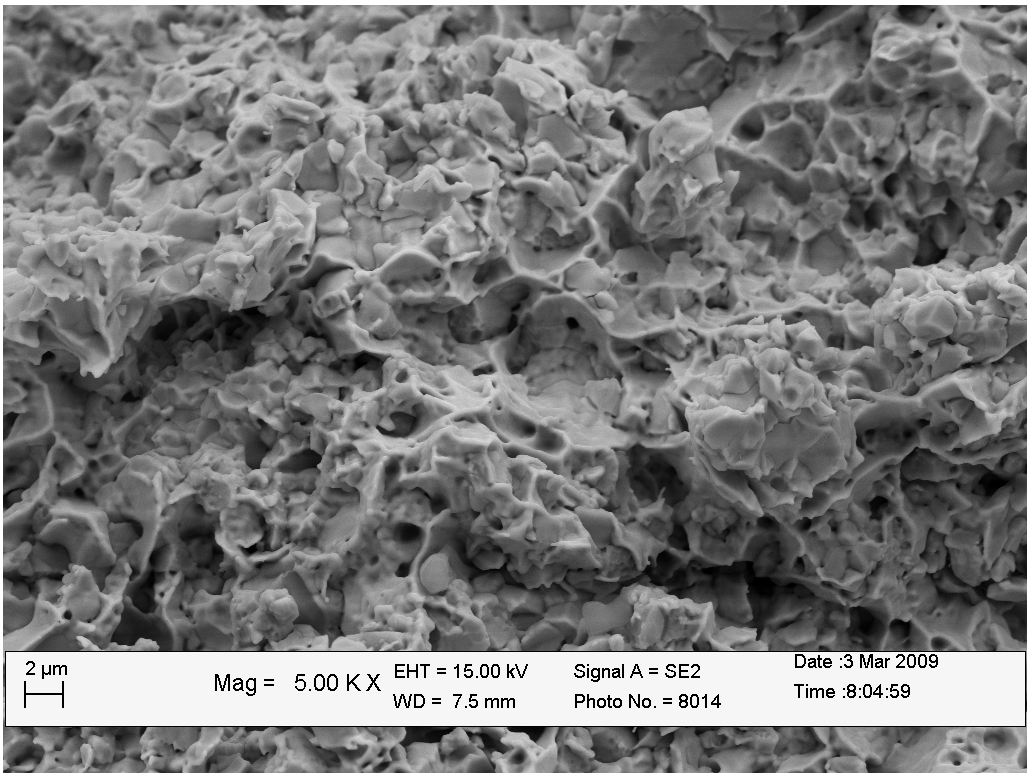

Figure 6.14: The fracture surface of the Mo-2Si-1B wt.% alloy tested at 1200°C.

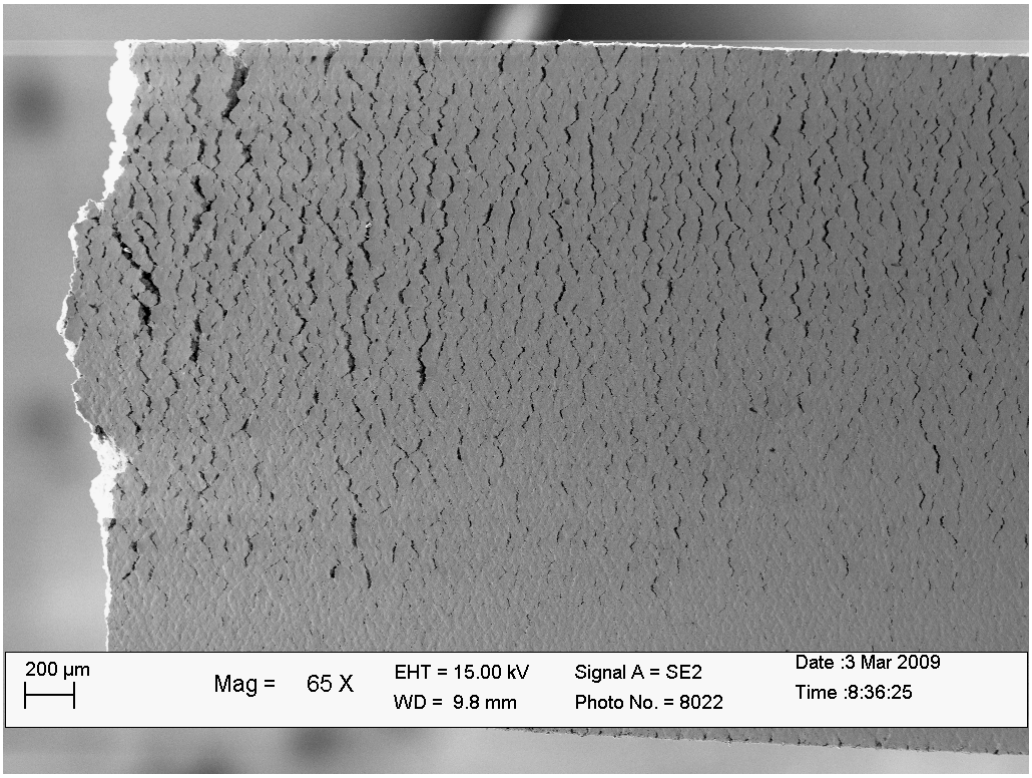

Figure 6.15: The necked region from the Mo-2Si-1B wt.% alloy tested 1200°C.

# CHAPTER 7

# OXIDATION RESISTANCE

The high-temperature oxidation of Mo-Si-B alloys takes place by two separate mechanisms. A transient period of rapid weight loss occurs during the first exposure to the oxidizing environment. In the initial stage, a porous layer forms that allows gaseous oxygen to diffuse to the glass/alloy interface and $MoO_3$ to evaporate. The degree of the transient weight loss reported varies widely, even for experiments conducted on alloys of the same composition, as reported in Chapter 2. After the surface scale seals and forms a dense layer, the ingress of oxygen is limited by molecular permeation through the glass.

Helmick et al. [55] studied the formation of borosilicate layers on Mo-3Si-1B wt.% alloys and reported that much of the transient weight loss was due to channels formed in the early stages of oxidation that extended to the alloy surface. They were able to eliminate the channels by slowing the initial rate of oxidation by controlling the oxygen partial pressures and gas flow rates. Following this research, a pre-oxidation method has been developed to create a continuous glass layer in a manner which minimizes the transient weight loss. The pre-oxidation technique has proven useful to study the initial formation of the glass layer and provided insights to potential improvements which could improve oxidation resistance. Further oxidation in air was examined for the pre-oxidized samples and compared to the untreated alloy.

### 7.1 Pre-Oxidation Treatment

A pre-oxidation technique was developed to limit the weight loss due to transient oxidation. The alloys were exposed to low oxygen partial pressures which allows the surface oxide layers to be formed in a controlled manner. This also dramatically slows the transient oxidation rate and allows for samples to be removed during the early stages of oxidation in order to study the formation of the borosilicate layer. Pre-oxidation was studied using the Mo-3Si-1B wt.% alloy processed with the hBN powder and sintered at 1600°C for 6 hours. The surfaces of the samples were ground to remove any surface variation and polished with 1200 grit sandpaper. The experiments were conducted in a controlled atmosphere tube furnace and the conditions required to form a continuous layer were studied for different flow rates and temperatures. The samples were heated to temperature in pure argon prior to exposure to the oxidizing mixture of Ar/0.1% $O_2$ (Airgas Products). In the first experiment, two flow rates were compared: 40cc/min, which corresponded to a gas velocity of 0.23cm/sec, and 120cc/min or 0.69cm/sec. The temperature profile of the furnace was measured and samples were placed in positions corresponding to 900, 1100, 1300 and 1500°C. Once at temperature, the samples were exposed to the oxidizing gas mixture for two hours. The mass changes of the samples are listed in relation to the original surface areas, Table 7.1.

Table 7.1: The specific mass changes of the samples pre-oxidized in a mixture of Ar/0.1% $O_2$ for 2 hours at two different flow rates.

| | Gas Flow Rate | |
|---|---|---|
| | 40cc/min | 120cc/min |
| Temperature | $\Delta m$ (mg/cm$^2$) | $\Delta m$ (mg/cm$^2$) |
| 900°C | 0.06 | 1.91 |
| 1100°C | 0.37 | 0.79 |
| 1300°C | 1.59 | -0.31 |
| 1500°C | 0.26 | -3.15 |

Surface micrographs of the samples tested with the flow rate of 40cc/min are compared in Figure 7.1. Note that different magnifications are used in the four micrographs. EDS was used to identify the phases present. In the 900°C micrograph the borosilicate glass appears as the brighter phase. In the rest of the micrographs the molybdenum oxide appears as the brightest phase and the borosilicate glass is darker. It can be seen that the coverage of the borosilicate glass increases with temperature. Figure 7.2 compares the surface of the 900°C sample to a representative microstructure of the base alloy. It is appears from these micrographs that the location of the glass droplets correspond to the location of the intermetallics in the microstructure. This provides an example of how the initial stages of oxidation may be linked to the microstructure. A fine distribution of the intermetallic phases will reduce the distance in which the glass layer has to flow and may limit the transient weight loss.

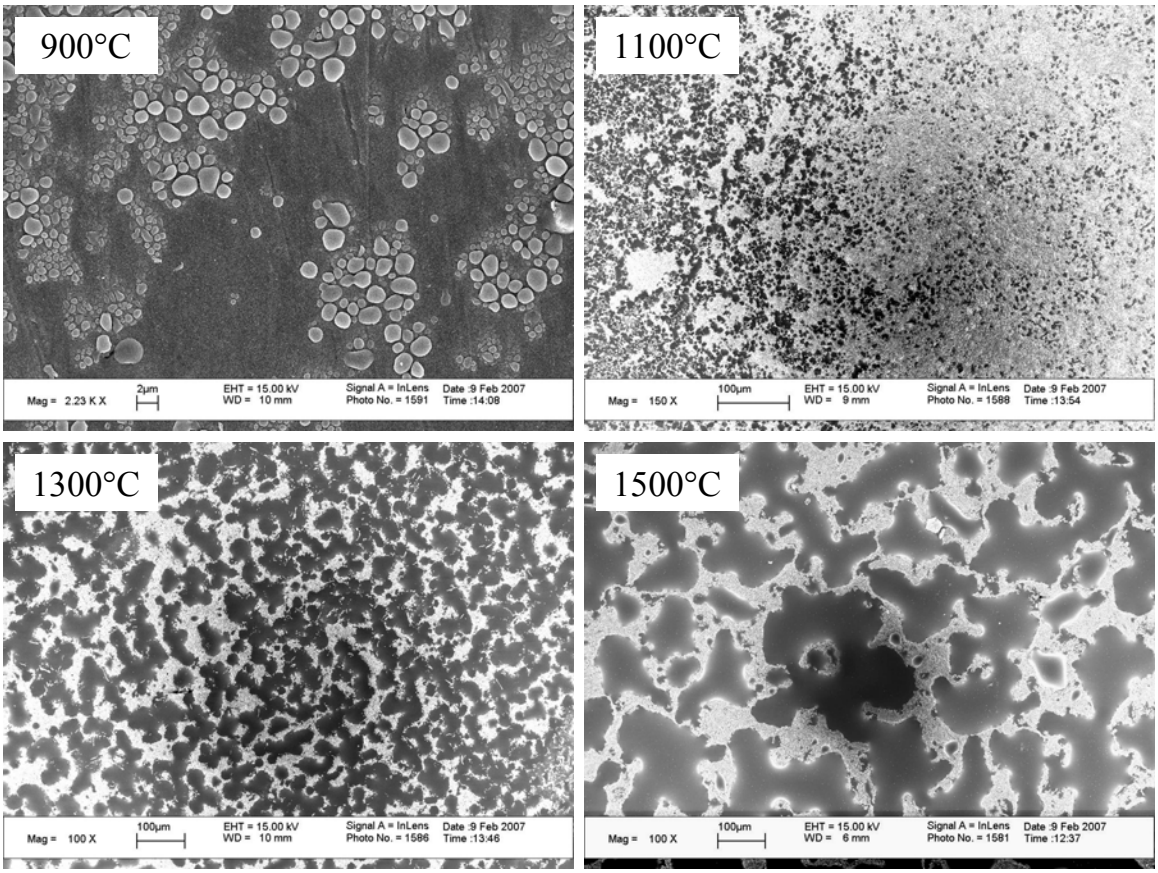


Figure 7.1: Surface micrographs of Mo-3Si-1B wt.% samples pre-oxidized in a mixture of 0.1% $O_2$ for 2 hours at a flow rate of 40cc/min. The borosilicate phase appears darker in the 1100-1500°C micrographs and the molybdenum oxide appears brighter.

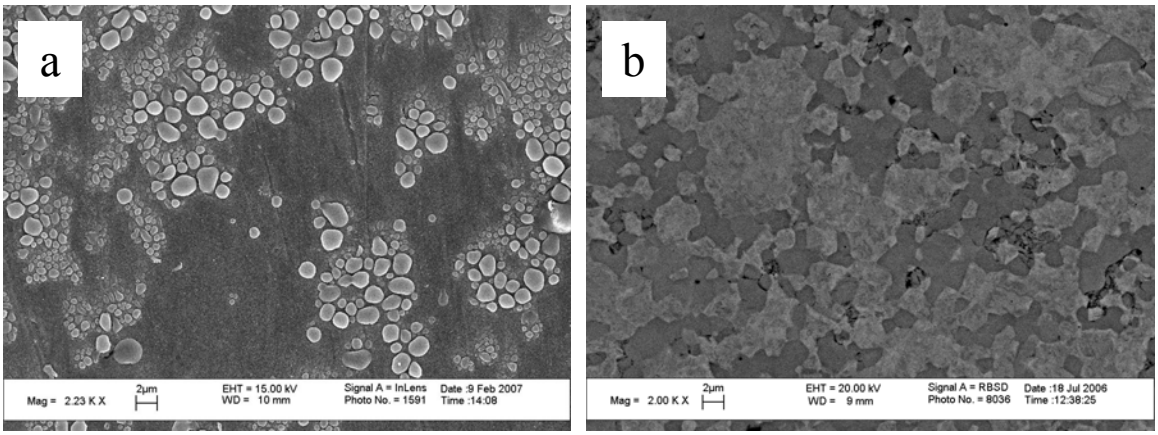


Figure 7.2: The surface of the sample pre-oxidized at 900°C compared to a representative microstructure of the base alloy, which illustrates the relationship between the location of the intermetallics and the formation of the glass layer.

The surfaces of the samples tested with the higher flow rate of 120cc/min are compared in Figure 7.3. The borosilicate glass appears as the darker phase in all four micrographs. The coverage of the glass was improved by the higher flow rate, an observation also reported by Helmick et al. [55]. This is in part because the samples are exposed to a higher quantity of oxygen over the given time period, but the increased flow rate also helps move the volatile molybdenum oxide away from the surface. The improvement in glass coverage was especially apparent at 1500°C where very little molybdenum oxide was visible on the surface and the glass layer was nearly continuous.

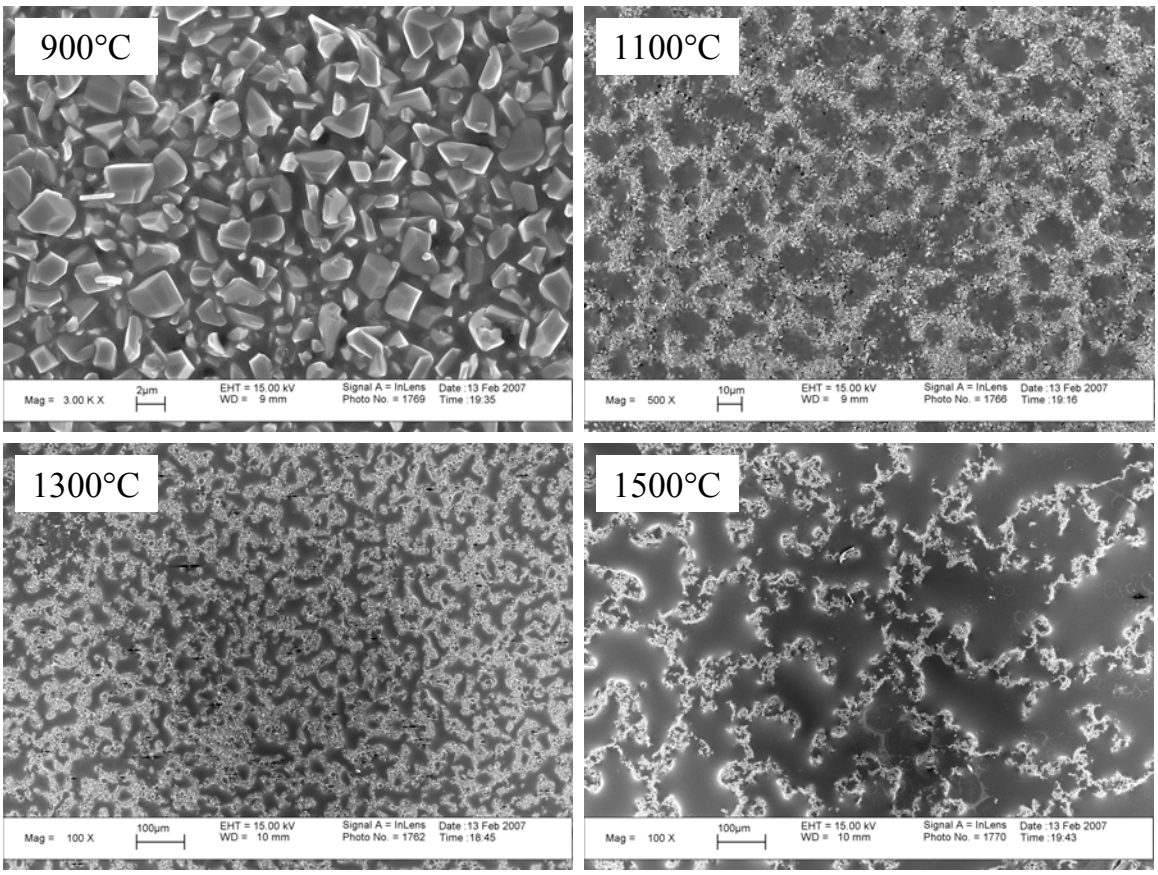

Figure 7.3: Surface micrographs of Mo-3Si-1B wt.% samples pre-oxidized in a mixture of 0.1% $O_2$ for 2 hours at a flow rate of 120cc/min. The borosilicate phase appears darker in all of the micrographs.

XRD analysis of the 1100°C and 1500°C samples identified the molybdenum oxide present on the surface of the samples as the $MoO_2$ phase. $MoO_3$ would form in air but the reduced oxide was formed due to the low oxygen partial pressure. $MoO_3$ has a low melting point and is easily volatilized, but $MoO_2$ has a high melting point and acts as a barrier to further oxidation. The large $MoO_2$ crystallites formed on the surface of the 900°C and 1100°C samples may limit the formation of the glass layer. The surface cross-sections of the samples tested with a flow rate of 120cc/min are compared in Figure 7.4.

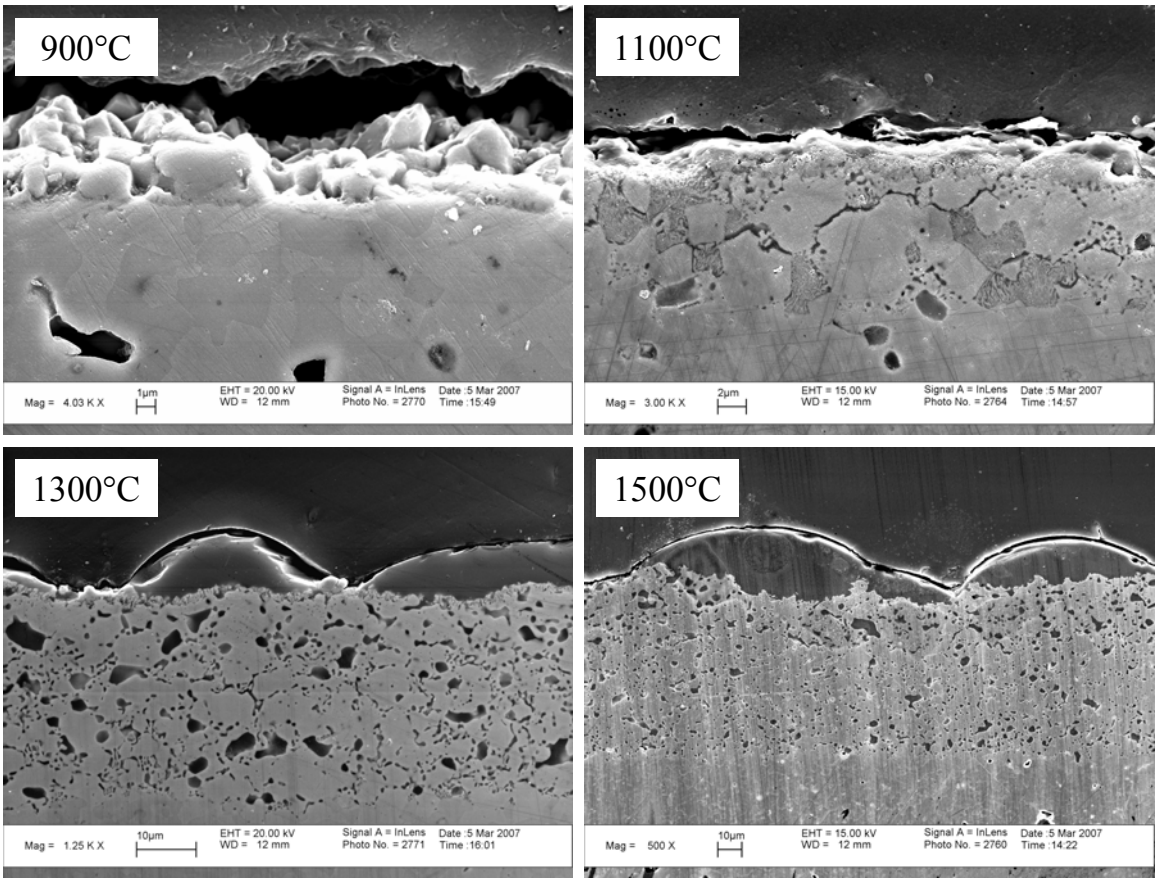

Figure 7.4: Cross-sections of the pre-oxidation surface layers for samples exposed to 0.1% $O_2$ for 2 hours at a flow rate of 120cc/min.

A thick borosilicate glass layer was formed on the surface of the pre-oxidized samples at 1300°C and 1500°C. Underneath the surface was a partially oxidized layer of pure molybdenum mixed with a network of borosilicate glass. As oxygen diffuses to the glass/alloy interface, silicon and boron are preferentially oxidized. The thickness of the partially oxidized layer appears to be controlled by diffusion of oxygen through the borosilicate glass regions. For diffusion controlled oxidation, the rate is given as:

$$\ln r = \ln r_o - \frac{E_a}{RT} \tag{7.1}$$

where $r$ is the oxidation rate, $E_a$ is the activation energy of oxygen diffusion, $R$ is the gas constant and $T$ is the temperature in Kelvin. The thicknesses of the oxidized layers were assumed to be directly proportional to the oxidation rate. The maximum and minimum oxidation affected thicknesses, $t$, were measured from the micrographs and are listed in Table 7.2. The ln($t$) was plotted versus $1/T$ and the slope of the line yielded an activation energy $E_a$ = 25.7 ± 3.6 kcal/mol, as illustrated in Figure 7.5.

Table 7.2: Oxidation affected layer thicknesses, $t$, of the samples pre-oxidized in 0.1% $O_2$ for 2h at a flow rate of 120cc/min.

| **t** | **t (average)** | **ln t** | **T** | **1/T** |
|---|---|---|---|---|
| μm | μm | μm | K | $K^{-1}$ |
| 1-3 | 2 | 0.69 | 1173 | 0.00085 |
| 10-14 | 12 | 2.48 | 1373 | 0.00073 |
| 30-40 | 35 | 3.56 | 1573 | 0.00064 |
| 70-100 | 85 | 4.44 | 1773 | 0.00056 |

The activation energy determined from the analysis of the oxidized layer thicknesses falls well within the range of the activation energy of oxygen diffusion reported for borosilicate glasses, Figure 7.6. This indicates that the thickening of the partially oxidized layer is controlled by oxygen diffusion though the glass phase.

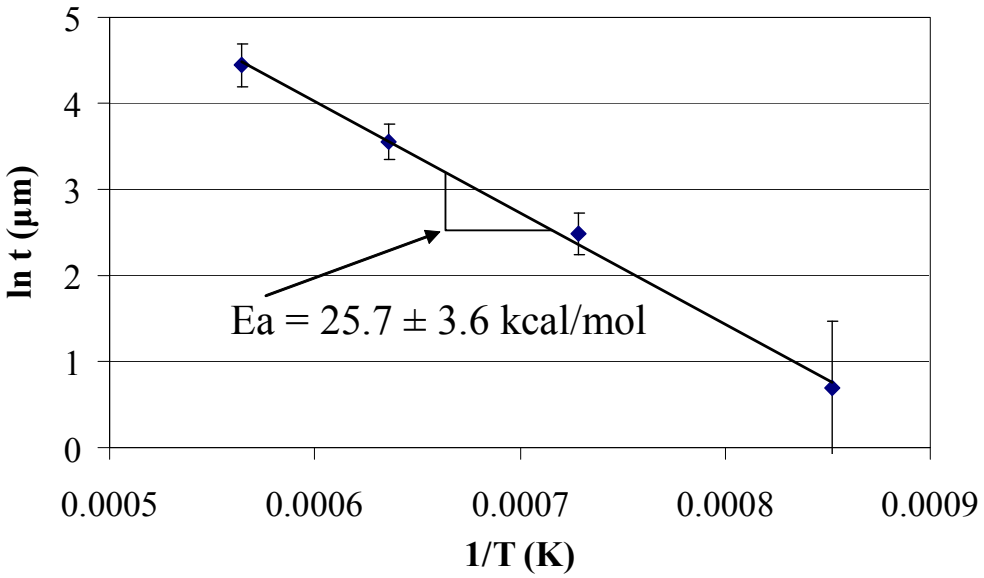


Figure 7.5: Partially oxidized layer thicknesses of samples pre-oxidized in 0.1% $O_2$ for 2h at a flow rate of 120cc/min, plotted versus temperature to calculate the activation energy.

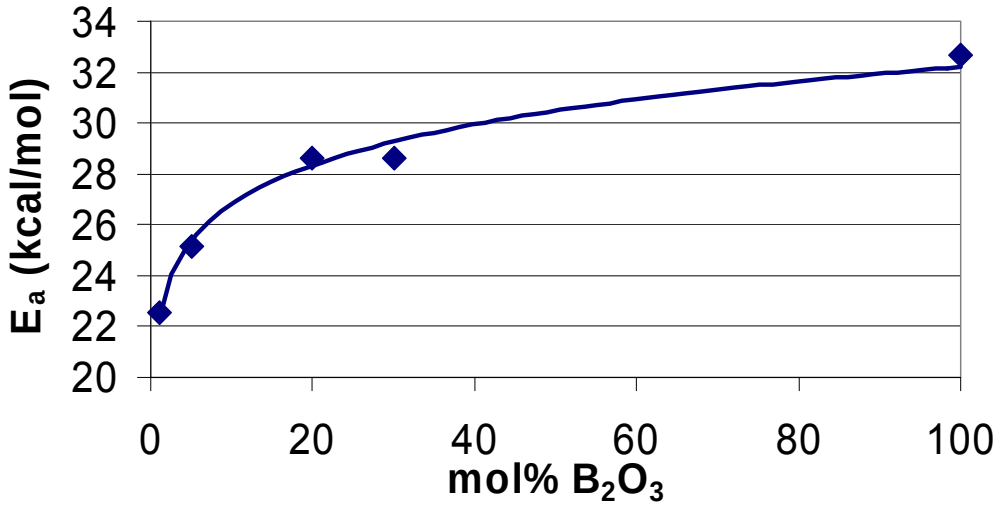


Figure 7.6: The activation energies of oxygen diffusion in borosilicate glasses calculated from oxygen diffusivity data reported by Schlichting [91].

The samples pre-oxidized at 1300°C and 1500°C had thick, oxidation affected regions but the surface oxide was still not completely continuous. A longer five hour pre-oxidation treatment at 1100°C was investigated in an attempt to create a completely continuous oxide layer with a minimally affected thickness. The surfaces of the samples pre-oxidized at 1100°C for 2 and 5 hours are compared in Figure 7.7. The borosilicate glass appears to wet the molybdenum oxide crystallites on the 2 hour sample. After 5 hours of pre-oxidation the polishing marks in the base alloy became visible and the $MoO_2$ crystallites had mostly evaporated. XRD confirmed that a small fraction of the $MoO_2$ phase was still present, but the largest $MoO_2$ peak height for the 5 hour sample was only 1% of the highest molybdenum peak, as compared 56% for the 2 hour sample. The borosilicate glass on the surface of the 5 hour sample formed into droplets and it appears that the glass is non-wetting on the surface of the alloy. Glass modifiers may be useful to improve wetting of the glass and to speed the formation of a continuous layer.

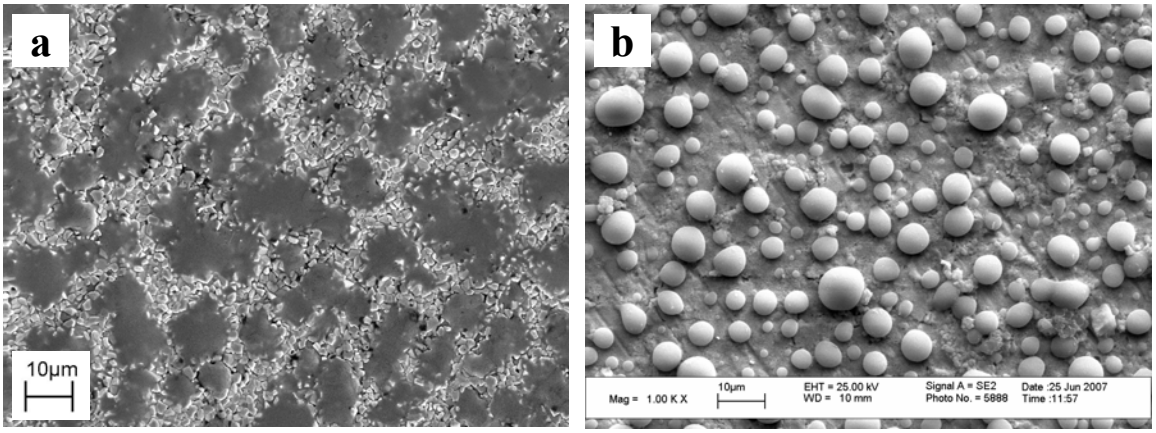

Figure 7.7: Surfaces of samples pre-oxidized in Ar/0.1% $O_2$ with a flow rate of 120cc/min at 1100°C for: (a) 2 and (b) 5 hours.

## 7.2 Oxidation Testing in Air

### 7.2.1 The Effect of Pre-Oxidation on Further Oxidation in Air

The effect of the pre-oxidation treatment on the oxidation resistance in air was examined. A Mo-3Si-1B wt.% sample was pre-oxidized at 1300°C for 3 hours in the Ar/0.1% $O_2$ mixture with a flow rate of 120cc/min. Isothermal oxidation tests were conducted in air at 1100°C and the oxidation rate of the pre-oxidized sample was compared to that of the untreated alloy. Testing was conducted in a box furnace and the samples were removed and weighed at periodic time intervals. The weight loss per unit area is plotted as a function of time in Figure 7.8. The transient weight loss was not completely eliminated by the pre-oxidation treatment, although much of the additional weight loss was likely due to evaporation of molybdenum oxide from the surface of the pre-oxidized layer. The transient weight loss ceased within 30 minutes and the total transient weight loss including the pre-oxidation treatment was -23mg/cm$^2$. Linear oxidation behavior was observed the remaining 29 hours of the test and the average weight loss was only 22μg/cm$^2$·h, as compared to 350μg/cm$^2$·h for the untreated alloy.

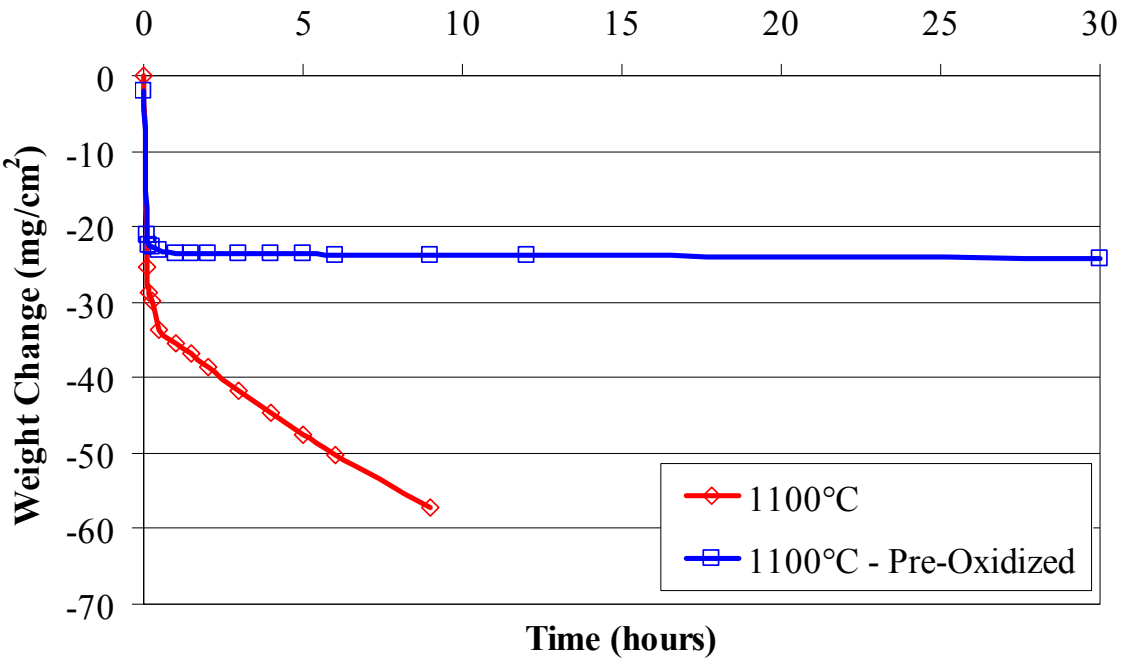


Figure 7.8: Oxidation tests conducted 1100°C in air on the Mo-3Si-1B wt.% alloy, for the untreated alloy and for a sample pre-oxidized at 1300°C for 3 hours.

The surface oxide cross-section from the untreated alloy is compared to the pre-oxidized sample before and after 30 hours of additional oxidation in air, Figure 7.9. The untreated sample formed a glass layer up to 25μm thick after 9 hours of oxidation. The pre-oxidation treatment created a surface glass layer with an average thickness of 8μm on top of a partially oxidized layer of molybdenum and borosilicate glass. After 30 hours of additional oxidation in air, there was no apparent change in the thickness of the surface glass. Further oxygen diffusion through the glass formed a $MoO_2$ layer at the glass/molybdenum interface. The pre-oxidation treatment was developed to limit transient weight loss, but it also resulted in a significant improvement of the steady state oxidation rate. It appears that the pre-oxidation treatment created a more oxidation resistant glass layer than was formed under normal exposure to air. There was a large

fraction of $MoO_2$ particles present in the glass layer of the untreated samples that were not present in the pre-oxidized layer. The low oxygen partial pressures during the pre-oxidation treatment may result in preferential oxidation of silicon and boron. The effect of molybdenum oxide on the diffusivity of oxygen in borosilicate glasses was not found in a review of the literature, but $MoO_3$ melts at 800°C and likely lowers the viscosity of the glass. The pre-oxidation treatment was conducted 200°C above the oxidation test, which may have improved the oxidation resistance of the borosilicate glass by increasing $B_2O_3$ evaporation.

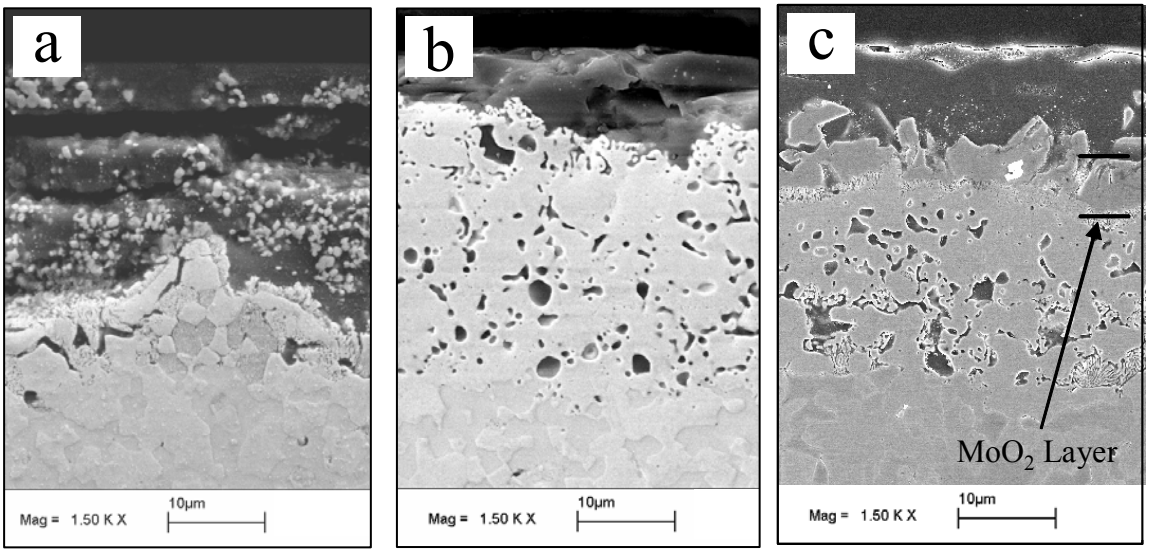


Figure 7.9: Cross-sections of oxidized Mo-3Si-1B wt.% samples: (a) Untreated sample oxidized at 1100°C in air for 9h, and the pre-oxidized sample (b) before and (c) after additional oxidation at 1100°C in air for 30h.

### 7.2.2 Oxidation Testing of the Untreated Mo-3Si-1B wt.% Alloy in Air

The pre-oxidation treatment provides a means to improve the oxidation resistance of Mo-Si-B components, but the technique may be of limited usefulness as thermal and environmental barrier coatings will likely be employed in many applications. However, it is important to study the inherent oxidation resistance of the alloys because of the potential for damage to the oxide layer or the applied coatings. Oxidation testing was conducted on the Mo-3Si-1B wt.% alloy. The measured weight losses were averaged for three samples at 1000°C and two at 1100°C and compared to results reported in the literature, Figure 7.10. It can be seen that alloys produced by reaction synthesis have superior oxidation resistance compared to the alloy tested by Sakidja et al., which had long periods of transient weight loss.

It has also been demonstrated that the microstructures of the alloys produced by reaction synthesis are continuous to the surface of the samples after sintering and HIPing. The oxidation resistance in air at 1000°C was measured for specimens in the as-fired state and compared to the previous oxidation tests for polished specimens, Figure 7.11. There was no significant difference in the oxidation behavior for the as-fired and polished surfaces. The oxidation rates of the reaction synthesis alloys are compared in Table 7.3, for both the transient and diffusion controlled regimes.

Table 7.3: Oxidation rates of reaction synthesis Mo-3Si-1B wt.% alloys.

| Temperature | Transient Mass Loss ($mg/cm^2$) | Linear Oxidation Rate ($\mu g/cm^2 \cdot hr$) |
|---|---|---|
| 1000°C – As-Fired | 45.2 ± 8.4 | -15.3 ± 4.3 |
| 1000°C – Polished | 43.2 ± 9.2 | -15.5 ± 4.9 |
| 1100°C – Polished | 45.3 ± 0.0 | -1380 ± 500 |

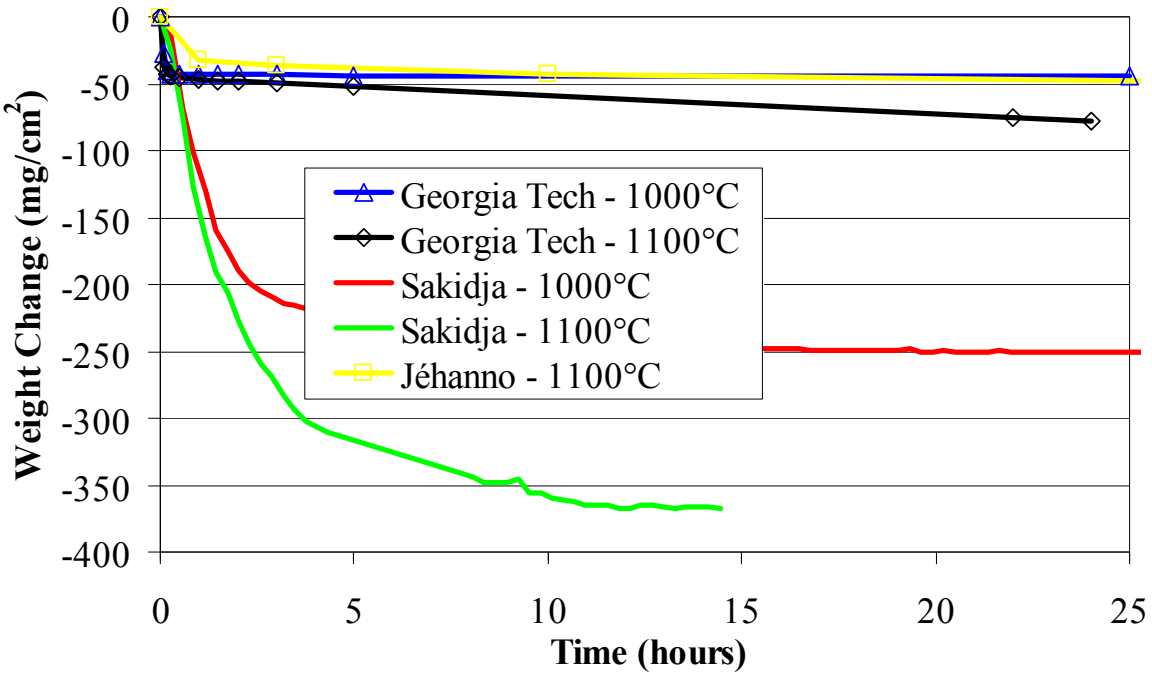


Figure 7.10: Oxidation of the Mo-3Si-1B wt.% alloy compared to similar test reported in the literature [59,60]. The error bars for the Georgia Tech data are within the data points.

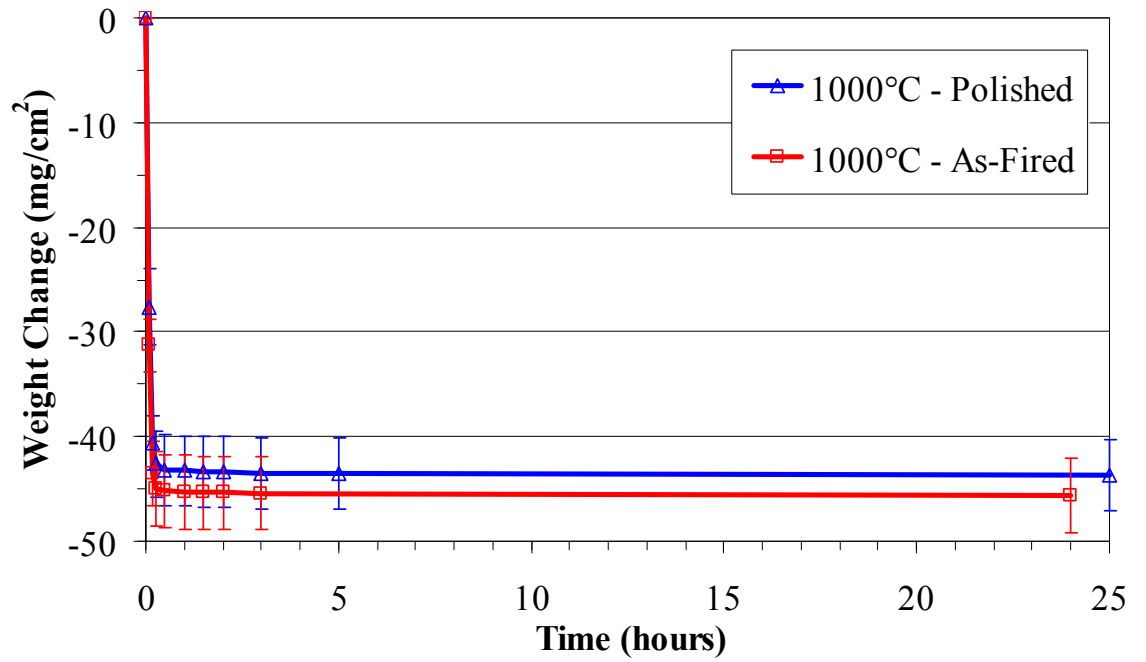


Figure 7.11: Isothermal oxidation of the Mo-3Si-1B wt.% alloy at 1000°C, compared for samples with polished surfaces and in the as-fired state.

The cross-sections of the oxidized surfaces are compared in Figure 7.12 for the 1000°C and 1100°C tests and there is relatively little difference in the thickness of the oxide layers. It was found that much of the weight loss observed for the 1100°C samples was the result of areas of localized damage where surface connected porosity resulted in internal oxidation. An extreme example of this behavior was observed for a sample tested at 1100°C that suffered catastrophic oxidation, Figure 7.13. The source of failure was a lamination crack that was connected to interconnected porosity in the center of the pellet and prevented densification during HIPing. When the oxidation occurs in pockets of internal porosity, the $MoO_3$ is not able to evaporate due to Knudsen effects. This is speculated to dramatically increase the oxygen diffusivity of the glass, which leads to catastrophic oxidation. For reliable oxidation resistance, the HIPing procedures must be refined in order to consistently achieve full density.

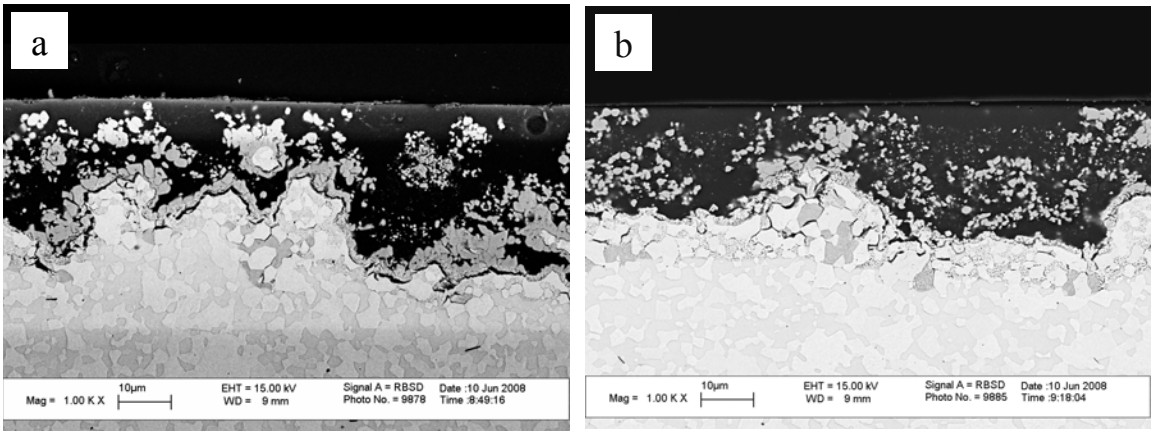

Figure 7.12: Cross-sections of Mo-3Si-1B wt.% samples oxidized in air at (a) 1000°C for 25 hours and (b) 1100°C for 24 hours.

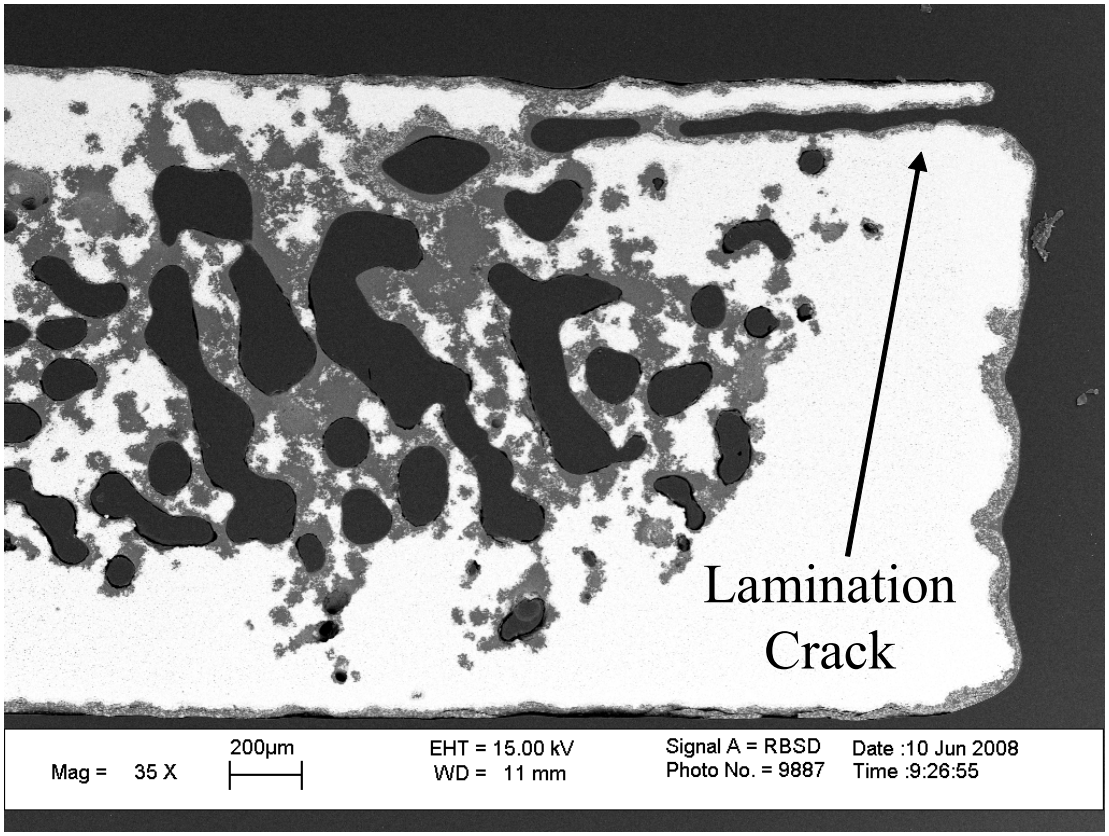

Figure 7.13: Cross-section of sample which failed by catastrophic internal oxidation at 1100°C, with the source of failure indicated.

### 7.3 Mechanism for the Thickening of the Surface Oxide

After a continuous borosilicate layer is formed, further oxidation is limited by oxygen diffusion through the glass. The reduced oxygen level at the glass/alloy interface causes the formation of the refractory $MoO_2$ phase rather than $MoO_3$. Further weight loss is limited by molybdenum oxide dissolution into the glass and evaporation from the surface. Investigation of the cross-section of a sample oxidized at 1100°C provides insight into the thickening mechanism of the surface oxide, Figure 7.14. In the BSE image the molybdenum is the brightest phase, the intermetallics appear slightly darker and the glass regions are black. Oxygen diffused through the glass and preferentially

oxidized the silicon and boron present in the intermetallics. This formed pockets of glass inside the alloy, the morphology of which is indicative of the intermetallic phase oxidized. The A15 phase has almost zero solubility of boron and the glass formed is nearly pure $SiO_2$. Pure silica has a very high viscosity at 1100°C (~$10^{13}$ Pa·s) and resists flowing, hence the lamellar structure. The T2 phase forms a high boron glass that is much less viscous (~$10^4$ Pa·s) and able to coalesce into pockets. A large specific volume increase results from the oxidation of the intermetallic phases which forces the glass to the surface.

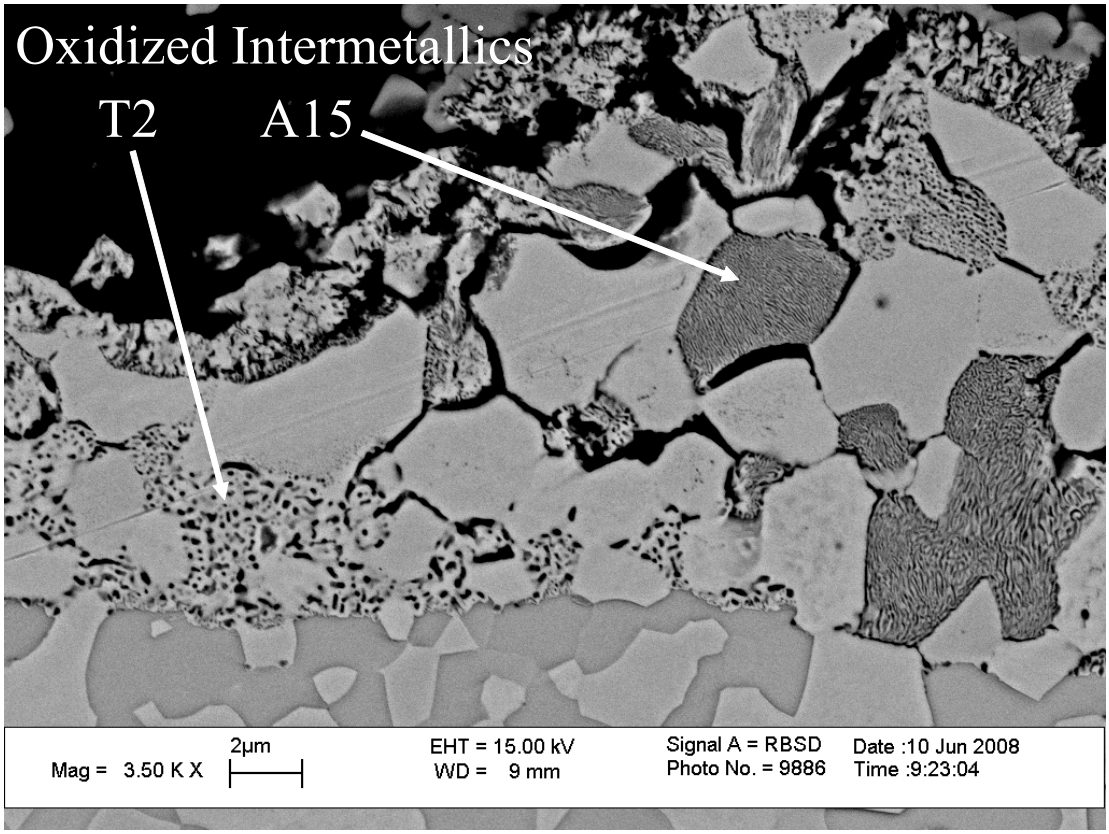


Figure 7.14: Cross-section of the oxide/alloy interface of a sample oxidized at 1100°C, which illustrates preferential oxidation of the intermetallics at the glass/alloy interface.

# CHAPTER 8

# OPTIMIZATION OF THE OXIDATION RESISTANCE OF Mo-Si-B ALLOYS

Upon the first exposure of Mo-Si-B alloys to a high-temperature oxidizing atmosphere, molybdenum, silicon and boron are oxidized. The $MoO_3$ evaporates and the borosilicate glass flows together to create a passivating layer [19]. In the initial transient stage of oxidation, a porous layer forms which allows oxygen to diffuse via the gas phase to the glass/alloy interface. Akinc and Meyer proposed that the initial porosity of the layer will dictate the oxidation rate if viscous flow does not seal the pores, in which case the oxidation rate is controlled by gaseous diffusion through the porous surface layer [2]. The $B_2O_3$ in the glass acts as a fluxing agent, lowering the viscosity and increasing the sintering rate of the glass scale. After an initial period of weight loss, the surface scale seals and the alloys undergo diffusion controlled oxidation due to molecular permeation of oxygen through the dense glass layer. The $B_2O_3$ has detrimental effects in this stage by increasing the oxygen permeability of the glass.

Experimental measurements show that the oxidation rate during transient oxidation is orders of magnitude greater than in the diffusion controlled regime, but there is no rigorously developed model that incorporates both stages of oxidation. A new model has been developed in this work to better understand the oxidation of Mo-Si-B alloys and to study the competing kinetic factors. This model considers the oxidation behavior as function of composition, including both the Si/B ratio and the volume

fraction of the $Mo_{ss}$ phase. A prevailing belief is that the microstructural coarseness affects the transient oxidation, but this assumption is difficult to verify as no single research group has reported the oxidation behavior of Mo-Si-B alloys for a range of intermetallic spacing. The model incorporates the role of microstructure by relating the intermetallic spacing to the initial level of porosity in the glass layer. The mechanism for the thickening of the oxide layer was discussed in Chapter 7, but at this time the rate at which thickening occurs is unclear. In this analysis the glass layer is assumed to remain a constant thickness defined by the oxidation that occurs during the transient oxidation stage. The oxidation rate in the diffusion controlled regime was modeled by linear oxidation kinetics, as was observed in this work and by Akinc and Meyer, rather than the parabolic kinetics observed by Parthasarathy et al. [56].

The exact oxidation behavior of Mo-Si-B alloys is too complex to model at this time. The effect of molybdenum oxide dissolved in borosilicate glasses is not reported in the literature. Further, the composition of the glass is not constant because the concentrations of $MoO_3$ and $B_2O_3$ change over time due to evaporation. The composition of the surface oxide was approximated as pure borosilicate mixtures with compositions equal to the Si/B ratio of the base alloy and the properties were based on the limited data available for pure borosilicate glasses.

The model was developed to investigate the role of the Si/B ratio and to highlight trends which may help guide the future development of more oxidation resistant alloys. The objective function of the model was the sum of the metal recession occurring during transient and diffusion controlled oxidation and an optimization algorithm was developed to minimize the total metal recession.

## 8.1 Oxidation Model

The oxidation of the alloy is modeled as occurring in two stages; oxidation during sintering of the porous glass layer, followed by oxidation due to oxygen permeation through the continuous glass layer. The first stage of oxidation leads to the large, transient weight losses which are experimentally observed due to the evaporation of $MoO_3$. In this phase the rate of oxidation is assumed to be proportional to the level of porosity in the glass layer and the oxidation rate of molybdenum. The rate of diffusion of gaseous oxygen to the glass/alloy interface is assumed to be much faster than solid state diffusion and permeation though the glass phase is not considered during the sintering stage. After the surface layer sinters to full density, further oxidation is limited by the rate of molecular diffusion in the borosilicate glass. The model is designed to calculate the thickness of the alloy oxidized during each stage of oxidation in order to determine the Mo-Si-B composition with the minimum metal recession for a given temperature.

### 8.1.1 Model Parameters

The sintering rate of the surface layer depends on the initial porosity, viscosity and surface tension of the glass. Permeability through the glass is dependent on the solubility and diffusivity of oxygen in the glass. Actual experimental data gathered from handbooks and journals was used in the analysis. The data was fit to functions using trendline functions generated by Microsoft Excel.

8.1.1.1 Volume Fraction Molybdenum Solid Solution

The volumes of the phases in the three-phase field were determined from the isothermal Mo-Si-B ternary phase diagram at 1600°C. The volume fractions are assumed to be constant across a wide temperature range as this phase region is known to be stable down to room temperature [1]. In order to calculate the phase ratios, the boron is assumed to reside fully in the T2 phase. In this case, the amount of boron in the alloy is directly proportional to the amount of the T2 phase present. This is supported by the molybdenum-boron binary phase diagram which indicates negligible boron solubility in molybdenum at 1600°C and below [92]. It is also known that there is little solubility of boron in the A15 phase. Recognizing that 2.07 at.% silicon goes into solution in the molybdenum phase, the remaining silicon available to form the A15 phase is known [92]. The final equation relating the volume fraction of molybdenum solid solution to the atomic percentage of silicon and boron is given as:

$$Mo_{SS}(vol.\%) = 100\frac{1027.6 - 41.7\chi_{Si} - 20.5\chi_{B}}{946.1 - 2.2\chi_{Si} - 6.6\chi_{B}} \tag{8.1}$$

8.1.1.2 Mo-Si-B Alloy Density

The density of the Mo-Si-B alloy was estimated as a function of the volume fraction of the molybdenum solid solution, which has a density of 10.05g/cc. The A15 and T2 phases have similar densities of 8.97 and 8.81g/cc respectively. The density of the intermetallics was averaged as 8.9g/cc, giving a composite density of:

$$\rho_{MoSiB} = 10.05 * V_f(Mo_{SS}) + 8.9 * (1 - V_f(Mo_{SS})) \tag{8.2}$$

8.1.1.3 Borosilicate Glass Density

Values for the density of borosilicate glasses as a function of boron oxide content obtained from Doremus were fit to a polynomial function, Figure 8.1 [96].

8.1.1.4 Glass Viscosity

The viscosity of the borosilicate glass was determined as a function of composition and temperature. The viscosities of glasses follow an Arrhenius relationship given by:

$$\eta = \eta_o \exp\left(\frac{-Q}{RT}\right) \tag{8.3}$$

where $Q$ is the activation energy and $\eta_o$ is a pre-exponential factor. Taking the logarithm of both sides, the equation becomes:

$$\ln \eta = \ln \eta_o - \frac{Q}{RT} \tag{8.4}$$

which is in slope-intercept form. The viscosity values used for low boron contents were taken from Urbain et al. and the values for high contents were taken from Brückner and Navarro [58]. The natural log of viscosity was plotted against inverse temperature for twelve compositions ranging from pure silica to nearly pure boron oxide, as illustrated for a portion of the sample data in Figure 8.2. The data sets were fit to linear trendlines and the slopes and intercepts were used to determine $Q$ and $\eta_o$, plotted as a function of composition in Figure 8.3 and Figure 8.4. The values of $Q$ and $\eta_o$ were fit to polynomial equations and input into Equation 8.3, creating a combined equation which relates the viscosity to both the composition and temperature.

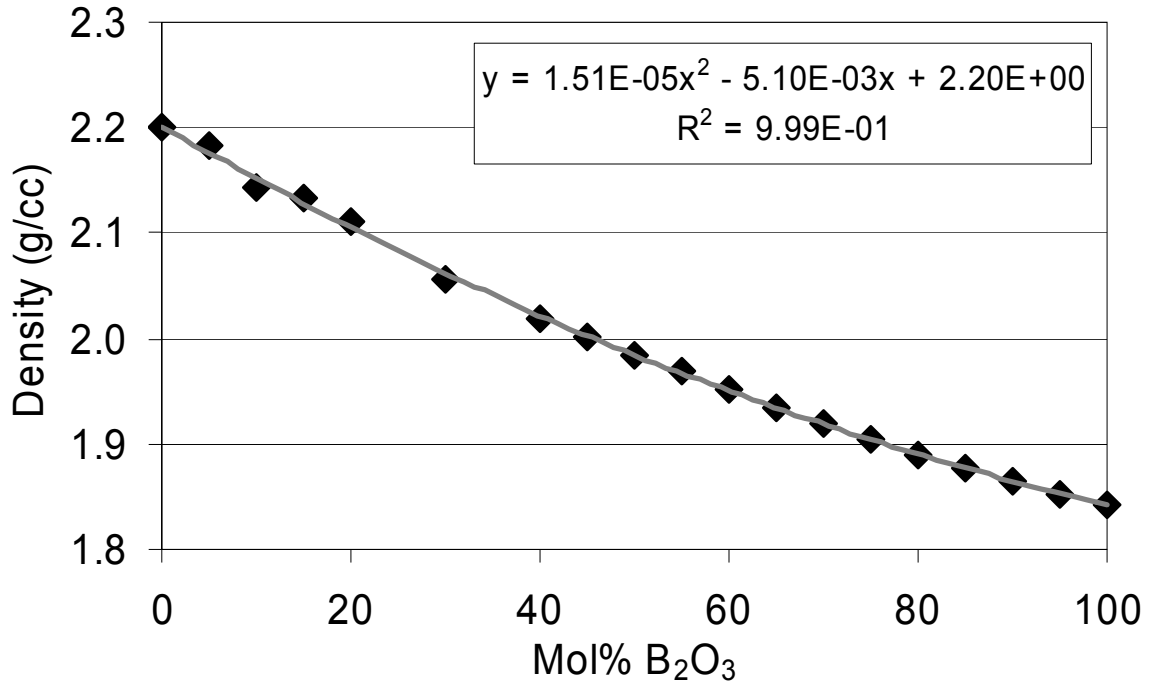


Figure 8.1: The density of borosilicate glasses as a function of $B_2O_3$ content, fit to data obtained from Doremus [96].

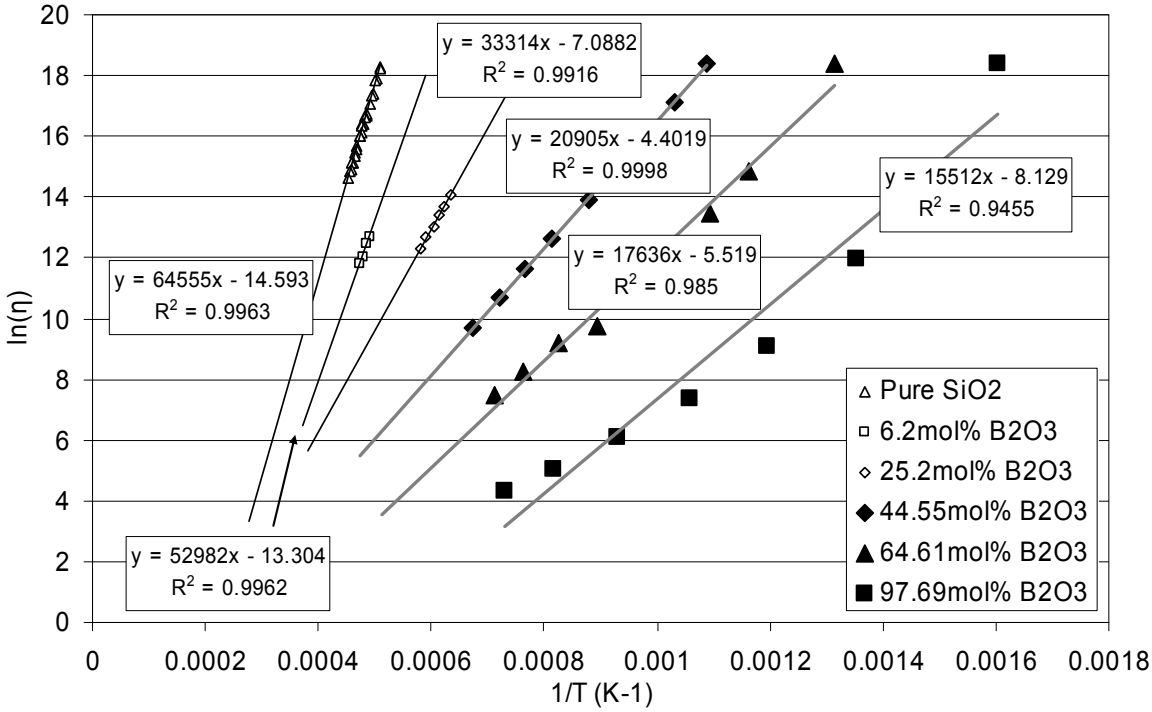


Figure 8.2: The viscosity (Pa·s) as a function of temperature for various borosilicate compositions, fit to data obtained from Urbain et al. and Brückner and Navarro [58].

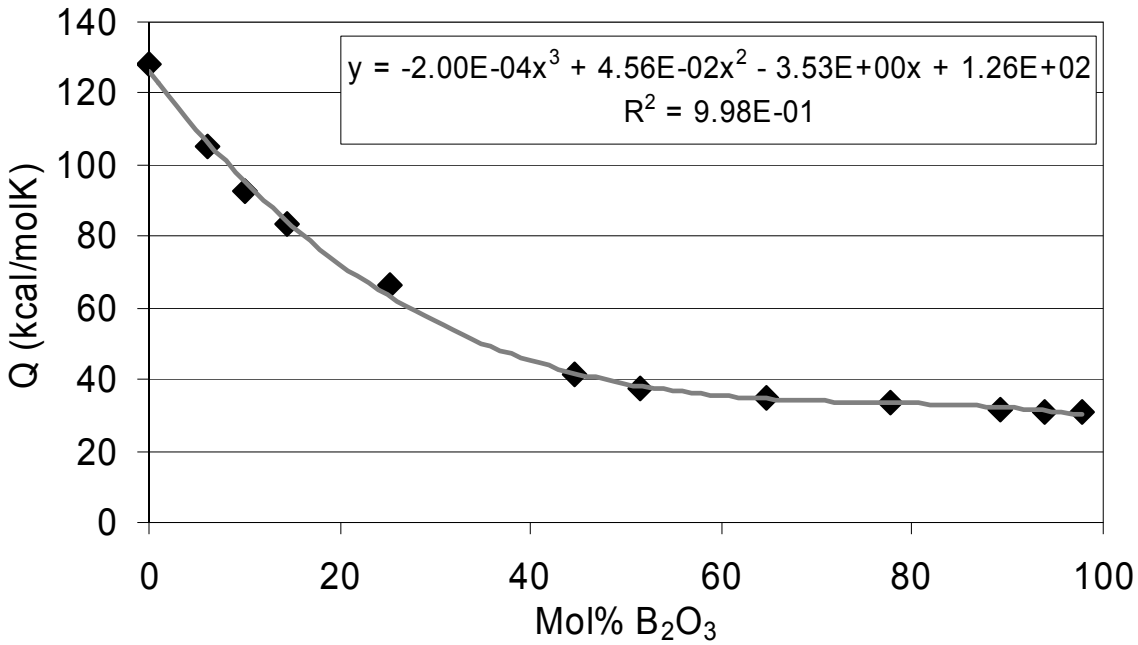


Figure 8.3: Activation energy, $Q$, of viscosity as a function of boron oxide content, calculated from the data plotted in Figure 8.2.

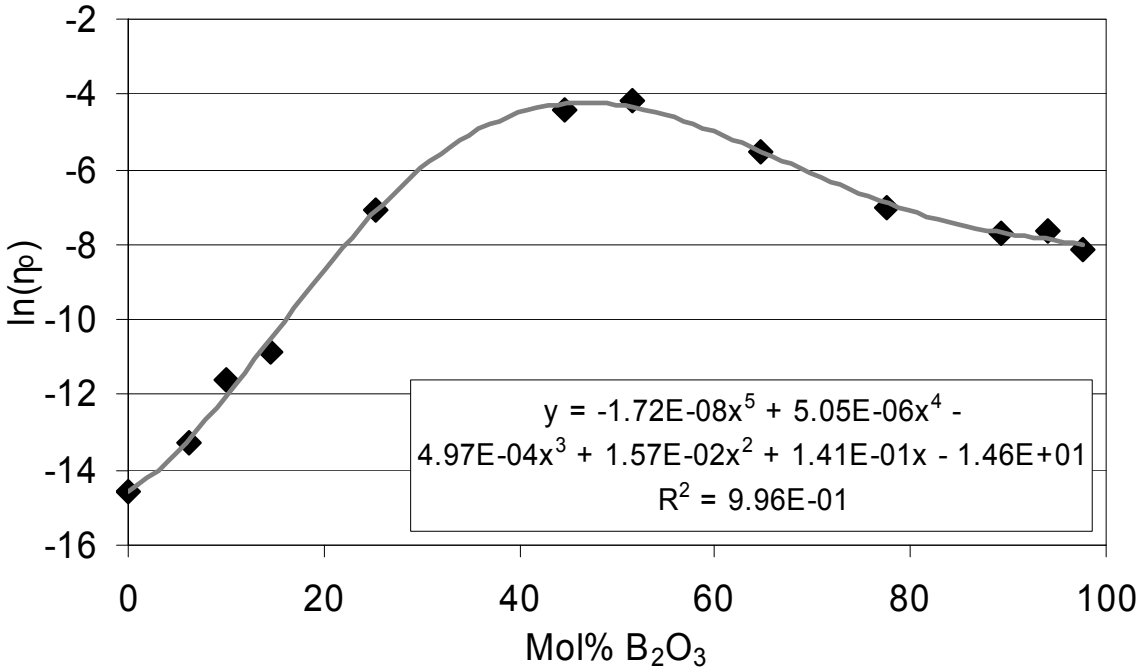


Figure 8.4: Viscosity pre-exponential factor $\eta_o$ (Pa·s) as a function of boron oxide content, calculated from the data plotted in Figure 8.2.

8.1.1.5 Oxidation Kinetics of Pure Molybdenum

The oxidation rate of pure molybdenum was given by Parthasarathy et al. [56]. The values are plotted in Figure 8.5 and a polynomial trendline was fit to the data using Microsoft Excel.

8.1.1.6 Diffusivity of Oxygen in Borosilicate Glasses

The diffusion of oxygen in glasses is a function of the composition of the glass and the temperature. Values of the diffusivity measured by Schlichting for various glasses as a function of temperature are plotted in Figure 8.6, where log($D$) is plotted against $10^4/T$.

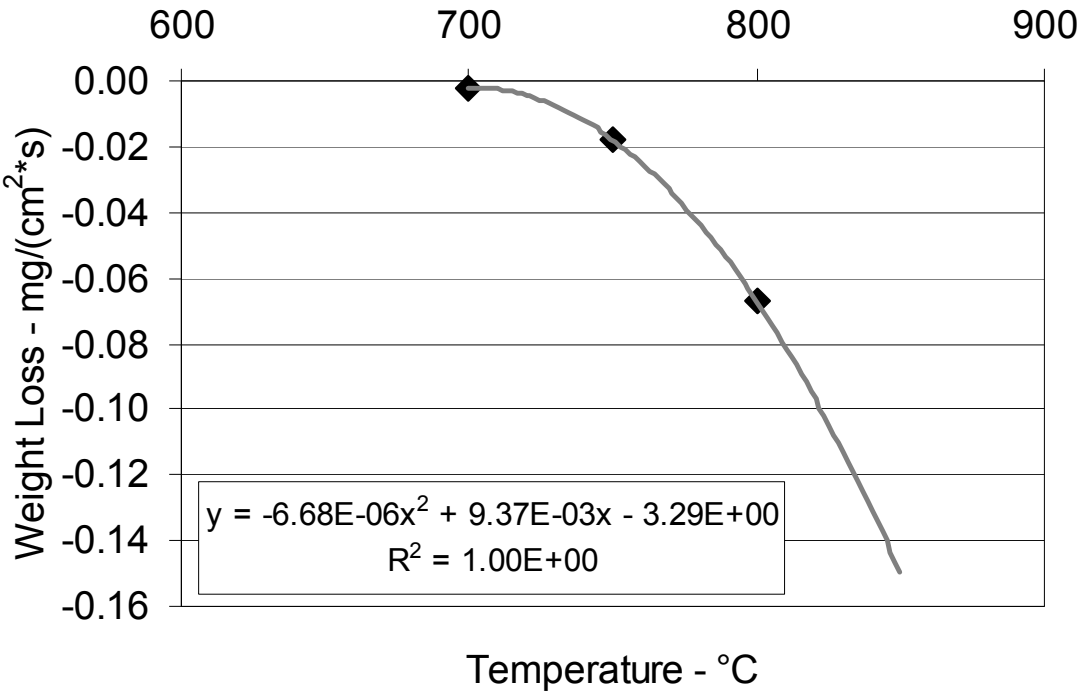


Figure 8.5: The temperature dependence for the oxidation rate of pure molybdenum, fitted to the values reported by Parthasarathy et al. [56].

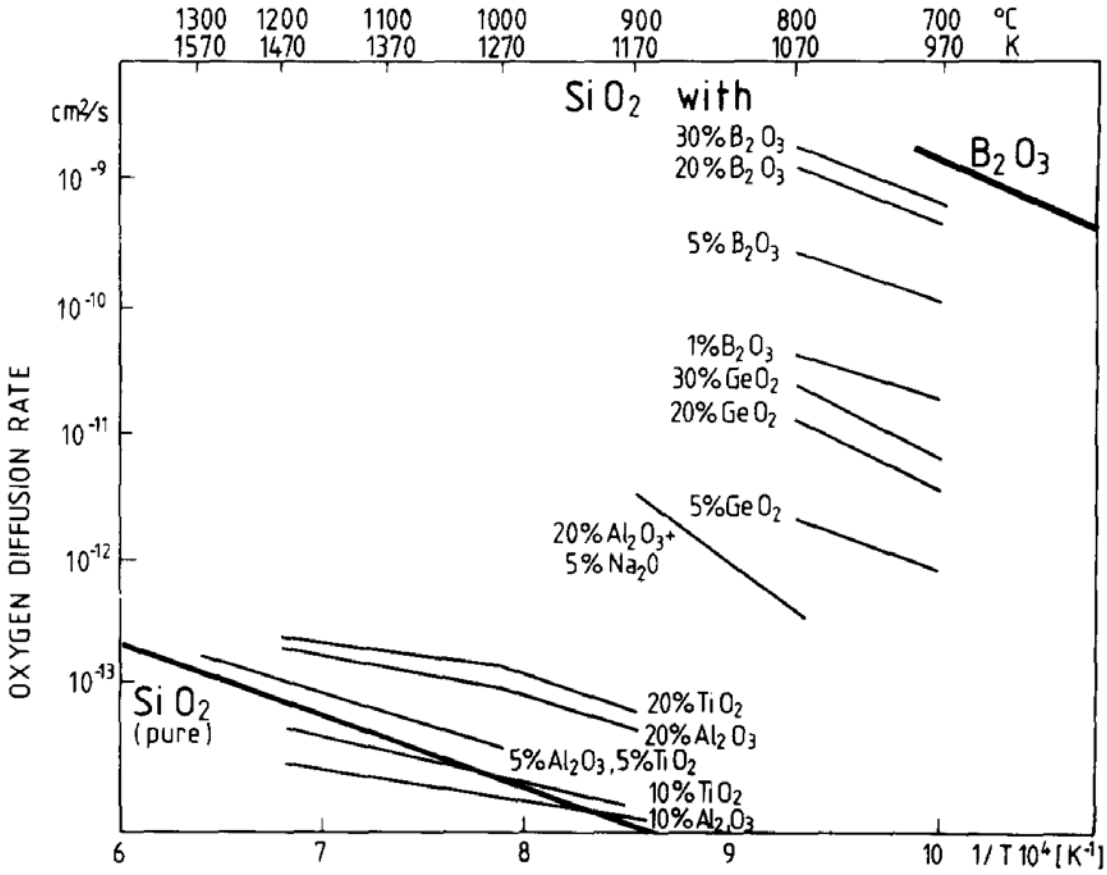


Figure 8.6: Oxygen diffusion rate in different silicate glasses as a function of temperature, reported by Schlichting [91].

The diffusion constant follows an Arrhenius relationship given by:

$$D = D_o \exp\left(\frac{-Q}{RT}\right) \tag{8.5}$$

where $Q_D$ is the activation energy for diffusion and $D_o$ is a pre-exponential factor.

Taking the logarithm of both sides, the equation becomes:

$$\ln D = \ln D_o - \frac{Q}{RT} \tag{8.6}$$

which is in slope-intercept form. Using the data plotted in Figure 8.6, the slope is equal to $-Q/R$ and the intercept is given as $\ln(D_o)$. Knowing the activation energy and pre-

exponential term, it is possible to calculate the diffusivity as a function of temperature. The values given for $Q_D$ and $D_o$ were assumed to be constant across a wider temperature range than was plotted by Schlichting, in order that this data could be used for the temperature range of interest in this project. This extension is valid assuming the diffusion mechanism does not change across the temperature range. The values of $Q$ and $D_o$ estimated from Figure 8.6 are given in Table 8.1.

In order to calculate the diffusion coefficient as both a function of temperature and composition, a function was fitted to the data from Table 8.1 for a range of temperatures. The natural log of the diffusion coefficient was plotted as a function of composition for six temperatures ranging from 970K to 1470K, as shown for three of the temperatures plotted in Figure 8.7. A logarithmic trendline was fit to each data set using Microsoft Excel. Because the natural log of zero is undefined, the composition value for pure silica was varied slightly to give the best fit for each curve. The highest value added was $8\times10^{-4}$ mol.%, which should have little effect on the analysis. Each curve was well fit, as evidenced by the high $R^2$ values obtained. The functions fitted to the diffusion data in Figure 8.7 are of the form:

$$\ln D = -A\ln(X) - B \tag{8.7}$$

where $A$ and $B$ are functions of temperature. The values of $A$ and $B$ are plotted as a function of temperature in Figure 8.8 and Figure 8.9, and their dependence on $T$ is given by a polynomial trendline determined using Microsoft Excel. Knowing the functional dependence of $A$ and $B$ with temperature, it is possible to calculate the value of the diffusivity for a given temperature and composition.

Table 8.1: The activation energy for diffusion, $Q_D$, and pre-exponential factor, $D_o$, for various glass compositions, extracted from diffusivity data reported by Schlichting [91].

| Mol.% $B_2O_3$ | $Q_D$ (kcal/mol) | $D_o$ |
|---|---|---|
| 0 | 27.6 | 8.35E-10 |
| 1 | 22.5 | 1.50E-06 |
| 5 | 25.1 | 3.50E-05 |
| 20 | 28.6 | 8.06E-04 |
| 30 | 28.6 | 1.19E-03 |
| 100 | 32.7 | 1.93E-02 |

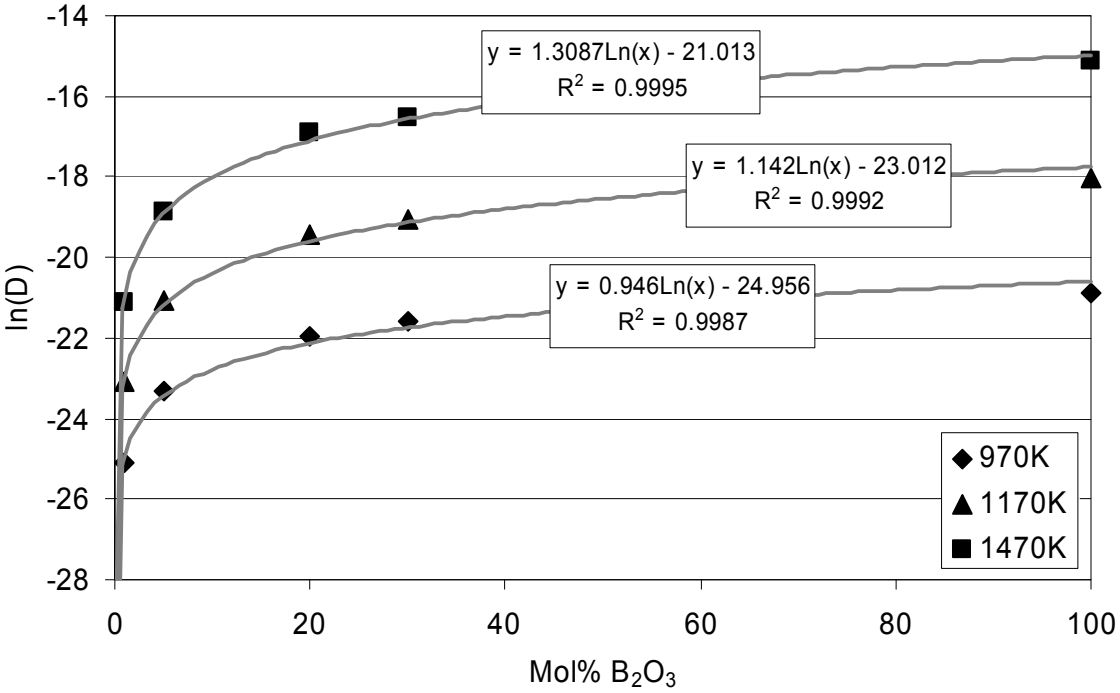


Figure 8.7: Plot of the diffusivity of oxygen in borosilicate glass as a function of composition for various temperatures, for data extrapolated from Schlichting [91]. The curve fit functions are shown with the corresponding $R^2$ values.

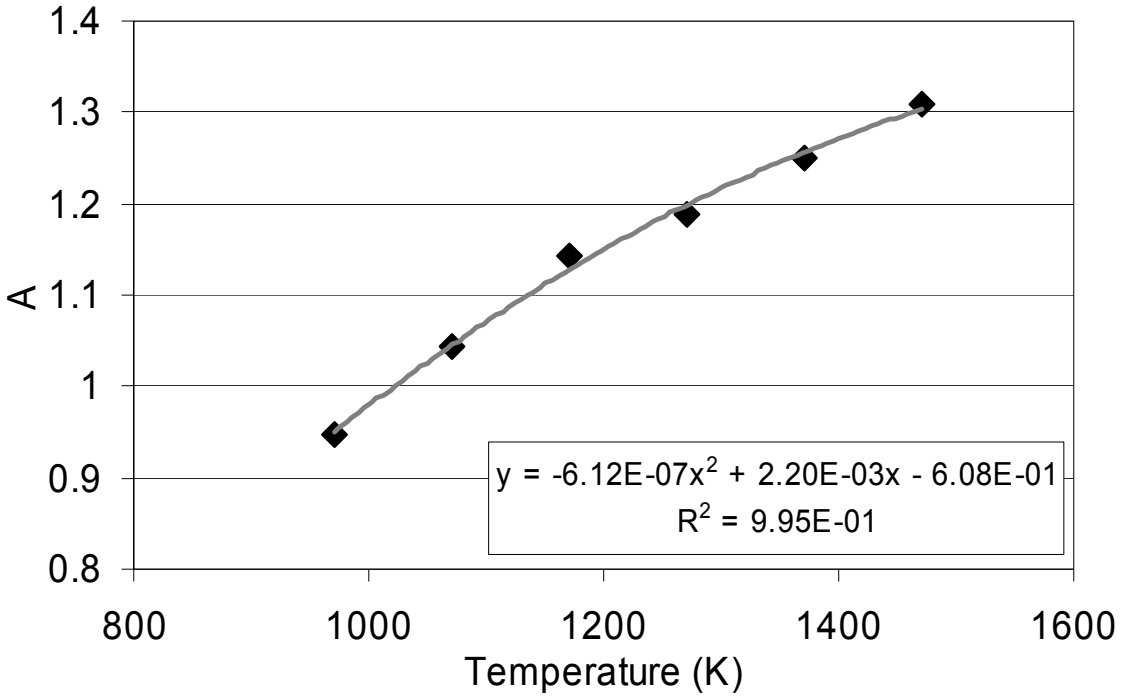


Figure 8.8: The temperature dependence of parameter *A* from Equation 8.7 used for curve fitting of the oxygen diffusivities plotted in Figure 8.7.

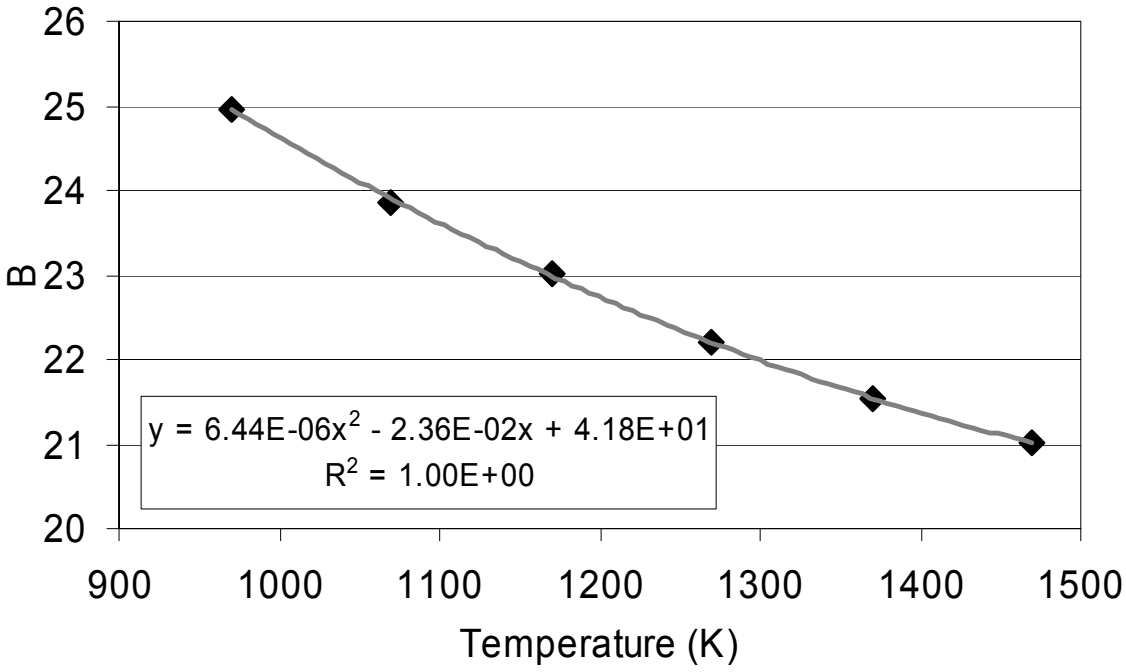


Figure 8.9: The temperature dependence of parameter *B* from Equation 8.7 used for curve fitting of the oxygen diffusivities plotted in Figure 8.7.

8.1.1.7 Solubility of Oxygen in Borosilicate Glasses

The diffusion of oxygen is proportional to its solubility and the diffusing species in silicate glasses is known to be $O_2$ [93]. Kajihara et al. measured the solubility of molecular oxygen in pure silica glass as a function of temperature between 800 and 1000°C [94]. The solubility follows an Arrhenius-type relationship given by:

$$S = S_o \exp\left(\frac{-\Delta H}{kT}\right) \tag{8.8}$$

where $T$ is in degrees Kelvin and $\Delta H$ and $S_o$ were found to be -0.17ev and $7.5\times10^{15}cm^{-3}$ respectively. The solubility values found in this range are in good agreement with those measured by Norton [95]. Using the expression to calculate the values of the solubility at 800 and 1000°C, it can be seen that the temperature increase lowers the solubility from $4.7\times10^{16}cm^{-3}$ to $3.5\times10^{16}cm^{-3}$.

While information on the solubility of oxygen in $B_2O_3$-$SiO_2$ binary glasses was not found, the diffusion of oxygen in pure $B_2O_3$ has been reported. Data from by Kohli and Shelby gives an approximate solubility of $1.3\times10^{17}cm^{-3}$ for argon in pure boric oxide at 800°C [58]. The solubility of gases is known to be proportional to their molecular diameters, thus the solubility molecular oxygen in glass will be approximately equal to that of argon due to their equal diameters [96]. Because of the close values for the solubility of molecular oxygen in $SiO_2$ and $B_2O_3$ and the small dependence on temperature, a constant solubility value of $10^{17}cm^{-3}$ was used in further calculations. This simplification is of little significance when compared with the values of the diffusion constant, which change many orders of magnitude across the temperature and composition ranges of interest.

8.1.1.8 Metal Recession Occurring During Sintering of the Surface Layer

The sintering of a glass on a rigid substrate tends to create pores oriented normal to the substrate. This is because as densification occurs, the pores cannot shrink in the plane of the substrate. This is a likely explanation for the channels which form in the borosilicate layer during the initial stages of oxidation in Mo-Si-B alloys, as observed by Helmick et al. [55]. These channels allow oxygen gas to directly react with the base Mo-Si-B alloy and lead to the large initial weight losses observed. After the protective glass layer has fully sintered, further oxidation is limited by gas diffusion through the dense glass layer. In order to calculate the metal recession which occurs during the initial sintering stage, a model for the oxidation rate as a function of the sintered glass density was developed. It is assumed that upon the first exposure to air at high temperatures, the A15 and T2 phase regions form a borosilicate layer preventing further oxidation in those regions. This leaves the molybdenum regions exposed to oxidation. At high temperatures $MoO_3$ is highly volatile and assumed to evaporate at a rate proportional to the temperature, as shown in Figure 8.5. The total quantity of molybdenum oxidized is a function of the oxidation rate, the exposed area and the time needed for a continuous glass layer to form.

An important first step in developing the model is to determine the sintering rate of the glass. Scherer and Garino present a model in which the glass layer consists of uniform cylindrical pores normal to the substrate with an inner radius of $r_1$ and an outer radius of $r_2$ which is chosen as to give the correct volume fraction of pores [97]. The value of $r_2$ is given by:

$$\frac{\rho_o}{\rho_s} = 1 - \frac{r_{1o}^2}{r_2^2} \tag{8.9}$$

where $r_{1_o}$ and $\rho_o$ are the pore radius and density at time $t_o$ and $\rho_s$ is the theoretical density of the glass. The expression for the density at time $t$ is given by:

$$K\left(t - t_f\right) = \frac{2}{\sqrt{\pi}}\left(\frac{\rho_s}{\rho_o}\right)^{1/3}\left[2\tan^{-1}\sqrt{1-\rho/\rho_s} - 3\sqrt{1-\rho/\rho_s}\right] \tag{8.10}$$

where $t_f$ is the time when densification is complete and $K$ is given by:

$$K = \left(\frac{\gamma}{\eta r_2\sqrt{\pi}}\right)\left(\frac{\rho_s}{\rho_o}\right)^{1/3} \tag{8.11}$$

where $\gamma$ is the surface energy of the glass. The surface energy of glasses varies little with temperature or composition and a constant value $\gamma = 0.28 J/m^2$ was used [98].

The values for the initial pore radius and density have been approximated from the microstructure of the material. The porous channels in the glass layer are assumed to be constant throughout the thickness, making the initial density of the glass proportional to the initial surface area of the alloy covered by glass. In this analysis, it is assumed that upon initial exposure to air, a thin glass layer is formed over the intermetallic grains, while the molybdenum grains are left exposed. For an isotropic material, the area fraction of an exposed phase in a random cross-section is equal to its volume fraction in the bulk. The initial density of the glass is thus equal to the volume fraction of the intermetallic phases. The initial pore radius is estimated by the microstructure of the material. Figure 8.10 shows SEM micrographs of Mo-Si-B alloys with varying compositions. Due to atomic contrast, the molybdenum phase appears lighter than the intermetallic phases. The average sizes of the molybdenum regions are on the order of 10μm and the value of $r_{1_o}$ has been set to this value for the purposes of this analysis.

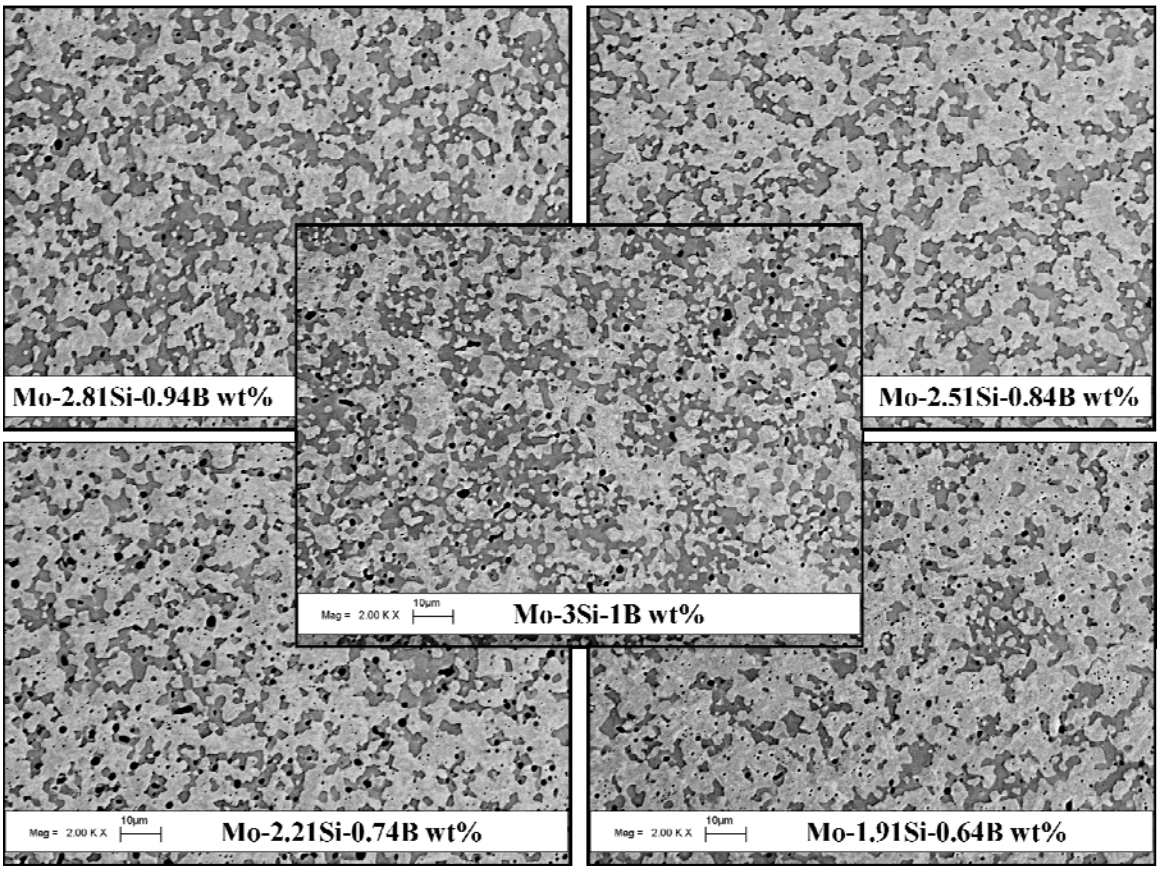

Figure 8.10: BSE micrographs of Mo-Si-B alloys of various compositions. The size of the molybdenum regions have been used to estimate the initial pore radius of the surface oxide layer.

An example sintering curve is plotted against a dimensionless time factor in Figure 8.11. Equation 8.10 is used to determine the time remaining to sinter to fully dense at a given relative density. The oxidation rate at a given time has been estimated by multiplying the oxidation rate of molybdenum ($mg/cm^2 \cdot h$) by the fraction of exposed molybdenum in the alloy, which is approximated as the percent porosity remaining in the glass layer. Figure 8.12 plots the oxidation rate of a sample as a function of time. The total weight of evaporated molybdenum per square centimeter is equal to the area under the curve. The integral has been evaluated using the trapezoid rule with the area split into ten intervals. Given the atomic fraction of molybdenum and the total quantity evaporated, it is possible to calculate the metal recession which occurs during sintering of the surface glass layer.

8.1.1.9 Metal Recession Due to Oxidation Permeation through the Borosilicate Layer

After sintering of the surface glass layer, further oxidation is due to diffusive flux of oxygen through the glass. The thickness of the glass in this analysis is calculated from the molybdenum weight loss occurring during sintering. The amount of silicon and boron remaining to form the glass layer is equal to the amount present in the layer which was oxidized during sintering. Knowing the amount of boron and silicon, as well as the density of a borosilicate glass of that composition, the thickness can be calculated. Fick's 1st Law is used to calculate the total quantity of oxygen diffused through the glass layer, where $J$ is the flux, $D$ is the diffusivity and $dc/dx$ is the change in concentration across the glass layer:

$$J = -D\frac{dc}{dx} \tag{8.12}$$

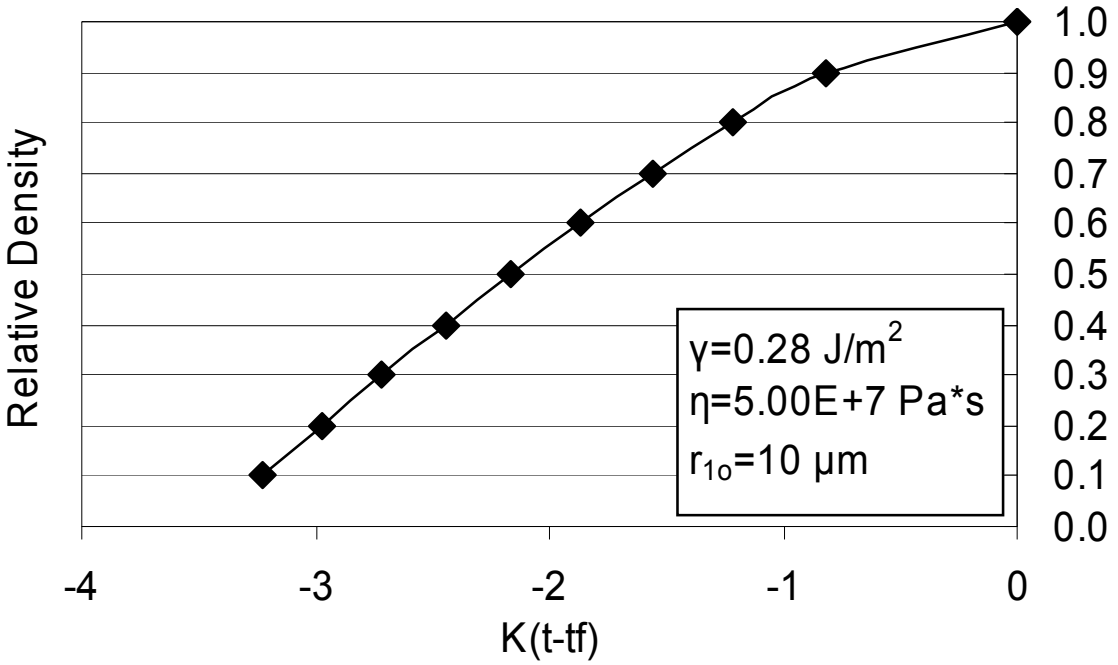


Figure 8.11: An example sintering curve plotting the relative density of the glass surface layer against a dimensionless time factor, for the initial conditions listed in the plot.

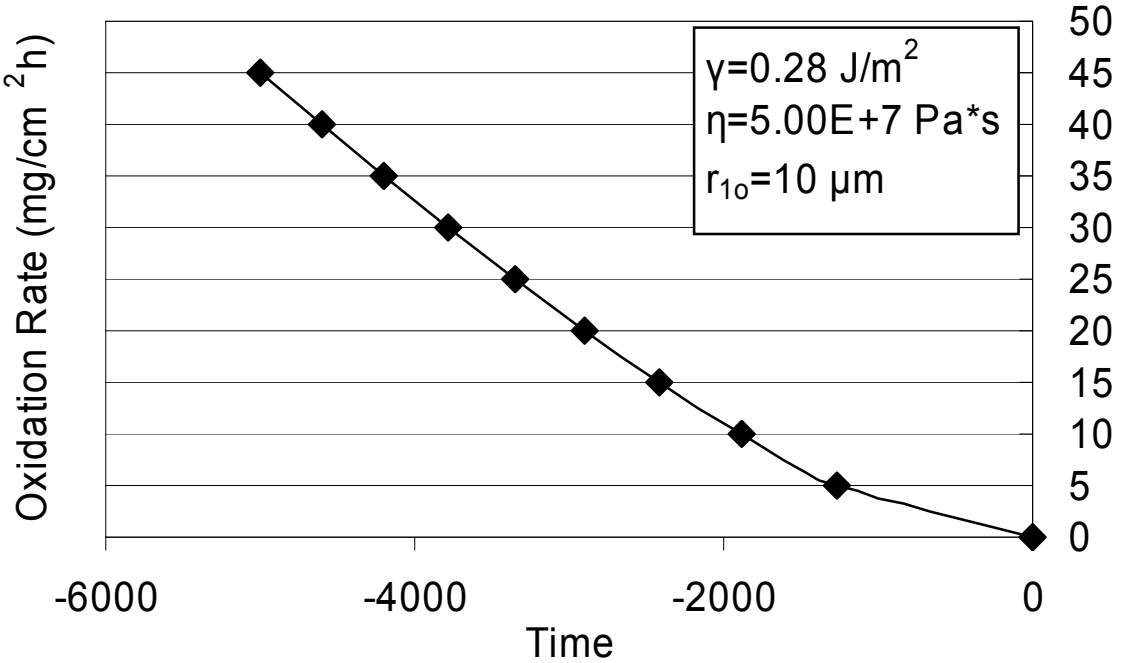


Figure 8.12: An example plot of the change in oxidation rate which occurs during the sintering of the surface glass layer, for the initial conditions listed in the plot.

The oxygen concentration at the surface of the glass can be assumed to be equal to the equilibrium concentration because the incorporation of $O_2$ into the glass is much faster than its diffusion in the glass [99]. As stated previously, the solubility of oxygen is assumed to be a constant value of $10^{17}$ $cm^{-3}$ and the concentration at the alloy/glass interface is assumed to be zero. The diffusivity is calculated from Equation 8.6, using the functions fit to parameters *A* and *B*. The flux is given in molecules/$cm^2$·sec. For a given time it is possible to calculate the total amount of oxygen diffused through the glass layer, which can be converted into the amount of metal recession due to permeation through the glass. In this analysis, the glass layer is assumed to remain a constant thickness defined by the amount of oxidation which occurs during the transient oxidation stage, which results in linear oxidation kinetics. Preferential oxidation of silicon and boron at the glass/alloy interface creates a layer of molybdenum mixed with a network of borosilicate glass. The volume change that occurs when the intermetallic phases are oxidized to form molybdenum, $SiO_2$ and $B_2O_3$ forces the glass to the surface. Future development of this model should factor in the thickening of the glass layer to more accurately predict the oxidation rates.

### 8.1.2 Model Objective Function

The objective function of the model, $F(\chi_{Si}, \chi_B)$, is the sum of the metal recession occurring during sintering and due to permeation of oxygen through the glass. Using the preceding parameters, a program was written in MatLab which calculates the total metal recession as a function of composition, temperature and time at temperature. The possible compositions are limited to the three-phase region of the phase diagram.

## 8.2 Optimization Algorithm

A combination of penalty and barrier methods were used to optimize the objective function for the given assumptions and constraints. The main advantage of these methods is they allow the use of unconstrained minimization techniques to be applied to constrained minimization problems. The minimization technique used was a pattern search. Zero$^{th}$ order minimization techniques such as this are useful when calculation of the gradient is difficult or prone to error [100]. This is the case with this model, where the objective function is a complex function of many factors and calculating the derivative of the function would be cumbersome. The applicability of this approach is also bolstered by the fact that the solution space is a convex space with a relatively narrow range of composition and temperature. A pattern search method would be less satisfactory if the sample space was spread over a large range, as is observed for the viscosity and diffusivity values which change many orders of magnitude over the range of compositions and temperatures examined.

### 8.2.1 Penalty and Barrier Methods

Barrier methods are useful in cases where feasibility must be maintained at all cost, as is the case in this analysis. The primary constraint on the algorithm is that the composition remains within the three-phase compatibility triangle of the phase diagram. For compositions which fall outside this region, Equation 8.1 yields negative values for the calculated volume percent molybdenum phase causing all further calculations to be invalid. The $Mo_{ss}$-A15-T2 region of the Mo-Si-B phase diagram is defined by the constraints:

$$g_1 = \chi_B - 2.059\chi_{Si} + 1.268 \leq 0 \tag{8.13}$$

$$g_2 = \chi_B + 2.037\chi_{Si} - 50.138 \leq 0 \tag{8.14}$$

$$g_3 = -\chi_B \leq 0 \tag{8.15}$$

The inverse barrier function used in the optimization is defined by the equation:

$$B(X) = -\sum_{i=1}^{m} \frac{1}{g_i(X)} \tag{8.16}$$

where $X=(\chi_{Si}, \chi_B)^T$. The function $B(X)$ is a continuous function that asymptotically approaches infinity as $X$ approaches the boundaries of the feasible space. Because the values of $g_i(x)$ are negative in the feasible region, $B(x)$ will always be positive in the feasible region. To prevent the search algorithm from crossing the asymptote, values of $B(x)$ which are negative are set equal to infinity, which creates an infinite barrier ensuring feasibility.

The multi-objective problem was modified into a single-objective problem by transforming the second objective of maximizing the percentage of the molybdenum solid solution into a goal, given as:

$$g_4 = Mo_{ss} \geq 50 vol.\% \tag{8.17}$$

which is written in terms of silicon and boron content as:

$$g_4 = \chi_B + 2.351\chi_{Si} - 32.110 \leq 0 \tag{8.18}$$

The goal was transformed into a penalty function, defined as:

$$P(x) = \sum_{i=1}^{n} \max\left[0, g_i(x)\right]^2 \tag{8.19}$$

which gives a value of $P=0$ for all composition values within the penalty constraint. The objective function to be minimized is then written as:

$$Z(X,r) = F(X) + rP(X) + \frac{1}{r}B(X) \tag{8.20}$$

The term $r$ is a scalar parameter which controls the penalty and barrier functions. The value of $r$ is increased with the number of search iterations, increasing the effect of the penalty functions and decreasing the effect of the barrier functions. The effect of Equation 8.19 is that the search algorithm is initially pushed away from the barriers, but still allowed to search the "infeasible" region within the low volume percent molybdenum region. As the number of iterations increases, the solution is pushed out of the penalty region and allowed to approach the barriers. In the analysis, the value of $r$ is increased by a factor of ten with each search iteration. The solution space is plotted in Figure 8.13 which plots the barrier constraints given by $g_1$, $g_2$, and $g_3$ as well as the subspace defined by the penalty function $g_4$.

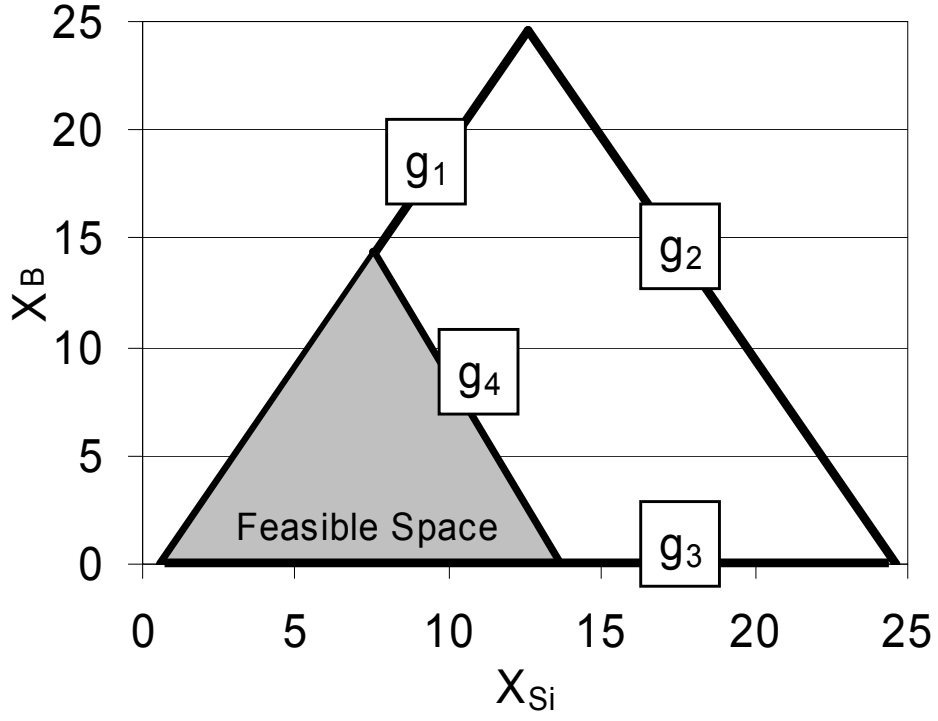


Figure 8.13: The solution space for the optimization algorithm, limited by constraints $g_1$, $g_2$ and $g_3$ which define the three-phase field, as well as the goal $g_4$ of $Mo_{ss} \geq 50$ vol.%.

### 8.2.2 Pattern Search Algorithm

A pattern search method is used to determine the minimum of the objective function. An initial position is first defined and the objective function evaluated at that point. The algorithm then takes an exploratory step to a new value of the position vector $X_k=(\chi_{Si}, \chi_B)^T$, as given by:

$$X_{k+1} = X_k + aS \tag{8.21}$$

where $a$ is the step size and $S$ is the search direction. The value of the objective function at the exploratory position is evaluated and compared to the previous value. If the value $Z_{k+1}(X,r)$ is a new minimum, the position vector $X_k$ is moved to this new position. This process is repeated until the exploratory steps find no further improvement. When this situation occurs the step size $a$ is halved, allowing the search algorithm to further converge on the minimum. The sequence continues until a termination condition is met, in this case when the step size is reduced to some resolution $R$. Another possible stopping criterion is when the difference of the objective function between $Z_k$ and $Z_{k+1}$ reaches some tolerance. The resolution in the position of the minimum was chosen as the stopping criteria because it was not readily apparent at the beginning of the analysis what the magnitude of the metal recession would be.

## 8.3 Oxidation Model Results

### 8.3.1 Metal Recession Model

Using the MatLab model derived for the metal recession, an example plot for the total metal recession that occurs after 1000 hours at 1000°C was generated as a function of composition for the alloys in the $Mo_{ss}$-A15-T2 phase triangle, as seen in Figure 8.14. Note that the lowest regions in the graph represent the areas of infeasibility which occur outside the $Mo_{ss}$-A15-T2 equilibrium, as shown by the barrier constraints in Figure 8.13.

The minimum metal recession of 0.54μm occurs at a composition of 17.25 at.% silicon and 14.19 at.% boron, corresponding to 2.1 vol.% of the molybdenum phase. It is of interest to note that the T2 phase which contains the largest fraction of silicon and boron performed poorly compared to an alloy with less silicon and boron, but this result can be explained in terms of the assumptions of the model. Because the initial density of the glass layer is set equal to the volume fraction of the intermetallic phases, the initial density of the glass layer on pure T2 is assumed equal to 100%. Furthermore, because the thickness of the protective glass layer is related to the amount of oxidation occurring during sintering, the thickness of the oxide layer goes to zero as the sintering time goes to zero. As the glass thickness approaches zero the flux of oxygen through the glass layer approaches infinity, causing the metal recession due to permeation to increase dramatically. This effect is observed in the model for all of the alloy compositions along the A15-T2 phase equilibrium line. A solution to this problem is to incorporate thickening of the oxide layer over time into the model.

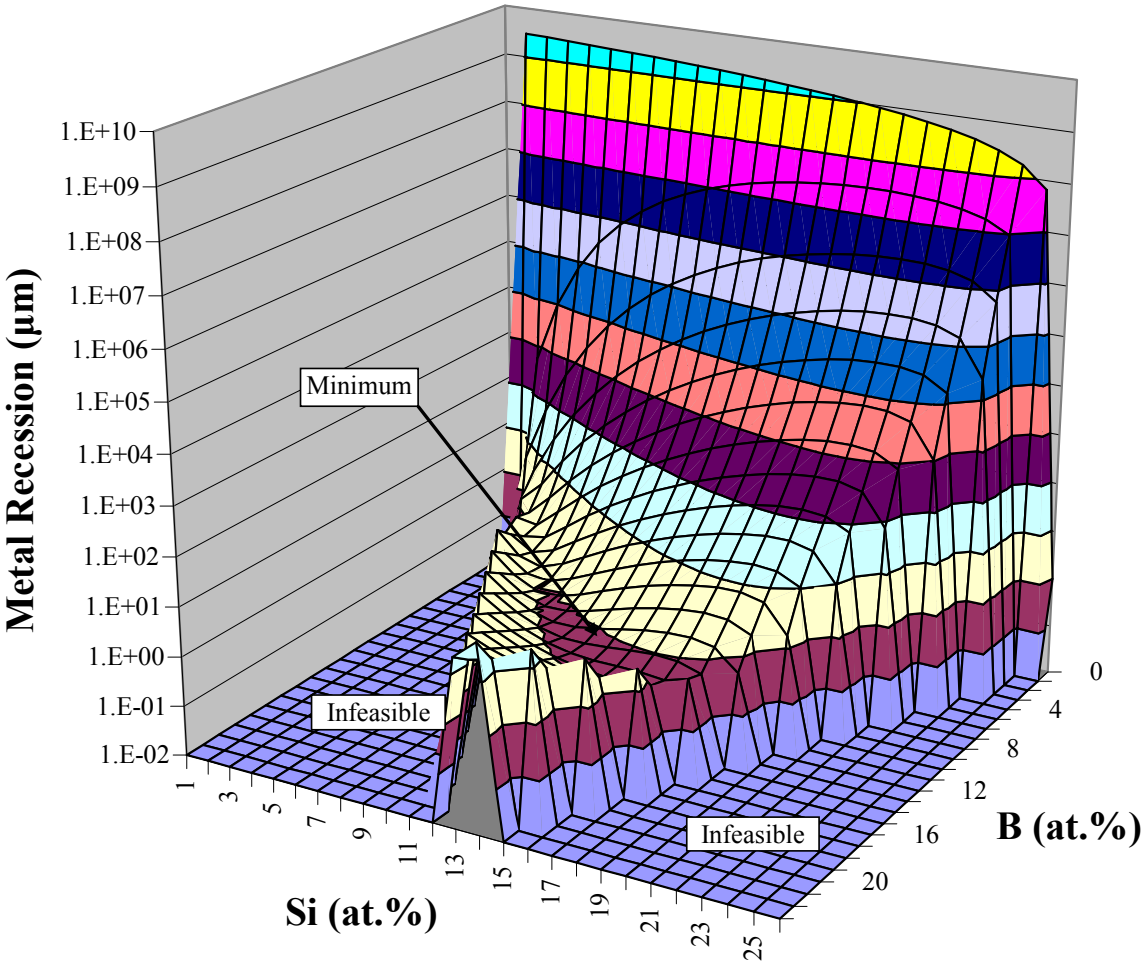


Figure 8.14: The calculated metal recession for alloys held at 1000°C for 1000 hours, plotted as a function of composition for the entire three-phase region of the phase diagram. The composition with minimum metal recession is indicated.

The metal recession which occurs during the sintering of the porous surface glass layer and due to oxygen permeation through the continuous glass layer are plotted in Figure 8.15 and listed in Table 8.2 for alloys with 50 vol.% $Mo_{ss}$ and a service life of 1000 hours at 1000°C. At a constant volume fraction of the intermetallics, the dominant mechanism is highly dependent on the silicon to boron ratio.

For high silica glasses the viscosity is high and the oxygen diffusivity is low, causing more oxidation to occur during the sintering stage and less due to diffusion. Glasses high in boron oxide sinter quickly due to their low viscosity but suffer from high oxygen permeability. The competing factors result in a minimum in the total metal recession rate.

### 8.3.2 Oxidation Model Optimization Routine – 4 Search Directions

The directions evaluated in the pattern search were initially along the four coordinate-axis directions. This search algorithm works well for starting points near the center of the feasible space but will not converge for starting points near the corners of the solution space, particularly near the pure molybdenum corner of the three-phase region. The problem is illustrated in Figure 8.16, where the initial point is (2,l) and the initial step size is 2. In this case the only feasible step direction is along the (1,0) direction. Figure 8.17 plots the metal recession at 1000°C for lines of constant boron content. It can be seen that at a constant boron content of 1 at.%, an increase in the amount of silicon causes a rapid increase in the metal recession.

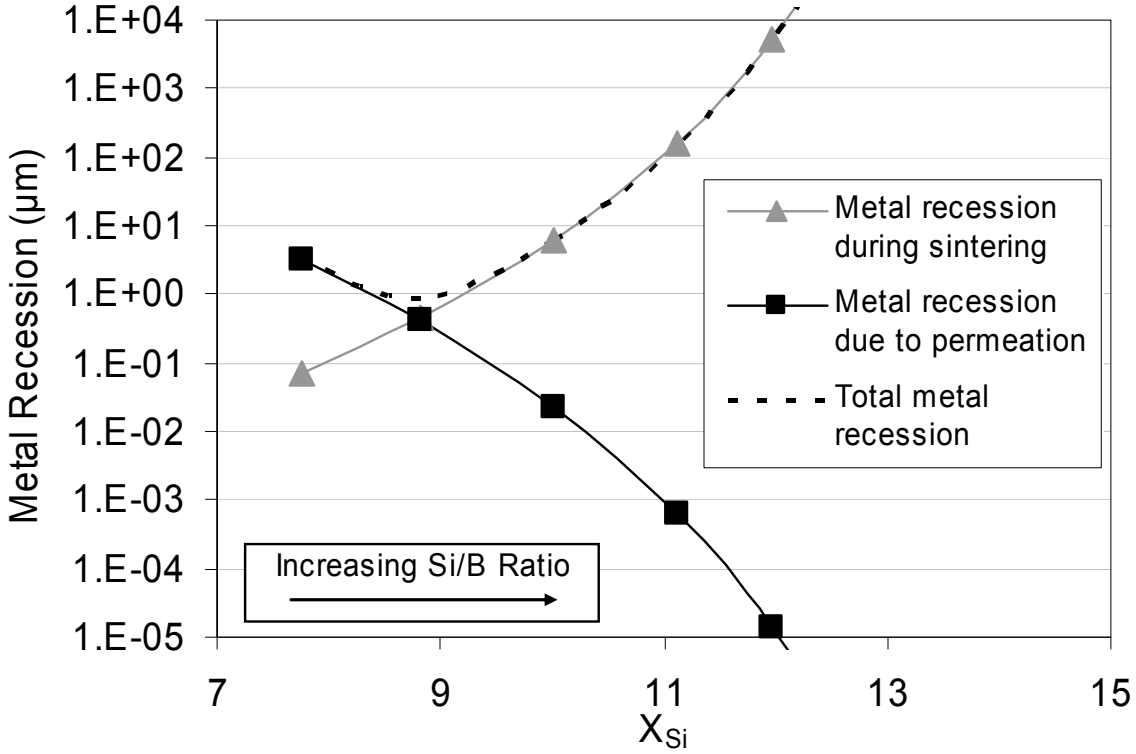


Figure 8.15: A comparison of the two mechanisms of metal recession, plotted as a function of the Si/B ratio for 50 vol.% $Mo_{ss}$ alloys held at 1000°C for 1000 hours.

Table 8.2: The calculated metal recession that occurs for 50 vol.% $Mo_{ss}$ alloys with varying Si/B ratios, for 1000°C for 1000 hours.

| $X_{Si}$ | $X_B$ | Si/B Ratio | Metal Recession (µm) | | |
|---|---|---|---|---|---|
| | | | Sintering | Permeation | Total |
| 13.66 | 0.0001 | 136600 | 1.35E+09 | 1.75E-16 | 1.35E+09 |
| 12.91 | 1.77 | 7.29 | 1.48E+06 | 1.87E-08 | 1.48E+06 |
| 11.97 | 3.98 | 3.01 | 5.01E+03 | 1.35E-05 | 5.01E+03 |
| 11.13 | 5.96 | 1.87 | 1.57E+02 | 6.54E-04 | 1.57E+02 |
| 10.02 | 8.57 | 1.17 | 6.29E+00 | 2.31E-02 | 6.31E+00 |
| 8.81 | 11.39 | 0.77 | 4.60E-01 | 4.05E-01 | 8.65E-01 |
| 7.77 | 13.86 | 0.56 | 6.86E-02 | 3.17E+00 | 3.24E+00 |

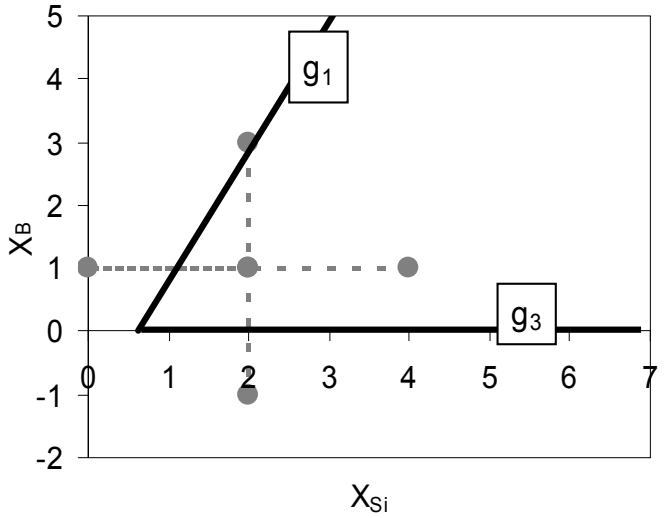


Figure 8.16: A schematic of the 4-direction pattern search algorithm used for the optimization routine.

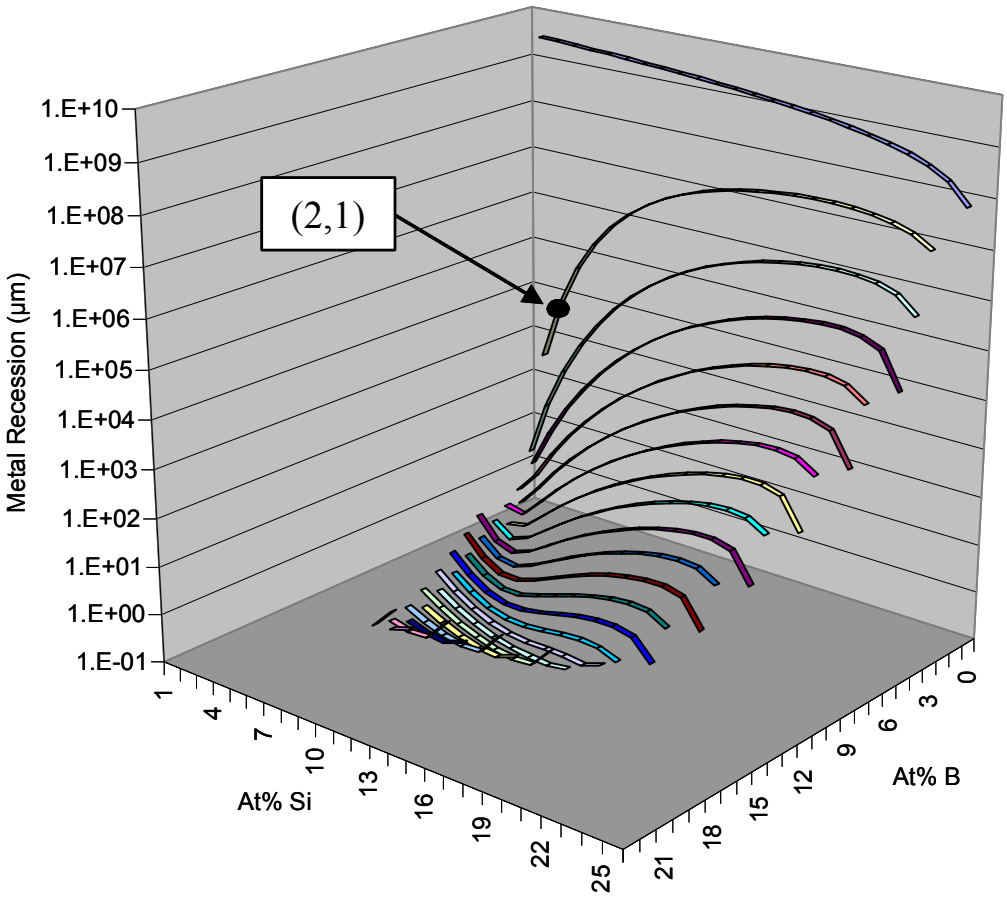


Figure 8.17: The total metal recession for 1000 hours at 1000°C for lines of constant boron content, which illustrates a sticking point for the 4-direction search algorithm.

With no possible direction steps, the search algorithm continues to reduce the step size until a suitable $X_{k+1}$ value can be found. The effect of this reduced interval is that by the time the search algorithm is able to move from the corner, the step size is extremely small and the time to convergence is very long. One possible solution to this problem is to increase the value of the barrier function, which forces the solution away from the barriers in the initial stages of the minimization. The effect of increasing the barrier height, by reducing *r*, is plotted in Figure 8.18, where *R* is the resolution in the position of the search algorithm. For the small barrier height the step size of the search algorithm starting in the corner drops quickly with increasing iterations, indicating the algorithm is stuck. After finally breaking free of that point the step size is so small that the solution does not converge even after 300 iterations, Figure 8.19. By increasing the barrier height the search position is pushed out of the corner and is able to find a solution as quickly as the searches with initial starting points in the middle of the feasible region. Figure 8.19 plots the convergence of *Z(X,r)* and also illustrates the effect of increasing the barrier height. Although the number of iterations to convergence is increased, the robustness of the algorithm is improved.

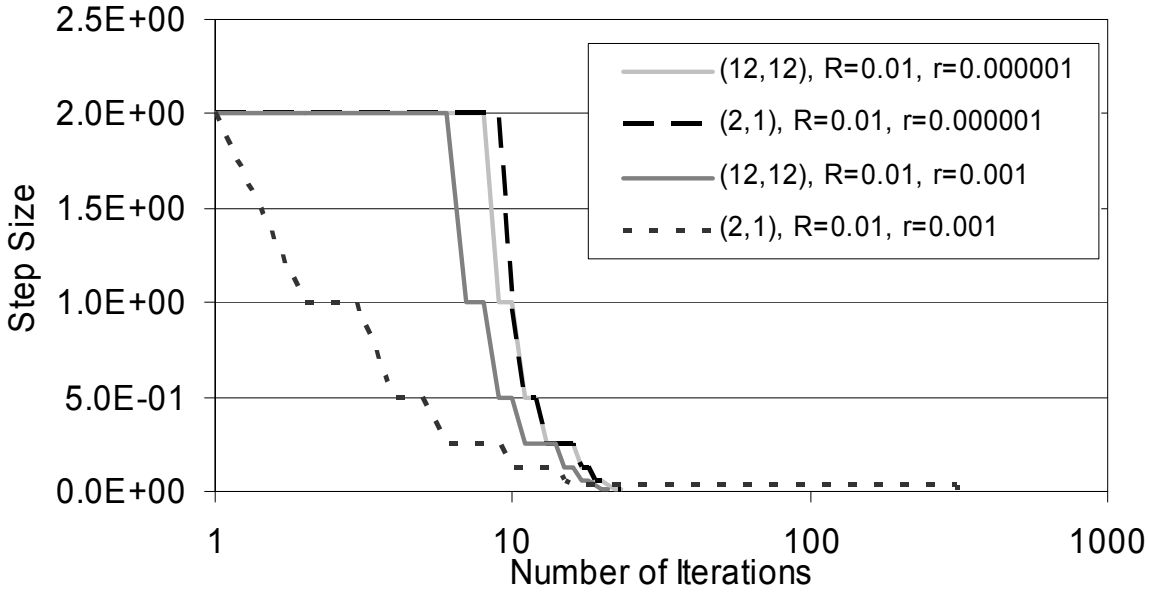


Figure 8.18: The change in the step size of the 4-direction search algorithm as a function of the number of iterations for different limits of resolution, $r$, and different starting positions ($X_{Si}$, $X_B$).

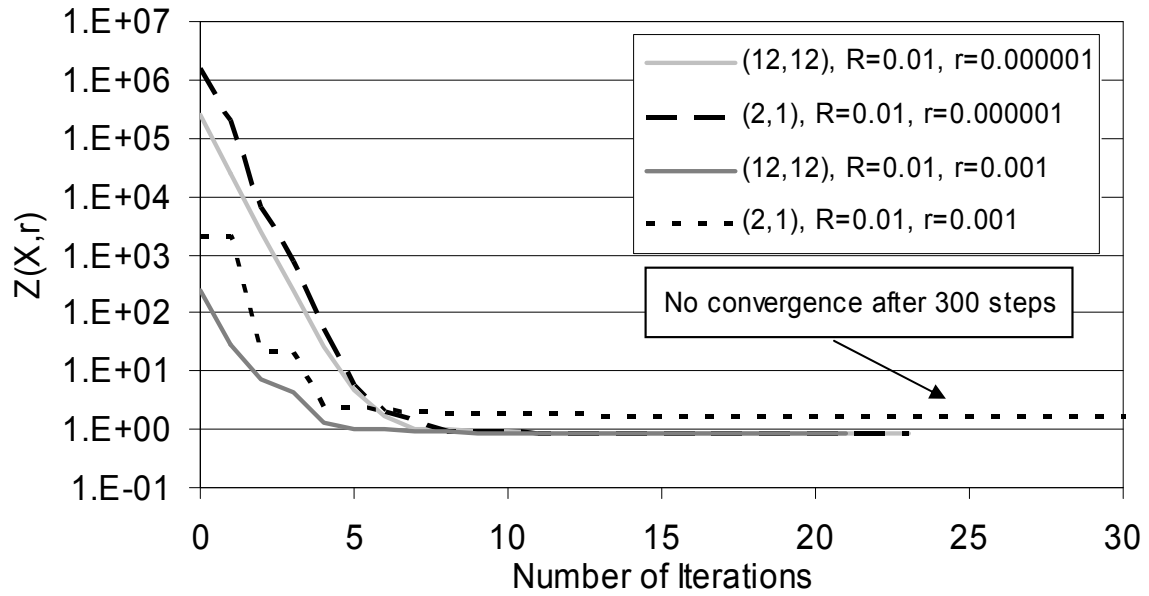


Figure 8.19: Convergence plots for the 4-direction search algorithm, illustrating the effect of different limits of resolution, $r$, and starting positions ($X_{Si}$, $X_B$).

### 8.3.3 Oxidation Model Optimization Routine – 8 Search Directions

To decrease the likelihood of the search algorithm getting stuck, the number of search directions $S$ was increased from four to eight. The (1,1) family of directions was searched in addition to the coordinate axis directions. Figure 8.20 plots the step size of the algorithm. It can be seen that increasing the number of search directions helps the algorithm converge more quickly, even for smaller barrier heights.

Figure 8.21 shows that by increasing the number of search directions, the number of iterations to convergence is not as dependent on the starting position. While doubling the number of search directions requires doubling the number of calculations in each iteration, it also reduces the probability of the search algorithm never converging to the minimum. This improvement in robustness results in an overall reduction in computational time. For a resolution in $X$=0.01, the computation time averaged at 12 seconds and only increased to 16 seconds at a resolution of 0.0001. In comparison, for the non-converging solution the time until the stopping criteria was over two minutes.

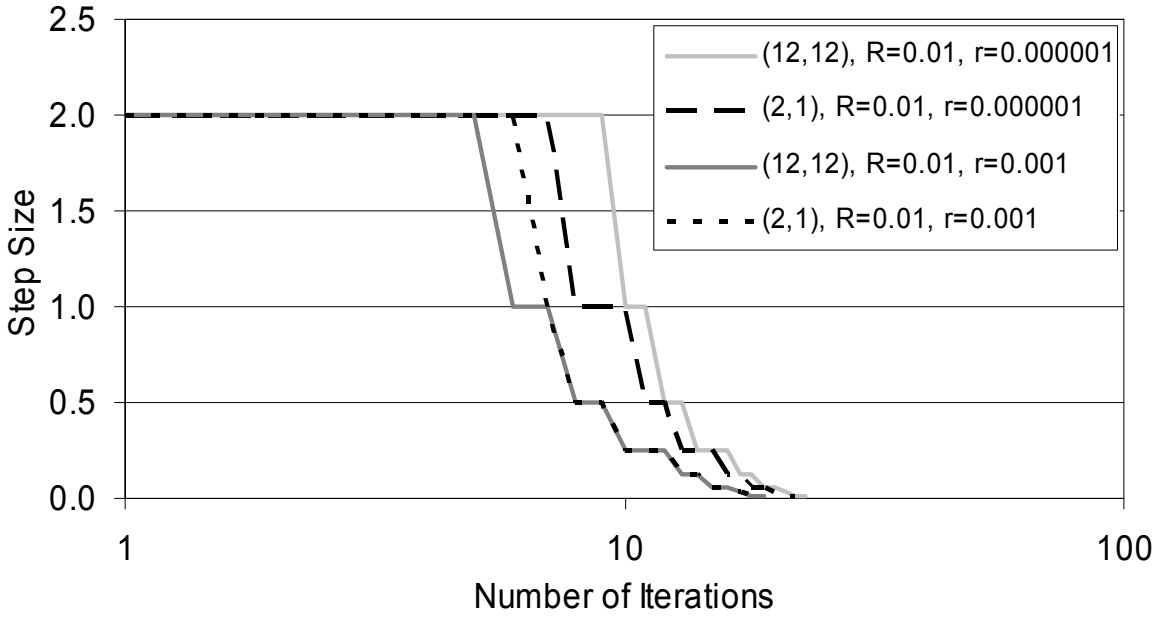


Figure 8.20: The change in the step size of the 8-direction search algorithm as a function of the number of iterations for different limits of resolution, $r$, and different starting positions ($X_{Si}$, $X_B$).

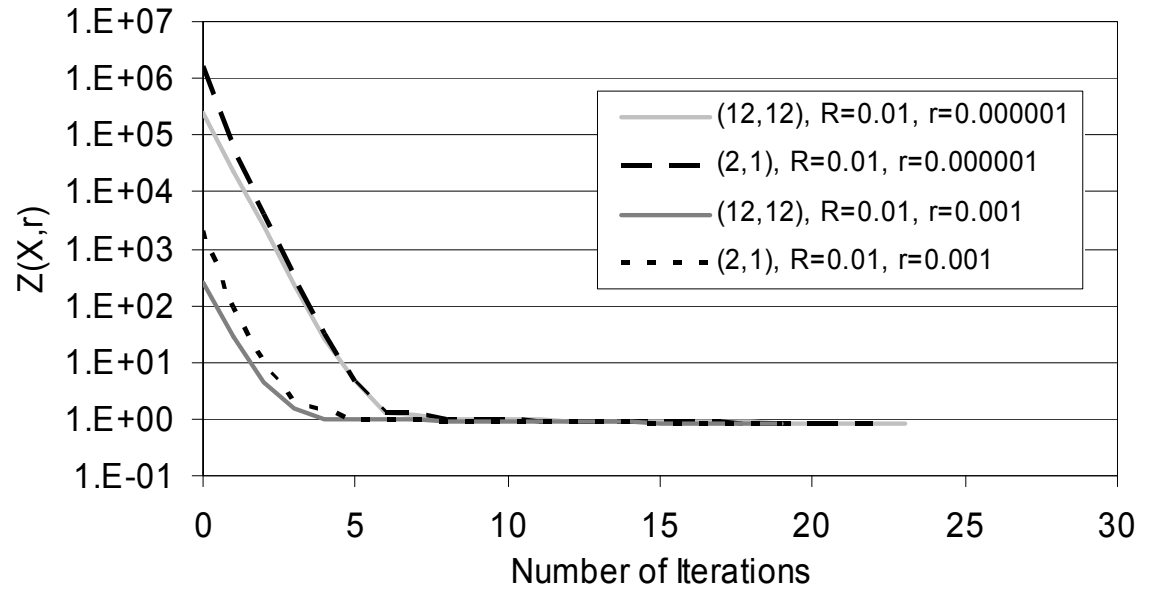


Figure 8.21: Convergence plots for the 8-direction search algorithm, illustrating the effect of different limits of resolution, $r$, and starting positions ($X_{Si}$, $X_B$).

### 8.3.4 Oxidation Model Optimization Results

Using the 8-direction search algorithm, the Mo-Si-B compositions with the minimum amount of metal recession due to oxidation were determined for a series of temperatures. The analysis was completed assuming a service life of 1000 hours and with the constraint that the $Mo_{ss}$ matrix must be no less than 50 vol.%. The compositions and the corresponding values of the metal recession are listed in Table 8.3 and the compositions are plotted on the phase diagram in Figure 8.22. The Si/B ratios of the optimized alloys are plotted in Figure 8.23 as a function of temperature.

As might be expected, the solutions with the least oxidation are found at the highest intermetallic contents allowed within the established constraints, but it can also be seen that the optimal proportions of the A15 and T2 phases vary with temperature. As the temperature is increased, the optimal composition shifts toward a higher A15 content. This shift is due to the two different mechanisms responsible for the oxidation. At high temperatures the increase in viscosity due to higher silica content is offset by the increase in temperature and a more silica rich glass is preferred for its lower oxygen permeation. Oxygen diffusion is less of a problem at low temperatures and higher boron oxide contents are needed to reduce the sintering time of the glass layer.

Table 8.3: The optimized Mo-Si-B compositions with the minimum metal recession at temperature *T*, for $Mo_{ss} \geq 50$ vol.%.

| Temperature (°C) | $X_{Si}$ | $X_B$ | Metal Recession (μm) |
|---|---|---|---|
| 800 | 7.78 | 13.81 | 0.30 |
| 1000 | 8.81 | 11.39 | 0.87 |
| 1200 | 10.02 | 8.56 | 1.64 |
| 1400 | 11.13 | 5.95 | 2.06 |
| 1600 | 11.97 | 3.97 | 1.76 |

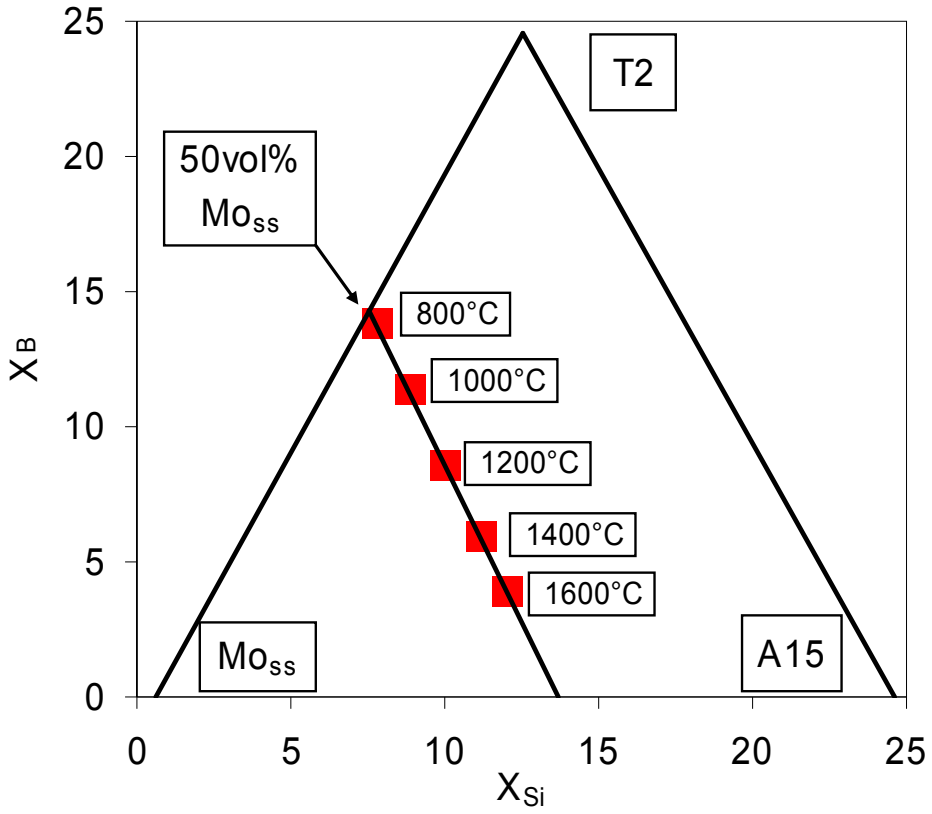


Figure 8.22: The optimized Mo-Si-B compositions with the minimum metal recession at temperature *T*, for $Mo_{ss} \geq 50$ vol.%.

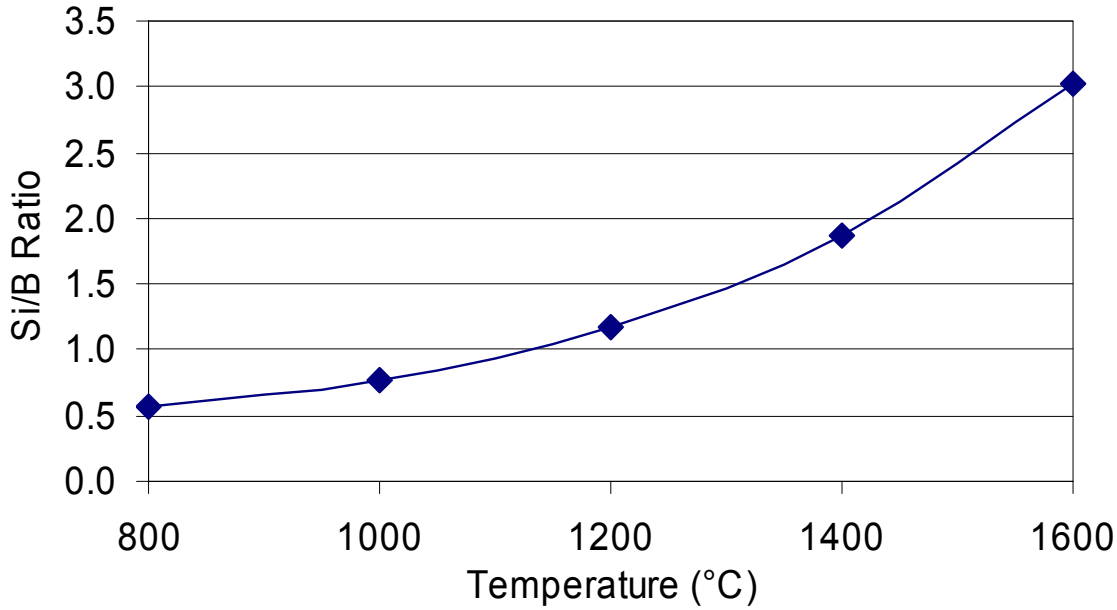


Figure 8.23: The Si/B ratio of the optimized composition for a given temperature and for $Mo_{ss} \geq 50$ vol.%.

## 8.4 Discussion of Oxidation Model Results

A model for the oxidation of Mo-Si-B alloys was developed which takes into account oxidation occurring in two regimes. The first part of the model calculates the thickness of metal oxidized during the initial exposure to a high-temperature oxidizing environment, when the porous glass is coalescing to form a protective layer. The second part of the model calculates the thickness of metal oxidized due to molecular permeation of oxygen through the glass layer. The model parameters were fit to experimental data in order to give the more realistic solutions.

The model was optimized using penalty and barrier methods. Barriers were used in order to ensure the solution remained in the three-phase boundary. A penalty method was used to ensure the molybdenum volume fraction remained above a minimum value of 50 vol.%. Analysis of alloys requiring higher $Mo_{ss}$ volume fractions could be done easily by changing the constraint which defines the penalty function.

For all temperatures, the optimum composition was found to lie on the 50 vol.% $Mo_{ss}$ line. The compositions are listed in Table 8.4, in terms of the weight ratios. The optimal composition moved toward higher silicon contents as the service temperature was increased. It is promising to note that the optimal composition calculated for a temperature of 1200°C had a 3/1 silicon to boron ratio by weight. This is equal to the ratio for the Mo-3Si-1 wt.% alloy, which has been the main focus in this work and has been identified as the primary composition of interest by Berczik, among others [4,5].

The formulation of the oxidation model is based on actual physical phenomena and materials parameters, nevertheless a number of assumptions and conjectures were required for its development. There are also many physical mechanisms not

incorporated, such as changes in the glass composition occur over time due to $B_2O_3$ evaporation and the effect of dissolved molybdenum oxide. The metal recession rates calculated may not be accurate in actual circumstance, but the model does point to trends and illustrates important factors for developing more oxidation resistant alloys.

Table 8.4: The optimized Mo-Si-B compositions (by weight) for a given temperature, assuming a fixed $Mo_{ss}$ volume fraction of 50%.

| **Temperature (°C)** | **Si (wt.%)** | **B (wt.%)** | **Si/B (By Weight)** |
|---|---|---|---|
| 800 | 2.77 | 1.89 | 1.5 |
| 1000 | 3.08 | 1.53 | 2.0 |
| 1200 | 3.44 | 1.13 | 3.0 |
| 1400 | 3.75 | 0.77 | 4.9 |
| 1600 | 3.98 | 0.51 | 7.8 |

# CHAPTER 9

# CONCLUSIONS AND RECOMMENDATIONS

The call for higher performance jet turbine engines has created the need for a new class of high-temperature structural materials. Mo-Si-B alloys are a leading candidate for the next generation of jet turbine engine blades and have the potential to raise the operating temperatures 300-400°C, which would dramatically increase power and efficiency. The alloys of interest are a three-phase mixture of the molybdenum solid solution ($Mo_{ss}$) and two intermetallic phases, $Mo_3Si$ (A15) and $Mo_5SiB_2$ (T2). In order to balance mechanical properties and oxidation resistance, the intermetallic phases must be present as a fine dispersion in a continuous $Mo_{ss}$ matrix. Much of the past research was focused on melt-based processing but primary solidification of molybdenum results in molybdenum dendrites in a brittle intermetallic matrix.

In this work, a novel powder metallurgical method was developed which uses the reaction of molybdenum, silicon nitride ($Si_3N_4$) and boron nitride (BN) powders to synthesize a fine dispersion of the intermetallic phases in a $Mo_{ss}$ matrix. The covalent nitrides are stable in oxidizing environments up to 1000ºC which allows for fine particle processing without the formation of silicon and boron oxides. This approach utilizes standard powder processing techniques and provides a means for creating Mo-Si-B alloys in a much less complex and expensive manner than previously demonstrated.

The reactions to form the intermetallics were studied by XRD and TGA. The reactions to form the T2 and A15 phases began at 1140°C and 1193°C respectively, and were completed at 1300°C in less than six hours. Quantitative phase analysis using the Rietveld method confirmed the phase contents achieved were equal to those predicted from the phase diagram.

The alloys were sintered in a high purity mixture of Ar/10% $H_2$. Low impurity levels were achieved with typical oxygen contents of 300-400ppm, carbon contents of 50-80ppm and nitrogen contents of 10-20ppm. Densities above 95% of theoretical were achieved by pressureless sintering at 1600°C and full theoretical density was achieved by a hot-isostatic pressing. Decreasing the sintering temperature from 1600°C to 1300°C reduced the grain sizes of all three phases by over a factor of two.

The A15 and T2 phases can not be differentiated in backscatter-electron images which prevents complete characterization of the microstructures. Electron-backscatter diffraction (EBSD) imaging was used to precisely define the location of all three phases in the microstructures and to create high-quality phase maps suitable for automated image analysis. The use of EBSD imaging also permitted precision measurement of volume fractions and grain size distributions of individual phases.

The powder metallurgy approach developed creates an opportunity to optimize microstructural parameters through changes in starting materials and processing conditions. The effect of the particle size and morphology was investigated for four BN powders. Numerical analytical tools, including two-point correlation functions, were used to quantify the clustering of the intermetallics in the $Mo_{ss}$ matrix. The distribution of the T2 phase was shown to be dependent on the size and morphology of the BN

reactant powder. The hBN powder resulted in large T2 clusters due to the large powder flakes. The 0.5μm and 1μm cBN powders gave a fine, homogenous dispersion of the phase, but the 0.125μm cBN powder resulted in significant clustering due to agglomeration of the high surface area powder. The reduced diffusion rates limited the redistribution of the T2 phase in alloys processed at 1300°C and further illustrated that the dispersion of the T2 phase is tied to the original dispersion of the BN reactant.

High-temperature tensile tests were conducted on the Mo-2Si-1B and Mo-3Si-1B wt.% alloys at a strain rate of $10^{-4}$ $s^{-1}$. Yield strengths of 580MPa at 1100°C and 480MPa at 1200°C were measured for the Mo-2Si-1B wt.% alloy. The yield strength of the Mo-3Si-1B wt.% alloy was 680MPa at 1100°C and 420MPa at 1300°C. A review of the pertinent literature reveals that these are among the highest strengths reported for these compositions, although the ductility of these alloys needs to be improved. A plastic strain of 1% was not observed until 1100°C for the Mo-2Si-1B wt.% alloy and 1200°C for the Mo-3Si-1B wt.% alloy.

The oxidation of the Mo-3Si-1B wt.% alloy was tested in air at 1000°C and 1100°C. A continuous glass layer formed within 30 minutes of exposure and a transient weight loss of less than 50mg/$cm^2$ was observed at both temperatures due to the fine spacing of intermetallic particles. The weight loss after the formation of the surface layer was 15.5 ± 4.9μg/$cm^2$·h at 1000°C and 1.4 ± 0.5mg/$cm^2$·h at 1100°C. Much of the weight loss observed for the 1100°C samples was the result of areas of localized damage where surface connected porosity resulted in internal oxidation. A pre-oxidation treatment at 1300°C reduced the 1100°C oxidation rate in air to only 22μg/$cm^2$·h.

An oxidation model was developed to better understand the oxidation of Mo-Si-B alloys and to study the competing factors which govern its behavior. The model factors in both stages of oxidation to identify compositions that minimize the total oxidation for a given temperature and service life. The formulation of the oxidation model was based on actual physical phenomena and materials parameters, and serves to illustrate important factors for developing more oxidation resistant alloys. The oxidation rates calculated may not be accurate in actual circumstance, but it is promising to note that the optimal composition calculated for 1200°C had a 3/1 silicon to boron ratio by weight. This is equal to the ratio for the Mo-3Si-1 wt.% alloy, which has been the main focus in this work and has been identified as the primary composition of interest by Berczik, among others.

The following the following recommendations are made for future research:

1. Surface aluminization of Mo-Si-B alloys was shown in the literature to significantly improve oxidation resistance, although diffusion of the layer into the interior of the material reduced the effectiveness over long times. The formation of bulk Mo-Al-Si-B alloys was demonstrated to be feasible using the powder processing method developed. At the time of the research, HIPing procedures had not been developed and the oxidation resistance of those alloys was hindered by residual porosity. Future research should be conducted on the oxidation resistance and mechanical properties of fully dense Mo-Al-Si-B alloys to evaluate the benefits of aluminum alloying additions.

2. The size and morphology of the BN nitride reactant powder was shown to affect the distribution of the T2 phase in the sintered alloys. There also appeared to be a correlation between the size of the A15 and T2 phase regions. Research should be completed to investigate the cause of the relationship between the distributions of the two phases and also to determine the effects of different sized $Si_3N_4$ reactant powders.
3. Continuing efforts should be conducted to consolidate the alloys at lower temperatures, which will reduce grain sizes and decrease the equilibrium concentration of silicon in the $Mo_{ss}$ matrix. This work should include attrition milling to reduce agglomeration and improve dispersion of raw materials. Studies should also be conducted to determine the time frame for the precipitation and dissolution of the A15 phase in the $Mo_{ss}$ matrix to evaluate if annealing can be used to reduce the silicon solid solution content.
4. The possibility exists to produce Mo-Si-B alloys in near final geometry using the reaction synthesis method and the powder processing techniques presented. Complex shape formation was demonstrated by cold-isostatic pressing and hot-isostatic pressing has been demonstrated to achieve full theoretical density. The strengths measured for the alloys prepared in this work using these procedures are higher than comparable alloys produced by forging and extrusion. The continued development of complex shape formation for Mo-Si-B alloys should be explored.

# REFERENCES


[1] J.H. Perepezko and D.M. Dimiduk, “Mo-Si-B alloys: Developing a Revolutionary Turbine-Engine Material”, *MRS Bulletin*, 28 (9) (2003), 639-645.

[2] M. Akinc, M.K. Meyer, M.J. Kramer, A.J. Thom, J.J. Huebsch, and B. Cook, “Boron-Doped Molybdenum Silicides for Structural Applications,” *Materials Science and Engineering A*, 261 (1-2) (1999) 16-23.

[3] J.H. Perepezko, R. Sakidja, and S. Kim, “Phase Stability in Processing and Microstructure Control in High Temperature Mo-Si-B Alloys”, *MRS Symposium Proceedings*, 646 (2001) N4.5.

[4] D.M. Berczik, “Method for Enhancing the Oxidation Resistance of a Molybdenum Alloy, and a Method of Making a Molybdenum Alloy,” U.S. Patent 5,595,616, January 21, 1997.

[5] D.M. Berczik, “Oxidation Resistant Molybdenum Alloy,” U.S. Patent 5,693,156, December 2, 1997.

[6] C.A. Nunes, R. Sakidja, Z. Dong, and J.H. Perepezko, “Liquidus Projection for the Mo-Rich Portion of the Mo-Si-B Ternary System,” *Intermetallics*, 8 (4) (2000), 327-337.

[7] P. Jéhanno, M. Heilmaier, H. Kestler, M. Böning, A. Venskutonis, B. Bewlay, and M. Jackson, “Assessment of a Powder Metallurgical Processing Route for Refractory Metal Silicide Alloys”, *Metallurgical and Materials Transactions*, 36A (2005) 515-523.

[8] S. Paswan, R. Mitra and S.K. Roy, “Isothermal oxidation behavior of Mo–Si–B and Mo–Si–B–Al alloys in the temperature range of 400–800°C,” *Materials Science and Engineering A*, 424 (2006) 251-265.

[9] M.R. Middlemas, "A Nitride-Based Reaction for the Formation of a Three-Phase Molybdenum-Silicon-Boron Intermetallic Alloy," M.S. Thesis, Georgia Institute of Technology, Atlanta, GA, 2005.

[10] M.R. Middlemas and J.K. Cochran, "Oxidation Behavior of Mo-Si-B Alloys Produced by Reaction Synthesis", *137th Annual Meeting Supplemental Proceedings: Materials Processing and Properties*, TMS, 3 (2008) 177-183.

[11] M.R. Middlemas and J.K. Cochran, "Dense, Fine-Grain Mo-Si-B Alloys from Nitride-Based Reactions", *JOM*, 60 (7) 2008 19-24.

[12] J.C. Zhao and J.H. Westbrook, "Ultrahigh-Temperature Materials for Jet Engines", *MRS Bulletin*, 28 (9) (2003) 622-630.

[13] P. Jéhanno, "Results of R&D Program Take Off", www.ffg.at/getdownload.php?id=1477, (accessed 01/27/09).

[14] D. Lide, ed., Handbook of Chemistry and Physics, Cleveland: CRC Press, 2008

[15] J.A. Shields and E.L. Baker, "Refractory Metals Forum: Molybdenum Alloys and Emerging Applications", *Advanced Materials & Processes*, 155 (1999), 61-66.

[16] B.P. Bewlay, M.R. Jackson, J.-C. Zhao, P.R. Subramanian, M.G. Mendiratta, and J.J. Lewandowski, "Ultrahigh-Temperature Nb-Silicide-Based Composites", MRS Bulletin, vol. 28, no. 9, Sep., pp. 646-653, 2003.

[17] B.P. Bewlay, M.R. Jackson, J.-C. Zhao, and P.R. Subramanian, "A Review of Very-High-Temperature Nb-Silicide-Based Composites", *Metallurgical and Materials Transactions A*, 34A (2003) 2043-2052.

[18] Siegfried Schider, Refractory Metals, Gemany: verlag moderne industrie AG & Co., 1991.

[19] M.K. Meyer, A.J. Thom, and M. Akinc, "Oxide Scale Formation and Isothermal Oxidation Behavior of Mo-Si-B Intermetallics at 600-1000ºC", *Intermetallics*, 7 (1999) 153-162.

[20] T.C. Chou and T.G. Nieh, "Mechanism of $MoSi_2$ Pest During Low Temperature Oxidation", *Journal of Materials Research*, 8 (1) (1993) 214-226.

[21] J.J. Petrovic, A.K. Vasudevan, "Key Developments in High Temperature Structural Silicides", *Materials Science and Engineering A*, 261 (1999) 1-5.

[22] D.M. Shah, D. Berczik, D.L. Anton, and R. Hecht, "Appraisal of Other Silicides as Structural Materials", *Materials Science and Engineering* , A155 (1992) 45-47.

[23] S. Ochiai, "Improvement of the Oxidation-Proof Property and the Scale Structure of $Mo_3Si$ Intermetallic Alloy through the Addition of Chromium and Aluminum Elements", *Intermetallics*, 14 (2006) 1351-1357.

[24] A.B. Gokhale and G.J. Abbaschian, "The Mo-Si (Molybdenum-Silicon) System", *Journal of Phase Equilibria*, 12 (4) (1991) 493-498.

[25] K.E. Spear and P.K. Liao, "The B-Mo (Boron-Molybdenum) System", *Bulletin of Alloy Phase Diagrams*, 9 (4) (1988) 457-466.

[26] I. Rosales and J.H. Schneibel, "Stoichiometry and Mechanical Properties of $Mo_3Si$", *Intermetallics*, 8 (2000) 885-889.

[27] J.H. Perepezko, R. Sakidja, S. Kim, Z. Dong, and J.S. Park, "Multiphase Microstructures and Stability in High Temperature Mo-Si-B Alloys", *Structural Intermetallics 2001: Proceedings of the Third Symposium on Structural Intermetallics*, TMS, (2001) 505-514.

[28] J.H. Schneibel, C.T. Liu, D.S. Easton, and C.A. Carmichael, "Microstructure and Mechanical Properties of Mo-$Mo_3Si$-$Mo_5SiB_2$ Silicides", *Materials Science and Engineering*, A261 (1999) 78-83.

[29] C.J. Rawn, J.H. Schneibel, C.M. Hoffmann, and C.R. Hubbard, "The Crystal Structure and Thermal Expansion of $Mo_5SiB_2$", *Intermetallics*, 9 (2001) 209-216.

[30] R. Sakidja, G. Wilde, H. Sieber, and J.H. Perepezko, "Microstructural Development of Mo(ss) + T2 Two-Phase Alloys", *MRS Symposium Proceedings*, 552 (1999) KK6.3

[31] R. Sakidja, J. Myers, S. Kim, and J.H. Perepezko, "The Effect of Refractory Metal Substitution on the Stability of Mo(ss) + T2 Two-Phase Field in the Mo-Si-B System", *International Journal of Refractory & Hard Materials*, 18 (2000) 193-204.

[32] M. Kumagai, K. Ito, and M. Yamaguchi, "On Mo-9Si-18B Alloys with T2-$Mo_{ss}$ Eutectic Microstructure: Mechanical Properties and Protective Silicide Coating", *MRS Symposium Proceedings*, 753 (2003) BB5.26.

[33] H. Choe, J.H. Schneibel, and R.O. Ritchie, "On the Fracture and Fatigue Properties of Mo-$Mo_3Si$-$Mo_5SiB_2$ Refractory Intermetallic Alloys at Ambient to Elevated Temperature (25°C to 1300°C)", *Metallurgical and Materials Transactions A*, 34A (2003) 225-239.

[34] R. Sakidja, S. Kim, J.S. Park and J.H. Perepezko, "Transition Metal Alloying and Phase Stability in the Mo-Si-B System", *MRS Symposium Proceedings*, 753 (2003) BB2.3.

[35] J.H. Schneibel, M.J. Kramer, Ö. Ünal, and R.N. Wright, "Processing and Mechanical Properties of a Molybdenum Silicide with the Composition Mo-12Si-8.5B (at%)", *Intermetallics*, 9 (2001) 25-31.

[36] P. Jéhanno, M. Heilmaier, H. Saage, M. Böning, H. Kestler, J. Freudenberger, and S. Drawin, "Assessment of the High Temperature Deformation Behavior of Molybdenum Silicide Alloys," *Materials Science and Engineering A*, 464 (2007) 216-223.

[37] A.P. Alur, N. Chollacoop, and K.S. Kumar, "High-Temperature Compression Behavior of Mo-Si-B Alloys", *Acta Materialia*, 52 (2004) 5571-5587.

[38] K.S. Kumar and A.P Alur, "Deformation Behavior of a Two-Phase Mo-Si-B Alloy", *Intermetallics*, 15 (2007) 687-693.

[39] T.G. Nieh, J.G. Wang, and C.T. Liu, "Deformation of a Multiphase Mo-9.4Si-13.8B Alloy at Elevated Temperatures", *Intermetallics*, 9 (2001) 73-79.

[40] J.H. Schneibel, M.J. Kramer, and D.S. Easton, "A Mo-Si-B Intermetallic Alloy with a Continuous α-Mo Matrix", *Scripta Materialia*, 46 (2002) 217-221.

[41] J.J. Kruzic, J.H. Schneibel, and R.O. Ritchie, "Fracture and Fatigue Resistance of Mo-Si-B Alloys for Ultrahigh-Temperature Structural Applications", *Scripta Materialia*, 50 (2004) 459-464.

[42] P. Jéhanno, M. Heilmaier, H. Saage, H. Heyse, M. Böning, H. Kestler, and J.H. Schneibel, "Superplasticity of a Multiphase Refractory Mo-Si-B Alloy", *Scripta Materialia*, 55 (2006) 525-528.

[43] M. Krüger, S. Franz, H. Saage, M. Heilmaier, J.H. Schneibel, P. Jéhanno, M. Böning, and H. Kestler, "Mechanically Alloyed Mo-Si-B Alloys with a Continuous α-Mo Matrix and Improved Mechanical Properties", *Intermetallics*, 16 (2008) 933-941.

[44] P. Jéhanno, M. Heilmaier, and H. Kestler, "Characterization of an Industrially Processed Mo-Based Silicide Alloy", *Intermetallics*, 12 (2004) 1005-1009.

[45] D. Sturm, M. Heilmaier, J.H. Schneibel, P. Jéhanno, B. Skrotzki, and H. Saage, "The Influence of Silicon on the Strength and Fracture Toughness of Molybdenum", *Materials Science and Engineering A*, 463 (2007) 107-114.

[46] P. Jain, A.P. Alur, and K.S. Kumar, "High Temperature Compressive Flow Behavior of a Mo-Si-B Solid Solution Alloy", *Scripta Materialia*, 54 (2006) 13-17.

[47] F. Chu, D.J. Thoma, K.J. McClellan, P. Peralta, F.X. Li, and E. Fodran, "Processing and Properties of $Mo_5Si_3$ Single Crystals and Alloys", *MRS Symposium Proceedings*, 552 (1999) KK6.7.2

[48] K. Ihara, K. Ito, K. Tanaka, and M. Yamaguchi, "Mechanical Properties of $Mo_5SiB_2$ Single Crystals", *Materials Science and Engineering A*, 329-331 (2002) 222-227.

[49] I. Rosales, "Synthesis and Characterization of $Mo_3Si$ Single Crystal", *Journal of Crystal Growth*, 310 (2008) 3833-3836.

[50] A. Misra, J.J. Petrovic, and T.E. Mitchell, "Microstructures and Mechanical Properties of a $Mo_3Si$-$Mo_5Si_3$ Composite", *Scripta Materialia*, 40 (2) (1999) 191-196.

[51] K. Ito, K. Ihara, K. Tanaka, M. Fujikara, and M. Yamaguchi, "Physical and Mechanical Properties of Single Crystals of the $Mo_5SiB_2$ Phase in the Mo-Si-B System", *Intermetallics*, 9 (2001) 591-602.

[52] H. Choe, D. Chen, J.H. Schneibel, and R.O. Ritchie, "Ambient to High Temperature Fracture Toughness and Fatigue-Crack Propagation Behavior in a Mo-12Si-8.5B (at.%) Intermetallic", *Intermetallics*, 9 (2001) 319-329.

[53] C.T. Liu, J.H. Schneibel, and L. Heatherly, "Processing, Microstructure, and Properties of Multiphase Mo Silicide Alloys", *MRS Symposium Proceedings*, 552 (1999) KK6.2.

[54] A.P. Alur and K.S. Kumar, "Monotonic and Cyclic Crack Growth Response of a Mo-Si-B Alloy", *Acta Materialia*, 54 (2006) 385-400.

[55] D.A. Helmick, G.H. Meier and F.S. Pettit, "The Development of Protective Borosilicate Layers on a Mo-3Si-1B (Weight Percent) Alloy," *Metallurgical and Materials Transactions*, 36 (12) (2005) 3371-3383.

[56] T.A. Parthasarathy, M.G. Mendiratta, and D.M. Dimiduk, "Oxidation Mechanisms in Mo-Reinforced $Mo_5SiB_2$(T2)-$Mo_3Si$ Alloys," *Acta Materialia*, 50, (7) (2002) 1857-1868.

[57] M.G. Mendiratta, T.A. Parthasarathy, and D.M. Dimiduk, "Oxidation Behavior of αMo-$Mo_3Si$-$Mo_5SiB_2$ (T2) Three Phase System", *Intermetallics*, 10 (2002) 225-232.

[58] O.V. Mazurin, Handbook of Glass Data: Part A, New York: Elsevier, 1983.

[59] R. Sakidja, F. Rioult, J. Werner, and J.H. Perepezko, "Aluminum Pack Cementation of Mo–Si–B Alloys," *Scripta Materialia*, 55 (2006) 903–906.

[60] P. Jéhanno, M. Böning, H. Kestler, M. Heilmaier, H. Saage, and M. Krüger, "Molybdenum Alloys for High Temperature Applications in Air", *Powder Metallurgy*, 51 (2) (2008) 99-102.

[61] F. Rioult, N. Sekido, R. Sakidja, and J.H. Perepezko, "Aluminum Pack Cementation on Mo-Si-B Alloys", *Journal of The Electrochemical Society*, 154 (11) (2007) C692-C701.

[62] C. Houngninou, S. Chevalier, and J.P. Larpin, "Synthesis and Characterization of Pack Cemented Aluminide Coatings on Metals", *Applied Surface Science*, 236 (2004) 256-269.

[63] L.E. Olds and G.W.P. Rengstorff, "Effects of Oxygen, Nitrogen, and Carbon on the Ductility of Cast Molybdenum", *Journal of Metals*, February (1956) 150-155.

[64] R.V. Krishnarao and J. Subrahmanyam, "Sintering of $MoSi_2$ by Reacting (Mo+$Si_3N_4$) Compacts", *Materials Science and Engineering A*, 352 (2003) 340-343.

[65] S. Singh, M.M. Godkhindi, R.V. Krishnarao, and B.S. Murty, "Synthesis of $Si_3N_4$- $MoSi_2$ In Situ Composites from Mechanically Activated (Mo+$Si_3N_4$) Powders", *Journal of Alloys and Compounds*, 381 (2004) 254-257.

[66] E. Benko and A. Wyczesany, "Calculations of the Chemical Equilibria in the Mo-B-N System", *Journal of the European Ceramic Society*, 14 (1994) 557-562.

[67] J. Edgar, Properties of Group III Nitrides, London: INSPEC, 1194.

[68] V.L. Solezhenko, "Thermodynamics of Dense Boron Nitride Modifications and a New Phase P,T Diagram for BN", *Thermochimica Acta*, 218 (1993) 221-217.

[69] I. Barin, Thermochemical Data of Pure Substances, 3rd Ed., Weinheim: VCH, 1995.

[70] E. Heikinheimo, A. Kodenstov, J.A. Van Beek, J.T. Klomp, and F.J.J. Van Loo, "Reactions in the Systems Mo-$Si_3N_4$ and Ni-$Si_3N_4$", *Acta Metallurgica Materialia*, 40 (Suppl.) (1992) S111-S119.

[71] A. Kumar and B.L. Eyre, "Grain Boundary Segregation and Intergranular Fracture in Molybdenum", *Proceedings of the Royal Society of London: Series A, Mathematical and Physical Series*, 370 (1743) (1980) 431-458.

[72] N. Solak, F. Ustel, M. Urgen, S. Aydin, and A.F. Cakir, "Oxidation Behavior of Molybdenum Nitride Coatings", *Surface and Coatings Technology*, 174-175 (2003) 713-719.

[73] H. Jenn and P. Ettmayer, "The Molybdenum-Nitrogen Phase Diagram", *Journal of the Less-Common Metals*, 58 (1978) 85-98.

[74] S. Suzuki, H. Matsui, and H. Kimura, "The Effect of Heat Treatment on the Grain Boundary Fracture of Recrystallized Molybdenum", *Materials Science and Engineering*, 47 (1981) 209-216.

[75] A.V. Krajnikov, A.S. Drachinskiy, and V.N. Slyunyaev, "Grain Boundary Segregation in Recrystallized Molybdenum Alloys and its Effect on Brittle Intergranular Fracture", *Refractory Metals and Hard Materials*, 11 (1992) 175-180.

[76] A. Kumar and B.L. Eyre, "An Electron Microscope Study of $Mo_2C$ Precipitates in Molybdenum – I. Crystallographic Relationships", *Acta Metallurgica*, 26 (1978) 569-577.

[77] P.S. Rudman, "The Solubility Limit and Diffusivity of Carbon in Molybdenum", *Transactions of the Metallurgical Society of AIME*, 239 (1967) 1949-1954.

[78] Büchi Mini Spray Dryer B-191 Operation Manual, Büchi Labortechnik AG, Flawil, Switzerland, 2000.

[79] Büchi Mini Spray Dryer B-290 Training Papers – Spray Drying, Büchi Labortechnik AG, Flawil, Switzerland.

[80] H. Berger, Ultrasonic Liquid Atomization: Theory and Application, New York: Partridge Hill, 2006

[81] R.A. Alfintseva, "Behavior of Boron Nitride and Aluminum Nitride Particles in a Molybdenum Matrix", *Powder Metallurgy and Metal Ceramics*, 10 (1971) 65-68.

[82] D. Palik and G. Ghosh, Handbook of Optical Constants of Solids, San Diego: Academic Press, 1998.

[83] L. Lutterotti; MAUD, version 2.062, www.ing.unitn.it/~maud/index.html

[84] R. Jenkins and R.L.Snyder, Introduction to X-Ray Powder Diffractometry, New York, NY: J. Wiley, 1996.

[85] W. Rasband; ImageJ, version 1.38x, http://rsb.info.nih.gov/ij/

[86] E. Underwood, Quantitative Stereology, Reading, MA: Addison-Wesley, 1970.

[87] A. Tewari, A.M. Gokhale, J.E. Spowart, and D.B. Miracle, "Quantitative Characterization of Spatial Clustering in Three-Dimensional Microstructures Using Two-Point Correlation Functions", *Acta Materialia*, 52 (2004) 307-319.

[88] R. Sakidja, H. Sieber, and J.H. Perepezko, "The Formation of Mo Precipitates in a Supersaturated $Mo_5SiB_2$ Intermetallic Phase", *Philosophical Magazine Letters*, 79 (6) (1999) 351-357.

[89] D.W. Richerson, Modern Ceramic Engineering, New York: Marcel Dekker, 1992.

[90] P. Jain and K. S. Kumar, "High Temperature Mechanical Behavior of a Mo-Si-B Solid Solution Alloy", *MRS Symposium Proceedings*, 980 (1999) 303-308.

[91] J. Schlichting, "Oxygen Transport Through Glass Layers Formed by a Gel Process", *Journal of Non-Crystalline Solids*, 63 (1984) 173-181.

[92] M. Hansen, Constitution of Binary Alloys, New York: McGraw-Hill, 1958.

[93] R.L. Meek, "Diffusion Coefficient for Oxygen in Vitreous $SiO_2$", *Journal of the American Ceramic Society*, 56 (6) (1973) 341-342.

[94] K. Kajihara, T. Miura, H Kamioka, M. Hirano, L. Skuja, and H. Hosono, "Spontaneous Oxygen Loading into $SiO_2$ Glass by Thermal Annealing", *Journal of Non-Crystalline Solids*, 349 (2004) 205-208.

[95] F.J.Norton, "Permeation of Gaseous Oxygen Through Vitreous Silica", *Nature*, 4789, (1961) 701.

[96] Doremus, Handbook of Glass Properties, New York: Academic Press, 1986.

[97] G.W. Scherer and T. Garino, "Viscous Sintering on a Rigid Substrate", *Journal of the American Ceramic Society*, 68 (4) (1985) 216-220.

[98] M.F. Yan, J.B. Macchesney, S.R.Nagel, and W.W. Rhodes, "Sintering of Optical Wave-Guide Glasses", *Journal of Materials Science*, 15 (1980) 1371-1378.

[99] K. Kajihara, T. Miura, H Kamioka, M. Hirano, L. Skuja, and H. Hosono, "Surface Dissolution and Diffusion of Oxygen Molecules in $SiO_2$ Glass", *Journal of the Ceramic Society of Japan*, 112 (10) (2004) 559-562.

[100] A.D. Belegundu, Optimization Concepts and Applications in Engineering, New Jersey: Prentice Hall, 1999.

# VITA

Michael Robert Middlemas was born and raised in Salt Lake City, Utah. He graduated from Murray High School in 1997. Michael attended the University of Utah and received a Bachelor of Science in Materials Science and Engineering with an emphasis on Ceramics and a Chemistry minor in 2003. While at the University of Utah, he conducted research at Ceramatec, Inc. where he completed his senior thesis entitled *Mixed-Potential Based Ceramic Sensors for Real-Time On-Vehicle $NO_x$ Monitoring for Mobile Sources*. He spent a semester abroad at the Luleå University of Technology in Luleå, Sweden and spent a summer at the Georgia Institute of Technology participating in the Summer Undergraduate Research Fellowship program under Dr. Michael Sacks.

Michael began his graduate studies at the Georgia Institute of Technology in the fall of 2003. He conducted his master's research under Dr. Joe Cochran and graduated with a Master of Science degree in Materials Science and Engineering in 2005 after completing his thesis entitled *A Nitride-Based Reaction for the Formation of a Three-Phase Molybdenum-Silicon-Boron Intermetallic Alloy*. Michael continued his graduate research with Dr. Cochran and graduated with his Doctor of Philosophy in Materials Science and Engineering with his dissertation entitled *Formation, Strength and Oxidation of Molybdenum-Silicon-Boron Alloys from Reaction Synthesis.*

Outside of his research, Michael is an active participant in the Georgia Tech outdoor recreation program, serving as a trip leader for the whitewater rafting and kayaking schools. Michael also enjoys road and mountain biking, cooking, and travelling. Michael is joined in celebrating the completion of his Ph.D. by his family. His father Bob Middlemas works as the buildings/grounds supervisor at Antelope Island State Park in Utah. Michael's mother Leslie Campbell is the librarian at Liberty Elementary School in Murray, Utah and his stepfather, Brad Campbell, works as the Director of Sales at Pemco Technologies.